EXPERIMENTAL INVESTIGATION MODELING AND OPTIMIZATION OF FRICTION STIR WELDING PROCESS

Thesis submitted to
Indian Institute of Technology Guwahati
for the award of the degree

Doctor of Philosophy

by

Biswajit Parida

Under the supervision of

Dr. Sukhomay Pal

Department of Mechanical Engineering
Indian Institute of Technology Guwahati
Guwahati 781039, Assam, India

January 2015

Department of Mechanical Engineering
Indian Institute of Technology Guwahati
Guwahati-781039
INDIA

CERTIFICATE

It is certified that the work contained in the thesis entitled "**EXPERIMENTAL INVESTIGATION MODELING AND OPTIMIZATION OF FRICTION STIR WELDING PROCESS"** submitted by **Mr. Biswajit Parida** to the Indian Institute of Technology Guwahati for the award of the degree of Doctor of Philosophy has been carried out under my supervision in the Department of Mechanical Engineering, Indian Institute of Technology Guwahati. This work has not been submitted elsewhere for the award of any other degree or diploma.

The thesis, in my opinion, has reached the standard fulfilling the requirements for the award of degree of Doctor of Philosophy in accordance with the regulations of the Institute.

Dr. Sukhomay Pal
Associate Professor
Department of Mechanical Engineering
Indian Institute of Technology Guwahati
Guwahati - 781039
INDIA

Dedicated to……

Mr. Rabindra Kumar Parida
Mrs. Minakhi Parida
My parents for their blessing and guidance…..

Mrs. Minarbha Parichha
My wife for her great understanding and encouragement…..

Master Baibhab Sampann Parida
My son for his love and affection…..

Dr. Subhrajit Parida
Mrs. Biswajita Nayak
My brother and sisters for their love, affection and inspiration…..

All of my Teachers and Friends
……for their inspiration, guidance and constant motivation.

Acknowledgement

I wish to express my deep gratitude to all those who have helped me in various ways during the tenure of my PhD work at IIT Guwahati. I have been supported and accompanied by many people and each one has played an indispensable role during my work. I am grateful to all of them.

I am greatly indebted to my supervisor Dr. Sukhomay Pal who inspired me to pursue research in the field of manufacturing. I am highly grateful to him for his guidance and encouragement during the research work. Without his support, advice and motivation, it would have just been an impossible task for me to carry over this research work. I am always gratitude to my supervisor for his endless freedom, encouragement, and motivation which he has provided to achieve this goal.

I would like to thank my doctoral committee chairman, Professor P. S. Robi for his valuable suggestions and encouragement during the period of my research work. Also, I would like to extend my appreciation to my doctoral committee members Dr. Pankaj Biswas and Dr. Chandan Das for their constructive criticisms and helpful suggestions which make thesis improvement. I am also grateful to the past and present heads of the mechanical engineering department Professor D. Chakraborty, Professor P. Mahanta and Professor A. K. Das for extending various facilities during the tenure of my doctoral programme.

I wish to express my sincere thanks to Mr. Sanjib Sarma, Mr. Rituraj Saikia, Mr. Pranjaul Pal, Mr. Jiten Basumatary, Mr. Nip Borah and Mr. Saiffuddin Ahmed, for their assistance whenever needed during experimentation. I am very much thankful to the Ex workshop superintendent Dr. D. K. Sharma and workshop staff Mr. Nandan Kanan Das, Mr. Chandan Banikya, Mr., Dilip Chetri, Mr. Dhaneswar Khaklary, Mr**.** Minesh C. Medhi, Mr., Mrinal Sarma, Mr. Dipak Kr. Deka, Mr. Manoj Kr. Baishya, Mr. Nidul Saikia, and Mr. Upen Gohain for their efficiency and cheerful readiness to help me in fabricating the experimental setup precisely and accurately.

My sincere thanks go to my friends Mr. S Dakhshinamoorthy, Mr. Srikant Prasad, Mr. Prakash Kr. Sahu, Mr. A. Muthuraja, Mr. Purnendu Kr. Mandal, Mr. V. Satheesh kumar, Mr. Bipul Das, Mr. G. N. Shelke, Mr. Deepak Kr. Yaduwanshi, Mr. N Yaadaiah, Mr. N Shiva, Mr. R. Kalidasan, Mr. P.V.S.S. Sreedhar, Mr. D. Anil Kr., Mr. B. M.

Barkachary, Mr. Arpan Kr. Mondal, Dr. Biswajit Nayak, Dr. Ratnakar Das, for their help, support and advice in different occasions of my PhD work.

I shall always be grateful to my parents Mr. Rabindra Kumar Parida and Mrs. Minakhi Parida for their great encouragement, guidance, love, affection, motiivation and warm blessings. The mental support I got from my brother (Dr. Subhrajit Parida), blessings from father in law (Mr. Kusso Parichha) and mother in law (Mrs. Bijoylaxmi Parichha) is very effective and highly influencing. Most deeply, I thank my wife Minarbha for her constant encouragement, support, patience and motivation for the completion of this work. Love and affection of my son (Dudul) and friends (Sumu, Tapu and Manu) are source of inspiration during my entire PhD programme.

I will always remain greatful to my teachers who have shown me a path to move on in my life. I want to give my sincere thanks to Professor Nitish Ranjan Mandal (OENA Dept., IIT Kharagpur), Professor Manas Mohan Mahapatra (ME & Ind. Dept., IIT Roorkee) and Professor Pankaj Biswas (ME Dept., IIT Guwahati) to provide me a platform to start my research work on such a dynamic and emerging field during my Master's research work. I also like to thank my M-Tech supervisor Professor S. Singh (ME Dept., KIIT University) for his motivation and blessings.

I may have missed out a few names in the above list; my sincere apologies are due for any such inadvertent oversight. Finally, I bow my head to the God Almighty in deepest gratitude and ask for his blessings.

22nd January 2015

Biswajit Parida

IIT Guwahati

Abstract

In today's modern world there are a number of different welding techniques that are getting used presently to join different similar as well as dissimilar metals. The number is growing further exponentially with growing demands and rapid progress in science and technology. Friction stir welding (FSW) is relatively an advanced solid state joining process in which no consumable materials are used. It is energy efficient and environment friendly process in which the heat required is generated due to the friction between the rotating tool and workpiece material. In the present work, a low cost simple fixture was developed for locating and clamping workpiece in a milling machine to conduct FSW. It holds the workpiece securely, without any gap formation between the interface during tightening as well as during FSW operations. It does not allow the workpiece to move along the direction of tool travel, due to horizontal force. From the extensive experimental investigation and Taguchi's single response and different multi-objective analysis techniques, it was found that spindle speed (RPM), tool geometry (TG), and pin diameter (PnD) were the three most significant factors of the FSW process. The newly proposed fuzzy assisted grey relational analysis (FZ-GRA) method is found to be suitable for selecting the optimal process parameters in FSW process. Experimental investigation also showed that the tensile properties increase with increasing RPM for all the considered tool geometries especially at lower PnD. Threaded and straight cylindrical tools showed best and least mechanical properties, respectively. The nugget zone hardness value increased with RPM for a particular TG and PnD. The microstructure revealed the phenomena of dynamic recrystallization in NZ, deformed grains in thermo mechanically affected zone and expanded grains in heat affected zone. Fractrographic sample showed ductile fracture for base material as well as good welded joints whereas defective joints showed a mixed mode of fracture. Several experimental cases were considered for finding an appropriate starting point and elimination of end hole defect. It was found that the starting issue i.e. the issue of providing some offset distance at the start of the weld to ensure defect free welding, can be resolved only by providing a proper restriction without adding any extra material. The end hole can be eliminated by providing a small rectangular piece with a size of bigger than the shoulder diameter and by moving the tool pin at some distance away from the end edges of the workpiece. Artificial neural network models were developed for prediction of weld quality parameters. It was found that radial basis function neural network (RBFN) models produce superior prediction as compared to back propagation neural network (BPNN) models for tensile strength, yield strength, ductility and bending angle. On the other hand BPNN model gave superior prediction for hardness. It was also found that the errors in prediction of joint properties from both BPNN and RBFN models are less. Four neuro-evolutionary models were also developed for determination of optimal input parameter setting for maximum weld quality as well as any desired combination of quality parameters. Among the proposed hybrid optimization algorithms particle swarm optimization gives the optimal solution with a relatively low population size and iteration number.

Keywords: Friction stir welding, Clamping system, Taguchi's method, Grey relational analysis, Utility concept, Desirability function approach, FZ-GRA, Artificial neural network, Neuro-evolutionary algorithms, Differential evolution, Particle swarm optimization.

List of Acronyms

% Elng.	% elongation
AA	Aluminium alloy
ACO	Ant colony optimization
Actl. Value	Actual value
AE	Acoustic emission
AL	Axial load
ANFIS	Adaptive neuro-fuzzy inference systems
ANN	Artificial neural network
ANOVA	Analysis of variance
AS	Advancing side
ASTM	American society for testing of materials
Avg.	Average
BA	Bending angle
BCGA	Binary coded genetic algorithm
BLX	Blend crossover
BM	Base material
BPNN	Back propagation neural network
CFD	Computational fluid dynamics
DE	Differential evolution
DF	Degrees of freedom
DFA	Desirability function approach
DOE	Design of experiment
DP	Dual phase
DT	Dwell time
DV	Overall desirability value
EA	Evolutionary algorithm
EC	Eddy current
EDX	Energy-dispersive X-ray spectroscopy

Err.	% Error
ET	Eddy current inspection
FB	Face bend
FE	Finite element
FSP	Friction stir processing
FSW	Friction stir welding
FZ-GRA	Fuzzy-GRA
GA	Genetic algorithm
GA-NN	Genetic-neural system
GFF	Generalized feed-forward
GMAW	Gas metal arc welding
GONNS	Genetically optimized neural network systems
GRA	Grey relational analysis
GRC	Grey relational coefficient
GRG	Grey relational grade
GTAW	Gas tungsten arc welding
H	High
HAZ	Heat affected zone
HRD	Nugget zone hardness
IHS	Harmony search
IR	Infra red
JLR	Joint line remnant
L	Low
LB	Larger-the-better
LHZ	Lower hardness zone
LM	Between low and medium
M	Medium
Max	Maximum
MFF	Modular feed-forward
MH	Between medium and high
Min	Minimum
MLFC	Multilevel adaptive fuzzy control
MLNN	Multi layers neural network
MPA-UT	Matrix phased array ultrasonic testing
MPCI	Multi-performance characteristic index
MS	Mean square deviation
MSE	Mean square error
NDE	Non-destructive evaluation
NDT	Non-destructive testing
NHN	Number of hidden neurons

NZ	Nugget zone
OA	Orthogonal array
PCBN	Polycrystalline cubic boron nitride
PD	Plunge depth
PnD	Pin diameter
Pred. Value	Predicted value
PSO	Particle swarm optimization
RB	Root bend
RBF	Radial basis function
RBFN	Radial basis function networks
RCGA	Real coded genetic algorithm
RPM	Tool revolution per minute
RS	Retreating side
RT	Radiographic inspection
SAW	Submerged arc weldment
SAXS	Small angle X-ray scattering
SB	Smaller-the-better
SBX	Simulated binary crossover
SC	Straight cylindrical
SD	Shoulder diameter
SEM	Scanning electron microscope
SN	Signal to noise
SOM	Self organizing map
SQ	Square
SS	Sum of squares
SZ	Stir zone
TA	Tilt angle
TC	Tapered cylindrical
TE	Tensile elongation
TFC	Tool with fillet and cavity
TFS	Tool with fillet and scroll
TG	Tool geometry
THRD	Threaded
TIG	Tungsten inert gas welding
TMAZ	Thermo-mechanically affected zone
TPL	Tool pin length
TRIP	Transformation induced plasticity
UC	Utility concept
UT	Ultrasonic inspection
UTS	Ultimate tensile strength

UV	Utility values
VH	Very high
VL	Very low
VVH	Very very high
VVL	Very very low
WBT	Weld bead thickness
WS	Welding speed
YS	Yield strength

Nomenclature

Z_i	Observed values of the i^{th} performance characteristic
$u_{ij,G+1}$	Trial vectors
$\|Y_i - C_j(n)\|^2$	Euclidean norm
$\overline{\Gamma_i}$	Mean GRG/UV/DV/MPCI value at the optimal level
$\hat{\Gamma}$	Predicted GRG, UV, DV and MPCI values
Γ_m	Total mean GRG/UV/DV/MPCI values
A_i^j	Area of the output's j^{th} membership function at i^{th} rule
$C_j(n)$	The j^{th} centre of the Gaussian function at the n^{th} iteration
$E_k^p(n)$	Error
$O_f(i)$	Objective function of the i^{th} individual in the population
$O_{jH}^p(n)$	Output from the j^{th} hidden neuron and k^{th} output neuron for p^{th} pattern
$O_{kO}^i(n)$	Output from k^{th} output neuron for i^{th} input pattern at the n^{th} iteration
$O_{kO}^p(n)$	Output of k^{th} output neuron for p^{th} pattern at the n^{th} iteration
$R_j^i(n)$	Output of j^{th} hidden neuron
$S_{kO}^i(n)$	Weighted sum of the k^{th} output neuron with i^{th} input pattern in the n^{th} iteration
T_k^p	Target output
$U_i(Z_i)$	Utility of the i^{th} attribute
$V_D(s_i)$	Decoded value of the string s_i
Y_i^p	The value of the i^{th} input neuron for the p^{th} pattern
$Z_i^{'}$	Minimum acceptable values of the i^{th} performance characteristic
$c_1 \& c_2$	Acceleration coefficients
$d_{max}(n)$	Maximum distance between chosen centers at the n^{th} iteration

f_i	Fitness of the i^{th} individual in the population
l_i	String length used to code the i^{th} parameter
par_i^t	i^{th} particle at the t^{th} iteration
$r_1 \& r_2$	Random numbers
$v_i^{(t)}$	Velocity of the i^{th} particle at the t^{th} iteration
$x_0^*(k)$	Reference sequence
$x_i^*(k)$	Comparability sequence
$\Delta_{0i}(k)$	Deviation sequence
γ_i	Grey relational grade
$\mu_S(x)$	Membership function
$\xi_i(k)$	Grey relational coefficient
$\sigma_j(n)$	Width of the Gaussian function at the n^{th} iteration
ω_i	Inertia added to the i^{th} particle
b_H	Bias at the hidden layer
b_O	Bias at the output layer
D	Single valued composite desirability
F	Constant factor
F-value	Fisher's ratio
L_H	Number of hidden neurons
L_i	Lower specification limit
L_I	Number of input neurons
L_O	Number of output neurons
O_i	Output of i^{th} neuron of the output layer
P	Total number of training patterns
P_i	Preference number
P-value	Probability of significance
Q_{ij}	Response of the i^{th} quality characteristics in the j^{th} experiment
R	Total number of rules
S	Activation function
S_j	j^{th} linguistic label or fuzzy set S
SS_e	Sum of squared deviations due to error
SS_F	Sum of squared deviations due to each factor
SS_T	Total sum of squared deviations about the mean
T_i	Target value
V_{ij}	Connection weight between the i^{th} input neuron and the j^{th} hidden neuron

$W_{\%\ Elng.}$	Weight assigned to the % Elng
W_{HRD}	Weight assigned to the HRD
W_i	Weight assigned to the i^{th} quality characteristic
w_i	Firing strength of the i^{th} rule
W_{jk}	Connection weight between the j^{th} hidden neuron and the k^{th} output neuron
W_{UTS}	Weight assigned to the UTS
W_{WBT}	Weight assigned to the WBT
W_{YS}	Weight assigned to the YS
$x_i(k)$	Response for the k^{th} performance characteristics of i^{th} experiment
X_{ij}	Measure of performance of i^{th} alternative with respect to j^{th} criteria
Y_i	i^{th} input data to the input layer
y_{max}	Maximum value of any parameter in the dataset under consideration
y_{min}	Minimum value of any parameter in the dataset under consideration
y_{norm}	Normalized value
α	Momentum co-efficient
γ_j	Mean response for j^{th} experiment
γ_m	Grand mean of the response
ζ	Distinguishing coefficient
η	Learning rate
η_1	Learning rate 1 (Weight)
η_2	Learning rate 2 (Center)
η_3	Learning rate 3 (Spread of Gaussian function)
η_j	SN ratio
$\mu_s(x)$	Membership function
$S(y)$	Logistic sigmoid function
$max\ x_i(k)$	Largest value of $x_i(k)$
$min\ x_i(k)$	Smallest value of $x_i(k)$

List of Figures

List of Tables

Contents

Chapter 1

Introduction

1.1 Background and Motivation

The history of joining metals goes back several millennia, with the earliest examples of welding from the Bronze Age and the Iron Age. From that time the process of welding has gone through several modifications, world wars caused a major surge in the use of welding processes, with the various military powers attempting to determine which of the several new welding processes would be the best. In today's modern world there are a number of different welding techniques to join different similar as well as dissimilar metals. They range from the conventional gas welding to laser welding. The three general categories in which all the types of welding can be divided are solid state welding, liquid state or fusion welding and solid-liquid state joining.

The fusion welding process involves the chemical bonding of the metal in the molten stage and may need a filler material. This filler material may be in the form of rod or a spool of wire. The process may also need an inert ambience in order to avoid oxidation of the molten metal. The major disadvantages in these welding techniques lies in melting and solidification of the metal to form the joint. This causes the joint properties such as tensile strength, fatigue strength and ductility of the weld to deteriorate. The disadvantages also include distortion, porosity, oxidation, micro segregation, hot cracking and other microstructural defects in the joint. It also limits the combination of the metals that can be

joined because of the different thermal coefficients of conductivity and expansion for different metals.

The solid state welding is the process where the joint is produced at temperature below the melting point temperature of the base metal without any filler material or inert ambience. In this type of welding the metals being joined retain their original properties as melting does not occur in the joint and the heat affected zone (HAZ) is also very small compared to fusion welding techniques where most of the deterioration of the strengths and ductility begins. Dissimilar metals can also be joined with ease as the thermal expansion coefficients and the thermal conductivity coefficients are less important as compared to fusion welding. Friction stir welding (FSW) is a newly developed solid state joining method in which the joined material is plasticized by the frictional heat generated between the surface of the plates to be welded and the contact surfaces of a special rotating tool. The tool is composed of two main parts, namely shoulder and pin. Shoulder is responsible for the generation of heat and containing the plasticized material in the weld zone, while pin mixes the material of the components to be welded, thus creating a joint. Though tools are designed for different applications may have slightly different shapes of the tool pin and shoulder, all tools maintain this same two elemental design. The schematic diagram of FSW process is shown in **Fig. 1.1**.

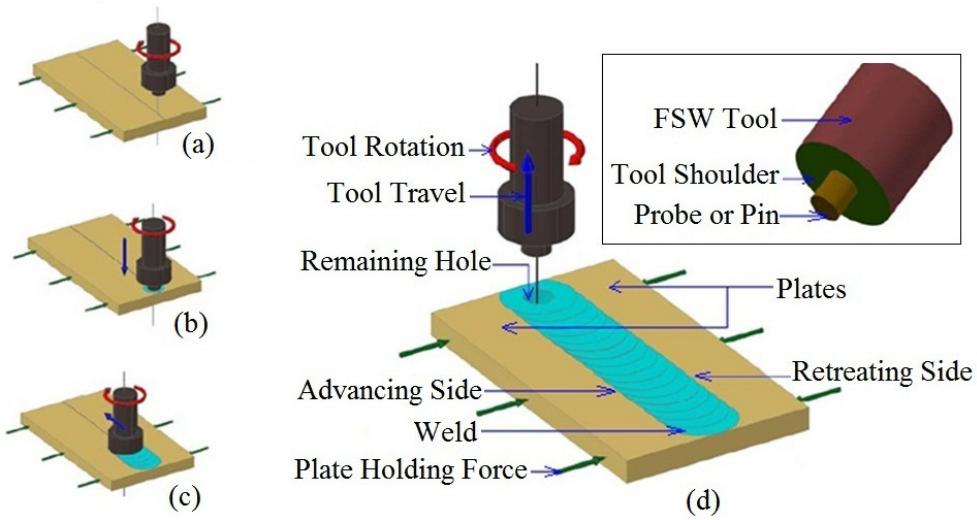

Figure 1.1 Friction stir welding process (a) positioning of plates, (b) pin and shoulder penetration, (c) tool travel and (d) pin removal.

The four basic steps involved in the process (shown in **Fig. 1.1**) can be stated as follows:

a) Positioning of the workpiece material so that the tool should travel along the joint line.

b) Tool penetration or plunging into the workpiece in rotating condition.

c) Tool travel along the joint line.

d) Tool removal at the end of the process leaving a hole of size equal to tool pin.

FSW has a number of process parameters that influences the joint quality both in terms of mechanical and metallurgical properties. The different process variables involved in FSW are shown in **Fig. 1.2**. The involvement of large numbers of process parameters makes it difficult to control the joint properties. However, all of them may not have equal influences on the weld qualities. Therefore, studying the relative importance of process parameters on the individual weld quality parameter and also to the collective quality characteristics are of great important. This may help to identify fewer significant parameters which control the weld properties. The selection of optimal process parameters settings which will ensure the desired weld quality characteristics is another important issue. The minimization of post welding works and material wastage is always important for a production unit. So for FSW process finding an appropriate starting point and elimination of end hole by some low cost methodologies is always going to be useful. Use of soft computational methods to model FSW process can be beneficial as these methods deal with complex and highly interactive processes.

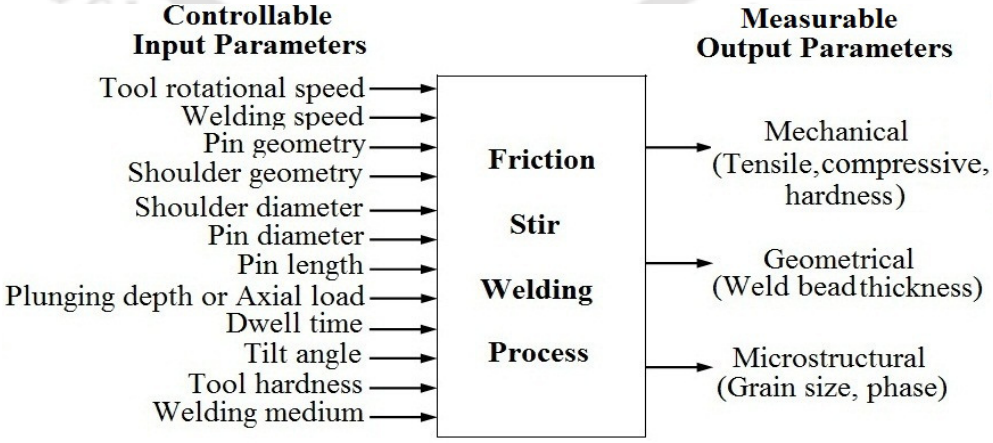

Figure 1.2 Friction stir welding process parameters

Due to the combined effect of frictional heating and plastic deformation, various zones are formed in FSW process. The different zones are shown in **Fig. 1.3**. Unaffected material or base material (BM) is remote from the weld, which has not been deformed. In this zone there is no change in microstructure as it is not affected either thermally or mechanically. HAZ which clearly lays close to the weld center material and experiences transient thermal cycle, which has modified the micro-structure and mechanical properties. In this zone expanded grains are available. Thermo-mechanically affected zone (TMAZ) lies between the HAZ and the nugget zone (NZ). In this region the material is plastically deformed by the stirring action of the friction stir welding tool and also the material is undergone a thermal cycle by the heat from the process. So the grains of the original microstructure are in a deformed state. Usually elongated grains are found in TMAZ. The recrystallized area in the TMAZ in aluminum alloys is called the nugget. It is the one which experiences the most severe plastic deformation and is a consequence of the way in which a tool consolidates material from the front to the back of the weld. The grains of the original microstructure in this region are also more refined than the TMAZ.

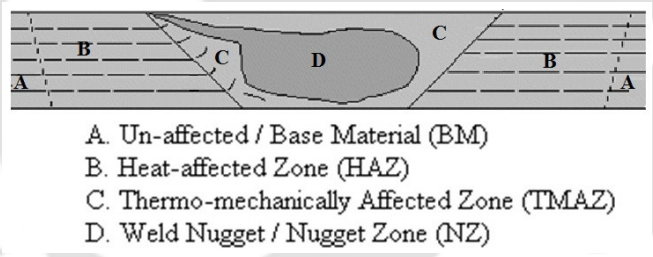

Figure 1.3 FSW joint with four distinct zones

The solid state nature of FSW immediately leads to several advantages over fusion welding methods since any problems associated with solidification are avoided. Issues such as porosity, solute redistribution, solidification cracking and liquation cracking are not prone in FSW. In general, FSW has been found to produce a low concentration of defects and is very tolerant to variations in parameters.

A number of potential advantages of FSW over conventional fusion welding processes have been identified as:

- The joint shows good strength, ductility and fracture toughness.

- Operating temperature below the melting point of the parent metal avoids most of the thermal defects related to conventional fusion welding.
- Very less deformation which makes the process suitable for welding of relatively thin plates.
- Improved safety due to the absence of toxic fumes or the spatter of molten material.
- No consumables - conventional steel tools can weld over 1000 m of aluminum and no filler or gas shield is required.
- Easily automated on a simple milling machine, hence lower setup costs and less training.
- Shows almost similar properties as in parent metals in weld which leads to obtain a structure of different parts as a single one.
- Simplifies dissimilar alloy welding.
- Can operate in horizontal and vertical positions, as there is no molten weld pool.
- Generally good weld appearance and minimal thickness under/over matching, thus reducing the need for expensive machining after welding.
- No grinding, brushing or pickling required in mass production.
- Low environmental impact.

Nevertheless, FSW is associated with few unique limitations. Insufficient weld temperatures, due to low rotational speeds or high traverse speeds, may result in long, tunnel defects running along the weld which may be in surface or subsurface level. Low temperatures may also limit the forging action of the tool and reduce the continuity of the bond between the materials from each side of the weld. Below listed are some of the limitations of FSW process.

- Cannot make joints which required metal deposition.
- Less flexible than manual and arc processes (difficulties with thickness variations and non-linear welds).

- Often slower traverse rate than some fusion welding techniques although this may be offset if fewer welding passes are required.

The FSW process is most suitable for components, which are flat and long (plates and sheets) but can be adapted for pipes, hollow sections and positional welding. The applications of the process are discussed below in detail.

- **Ship Building and Marine Industries:** The shipbuilding and marine industries are two of the first industry sectors, which have adopted the process for commercial applications. The process is suitable for the following applications in: panels for decks, sides, bulkheads and floor, helicopter landing platforms, marine and transport structures, refrigeration plant etc.
- **Aerospace Industry:** At present the aerospace industry is welding prototype parts by FSW. Opportunities exist to weld skins to spars, ribs, and stringers for use in military and civilian aircraft. This offers significant advantages compared to riveting and machining from solid, such as reduced manufacturing costs and weight savings. The process can therefore be considered for: wings, fuselages and empennages, cryogenic fuel tanks for space vehicles, aviation fuel tanks, military and science rockets etc.
- **Railway Industry:** The commercial production of high speed trains made from aluminum extrusions which can be joined by FSW has been published. Applications include: high speed trains, railway tankers and goods wagons, container bodies etc.
- **Land Transportation:** The FSW process is currently being experimentally assessed by several automotive companies and suppliers to this industrial sector for its commercial application. Potential applications are engine and chassis cradles, attachments to hydro formed tubes, truck bodies, mobile cranes and fuel tankers, buses and airfield transportation vehicles, motorcycle and bicycle frames.

- **Other Industry Sectors:** FSW can also be considered for electric motor housing, cooking equipment and kitchens, gas tanks and gas cylinders and connection of aluminum or copper coils in rolling mills.

1.2 Objectives of the Research

The present work aims in developing a simple low cost fixture to carryout FSW operations in a milling machine. Then an extensive experimental investigation need to be carried out to find significant and optimized FSW process parameters and their effect on joint properties. Some experimental methodologies have to be developed to provide a solution for appropriate start point and elimination of end hole and finally modeling of joint quality by soft computational methods. The detail objectives of the thesis work are as follows:

- ✓ Design and develop an adjustable fixture suitable to carry out FSW operations.
- ✓ Investigation of the influences of process parameters on the weld qualities.
- ✓ Studies of various Taguchi assisted multi-objective optimization techniques for FSW application.
- ✓ Investigation to find an appropriate starting point and elimination of end hole defect in a view to maximize the joint length in FSW.
- ✓ Modeling of weld quality using artificial neural network.
- ✓ Optimization of process parameters using neuro-evolutionary techniques.

1.3 Contribution of the Thesis

The important contributions of the present work are summarized as follows:

- A low cost fixture or clamping system has been developed which can be used to carry out FSW operations efficiently on milling machine.
- Detailed experimental investigation considering most of the process parameters has been done to find out their influence on joint properties. A new fuzzy assisted grey Taguchi method has been proposed for the optimization of multiple

weld quality properties. Effect of significant parameters on weld quality has also been studied.

- By applying different experimental approaches solutions to appropriate starting position and end hole type of defect have been achieved. This will prevent the material wastage and post processing work required after welding.
- Computer codes in 'C' programming language have been developed for multi layers neural network (MLNN) and radial basis function networks (RBFN). The prediction capabilities of these neural network models for different input parameters affecting weld quality values have been evaluated. The weld quality values for any combination of process parameters can be determined using the developed models.
- Computer codes in 'MATLAB' programming language have also been developed for Neuro-EAs (Evolutionary Algorithms) models. The optimal parameter setting in FSW process for any desired weld quality parameters can be evaluated through this program.

1.4 Organization of the Thesis

The thesis has been organized in eight chapters. Overviews of the contributions made in those chapters which are as follows:

The *first chapter* is an introductory one, which states the working principle of the friction stir welding process, advantages and applications of FSW in various fields, objectives and contribution of the present work.

The *second chapter* gives a thorough outline of the current state-of-the-art and various developments in FSW process. It gives the brief details of the research work in the area of experimentation, modeling and optimization process carried by the various researchers in this field.

Chapter 3 includes the design, development and fabrication of a low cost clamping system to carry out FSW process in milling machine.

The *fourth chapter* focuses on extensive experimental works which include Taguchi's design of experiments methods, and identification of influencing parameters by single objective as well as multi objective analysis techniques. Finally the detailed effect of the significant parameters on joint properties has been discussed in this chapter.

In *Chapter 5* different experimental cases for finding appropriate starting point and elimination of end hole type of defect have been illustrated.

The overview of ANNs used in the present work is provided in *Chapter 6*. Thereafter weld quality prediction by different ANN models and a comparative study between those models are discussed.

Chapter 7 concerns application of Neuro-EA techniques to process optimization problem, *i.e.*, selection of optimal parameter setting for any desired weld quality parameters.

The *eighth chapter* concludes this thesis and suggests future scopes for research.

Finally, a list of relevant references is presented in *References* and the fuzzy rules base (see Appendix-I) are described in *Appendix*.

Chapter 2

Literature Review

2.1 Introduction

The unique combination of light weight and relatively high strength makes aluminum the second most popular metal for the fabrication of different structures in recent years. The challenges in welding of aluminum alloys are in the selection of correct filler rod and reduction in the amount of heat input to the weld. A feasible solution to overcome these difficulties is the use of FSW, with no use of filler material and considerably less heat input to the welded joint. Also this process has got remarkable advantages over other welding process used to weld Aluminum alloys. It is a solid state welding invented by The Welding Institute (TWI), Cambridge, UK in 1991[Thomas *et al.*, 1991] and creates weld by the combined action of frictional heating and mechanical deformation. The maximum temperature reached is of the order of 0.8 of the melting temperature of base metal. It is being considered as a thermo-mechanical process, which transforms heterogeneous microstructure of base metal to more homogeneous microstructure.

During the last few years, a lot of promising research has been performed on this joining technique and the number of publications has been increasing day by day. **Figure 2.1** depicts the number of research papers published (articles published in the international journals only) since its discovery in 1991. There has been a substantial increase in funding to support the research related to FSW. Number of research publications has also been increased significantly after 2005.The bulk of the FSW published data are related to

aluminum alloys, important results are now available for other metals and alloys. **Table 2.1** and **2.2** give an overview of different similar and dissimilar materials used to weld using FSW process.

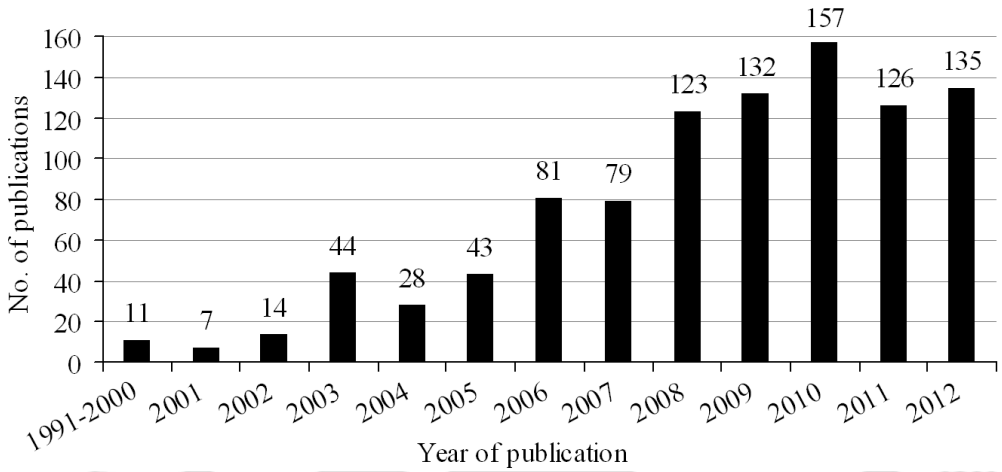

Figure 2.1 Year-wise numbers of publications

The literatures have been divided into different sections according to the present research objectives as well as other important areas of FSW processes and sub-processes. The first section contains the literatures for experimental set up development in a view to carry out FSW in a milling machine and development of a low cost fixture. It is followed by a review of different experimental works and use of different analysis techniques used for finding the influence of process parameters. Various attempts made by different researchers to eliminate the end hole type of limitation in FSW process was reviewed thereafter. Then various modeling and optimization techniques used in FSW process were reviewed. The process defects and different advanced testing techniques are discussed in the next review. Finally few research works related to FSW process condition monitoring have been reviewed. The details of these reviews were discussed in subsequent sections.

Table 2.1 Similar Materials Welded using FSW Process

Material		References
Aluminium	Commercial Grade	[Dequing and Shuhua, 2004; Dalder *et al.*, 2008; Ghosh *et al.*, 2010; Bakavos *et al.*, 2011; Kurt *et al.*, 2011; Parida *et al.*, 2011; Rajakumar and Balasubramanian, 2012; Cui *et al.*, 2012; Yadav and Bauri, 2012]
	Al-4.5Mg-0.26Sc	[Cabello *et al.*, 2011; Subbaiah *et al.*, 2012]
	High-strength age-hardened	[Grujicic *et al.*, 2010]
	Aluminum die casting alloys	[Kim *et al.*, 2006]
	1xxx series	[Boz and Kurt, 2004; Wei *et al.*, 2007; Balasubramanian, 2008; Biswas and Mandal, 2011; Xue *et al.*, 2011]
	2xxx series	[Fonda *et al.*, 2004; Fonda *et al.*, 2007; Elangovan and Balasubramanian, 2008b; Balasubramanian, 2008; Fratini *et al.*, 2009; Arora *et al.*, 2009; Cerri and Leo, 2009; Giles *et al.*, 2009; Cerri *et al.*, 2010; Bitondo *et al.*, 2010; Liu *et al.*, 2011a; El-Hafez, 2011; Zahmatkesh *et al.*, 2010; Arora *et al.*, 2010; Srinivasan *et al.*, 2010; Hui-jie *et al.*, 2010; Rafi *et al.*, 2010; Jolu *et al.*, 2010; Malarvizhi and Balasubramanian, 2011; Aval *et al.*, 2011a; Steuwer *et al.*, 2011; Li *et al.*, 2011; Liu *et al.*, 2011b; Forcellese *et al.*, 2012; -Liang *et al.*, 2012; Xu *et al.*, 2011; Liu *et al.*, 2012; Liu *et al.*, 2012; Zhang *et al.*, 2012; Aydin *et al.*, 2012]
	5xxx series	[Boz and Kurt, 2004; Attallah *et al.*, 2007; El-Danaf *et al.*, 2010; Ghosh *et al.*, 2010; Zhou *et al.*, 2010; Kumbhar *et al.*, 2011; Chen *et al.*, 2011; Karthikeyan and Senthil Kumar, 2011; Miyazawa *et al.*, 2012; Blignault *et al.*, 2012; Haghshenas *et al.*, 2014]
	6xxx series	[Sato and Kokawa, 2001; William and Arbegast, 2003; Boz and Kurt, 2004; Fujii *et al.*, 2006; Scialpi *et al.*, 2007; Tozaki *et al.*, 2007; Adamowski and Szkodo, 2007; Ceschini *et al.*, 2007; Cabibbo *et al.*,

		2007; Liu *et al.*, 2007; Elangovan *et al.*, 2008; Balasubramanian, 2008; Simar *et al.*, 2008; Elangovan and Balasubramanian, 2008a; Cavaliere *et al.*, 2008; Hwang *et al.*, 2008; D'Urso *et al.*, 2009; Cerri and Leo, 2009; Cerri and Leo, 2009; Lakshminarayanan *et al.*, 2009; Toktas and Toktas, 2012; Zhang *et al.*, 2009; Rodrigues *et al.*, 2009; Donati *et al.*, 2009; Chen, 2009; Lammlein *et al.*, 2009; D'Urso and Giardini, 2010; Tansel *et al.*, 2010; Cerri *et al.*, 2010; Rajakumar *et al.*, 2010; Kim *et al.*, 2010; Rajakumar *et al.*, 2011a; Li *et al.*, 2011; Heidarzadeh *et al.*, 2012; Cui *et al.*, 2012]
	7xxx series	[Su *et al.*, 2003; Rhodes *et al.*, 2003; Record *et al.*, 2007; Kumar and Kailas, 2008a; Kumar and Kailas, 2008b; Balasubramanian, 2008; Brown *et al.*, 2009; Robson *et al.*, 2010; Gaafer *et al.*, 2010; Rafi *et al.*, 2010; Azimzadegan and Serajzadeh, 2010; Lorraina *et al.*, 2010; El Rayes *et al.*, 2011; Rajakumar *et al.*, 2011b; Sullivan *et al.*, 2011; Sharma *et al.*, 2012; Gupta *et al.*, 2012]
	8xxx series	[Lertora and Gambaro, 2010]
	Aluminium–silicon based alloys of A319, A356, and A413	[Xue *et al.*, 2011]
	Sc-modified Al-Zn-Mg-Cu alloy	[Ren *et al.*, 2008]
	RDE-40 Al alloy	[Lakshminarayanan and Balasubramanian, 2008]
	Aluminum single crystal	[Fonda *et al.*, 2007]
	Al–Mg–Si alloy	[Ren *et al.*, 2007]
	Al-Cu	[Zhang *et al.*, 2012]
	Al–Cu–Mg–Ag	[Nikulin *et al.*, 2012]
Steel	High Carbon	[Cui *et al.*, 2007; Konkol and Mruczek, 2007; Khodir *et al.* 2012]
	304 stainless steel	[Chen, 2009]
	HSLA-65 steel	[Yeni *et al.*, 2008; Barnes *et al.*, 2012]
	SAF 2205 duplex stainless steel	[Saeid *et al.*, 2008]
	High nitrogen-containing	[Miyano *et al.*, 2011]

	stainless Steel	
	409 SS	[Cho *et al.*, 2011]
	High strength steel	[Miles *et al.*, 2009; Cho *et al.*, 2012; Fujii *et al.*, 2014; Han *et al.*, 2014]
Magnesium	AZ31	[Padmanabhan and Balasubramanian, 2010; Fu *et al.*, 2012; Forcellese *et al.*, 2012; Venkateswarlu *et al.*, 2013]
	Mg-Zn-Y-Zr	[Xie *et al.*, 2007]
	AMX602	[Chen *et al.*, 2012]
	AZ61A	[Rose *et al.*, 2012; Rajakumar *et al.*, 2013b]
	Glass/Mg Alloy	[Shin *et al.*, 2012]
	Mg-3Al-1Zn alloy	[Chen *et al.*, 2013]
Brass	63% Cu-37% Zn	[Cam *et al.*, 2009; Sun *et al.*, 2014; Xu *et al.*, 2014]
	Ti-6Al-4V	[Pilchak *et al.*, 2011; Chen *et al.*, 2011]
	Copper	[Sakthivel and Mukhopadhyay, 2007; Gaafer *et al.*, 2010; Leal *et al.*, 2011]

Table 2.2 Dissimilar Materials Welded using FSW Process

Material		**References**
Aluminium	6061-T6 / 7075-T6	[Colligan, 1999]
	2024-T4 / 7175-T73511	[Buffa *et al.*, 2009]
	A356 / 6061	[Ghosh *et al.*, 2010]
	2024-T4,T3 / 7075-T6	[Khodir and Shibayanagi, 2008; Acerra *et al.*, 2010; Azimzadegan and Serajzadeh, 2010; Silva *et al.*, 2011]
	2219-T87 / 5083-H321	[Koilraj *et al.*, 2012]

	5086 / 6061	[Aval *et al.*, 2011a; Aval *et al.*, 2011b]
	6082-T6 / 2024-T3	[Scialpi *et al.*, 2008; Cerri and Leo, 2009; Cerri *et al.*, 2010]
	5182-H111 / 6016-T4	[Leal *et al.*, 2008]
	2024- T6 / 5083-H321	[Sundaram and Murugan, 2010]
	7175-T7351 / 2024-T4,T3	[Chao *et al.*, 2001; Fratini *et al.*, 2010]
	1050 / 5083	[Sarsilmaz and Caydas, 2009]
	2050-T3 / 7449-TAF	[Eberl *et al.*, 2010]
	5182 / 6022	[Soundararajan *et al.*, 2007]
	5083-O / 6063-T6	[Leal and Loureiro, 2008]
	6061-T6 / 6082-T6	[Moreira *et al.*, 2009]
	5083 / 6082	[Leitao *et al.*, 2012]
Others	Al-5083 / St-12 alloy	[Movahedi *et al.*, 2012]
	6061/ ZrB_2 composite	[Dinaharan and Murugan, 2012]
	Aluminum / Copper	[Zadeh *et al.*, 2008; Galvao *et al.*, 2012]
	6061/(0, 5 and 10 wt.% of ZrB_2)	[Dinaharan and Murugan, 2012]
	5754 / AZ31	[Simoncini and Forcellese, 2012]
	Al / Mg	[Venkateswaran and Reynolds, 2012; Li *et al.*, 2012; Suhuddin *et al.*, 2013]
	Polyethylene / Polyprophylene	[Bozkurt, 2012]

2.2 Literature-1: Experimental Set-Up Development

Now-a-days readymade FSW machines [Dequing and Shuhua, 2004; Fujii *et al.*, 2006; Tozaki *et al.*, 2007; McNelley *et al.*, 2008; Xue *et al.*, 2011; Rajakumar *et al.*, 2011a and 2011b] are available. But these machines are expensive. Alternatively, a modified vertical milling machine can be used as FSW machine [Boz and Kurt, 2004; Scialpi *et al.*, 2007; Record *et al.*, 2007; Elangovan *et al.*, 2008; Hwang *et al.*, 2008; Elangovan and Balasubramanian, 2008a; Elangovan and Balasubramanian, 2008b; Kumar and Kailas, 2008a; Kumar and Kailas, 2008b; Parida *et al.*, 2011; Movahedi *et al.*, 2012; Sharma *et al.*, 2012; Aydin *et al.*, 2012; Toktas and Toktas, 2012]. The key issues in adapting a milling machine as FSW machine include design of a proper fixture to hold the workpiece, position it correctly with respect to the FSW tool, and support it during welding operation and measurement of forces acting on the workpiece. When the FSW tool is plunged into the workpiece interface, it applies a lateral force to the workpiece and hence the gap increases. The main problem of this gap is that, the material extruded from the processing zone and the welded part's effective cross-sectional area around the gap decreases. This can cause defective or weak weld. Different forces generated during the process are shown in **Fig. 2.2**.

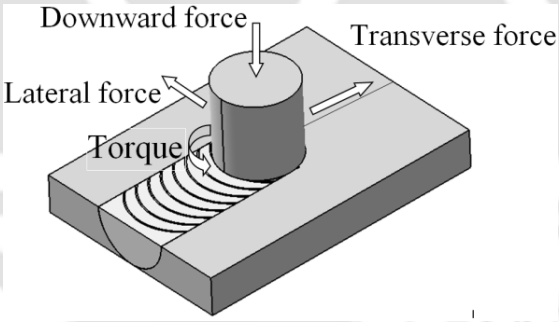

Figure 2.2 Forces acting during FSW process

Richter-Trummer *et al.* [2012] found that higher clamping forces lead to lower distortion and a more uniform residual stress distribution through the thickness. Record *et al.* [2007] reported plunge depth as one of the most significant factors of the FSW process which in turn depends upon plunging or downward force. The variations in axial force produced welds with inconsistent microstructure and tensile strength [Davis *et al.*, 2010]. Kandasamy *et al.* [2011] prepared a special fixture with a heating element and a copper

backing plate for reducing the temperature gradient. They found superior mechanical properties compared to conventional one due to uniform extrusion of alloys. Fratini *et al.* [2010] prepared a fixture to overcome the shortcomings of FSW of titanium alloys with particular attention to the choice of the materials and to the cooling systems, both under the backing plate and around the tool. Baghel [2012] developed a fixture that accommodates both backing plate and metal plate to be welded.

The key issues during the FSW processes are:

- Requirement of milling machine with high spindle motor power.
- A sufficiently rigid set up to avoid vibration during the welding process.
- Alignment of tool travel with the joint line.
- To minimize the presence of gap between the workpieces.
- To restrict the sidewise as well as the transverse movement of the workpiece during welding process.

The gap and the objective relevant to the current literature survey is listed below,

➢ **Gap:**

The fixture required to carry out FSW process efficiently in a conventional milling machine is not well discussed.

➢ **Objective-1:**

Design and fabrication of a low cost adjustable fixture for a vertical milling machine to hold and support the base material to be welded.

2.3 Literature-2: Experimental Investigation

There are a number of parameters affecting FSW process. They are in terms of joint properties both in mechanical and metallurgical aspect. In material flow the tool geometry plays a vital role which governs the traverse rate at which FSW can be conducted. The tool design also governs the heat generation, plastic flow, power required and the uniformity of microstructure and mechanical properties. The parameters that affect the weld quality are the machine spindle speed or tool revolution per minute (RPM), the rate at which tool travels or

welding speed (WS), axial load (AL) or plunge depth (PD), tool geometry (TG), pin diameter (PnD or d), shoulder diameter (SD or D), tool pin length (TPL), dwell time (DT), tilt angle (TA), tool hardness, number of passes, welding medium etc.

In FSW process the heating results primarily from the friction between pin and workpiece in the initial stage of tool plunge [Heidarzadeh *et al.*, 2012]. The function of the tool is to 'stir' and 'move' the material at the same time the shoulder provides confinement for the heated volume of material [Boz and Kurt, 2004; Elangovan *et al.*, 2008; Elangovan and Balasubramanian, 2008a; Tozaki *et al.*, 2007; Elangovan and Balasubramanian, 2008b; Leal and Loureiro, 2008]. Two very important parameters in FSW process are the tool rotation rate in clockwise or counter-clockwise direction and the tool traverse speed. The heat generation rate, temperature field, cooling rate, force, torque, and the power depend on these variables [Record *et al.*, 2007; Zhang *et al.*, 2009; Dinaharan and Murugan, 2012]. Another important process parameter is the angle that the tool makes with the vertical axis *i.e.* tilt angle. A suitable tilt of the spindle towards trailing direction ensures that the shoulder of the tool holds the stirred material and moves it efficiently from the front to the back of the pin. Further, the insertion depth of pin into the workpieces is important for producing sound welds. The important reviews on different process parameters and their effects on mechanical and metallurgical properties are discussed in following sections and sub-sections.

2.3.1 Process Parameters

2.3.1.1 Tool Geometry

The tool pin dimensions are critical to produce sound weld [Dequing and Shuhua, 2004]. Scialpi *et al.* [2007] studied the influence of shoulder geometry on microstructure and mechanical properties of friction stir welded 6082 aluminum alloy. They found that the tool with fillet and cavity (TFC) crown was the best in terms of crown quality and tool with fillet and scroll (TFS) and TFC showed a higher strength and elongation. Fujii *et al.* [2006] reported that for 1050-H24 material a columnar tool without threads was the best in terms of mechanical properties. The tool shape was not significant for 6061-T6. The triangular prism tool and the tool having column with threads were suitable for high and medium rotational speeds. The tool shape was not significant for lower rotational speeds. Boz and Kurt [2004]

concluded that screw type tool with higher pitch acted like a drill rather than a stirrer and propelled the weld metals outwards. As a result of this weld metal was accumulated towards the stirrer shoulder and therefore the welding process could not be affected. The best bonding was obtained with lower pitched stirrers but it had no effect on mechanical and metallographic properties. The square cross-section stirrer showed poor mechanical and metallographic properties.

Elangovan and other researchers [Elangovan *et al.*, 2008; Elangovan and Balasubramanian, 2008a; Elangovan and Balasubramanian, 2008b] studied the effects of tool pin profile on the formation of FSP/FSW zone in 6061and 2219 Al alloy. They found that square pin profiled tools produced defect-free region. The joints produced by square pin tool showed superior tensile properties. The tool shape was not significant for lower rotational speeds. The square cross-section stirrer showed poor mechanical and metallographic properties. Also in friction stir spot welds of 6061 Al alloy the tensile shear strength increased with increasing probe length [Tozaki *et al.*, 2007], while the cross-tension strength was not affected significantly by probe length. Kumar and Kailas [Kumar and Kailas, 2008b] observed that the pin transfers the material layer by layer, while the shoulder transfers the material by bulk. They also observed onion ring pattern in the weld zone. It is formed due to the combined effect of geometric nature of the pin driven material flow and vertical movement of the material due to shoulder interaction. The FSW of T-joints requires a large amount of heat input due to the necessary forging action aimed to fulfill the joint fillets [Acerra *et al.*, 2010]. A slight increase of tool shoulder diameter permit to obtain sound welds even with larger tool feed rate [Acerra *et al.*, 2010].

D'Urso and Giardini [2010] found that threaded tool was effective compared to plane tool for AA6022-T4 aluminum alloy lap joints. Leal *et al.* [2011] found that the tools with conical cavity shoulders require higher spindle torques than flat shoulder tools. It had lesser effect on microstructure, hardness and the formation of defects compared to the rotational speed. Bigger tool provides higher joint resistance [Donati *et al.*, 2009], but sometimes high temperatures may be reached in T-joints of AA6082-T6 aluminium alloy. Leal *et al.* [2008] found welds with excellent appearance but some reduction in thickness when used tool shoulder with conical cavity. Whereas scrolled tool shoulder gave less smooth weld without reduction in thickness. In case of scrolled tool shoulder, the amount of material moved from

the advancing to the retreating side of the tool was much higher than that of conical cavity tool.

Out of different considered tool pin geometries in previous studies straight cylindrical tools produced weakest joints compared to other tool geometries [Elangovan and Balasubramanian, 2007; Shanmuga Sundaram and Murugan, 2010]. But due to its lowest fabrication cost and best self cleaning phenomena (increases the tool life and its pin profile effectiveness) it is the most widely used type of TG. Apart from basic straight cylindrical tool pin, many researchers used different types of tool pin geometries in order to investigate their effects on joint properties. These are tapered cylindrical [Liu *et al.*, 2012; Imam *et al.*, 2013; Sharma *et al.*, 2012; Elangovan and Balasubramanian, 2007; Elangovan and Balasubramanian, 2008b], threaded [Boz and Kurt, 2004; Elangovan and Balasubramanian, 2007; Elangovan and Balasubramanian, 2008b; Rajakumar *et al.*, 2011b; Silva *et al.*, 2011; Liang *et al.*, 2012; Hao *et al.*, 2013], conical threaded [Zhang *et al.*, 2012], square [Elangovan and Balasubramanian, 2007; Elangovan and Balasubramanian, 2008b; Heidarzadeh *et al.*, 2012; Imam *et al.*, 2013], triangular [Elangovan and Balasubramanian, 2007; Elangovan and Balasubramanian, 2008b], tapered cylinder with grooves [Shanmuga Sundaram and Murugan, 2010], tapered square [Shanmuga Sundaram and Murugan, 2010; Imam *et al.*, 2013], tapered hexagon [Shanmuga Sundaram and Murugan, 2010], paddle shaped [Shanmuga Sundaram and Murugan, 2010] tool geometry. Among the above used tool pin geometries straight and tapered cylindrical tools are the simplest ones. Then in fabrication complexity and economy point of view the next simple tool pin geometry is threaded cylindrical tools. Rajakumar *et al.* [Rajakumar *et al.*, 2010; Rajakumar *et al.*, 2011a; Rajakumar *et al.*, 2011b; Rajakumar and Balasubramanian, 2012] found defective joints for a PnD of less than 2.5 mm and greater than 7.5 mm. The images of various FSW tools used by different researchers are shown in **Fig. 2.3**.

De *et al.* [2014] studied the tool durability while joining 1018 C-Mn steel by FSW process. They observed an enhancement in tool durability with an increase in either the tool shoulder diameter or the tool RPM. This is due to the enhancement in workpiece temperature. While in other hand a higher tool traverse rate reduces peak temperature, increases stresses on the tool leading in the reduction of tool durability. Similar work was done by DebRoy *et al.* [2014] during FSW of an aluminium alloy. The tool durability maps

developed by them are useful in analyzing how the thicker plates and higher tool traverse rates affect adversely to the tool durability. In their review article Rai *et al.* [2011] discussed about different FSW tool materials and tool geometries (which includes both the tool shoulder and pin) used for soft as well as hard workpiece material. They have also reviewed the tool wear and deformation during the FSW process. The material adhesion phenomena of various pin geometries are analyzed by Mehta *et al.* [2014]. They observed that due to adhesion, polygonal tool pins lose its functionality and experience severe stresses under specific conditions. But the permanent adhesion of the plasticized material can be avoided by reducing the number of sides of the polygonal pins

Figure 2.3 FSW tool geometries

[a: Ghidini *et al.*, 2005; b: Gaafer *et al.*, 2010; c: Balasubramanian, 2008; d: Arora *et al.*, 2010; e:Lammlein *et al.*, 2009; f:Hui-jie and Hui-jie, 2009; g: Miles *et al.*, 2009; h: Thomas et al., 2005; i: Aval *et al.*, 2011; j,k:-Zhang *et al.*, 2012; l: Sakthivel *et al.*, 2009; m: Forcellese *et al.*, 2012; n: D'Urso *et al.*, 2009; o: Scialpi *et al.*, 2007]

2.3.1.2 Tool Rotational Speed

The rotational speed significant affects the UTS [D'Urso *et al.*, 2009]. Kim *et al.* [2006] investigated the effect of welding speed and rotation speed on the microstructure in the stir zone by measuring the Si particle distribution in the aluminum die casting alloys. They found fine recrystallized grains in nugget zone (NZ). Tozaki *et al.* [2007] reported that the tensile shear strength was increased and the cross-tension strength was decreased with increasing tool rotational speed and tool holding time for FSSW of 6061 Al alloy joints. Balasubramanian [2008] developed empirical relationships between the base metal properties such as yield strength, elongation and hardness and the tool rotational speed. The author found that the developed relationships can be effectively used to predict the FSW process parameters to fabricate defect free joints from the known base metal properties. Buffa *et al.* [2009] found an operative parameter range of 300 to 500 rev/min of rotational speed to weld AA2024-T4 with AA7175-T73511 for both T-joint and lap joint using FSW process. Kwon *et al.* [2009] found defect-free welds from 500 to 3000 rev/min to weld aluminium plates using FSW. The grain size decreased with increase of the tool rotation speed. The average hardness of the NZ reaches a level about 33% greater than that of the BM at 500 rev/min.

Heidarzadeh *et al.* [2012] found improved tensile properties with increasing tool rotational speed up to a maximum value which then decreased. The same trends were obtained by various other researchers while increasing tool RPM [Heidarzadeh *et al.*, 2012; Sharma *et al.*, 2012; Zhang *et al.*, 2012; Simoncini and Forcellese, 2012; Hao *et al.*, 2012]. This is due to the formation of tunnel and void type of defects at higher rotation rates. Ghosh *et al.* [2010] welded A356 and 6061 aluminum alloys under tool rotational speed of 1000 to 1400 rev/min. The thermal stress was found to be reduced at lower tool rotational speed. The joint surface was found poorer for commercially pure copper and Al FSW joints as the rotation rate increased [Xue *et al.*, 2011]. The tensile properties lowered at lower rev/min. The joints showed sound bending properties at 600 rev/min. The friction stir welded joints of AA7075-T6 showed higher strength [Rajakumar *et al.*, 2011b] at 1400 tool rev/min due to the fine grained microstructure of weld nugget and uniformly distributed finer $MgZn_2$ particles in the weld nugget. El-Hafez [2011] reported an increase in consumption of welding power with increased rotation speed. The measured power agrees with

corresponding values calculated using a model established by Heurtier *et al.* [2006], especially at lower rotation speed. But the theoretical results exceed the experimental results at higher speeds which could be due to the increase of slipping between the tool and the metal at higher rev/min.

Lertora and Gambaro [2010] advised to use slightly higher welding ratios (rotational speed / welding speed) for AA8090 Al-Li alloy to obtain bigger equiaxial grains and fewer precipitates at the grain boundaries. In friction stir welds of Ti-6Al-4V, Zhou *et al.* [2010] found stir zone (SZ) temperature below the β-transus temperature and bimodal microstructure with a rotation speed of 400 rev/min. When rotation speeds of 500 and 600 rev/min were used the SZ temperature was above the β-transus temperature and thus a full lamellar microstructure characterized by basket-weave α+β lamellae was developed. The temperature generated at the shoulder is mainly affected by the spindle speed [Record *et al.*, 2007] so it is one of the most significant factors of the FSW process. The joint strength for friction stir lap welded joints of Al-5083 and St-12 alloy sheets were improved by increasing the tool rev/min [Movahedi *et al.*, 2012]. Liu *et al.* [2012] reported an increase in tensile properties of 2219-T6 aluminum alloy joints with increased rotational speed (keeping welding speed constant) or increased welding speed (keeping rotational speed constant) to a maximum value, and then it was decreased due to the occurrence of void defects.

Toktas and Toktas [2012] observed an increase in hardness values with the rotation speed and at low welding speed the yield and the UTS were increased by the rotation speed. Sharma *et al.* [2012] found a decreased average grain size of α-aluminum present in weld nugget with decreasing rotary speed. Also the minimum hardness region was shifted [Sharma *et al.*, 2012; Aydin *et al.*, 2012] from heat affected zone (HAZ) to weld NZ. The corrosion resistance property of 7475 aluminum joints increased [Gupta *et al.*, 2012] with increasing rev/min from 300 to 1000 and SZ shown better corrosion resistance compared to thermo-mechanically affected zone (TMAZ). Koilraj *et al.* [2012] reported an optimum rotational speed of 700 rev/min for carrying out FSW of AA2219-T87 and AA5083-H321. Higher spindle torques was required for the tools with conical cavity shoulders [Leal *et al.*, 2011]. Aval *et al.* [2011c] found weaker welds and coarser grain size in the weld nugget with increasing rotational speed in FSW of AA5086-AA6061 Al alloys. Fu *et al.* [2012] observed porosities and insufficient penetration in clockwise rotation of tool during welding

of AZ31B magnesium alloys. However, the counterclockwise rotation was found beneficial for improving the mechanical property of the joints.

2.3.1.3 Welding Speed

The tool traverse speed (*i.e.*, welding speed) has a strong effect on micro-hardness and tensile strength of aluminium alloys [Dequing and Shuhua, 2004; Adamowski and Szkodo, 2007; D'Urso *et al.*, 2009; Liu *et al.*, 2012]. Sakthivel *et al.* [2009] reported fine equiaxed and more homogenous grains in NZ at lower welding speed. The size of the weld zone became wider when decreased the traverse speed but the hardness slightly increased with the increased of welding speed. The ultimate tensile strength increased with decreasing traverse speed. The best mechanical properties were obtained at lower traverse speed due to the occurrence of homogenous grains and higher heat input. The resistance of the material increased with the increased of travel speed during FSW [Adamowski and Szkodo, 2007].

During the welding of Si particle distributed aluminum die casting alloys, the particles size decreased [Kim *et al.*, 2006] with the increasing welding speed. Cavaliere *et al.* [2008] reported for AA6082 Al alloy that the nugget mean grain size was changed by increasing the advancing speed from 40 to 165mm/min and no further variations was observed up to 460 mm/min. The yield strength was recorded to increase from the lower speeds to 115 mm/min and then started to decrease by increasing the welding speed. This is due to a strong hardening phenomenon taking place over a certain welding speed, for which the stirring effect is presumably less efficient and the material originated from the leading edge in one single sheet does not travel enough into the coupled sheet material. The ductility of the material showed the similar behavior but restarted to increase after 165 mm/min. The material welded with the speed of 115 mm/min exhibited the best fatigue properties and the higher fatigue limit. In another study of AA2219 Al alloy, a welding speed of 0.76mm/s showed superior tensile properties [Elangovan and Balasubramanian, 2008b]. Sound joints were obtained with welding speeds of 100 to 800 mm/min [Zhang *et al.*, 2012]. The hardness increased as the welding speed increased upto a certain value and then remains unchanged [Zhang *et al.*, 2012].

Buffa *et al.* [2009] reported an operative parameters range of 30 to 100 mm/min for advancing speed in T joint or a lap joint of 2024-T4 and 7175-T73511 Al alloys. Ghosh *et*

al.[2010] friction stir welded A356 and 6061 aluminum alloys and found fine grain size of 6061 alloy near interface and reduced residual thermal stress at lower traversing speed. In an investigation of underwater FSW of 2219 aluminum alloy, Liu *et al.* [2011b] observed an increase in grain size in the NZ with increase of welding speed from 50 to 150 mm/min which decreased abruptly at 200 mm/min. The tensile strength also increased with increasing the welding speed. At low welding speed of 50 mm/min, the joint is fractured in the HAZ adjacent to the TMAZ on the RS, while an increase in the welding speed to 100 and 150 mm/min caused to occur at the TMAZ adjacent to the NZ on the advancing side. A welding speed of 60 mm/min yielded higher strength properties [Rajakumar *et al.*, 2011b] for friction stir welded joints of AA7075-T6 alloy. El-Hafez [2011] found an increase in hardness of the HAZ with increase in welding speed for AA2024-T35 joints. It had a little effect on consumed power. The axial thrust and horizontal force are affected significantly by the welding speed [Arora *et al.*, 2010].

Record *et al.* [2007] concluded that feed rate is one of the most significant factor. The weld zone defects reduced and the joint strength improved by decreasing the travel speed for lap welding of Al-5083 and St-12 alloy sheets [Fu *et al.*, 2012]. Sharma *et al.* [2012] reported a decreased average grain size of α-aluminum present in weld nugget with increasing welding speed. The UTS, percentage elongation, energy absorbed and joint efficiency decreased with increase in welding speed. With an increased in welding speed the minimum hardness region was shifted from HAZ to NZ [Sharma *et al.*, 2012]. The hardness of the softened region decreased with decreasing the welding speed [Aydin *et al.*, 2012]. Gupta *et al.* [2012] found maximum tensile strength with a traverse speed of 50 mm/min for 7475 aluminum joints. Koilraj *et al.* [2012] found 15 mm/min as optimum speed for AA2219-T87 and AA5083-H321 alloys. Weaker welds and coarser grain were found in the weld nugget with decreasing welding speed during dissimilar welding of AA5086–AA6061 aluminum alloys [Fu *et al.*, 2012]. Steuwer *et al.* [2011] reported a decrease in width of the tensile section of the residual stress profile with increasing traverse speed for W-Re tool material. The mean hardness and UTS of the NZ increased with increasing traverse speed [El-Rayesa and El-Danaf, 2012].

2.3.1.4 Axial Load or Plunging Depth

An axial force of 7 kN showed superior tensile properties in FSW joints of AA6061 Al alloy [Elangovan *et al.*, 2008]. Kumar and Kailas [2008a] reported defects free 7020-T6 Al alloy welds above 8.1 kN AL and maximum strength was produced at 8.8 kN load. The axial thrust was affected significantly by shoulder diameter and welding speed [Steuwer *et al.*, 2011]. Record *et al.* [2007] reported plunge depth as one of the most significant factors of the FSW process which in turn depends upon plunging force. The temperature generated at the shoulder also depends on the axial force.

2.3.1.5 Tool Tilt Angle

The weld nugget shapes were affected by the tool tilt angle [Barlas and Ozsarac, 2012]. The authors found best results at a tool rotation speed of 1100 rev/min and tool tilt angle of 2 deg during the counter clockwise rotation of the tool for joining Al 5754 alloy. The joint showed a tensile strength of 86% as compared to the base metal. The optimal tool tilt angle for FSW of AA6061 Al alloy and SS400 low-carbon steel for impact quality was 1 degree [Chen, 2009]. Weld trials showed a narrower basin-shaped weld nugget with changing of the tool tilt angle from 0º to 2º [Chen, 2009]. The tilt angle was found the least contribution (5.96%) welding parameter [Bozkurt, 2012; Robson *et al.*, 2010] compared to tool rotational speed and welding speed. The thickness of the welding zone of friction stir welding of polyethylene [Arici and Selale, 2007; Squeo *et al.*, 2007] decreased with increasing tool tilt angle due to excess flashing. This affected the tensile strength of the joint. The fatigue strength of friction stir welded A6005-T5 Extrusion became better with the increase in tilting angle [Kim *et al.*, 2010]. In the fiction stir welding of polyethylene sheets the tilt angle was found to be the least contribution welding parameter [Bozkurt, 2012]. The use of scrolled shoulder which consists of a flat surface with a spiral channel cut from the edge of the shoulder towards the centre facilitate to carry out the welding process with zero tilt angle [Mishra and Mahoney, 2007; Yan *et al.*, 2010; Yan *et al.*, 2010]. This is due to the direct deformation of the material from the edge of the shoulder to the pin.

2.3.1.6 Number of Passes

Robson *et al.* [2010] reported a decrease in the strength as the number of weld passes increased in the HAZ as the number of welding pass increase. The strength reduction was

greatest after the first pass and the reduction in strength on subsequent passes became increasingly small. The voids produced by single pass or two overlapping passes along the entire length of the welds can be eliminated by three or four overlapping passes [Leal and Loureiro, 2008]. HAZ hardness and transverse tensile strength were reduced with increasing number of passes [Steuwer *et al.*, 2011]. El-Rayesa and El-Danaf [2012] addressed an increase in the SZ-grain size, more dissolution and re-precipitation with simultaneous intense fragmentation of second phase particles with increasing number of passes. It was also accompanied by an increase in the average mis-orientation angle and fraction of high angle grain boundaries.

2.3.1.7 Others

The hardness and compressive strength increased, and grain size became finer with increased of Re concentration in Iridium (Ir) based tool for welding of high temperature materials [Miyazawa *et al.*, 2011]. The degree of tool wear of the Ir based alloy tool was less when the rotation pitch of 0.3 was used to join 304 stainless steel plates [Miyazawa *et al.*, 2012]. It was less than or equal to that of the PCBN tool. Zaeh and Gebhard [2010] studied the dynamical nature of the process forces generated in FSW and their effect on the machine structure. In friction stir welded copper joints [Xue *et al.*, 2011] the HAZ of air cooled joint exhibited a very low dislocation density where as that of water cooled joint retained the initial microstructure of the PM with a high dislocation density. The strength nearly equal to the base metal was achieved with rapid water cooling. . Liu *et al.* [2011a] found an increase in the homogeneity of mechanical properties of the joint in underwater FSW of 2219-T6 aluminum alloy. Water cooling during FSW [Xu *et al.*, 2012] refined the NZ grains further compared to air cooling. Mofid *et al.* [2012] observed that the underwater welded joint had smoother interface and less intermixing. The NZ of air welded joint displayed complex flow patterns. Improved tensile strength and decreased plasticity [Hui-jie *et al.*, 2010; Zhang *et al.*, 2012] due to underwater FSW.

2.3.2 Microstructural studies

The heat associated with SZ results in significant microstructural evolution within and around the three zones i.e. nugget zone, thermo-mechanically affected zone, and HAZ. A typical cross-section of the FSW joint with number of zones is shown in **Fig. 1.3** of Section

1.1, Chapter-1. The microstructure of the friction stir welded joints also depends on base materials. Su *et al.* [2003] reported that in AA7050 the transformation of elongated grains with 1-2µm cells in the TMAZ into 1-4µm equiaxed structure with many high angle boundary (HAB) in the nugget. Hassan *et al.* [2003] reported a consistent crystallite size in the nugget with structures developed in torsion to the same strain at equivalent temperatures and strain rates. Cam *et al.* [2009] considered a conical tool made of hot work steel with nonstandard helical threads and rounded tip to join brass plates. The grain size in the stir zone became finer with lowering heat input. Cabibbo *et al.* [2007] carried out joining of AA6056 plates at a rotational speed of 1800 rev/min and welding speed of 15 mm/s. The grain structure was fine equi-axed in the NZ, highly elongated with very small cells in the retreating side of TMAZ and slightly elongated coarse grains in the HAZ. Han *et al.* [2014] observed remarkable contribution of mechanical force in transformation of boundaries from LAGBs to HAGBs, and grain refinement of friction stir welded ferritic steels.

Wei and Nelson [2011] used a convex scrolled shoulder step spiral tool. They found a linear relationship of heat input with ferrite grain size and bainite lath size. Pseudo heat index, power and advance per revolution exhibit nonlinear relationships with post-weld microstructures. The differences in TG and welding parameters induced significant changes in the material flow path as well as in the NZ microstructure of AA6016-T4 welds [Rodrigues *et al.*, 2009]. Yeni *et al.* [2008] reported recrystallized fine grain structured NZ. The grain sizes increased from the weld region to the base metal. The welding was carried out using two different helical angles of the threaded pin, namely right and left helical. For right helical pin, two different shoulder diameters were utilized. The fine grain evolution in FSP of 7050 aluminum alloy was initiated by recrystallization [Rhodes *et al.*, 2003]. In aluminum single crystal the shear deformation generated by the FSW process gradually rotated and grew in size and mis-orientation as the welding deformation continues [Fonda *et al.*, 2007]. Fujii *et al.* [2014] reported an excellent balance between the tensile properties like strength and ductility in FSWed steel plates due to the formation of the mechanically stabilized metastable austenite phase. Ramanjaneyulu *et al.* [2013] joined 5 mm thick AA2014-T6 aluminum alloy. They used a number of different TG among which hexagonal tool pin showed a relatively rapid rate of temperature rise. This tool also resulted in fine

microstructure in the NZ and thinner TMAZ. Non-circular tool pins results in thoroughly stirred weld zone.

For 2519 aluminium joints [Fonda *et al.*, 2004] soft band of microhardness, corresponding to the typical fracture location in the welds was found to be located at the boundary between the TMAZ and HAZ. The primary cause of softening at the TMAZ/HAZ boundary was due to coarsening and transformation of the strengthening precipitates during the welding process. Ceschini *et al.* [2007] examined microstructure, tensile and fatigue properties of AA6061 MMC (aluminium alloy matrix, reinforced with 20 vol.% of Al_2O_3 particles) FSW joints. They found that the comminuting effect induced on the ceramic reinforcement led to a significant reduction of the reinforcement particles area and to their roundness. The matrix inter-particles hardness decreased from the base material to the middle line of the FSW zone. Attallah *et al.* [2007] carried out quantitative microstructural studies of AA5251 aluminium alloy joint. They found that the TMAZ/NZ strength was primarily controlled by grain boundary strengthening. Xie *et al.* [2007] joined 6 mm thick Mg-Zn-Y-Zr plate. During FSW, fine and equiaxed recrystallized grains of 6.8 μm were generated. Sakthivel and Mukhopadhyay [2007] investigated the FSW of 2 mm thick copper sheet. They found finer NZ microstructure than the parent metal due to dynamic recrystallization. The hardness of the NZ was higher than the TMAZ, HAZ, and BM due to the presence of fine grains. Scialpi *et al.* [2008] performed mechanical and microstructural analysis of dissimilar and similar jointed for micro-FSW butt welds. They found a new equiaxed fine grain structure in the NZ. In another investigation, Zadeh *et al.* [2008] studied microstructural and mechanical properties of Al/Cu lap joints. They observed a black area, which consisted of inter-metallic compounds of Al_4Cu_9, AlCu and Al_2Cu near Al/Cu interface. Low rotational speed resulted defective joints.

Fonda *et al.* [2007] investigated the microstructural evolution in FSW of 2195 Al-Li alloy. They observed large, un-deformed grains far from the tool to the refined grains near the tool. Simar *et al.* [2008] studied the effect of the welding speed on the microstructure and mechanical properties of friction stir welded Al alloys. They found occurrence of dissolution of the precipitates and formation of coarse precipitates in HAZ. The strain hardening capacity of the NZ is larger than that of the HAZ. Sudhakar *et al.* [2014] used FSP to enhance wear and ballistic resistance behavior of armour grade AA7075 aluminium

alloy. They observed fine and uniform microstructure. The processing with boron carbide powder enhanced the wear resistance behavior and ballistic performance. Giles *et al.* [2009] conducted friction stir processing on AA2099 plate. They found equiaxed grains during FSP. Hui-jie and Hui-jie [2009] used FSW process to repair groove defect. They found that the offset repair welding process was superior to the symmetrical repair welding process. In the symmetrical repair welding process, a large number of fine cavity defects occurred. Ramesh Babu *et al.* [2014] performed FSP on AZ31B magnesium alloy by varying AL, RPM and traverse speed. They found AZ31Bmagnesiumalloy to exhibit superplastic forming characteristics at elevated temperatures. The obtained grain sizes are also stable at the high temperatures required for the superplastic flow.

Brown *et al.* [2009] studied the effect of multiple passes on the weld properties for 7050-T7451Al alloy. They found that the force in x-direction was reduced when welding through previously welded material as compared to that in the base metal. The grain size and hardness of the nugget were unchanged and temperature remained same. El-Danaf *et al.* [2010] found fine equiaxed grains with high angle grain boundaries in the nugget as compared to the elongated grains in the base metal by FSP of commercial 5083 Al alloy. The processed materials exhibited higher strain rate sensitivity, less forming loads and higher ductility. Arora *et al.* [2010] characterized the microstructure evolution of AA2219 aluminum alloy. There was dissolution of second phase particles in NZ and TMAZ. Electron backscatter diffraction analysis indicated a continuous dynamic recrystallization process leading to formation of fine equiaxed grain structure in the weld nugget. Lorrain *et al.* [2010] analyzed the material flow with unthreaded pin during the FSW of 7020-T6 aluminium alloy. They found same features with threaded tools. From the macro-sections of the joints, it was seen that the zone influenced by the shoulder rotation along the thickness was thicker when increasing the product of the plunge force and the rotational speed and for the cylindrical pin than for the tapered pin with three flats. Xue *et al.* [2011] prepared pure copper joints by FSW and cooled it rapidly in order to strengthen it equally. The HAZ of air cooled joint achieved at 800 rev/min exhibited a very low dislocation density. The HAZ of water cooled joint achieved at 400 rev/min retained the initial microstructure of the BM with a high dislocation density. At rapid cooling the duration at higher temperatures of the HAZ

were reduced. The strength nearly equal to the base metal was achieved at 400 rev/min with rapid water cooling.

Miyano *et al.* [2011] welded stainless steel plates with a Si_3N_4-based tool at various welding speeds. They found very fine grained structures and higher hardness values in the stir zones. Cho *et al.* [2011] reported a fine-grained microstructure in the NZ of friction stir butt welded of 409 SS plates. The fraction of low angle boundaries in the SZ was significantly increased as compared to that in the BM. The amounts of both heat input and plastic deformation to the welded material increased with increase in plunging depth. Bakavos *et al.* [2011] studied the effect of pin-less tool on friction stir spot welding thin aluminum sheet. They found a complex material flow in the weld zone. With profiled tools, a high depth of penetration of the deformation zone and a strong intercalated interface was observed. Azimzadegan and Serajzadeh [2010] reported a reduced grain size in the NZ of AA7075-T6 at relatively high rotational speeds. Zadpoor *et al.* [2010] studied the global and local mechanical properties and microstructure for two friction stir welded aluminium alloys namely, 2024-T3 and 7075-T6. They found heterogeneous texture in NZ. Large intermetallic particles were observed in the HAZ and NZ. The yield strength and plasticity parameters drastically vary around the weld centerline. Liu *et al.* [2011a] carried out underwater FSW of 2219-T6 aluminum alloy. They concluded that there was an increase in the homogeneity of mechanical properties of the joint. The softening regions of the layers in underwater joint are significantly narrowed compared with the normal joint.

Steuwer *et al.* [2011] used different techniques to map the microstructure of Al-Li AA2199 friction stir weld. Differential scanning calorimetry and lattice spacing measurements using neutron diffraction showed that the hardness distribution across the HAZ, TMAZ and nugget could be explained by the density and size of second phase precipitates. Equiaxed grains in NZ with strong in-grain misorientation and presence of grain-interior dislocation was reported in FSW of 5052 Al alloy [Kumbhar *et al.*, 2011]. Li *et al.* [2011] reported material-loss defects in friction stir welds due to poor migration of plastic deformed material flow or insufficient heat generated by tool/workpiece frictional heat source. Ultrasonic C-scan testing was good at porosity and tiny voids detection while fluorescent penetrating fluid inspection was suitable for revealing the hidden root crack like flows. Ahmed *et al.* [2011] used a stationary shoulder with tri-flat design tool to weld 5082

Al alloy. The static shoulder was reduced the shoulder-affected region relative to the rotating shoulder. The whole plate thickness of the weld showed to be dominated by a strong simple shear texture. Srinivasu *et al.* [2014] used a FSP as a surfacing technique to improve the wear resistance of cast Al-Si alloy. The process was found to be able to refine the microstructure and form hard surface composite. This is by reinforcing boron carbide particles in the aluminium matrix which subsequently improved the hardness and wear resistance of the alloy.

The microstructure evolution and mechanical properties of friction stir processed pure aluminium was studied by Yadav and Bauri [2012]. They found equiaxed fine grains with well defined grain boundaries. It was found that grain size varied from the top to the bottom of the NZ of AA2017A- T451 welded plates [Ahmed *et al.*, 2012]. Khodir *et al.* [2012] investigated the joint properties of FSWed 2 mm thick SK4 high carbon steel plates. They concluded with a homogenous structure of spheroidized cementite and fine ferrite grains in NZ at 100 RPM. A significant increase in hardness value was also observed above 100 RPM. Both the tensile and yield strength values increased with increase in rotational speed.Liang *et al.* [2012] welded 2519-T87 aluminum alloy and found dynamically recrystallized NZ where the grain size increased from the center of NZ to TMAZ. This led to the gradual reduction of the micro-hardness. Fu *et al.* [2012] investigated the types, distributions, dissolution and precipitation behaviors of the precipitates in different regions of the top surface of friction-stir welded AA2524-T3 aluminum joints. Microscopic observations showed that the types of precipitate phases were the circular Al_2Cu phase, the small, rod-shaped Al_2CuMg phase, and the larger bulk like Fe-containing impurity phase. Liu *et al.* [2009] used a W-Re pin tool to weld thermo-hydrogen processed Ti-6Al4V alloy. They found that the NZ temperature was below the β-transus temperature, and a microstructure characterized by DRX α and transformed β composed of acicular martensite α' and lamellar α+β was developed in the NZ. For the same material Kitamura *et al.* [2014] reported a decrease in prior β grain size when the peak temperature goes beyond the β-transus temperature. They also concluded that the cooling rate depends largely on WS.

Chen *et al.* [2011] found coarser grains in FSW of AA5083-H18 sheets due to abnormal grain growth. The percentage of low angle grain boundaries varied opposite to grain size with grains smaller than 3 μm. In FSP of Al 2024-T4 homogeneous and fine equiaxed grains

with average size of 4 µm were found in NZ [Zahmatkesh *et al.*, 2010]. It also showed the region for maximum hardness. The process was found to be beneficial in improving wear resistance. Li and Shen [2010] prepared a new type of joint, namely lap-butt joint of dissimilar aluminum alloys. They observed three micro flow-patterns in SZ such as circumfluence, laminar flow and turbulent flow. During high temperature plastic deformation the 6082 alloy was sensitive to flow softening [Leitao *et al.*, 2012]. At the same time 5083 alloy displayed steady flow behavior at increasing temperatures. In dissimilar FSW of $Zr_{55}Cu_{30}Ni_5Al_{10}$ bulk metallic glass (BMG) to pure Al Sun *et al.* [2014] observed absence of intermetallic compounds in the SZ. Good joints showed 91% of tensile as compared to BM. Dinaharan and Murugan [2012] used FSW process to join aluminum matrix composites and found a homogenous distribution of ZrB_2 particles in NZ and parallel band like distribution in TMAZ. Chen *et al.* [2012] welded non-combustive AMX602 magnesium alloys. They found equiaxed grains in NZ caused by dynamic recrystallization during FSW. Fully recrystallized microstructure was observed in FSW of dissimilar alloys (Al and Mg) [Venkateswaran and Reynolds, 2012]. At the lower rotational speeds the joints exhibited an s-shaped interface. The tensile strength increased with increasing interface length due to higher mechanical interlocking.

Cho *et al.* [2012] joined high-strength line pipe steel by FSW process. They observed homogeneous grains in TMAZ and acicular-shaped bainitic ferrites in NZ. Due to this the hardness of NZ was higher than other regions. Hu *et al.* [2012] prepared thin-walled aluminum alloy tube by friction stir welding combined with spinning. They found microstructure heterogeneity of joint. Mofid *et al.* [2012] welded dissimilar alloys using FSW process. They observed that the underwater welded joint had smoother interface and less intermixing. The NZ of air welded joint displayed complex flow patterns. In double sided FSW of Mg alloy Chen *et al.* [2013] observed a random crystallographic texture and diversified material flow in the weld zone. Wang *et al.* [2010] joined AA6082 and AA7449 alloys. Above 720 °K, they observed slight softening in AA7449. The flow stress curve for AA6082 was not reduced. Jiang and Kovacevic [2004] joined 6061 Al alloy and AISI1018 steel and found defects free joints. The high joint strength was observed from tensile failure location which is at the boundary between the NZ and TMAZ. The average NZ hardness

was found to be higher than base Al alloy. Fine Al-Fe intermetallics and coarse steel pieces were observed in the SZ.

Khodabakhshi *et al.* [2014] investigated the post-annealing effect on the joint properties of friction stir processed Al-Mg-TiO_2 nano-composites. They observed the formation of Al_3Ti and MgO nano-particles at the interfaces. The yield strength and hardness increased whereas tensile strength and elongation reduced with increasing the concentration of TiO_2 nano-particles. Galvao *et al.* [2012] studied the formation and distribution of brittle structures during FSW of Al and Cu. They varied the tool shoulder geometry and observed completely different morphology and inter-metallic content weld nugget. The material flow mechanisms had a strong influence on the phase content of the mixtures. Liu *et al.* [2012] introduced external non-rotational shoulder for FSW of 2219-T6 aluminum alloy. They found fine and equiaxed grains in NZ. The designed tool system reduced the asymmetry and in-homogeneity. Xu *et al.* [2012] varied the cooling of aluminum alloy joints. They found that water cooling during FSW refined the NZ grains further compared to air cooling. Khorrami *et al.* [2012a; 2012b] welded severely plastic deformed aluminum sheets. Elongated grains in TMAZ and equiaxed grains in NZ were found. The stir zone grain size increased with decreasing revolution pitch. The amount of recrystallized grains in HAZ was increased with increasing of strain values.

Izadi *et al.* [2013] used FSP to modify the microstructure of sintered Al-SiC composites. They observed uniformly distributed SiC particles and improved microhardness in the stir zone. It also helps in elimination of porosity. They [Izadi *et al.,* 2013] also studied the mechanical and microstructural properties of friction stir processed Al 5059 alloy. BM microstructure was found to have $Al_6(Mn,Fe)$ type particles. FSP induced insignificant grain growth in Al 5089. Sun *et al.* [2013] used an external heat source to preheat the 3.2 mm thick S45C steel plates and subsequently joined it by FSW process. They have used a laser heating system. They found that the frictional heat between the tool and the workpiece reduced significantly for preheating on the AS whereas total heat input into the workpiece was at its highest point for preheating on the RS. Lim *et al.* [2009] produce an aluminium alloy reinforced with multi-walled carbon nano-tubes by FSP. An improved distribution of nano-tubes in the Al-alloy matrix was observed with increasing RPM and PD. In their study Khodabakhshi *et al.* [2014] investigated friction-stir welded AA5059 aluminum alloy to

high density polyethylene joint. They obtained defect free welds at 710 RPM and WS of 63 mm/min. Traverse tensile fracture showed higher tensile strength in the SZ than that of the AA5059/HDPE interface.

Santos *et al.* [2011] conducted electrical conductivity field analysis for evaluation of joints in AA6013 and AA7075 alloys. They observed that the process significantly changed the electrical conductivity of the welded materials, as a consequence of microstructural modifications in different zones. The electrical conductivity decreased in the NZ and increased in the TMAZ and HAZ. Dumont *et al.* [2006] carried out microstructure mapping in 7449 aluminium alloy joints using small angle X-ray scattering (SAXS). They found that SAXS can provide very detailed maps and showed the correlation between the distribution of heat input across the welds and the consequent precipitate microstructures. In another work Rosado *et al.* [2010] used a new type of non-destructive testing (NDT) system in terms of a new type of eddy currents probe to address micro size superficial defects in welded joints. This technique was able to detect defects as small as 60 µm. **Table 2.3** lists types of workpiece materials, types of tools and welding condition used in various works to study microstructural and mechanical properties.

Table 2.3 Studies of Mechanical Properties and Microstructure

Workpiece Material	Tool Material	Operating Parameters* (REV/MIN, WS (mm/min), AL (kN), PD (mm), TA (º), Others)	Remarks	Reference
6061 Al alloy	High carbon steel	REV/MIN: 1200, WS: 75, AL: 7	Square pin profiled tool produced good joints; shoulder diameter of 18 mm showed superior tensile properties.	[Liu and Ma, 2008]
			FSW exhibited strength enhancement of 34% compared to GMAW and 15% compared to GTAW; fine, equiaxed grains in NZ.	[Lakshminarayanan *et al.*, 2009]
	Highly wear resistant steel	-	Proof strength and UTS decreased to 43% and 28% respectively respect to the base material.	[Ceschini *et al.*, 2007]
	-	REV/MIN: 400-1600, WS: 100-400	Joints welded at 400 mm/min exhibited higher strength with 45º shear fracture; WS was the dominant factor in determining the tensile properties and fracture mode.	[Ren *et al.*, 2007]
	High carbon steel	REV/MIN: 862-1337, WS: 32.43-127.5, AL: 5.62-10.37	Highest hardness value of 121 HV obtained at 1100 rev/min.	[Rajakumar *et al.*, 2011a]
	H13 steel	REV/MIN: 400-600, WS: 50, PD: 0.1, TA: 2.5	Lowest hardness in the HAZ on advancing side; tensile properties along the skin higher than those along the stringer.	[Cui *et al.*, 2012]
2024-T3 & 7075-	-	REV/MIN: 215, WS: 113	YS reduced and exhibited rate sensitivity.	[Chao *et al.*, 2001]

T7351				
2024T3 & 6082T6 Al alloy	56NiCrMoV7 tool steel	REV/MIN: 2085-1800, WS: 460-762	Stress decreased with increasing strain rate; modifications in grain size.	[Cerri and Leo, 2009]
Brass	Hot work steel, X32CrMo33	REV/MIN: 1250-1600, WS: 100-225, PD: 2.8	Grain refinement in NZ; strength and ductility performance of 105 and 84%, respectively at 1250(rev/min) & 125(WS).	[Cam *et al.*, 2009]
		REV/MIN: 600, WS: 200, PD: 3	Rapid cooling by liquid CO_2 improved the thermal cycle leading to defect free SZ; can significantly reduce the post-annealing effect; results in ultrafine grains with a high dislocation density.	[Xu *et al.*, 2014]
	WC-based alloy tools	REV/MIN: 750-1200, WS: 200-800, TA: 3	refined grains and much denser twins and dislocations in the stir zones; improved tensile strength about 380 MPa.	[Sun *et al.*, 2014]
6056 Al alloy	-	REV/MIN: 1800, WS: 900, TA: 3	Strain rate and temperature gradients are steeper in advancing side than retreating; UTS and YS were 90% and 66% respectively of the base alloy.	[Cabibbo *et al.*, 2007]
Al alloy	-	REV/MIN: 1000, WS: 50-175	Fine equiaxed grains in NZ; UTS increased with decreasing WS.	[Sakthivel *et al.*, 2009]
7075	-	REV/MIN: 350, WS: 120	Microstructure depends on the tool design, processing parameters and cooling rate.	[Su *et al.*, 2005]
	H13 tool steel	REV/MIN: 100-1400, WS: 40-80, TA: 3	REV/MIN of 1300 the WS of 40 mm/min produced defect-free weld.	[Azimzadegan and Serajzadeh, 2010]
2024 & 7075 Al	H13 steel quenched at	REV/MIN: 1040, WS: 104,	Recrystallization phenomena occurred; inhomogeneous decrease of the mechanical characteristics.	[Barcellona *et al.*, 2006]

alloy	1020 ◦C SKD61 -	PD: 2.9, TA: 2 REV/MIN: 1200, WS: 42-198 REV/MIN: 400-2000, WS: 254, AL: 9.8-13.4, TA: 3	Maximum tensile strength of the joints of 423MPa at 1.7 mm/s(WS) when 2024 alloy plate on advancing side. Weld efficiency in terms of tensile strength at 1000 rev/min was 96%; minimum hardness value of naturally aged samples was 88% of BM.	[Khodir and Shibayanagi, 2008] [Silva *et al.*, 2011]
Al & Cu	Tool steel SPK quenched and tempered tool steel	REV/MIN: 151-1400, WS: 57-330 REV/MIN: 750-1500, WS: 30-375, TA: 3	Different microhardness levels from 136 to 760HV0.2 were produced in NZ Shear load decreased with increasing rev/min and decreasing WS.	[Ouyang *et al.*, 2006] [Zadeh *et al.*, 2008]
2095 Al alloy	-	REV/MIN: 1000, WS: 252	Fine equiaxed grain structure with high grain boundary misorientation angles.	[Salem, 2003]
6016-T4 Al alloy	-	REV/MIN: 180-320, WS: 1800-1120, PD: 2.5, TA: 0	Reduction in elongation of 30% and 70%, respectively for the conical and scrolled shoulder welds.	[Rodrigues *et al.*, 2009]
Mg-Zn-Y-Zr alloy	-	REV/MIN: 800, WS: 100, TA: 2.5	Joining efficiency was 95% of BM.	[Xie *et al.*, 2007]

01420 Al-Li alloy	1Cr18Ni9Ti stainless steel	REV/MIN: 400-1960, WS: 23.5-85.7, AL: 1-7	UTS of the joints were 86% of BM; bending angle of the joints can reach 180º.	[Wei *et al.*, 2007]
Cu	-	REV/MIN: 1000, WS: 30	Higher NZ hardness; joint efficiency of 85%.	[Sakthivel and Mukhopadhyay, 2007]
	-	REV/MIN: 400-800, WS: 50, PD: 0.2, TA: 2.5	YS exhibited a linear correlation with the lowest hardness values in HAZ.	[Xue *et al.*, 2011]
Steel HSLA 65	PCBN	REV/MIN: 300-600, WS: 51-203, TA: 0.5	Ferrite grain size and bainite lath size increased 150% with increasing heat input of 2.27 kJ/mm.	[Wei and Nelson, 2011]
	WC-based material	REV/MIN: 600, WS: 50-250, AL: 14, PD: 1.7, TA: 3	NZ consisted of fine equiaxed grains of α and γ phases; tensile strength and hardness increased with the increasing WS.	[Saeid *et al.*, 2008]
	Si_3N_4-based material	REV/MIN: 400, WS: 100-300, TA: 3	WS of 100mm/min and a rev/min of 400 were the most preferable conditions.	[Miyano *et al.*, 2011]
	PCBN	REV/MIN: 1100-600, WS: 7.62-254, PD: 1.65, TA: 0	Fine-grained microstructure in NZ; increase in PD decreased grain size and increased the hardness of NZ.	[Cho *et al.*, 2011]
	PCBN	REV/MIN: 324-1200,	Different weld properties were obtained depending on the welding	[Miles *et al.*, 2009]

	PCBN & W-Re tool	WS: 150-198, AL: 9-16 REV/MIN: 400-600, WS: 50-500, AL: 12-55, End force(kN): 0.3-15	parameters used. NZ microstructure was found to be a mixture of martensite, bainite, and pro-eutectoid ferrite.	[Barnes *et al.*, 2012]
2024 & 6082 Al alloy	56NiCrMoV7-KU material	REV/MIN: 1810-2085, WS: 460-762	Grain dimension of less than 3 µm in NZ; fatigue limits in the range 40-75 MPa.	[Scialpi *et al.*, 2008]
7050-T7451 Al alloy	H13 tool steel	REV/MIN: 540, WS: 408, AL: 28, 5 no. of passes	Residual stress and *x*-force reduced with number of passes.	[Brown *et al.*, 2009]
6061-T6 & 6082-T6 Al alloy	-	REV/MIN: 1120, WS: 224, TA: 2.5	Failures occurred near the weld edge line.	[Moreira *et al.*, 2009]
2219 Al alloy	H13 steel	REV/MIN: 400, WS: 180, PD: 10.6	Joint efficiency of 72%; corrosion resistance of the NZ was better than BM.	[Srinivasan *et al.*, 2010]
	-	REV/MIN: 800, WS: 100, AL: 4.6, Welding medium (air and	Improved tensile strength and decreased plasticity due to underwater FSW.	[Hui-jie *et al.*, 2010]

		water) PD: 7-35, TA: 2		
	H13 tool steel		40% of Al_2Cu precipitates dissolved in NZ; hardness decreased from BM to the joint line; reduced tensile strength.	[Arora *et al.*, 2010;]
7020 Al alloy	H13 steel	REV/MIN: 1120-1800, WS: 20-80, TA: 3	Average size of the α-Al primary phase and ductility increased with increasing rev/min.	[Gaafer *et al.*, 2010]
2198 T3 Al alloy	-	REV/MIN: 500-900, WS: 150-300, Specimen position; run-in side, centre & out side	UTS increased with decreasing rev/min; higher YS at higher WS.	[Bitondo *et al.*, 2010]
Ti-6Al-4V	W-1 pct La_2O_3 tool	REV/MIN: 120-800, WS: 50.8-203.2	25% of the heat transferred out of the workpiece and into the tool; fine, interpenetrating α platelets and small α colonies in NZ.	[Pilchak *et al.*, 2011]
2199-T8E74 Al alloy	-	REV/MIN: 800, WS: 400	Hardness distribution exhibited a U-shaped profile.	[Steuwer *et al.*, 2011]
5052 Al alloy	High speed steel tool	REV/MIN: 1120-1400, WS: 60-100, TA: 3	Equiaxed grains with strong in-grain misorientation and presence of grain-interior dislocation structure in NZ.	[Kumbhar *et al.*, 2011]
Mg alloy	H13 tool steel	REV/MIN: 2000-3000, WS: 30-70, TA: 2	Flow stress values of joints were lower than BM.	[Forcellese *et al.*, 2012]
	SKD61 tool steel	REV/MIN: 110, WS: 200-400, AL: 8, TA: 3	Equiaxed grains in NZ; tensile strength and micro-hardness lowered.	[Chen *et al.*, 2012]
	High carbon	REV/MIN: 1000-2000,	Rev/min of 1,600, WS of 40.2 mm/min, and AL of 3 kN showed	[Padmanaban and

	steel	WS: 22.2-135, AL: 2-4	higher tensile properties.	Balasubramanian, 2010]
	High carbon steel	REV/MIN: 1200, WS: 30-150, AL: 5	WS has significant influences on the formation of defects in NZ, grain size and hardness of NZ.	[Rose *et al.*, 2012]
	High carbon steel	Tool shoulder diameter:15, 18,21 D/d ratio: 2.5, 3 and 3.5	FSP produced uniformly refined and equiaxed homogeneous microstructure with fine dynamically recrystallized grains and improved mechanical properties.	[Venkateswarlu *et al.*, 2013]
	High carbon steel	REV/MIN: 1200, WS: 90, AL: 5	The tensile strength and yield strength is enhanced by approximately 12% and 18% as compared to pulsed gas tungsten arc welding joints.	[Rajakumar *et al.*, 2013a]
	High carbon steel	REV/MIN: 800-1600, WS: 30-150, AL: 3-7	Joint efficiency of 82 % has been found 1,194 rev/min, WS of 92.19 mm/min and AL of 5.05 kN	[Rajakumar *et al.*, 2013b]
2017A-T451 Al alloy	-	REV/MIN: 300, WS: 120, TA: 2	Weld efficiency of 90%; partial recovery of hardness in NZ.	[Ahmed *et al.*, 2012]
2519-T87 Al alloy	-	REV/MIN: 250, WS: 30	The θ' precipitates are larger in size and lower in density in HAZ than TMAZ.	[Liang *et al.*, 2012]
6061/ZrB_2 composites	High carbon high Cr steel	REV/MIN: 1150, WS: 50, AL: 6	Parallel band like distribution of ZrB_2 particles and rotated elongated grains in TMAZ; reduced ductility and wear rate.	[Dinaharan and Murugan, 2012]
Al and Mg	H13 steel	REV/MIN: 600-3000,	Grain refinement in NZ.	[Simoncini and

alloy		WS: 30-300, TA: 2 REV/MIN: 780,		Forcellese, 2012]
	-	WS: 30, TA: 2°	The hardness of NZ is higher than those of TMAZ and HAZ.	[Li *et al.*, 2012]
	High carbon high Cr steel	REV/MIN: 1900, DT: 2 sec.	The plastic deformation and high-temperature exposure induced the grain boundary and the interfacial diffusion causing local melting.	[Suhuddin *et al.*, 2013]
Al-Mg-Sc alloy	M2 steel	REV/MIN: 650, WS: 158, AL: 23	Fine, fragmented and dynamically recrystallized grains in NZ.	[Subbaiah *et al.*, 2012]
1100 Al alloy	-	REV/MIN: 562-1037, WS: 40.54-159.5, AL: 3.62-8.37	Maximum tensile strength of 105 MPa, hardness value of 67 HV, and minimum corrosion rate of 0.699×10-4 in NZ with 893(rev/min), 100 mm/min (WS), 6.5 kN (AL), shoulder & pin diameter of 14.8 mm & 4.9 mm and 45.4 HRc(tool hardness)	[Rajakumar and Balasubramanian, 2012]
Glass/Mg alloy	Sintered hard metal	REV/MIN: 2700,3400, PS: 3-12,	The increment in the tool rev/min increased the heat input to the NZ and resulted in a lower vertical load and higher temperature. The load increased and the temperature decreased with increase in plunge speed.	[Shin *et al.*, 2012]
High density polyethylene	SAE 1050 steel	REV/MIN: 1500-3000, WS: 45-115, TA: 1-3	UTS and joint efficiency improved by 112% and 105% of BM; optimum welding parameters for UTS 3000(rev/min), 115 mm/min (WS) and 3º (TA).	[Bozkurt, 2012]

* REV/MIN: Tool rotational speed, WS: Welding speed, AL: Axial load, PD: Plunging depth, TA: Tilt angle, PS: Plunging speed, DT: Dwell time, UTS: Ultimate tensile strength, YS: Yield strength, PCBN: Polycrystalline cubic boron nitride.

2.3.3 Mechanical Properties

The heat generation in FSW process leads to substantial change in post welds mechanical properties such as strength, ductility, fatigue, and fracture toughness. Aluminum alloys are classified into heat treatable alloys and non heat treatable (solid-solution-hardened) alloys. FSW creates a softened region around the weld center in a number of precipitation-hardened aluminum alloys. A number of investigations demonstrated that the change in hardness in the friction stir welds is different for precipitation-hardened and solid-solution-hardened aluminum alloys.

Cerri and Leo [2009] studied the deformation of 0.8 mm thick 2024T3 and 6082T6 aluminium alloys joined by FSW process in warm and room temperature. They have conducted tensile tests at temperatures and strain rates of 170–230 ºC and 10^{-3}–10^{-5} s^{-1} respectively. They concluded that the flow stress decreased with increasing temperature and decreasing strain rate whereas the ductility was quite independent of temperature and strain rate. Liu and Ma [2008] found that the change in the shoulder and pin diameters and the rotation speed changed the position and inclination of the lower hardness zones (LHZs), but did not affect the hardness values along the LHZs. They also observed that with increasing the welding speed hardness values, along the LHZs, heating and cooling rates increased. However, the change in the shoulder and pin diameter and the tool rotation rate did not exert a noticeable effect on the heating and cooling rates and the dissolution time. The tensile strength of joints increased with increasing the welding speed and was independent of the dimension of the shoulder and pin and the rotation rate. Lakshminarayanan *et al.* [2009] welded AA6061 aluminum alloys using three different welding processes, namely gas tungsten arc welding (GTAW), gas metal arc welding (GMAW) and FSW. Very low hardness was recorded in the GMAW joints and the maximum hardness was recorded in the FSW joints. Longhurst *et al.* [2010] investigated the use of torque instead of force to control the FSW process. Due to the highly nonlinear relationship between axial force and the process parameters, the use of force control is restricted to a range of processing parameters. They found torque control had the potential to increase the range of processing variables suitable for stable control. The FSW process reduced [Chao *et al.*, 2001] the yield stress of both AA2024-T3 and AA7075-T7351 under both high strain rate and quasistatic loading

conditions. For both the materials, strain hardening was similar at various strain rates. Cam *et al.* [2009] also concluded that higher rotational and traverse speeds should be employed for higher strength values. On the other hand, lower rotational and traverse speeds led to higher ductility.

The UTS and nugget hardness of friction stir welded AA1050/AA5083 couples increased with traverse speed but decreased with tool rev/min [Sarsilmaz and Caydas, 2009]. It was also found that the traverse speed was the most influencing factor for UTS and nugget hardness [Sarsilmaz and Caydas, 2009]. Sakthivel *et al.* [2009] found best mechanical properties at lower welding speed due to the occurrence of homogenous grains and higher heat input. This refinement is due to the dynamic recrystallization [Su *et al.*, 2005; Barcellona *et al.*, 2006; Ouyang *et al.*, 2006], which is a combined action of high rate strain and elevated temperatures. Such a structure is characterized by a very low level of residual stresses, excellent ductility and mechanical properties superior to those of HAZ [Salem, 2003]. Sato and Kokawa [2001] welded extruded 6063-T5 plates keeping the travel speed and the tool shoulder diameter constant. They concluded that the minimum hardness determined global yield and UTS of the welded joint. Xu *et al.* [2014] observed 13% increase in yield stress of the NZ of FSWed Cu joints compared to BM with rapid cooling. This is due to the occurance of ultra grain refinement and dislocation strengthen mechanism in the weld zone. Dalder *et al.* [2008] used bobbin tool or self-reacting tool to join thick-walled aluminum pressure vessels using FSW process. They found that to restore the welds to near base metal strength, ductility, and toughness post weld treatment namely, quenching and artificial aging were necessary.

Inada *et al.* [2010] proposed friction powder processing to solve the problem of gap generation in FSW process. They used Al and Cu powder having average grain sizes of 89 µm and 106 µm, respectively to join A1050-H24 plates. They found no defect for a 1 mm gap, tunnel hole type defect for a 2 mm gap and groove-like defect for a 3 mm gap without adding power to the gap. The defect formation decreased significantly and the mechanical properties of the joint were also enhanced by adding powder to the gap. Because of the refinement of the ductile ferrite structure at lower RPM, Xu *et al.* [2014] found an improved tensile and toughness properties of FSWed low alloy steel. Jolu *et al.* [2010] investigated the effect of joint line remnant (JLR) on the fatigue lifetime of FSW joints of a 2198 Al alloy.

They observed a decrease in hardness in weld zone. The difference between the fatigue strength at 1,00,000 cycles of sound welds and the base material is less pronounced. The effect of the JLR defect on the fatigue properties found to be low. Eberl *et al.* [2010] prepared dissimilar FSW joint of 20 mm thick 2050 and 7449 alloy. They used tri-flat threaded pins. They concluded that the joint efficiency decreased due to high thickness. The required energy per unit length increased due to the decrease in the advancing speed and an increase in the in plane force opposite to the advance. Yeni *et al.* [2008] reported that left helical screw threaded pin yielded higher mechanical properties and relatively higher hardness values throughout the weld region. This may be due to smaller average grain diameter in the NZ compared to joints produced by right hand screw threaded pin. Due to the post weld aging process they also observed no significant decrease in hardness throughout the weld region. The increase in tool speed increased deformation as well as increased the frictional and deformation heating to the extent that recrystallization occurred. The heat generated by the rotating tool is a function of the rotation speed and the external cooling rate.

Ceschini *et al.* [2007] examined tensile and fatigue properties of AA6061 FSW joints. They found that elongation to failure increased of about 64%. The cyclic stress response curves showed evidence of progressive hardening to failure of the FSW composite and a progressive softening of the base material, at all cyclic strain-amplitudes. Xie *et al.* [2007] joined 6 mm thick Mg-Zn-Y-Zr plate and found lower strengths and elongation of the joints than the parent material. Ren *et al.* [2007] friction stir welded Al-Mg-Si alloy plates. They observed lowest hardness distribution profiles at 45º angle with the butting surface of the joints welded at the higher traverse speed. The lowest hardness profiles near to the butting surface i.e. weld nugget region were observed at the lower traverse speed. At 400 mm/min the joints exhibited higher strength with a 45º shear fracture, whereas a lower tensile strength was observed at 100 mm/min. Wei *et al.* [2007] investigated the effect of welding parameters on the quality of the Al-Li FSW joints. When pressure exceeded certain value, it caused depression and waving burrs, and deteriorate the surface quality of the joints. But tunnel and groove type defects appeared at low pressure. The hardness values within the SZ were higher than those of the BM. Soundararajan *et al.* [2007] investigated friction stir lap welding of AA5182 and AA6022 aluminum alloys. They found that the placement of

AA6022 aluminum alloy on top produced a stronger nugget compared to its reverse order. They also observed that placement in the different orders over each other affected the final weld quality and mechanical properties.

The hardness values in the TMAZ were lower than the HAZ. According to Paglia and Buchheit [2008] the sensitization of the microstructure that occurs during welding is responsible for the corrosion susceptibility of the HAZ region of the Al alloy welds. Saeid *et al.* [2008] studied the effect of the welding speed on the microstructure and mechanical properties of the NZ in FSW of stainless steel and found that sound joints were produced at welding speeds of 50, 100, 150, and 200mm/min and a groove like defect was found at the speed of 250 mm/min, due insufficient heat input. Ren *et al.* [2008] investigated the effect of initial butt surface on the formation of the zigzag line and tensile properties of friction stir welded Al-Zn-Mg-Cu alloy. They found that the zigzag line did not show up and exerted no effect on tensile properties and fracture behavior of 7075Al welds that exhibited a 45º shear fracture on the HAZ. Leal and Loureiro [2008] carried out a number of overlapping friction stir welding passes on 5083-O and 6063-T6 Al alloys. They found that for AA5083-O the single pass or two overlapping passes produced voids along the entire length of the welds and can be eliminated by three or four overlapping passes. It produced a modest increase in hardness. For 6063 FSW leads to a substantial decrease in hardness and in tensile strength in the TMAZ and HAZ due to the dissolution and coarsening of strengthening precipitates. Overlapping passes produced a marginal increase in the hardness and tensile strength of the welds.

Khodir and Shibayanagi [2008] studied the microstructure and mechanical properties of dissimilar joints of 2024-T3 to 7075-T6 Al alloy. They found that the rise in welding speed caused formation of kissing bond and pores especially when the 2024 Al alloy plate was located on the retreating side. Minimum hardness was observed in the HAZ of both sides and their values increased with welding speed. In case of dissimilar and similar micro-FSW butt welds [Scialpi *et al.*, 2008] tensile tests showed that the failure occurs in the NZ due to irregularities in thickness rather than the presence of defects. Excellent fatigue properties were also found. HAZ hardness and transverse tensile strength were reduced with increasing number of passes for 7050-T7451 Al alloy [Brown *et al.*, 2009]. Moreira *et al.* [2009] welded two dissimilar aluminum alloys. They concluded that the welded joints of AA6082-

T6 material revealed lower yield and ultimate stresses and the dissimilar joints displayed intermediate properties. The hardness profile of the dissimilar joint was lower in the AA6082-T6 alloy plate side. Srinivasan *et al.* [2010] found weakest region in the NZ/TMAZ interface of AA2219-T87 aluminium alloy joints. Yigezu *et al.* [2014] studied the effects of process parameters on FSWed Al + 12%Si/10 wt%TiC composites. Tool RPM and TG were found to be the most influencing parameters. They also developed multiple regression equations which predicted the influence of the input parameters with in an error of 10%.

Rajakumar *et al.* [2010] established empirical relationships to predict grain size and UTS of AA6061-T6 aluminium alloy joints. They conducted experiment using central composite rotatable design [Montgomery, 1984] which was found most efficient tool in response surface methodology to establish the mathematical relation of the response surface using the smallest possible number of experiments without losing its accuracy [Gunaraj and Murugan, 1999]. Hui-jie *et al.* [2010] carried out underwater FSW of 2219 aluminum alloy. They observed that underwater joint exhibited lower hardness in the NZ and higher hardness in the TMAZ and HAZ compared with the normal FSW joint. The tensile strength and hardness of the NZ of AA7020-O Al alloy joints increased with increasing the welding speed [Gaafer *et al.*, 2010]. Higher friction pressure, spindle speed and burn-off length and lower upset pressure were recommended for friction welding of 13 mm diameter rods of AA7075-T6 Al alloy [Rafi *et al.*, 2010]. El Rayes *et al.* [2011] analyzed the microstructural and high-temperature mechanical properties of friction stir processed 7010 aluminum alloy. They found enhanced ductility. The activation energy was independent to strain rate. The threshold stress decreased with increasing temperature. Kumar *et al.* [2014] investigated the influence different process parameters on friction stir butt welding of Al-4.5%Cu/TiC metal matrix composites. They obtained better UTS and ductility by 1 mm flat shoulder surface with concavity of 7° tool at 500 RPM. NZ showed lowest hardness values whereas HAZ showed the highest values.

Silva *et al.* [2011] carried out stop action technique to study the material flow of dissimilar 2024-T3 and 7075-T6 Al alloys. In this technique FSW machine was suddenly switched off to stop both translation and spindle drives. They did not observe onion ring formation. A sharp transition from HAZ/TMAZ to NZ was observed in the advancing side. The minimum hardness value of the samples was found in the HAZ of retreating side. The

pin tool played an important role in the material flow and mixing pattern. Rajakumar *et al.* [2011a] used response surface methodology to predict tensile strength, hardness and corrosion rate of AA6061-T6 aluminium alloy joints. The welding speed of 80 mm/min, axial force of 8 kN, shoulder diameter of 15 mm, pin diameter of 5 mm and tool hardness of 45 HRc, resulted in maximum strength properties compared to other process parameters. Kurt *et al.* [2011] incorporated SiC particles into the commercially pure Al by FSP to modify the surface. They found that heat input increased with increasing rotation speed and lowering travelling speeds. FSP treatments decreased the grain size, increased the hardness and improved the formability of plain samples. The microhardness increased with increasing travelling speed and rotation speed. FSW joints of AA2219 aluminium alloy exhibited higher fatigue strength and fatigue life compared to GTAW) and electron beam welding processes [Malarvizhi and Balasubramanian, 2011]. The process offered better reduction in fatigue notch and notch sensitivity factors. The post-weld aged FSW joints showed superior tensile properties, ideal microstructures, preferable strengthening precipitates and favorable residual stress field in the weld region

Cerri *et al.* [2010] investigated the microstructural evolution and mechanical behavior of 6082T6-6082T6, 2024T3-2024T3, and 6082T6-2024T3 thin friction stir welded joints. They found a decrease in flow stress with increasing temperature and decreasing strain rate. The ductility of the joints was poor and independent of temperature and strain rate. Kim *et al.* [2010] found superior mechanical properties for FSW welded sheets as compared to GMAW. The tensile strength of the joints increased with increase in welding speed whereas the fatigue performance decreased. The hardness was better for increasing rotation speed but the tensile and fatigue strength got worsen. The fatigue strength became better with the increase in tilting angle. Bitondo *et al.* [2010] used ANOVA and desirability function technique to determine the significant parameters and set the optimal level for each parameter for AA2198-T3 welds. They found that UTS showed a strong dependence on the rotational speed. Lorrain *et al.* [2010] analysed the material flow in FSW by using unthreaded pins. The presence of flat faces on a pin creates a pulsating action which changes the flow generated by the shoulder and consequently reduces the role of the shoulder.

Pilchak *et al.* [2011] welded mill-annealed Ti-6Al-4V plates. They found an increase in tool temperature with increasing rev/min and weld power input. The torque, x, and z

forces decreased with increased rotational speed. The weld power increased with increased rotational and welding speed. Specimen welded at lower rotation speeds exhibited superior mechanical properties in terms of the UTS [Kumbhar *et al.*, 2011]. Sullivan *et al.* [2011] investigated the failure mechanisms of friction stir welded AA7010-T7651 and simulated the weld zone microstructures. The samples showed hardness loss due to over-ageing in the weld HAZ. The ballistic performance increased linearly with hardness until very high strength temper conditions were reached due to a transition to pseudo-brittle fracture. By macro and micro observations, Cui *et al.* [2012] studied the formation mechanism and distributions of various types of defects in friction stir welded AA6061-T4 T-joints. The welds were classified as series A (T-lap), B (T-butt-lap), and C (T-butt). According to rev/min these were again classified as 1 for 400, 2 for 500 and 3 for 600 rev/min. They observed tunnel defects in B1 and C1 T-joints. Kissing bond defects were observed at stringers' roots on advancing side in most of the T-joints. Along the skin tensile properties were much higher than those along the stringer.

Zhang *et al.* [2012] conducted underwater FSW of Al-Cu aluminum alloy and found better in contrast to the normal HAZ. It resulted in the variation of tensile behavior and the improvement in mechanical properties of the underwater joint. Forcellese *et al.* [2012] used pin and pin-less tool configurations to join AZ31 thin sheets by FSW process. They concluded that both UTS and ductility increased with rising rotational speed/welding speed ratio until a peak value and then decreased as the ratio further increased. Higher strength and ductility were found in case of pin tool configuration and a more homogeneous microstructure was obtained using the pin-less tool configuration. Miles *et al.* [2009] focused on the properties and microstructures of friction stir welded high strength steel sheets. Three types of materials, namely dual phase (DP) and transformation induced plasticity (TRIP) steels; in particular DP 590, TRIP 590 and DP 980 were used. They found that during transverse tension testing in DP 590 and TRIP 590, the joints did not fail in the HAZ or in the NZ. The HAZ produced in DP 980 was more pronounced than in the 590 materials. Xu *et al.* [2011] employed micro-indentation technique to study the hardness and elastic modulus of NZ in friction stir welded 2219-O aluminum alloy. Both of the average hardness and elastic modulus in increasing order was found to be base material, bottom,

middle and top of the NZ. Both the indentation depth and the residual impressions size increased with the increase in grain size.

Li and Shen [2010] prepared a new type of joint, namely lap-butt joint of dissimilar aluminum alloys. They found an average tensile strength of 159 MPa. Aonuma and Nakata [2012] found a higher tensile strength of the Mg-Zn-Zr alloy and titanium FSW joint than that of the pure magnesium and titanium joint. A joint efficiency of about unity was found in friction stir welded Al-Cu-Mg-Ag sheets [Nikulin *et al.*, 2012]. The FSW process reduced the elongation of the joints. Simoncini and Forcellese [2012] used pin-less and pin tool configurations to join AA5754 and AZ31 thin sheets. They found lower value of ductility and flow stress and pin-less tool provided highest tensile strength and ductility. Trimble *et al.* [2012] investigated the tool forces during FSW. They found maximum force during the plunge stage which was reduced about 35% during the translational stage. Barnes *et al.* [2012] used different welding speed and tool material for welding of HSLA-65 steel. They concluded that the nugget hardness was influenced by tool traverse speed, rotation speed, and material. The joint microstructure and hardness were also influenced by the tool material and design. The tensile strength of the FSW joint with water cooling [Xu *et al.*, 2012] was nearly same as of the BM. The strain-hardening capacity of the welds was enhanced in middle and bottom slices than in the BM and top slice with water cooling.

Shahri and Sandstrom [2012] analysed the influence of clamping and welding procedure on fatigue life of 6005A-T6 aluminium alloy. They carried out two types of welding procedure, namely side by side welding and simultaneous welding from both sides. They found that the clamping procedure influenced significantly the tensile residual stresses and fatigue life. Yu-hua *et al.* [2012] studied the interface characteristics of FSW lap joints of dissimilar alloys. They found that the amount of Ti particles stirred into the stir zone decreased with increased welding speed or decreased of tool rotation rate. The failure loads of joints decreased with the increasing welding speed. Subbaiah *et al.* [2012] studied the microstructure and mechanical properties of Al-Mg-Sc alloys. They concluded with more joint strength. Khorrami *et al.* [2012a; 2012b] welded plastic deformed aluminum sheets and found that the hardness value of NZ was reduced. The strength of the joint reduced with increased rotation speed. Hu *et al.* [2012] found same micro-hardness and tensile properties of NZ were same as base metal.

Rajakumar and Balasubramanian [2012] established the relationship between the FSW parameters and the responses. They used multi-objective optimization in the RSM to maximize the strength and minimize the corrosion rate. The sensitiveness of the parameters in decreasing order were rotational speed, axial force, welding speed, shoulder diameter, pin diameter, and tool material hardness. Bozkurt [2012] found tool rotation speed and tilt angle were the most and least contributing parameter, respectively in FSW of high density polyethylene and polypropylene sheets. It was found that the base material plastic behavior and plate's thickness had strong influence on torque registered during welding [Leitao *et al.*, 2012].

2.3.4 Techniques for Finding the Significant Process Parameters

Taguchi's design of experiment (DOE) method is an effective and efficient tool to enhance the product and process performance. This method also improves the design and system by reducing the experimental time and cost significantly [Montgomery, 2006]. The complexity of large number of experimental runs with increasing number of process parameters and their levels can be solved by this method. For evaluating the process parameters a statistical measure of responses, named signal to noise (SN) ratio is used [Montgomery, 2006]. In addition a statistical test called analysis of variance (ANOVA) can be executed for identification of the individual process parametric effects on the output responses [Montgomery, 2006]. Some researchers [Lakshminarayanan and Balasubramanian, 2008; Khalid Rafi *et al.*, 2010; Vidal *et al.*, 2010; Colligan *et al.*, 2003; Koilraj *et al.*, 2012; Bozkurt, 2012; Shojaeefard *et al.*, 2012; Puviyarasan and Senthil Kumar, 2012; Salehi *et al.*, 2012; Bozkurt and Bilici, 2013] have used Taguchi's orthogonal array (OA) design of experiment method for selection of optimal levels of process parameters setting in FSW process. But it appeared that in most of the works three or four process parameters were taken into account. Though Record *et al.* [2007] studied the effect of nine input parameters (RPM, WS, PD, TPL, weld cooling, X start distance, weld location, pre-weld cooling and DT) on measured process outputs (Forces generated in X-, Y- and Z-directions, thermal histories at pin center, root and shoulder, motor power and shoulder depth), but the study was based on bead on plate basis for friction stir processed 7075-T7351

aluminium alloy. They found that RPM, PD and traverse rate were the most significant factors that influence the FSW process.

However, traditional Taguchi method cannot solve multi-objective analysis problems. To overcome this, the Taguchi method is coupled with different theories like grey relational analysis (GRA), utility concept (UC) and desirability function approach (DFA) [Lim *et al.*, 2006; Walia *et al.*, 2006; Datta *et al.*, 2008; Gaitonde *et al.*, 2008; Heidari and Razmi, 2012; Periyasamy *et al.*, 2013; Karande *et al.*, 2013; Sivasakthivel *et al.*, 2014]. These approaches can solve multi-response problems simultaneously. Some researchers [Vijayan *et al.*, 2010; Aydin *et al.*, 2010; Chien *et al.*, 2011; Prasanna *et al.*, 2013; Kumar *et al.*, 2013] used Taguchi's OA experiment combined with GRA for selection of optimum levels of process parameters setting in FSW process. Vijayan *et al.* [2010] optimized the parameters like RPM, WS and AL with respect to output parameters like UTS and power. Chien *et al.* [2011] considered RPM, WS, TA and TPL. They found the best multiple weld qualities at 1800 rpm, WS of 180 mm/min, TA at 1° and TPL of 2.9 mm. Prasanna *et al.* [2013] considered RPM, WS, TPL and tool pin offset for multiple performance characteristics namely UTS, % elongation and hardness. The optimal parameter combinations for considered 6061 Aluminum alloy were 800 rpm, 10 mm/min (WS), 5.7 mm (TPL) and 0.4 mm (offset distance). Kumar *et al.* [2013] carried out grey based Taguchi analysis to optimize the process parameters for FSW of AZ31B Mg Alloy. TPL, RPM and WS were the considered process parameters with respect to hardness, ductility and UTS. TPL was found to be the most influencing parameter with 45.09% contribution. Aydin *et al.* [2010] applied GRA and Taguchi method for optimization of FSW parameters. They found an optimum RPM, WS and SD of 2140 rpm, 80 mm/min and 15 mm, respectively for best joint quality. Karande *et al.* [2013] proposed utility concept (UC) and desirability function approaches (DFA) to select appropriate material for different industrial applications. Walia *et al.* [2006] applied utility theory and Taguchi quality loss function for simultaneous multi response optimization in centrifugal force assisted abrasive flow machining process.

Though there are literatures on application of Taguchi coupled analysis techniques for FSW process, they are few. Most of the published works covered the effects of only three or four input parameters on two to three output responses, simultaneously, keeping all other parameters constant. The parameters like TPL and DT have not been taken frequently into

account which may have influence over joint strength and heat generation. The analysis of FSW process by considering most of the possible parameters has not been reported yet.

The gaps and the objectives from this section of literature study are discussed below.

- **Gaps:**
  - Detailed experimental investigation considering most of the process parameters is rare.
  - Implementation of Taguchi coupled multi objective analysis techniques to identify the significant process parameters for FSW are few.
- **Objective-2:**

  Identification of significant process parameters.
- **Objective-3:**

  Studying the effect of significant process parameters on joint properties.

2.4 Literature-3: Start and End Limitations

The usual practice of carrying out the FSW process [Chao *et al.*, 2001; Kimapong and Watanabe, 2004; Mishra and Ma, 2005; Record *et al.*, 2007; Konkol and Mruczek, 2007; Firouzdor *et al.*, 2009; Biswas and Mandal, 2011; Heidarzadeh *et al.*, 2012; Fujii *et al.*, 2013; Huang *et al.*, 2013] is shown in **Figs. 5.1(a)** and **(b)** (shown in Chapter-5, Section-5.2). It can be observed that the need of some offset distance both at start and end of the plates for welding results in material wastage as well as post welding machining works. There are very few published literatures about refilling or repair of end hole in FSW welds. Huang *et al.* [2011] developed filling friction stir welding (FFSW) to repair the end hole. The end hole was repaired by the combined use of plastic deformation and flow of the consumable joining tool. But in the process three different sub processes need to be carried out namely, FSW, FFSW and friction stir processing. And also each time the tool and shoulder geometry and tool material need to be different which makes the technique time taking and complex. However the double acting, retractable or auto adjusting FSW tools [Ding and Oelgoetz, 1996; Allen and Arbegast *et al.*, 2005; Su *et al.*, 2006; Uematsu *et al.*, 2008] consisting of outer shoulder and inner pin, were developed in order to eliminate or

refill the end hole. Uematsu *et al.* [2008] used a double acting tool which consists of outer flat shoulder and inner retractable probe. It was used in friction stir spot welding process in which initially the tool was plunged into workpieces in a conventional way. After joining the inner pin was retracted into the outer shoulder and then the flat face of the tool is again plunged in order to refill the end hole. Ding and Oelgoetz [1996] patented a hydraulically actuated auto adjusting pin tool. In this process the pin can be incrementally withdrawn from the workpieces which eliminates the end hole in the weld. The system consists of welding head housing with a motor connected to the controller instrument. The arbor forms an interior cylinder and supported by bearings. As the welding head progresses the controller senses any pressure variation on the lower face of the shoulder housing. It adjusts the arbor to keep the vertical pressure constant. In order to keep the pin at a proper depth in the workpieces regardless of their thicknesses, the piston moves towards the workpieces this extends the pin further from the shoulder. This operation was used to incrementally withdraw the pin during the final stage of the process to eliminate the end hole.

From the published research works it has been seen that the appropriate starting position for tool plunge has not been reported yet. Also there was no discussion about the possible techniques for avoiding post weld machining work and material wastage due to inevitable offsets of the tool (shown in **Figs. 5.1(a)** and **(b)**) at the start and end of the weld. Though some methodologies have been developed for elimination of end hole, these are very complex and uneconomical. Therefore in the present work, various ideas are formulated to find out an appropriate starting position without material wastage and elimination of end hole. The influence of various considered ideas on the weld strength is also studied. Altogether the aim of the proposed work is relied on increasing the effective joint length by avoiding any possible material wastage. The detailed experimental methodologies followed in this work are given in the Chapter-5.The gaps and the objective relevant to the current literature section are discussed below,

- **Gaps:**
  - The exact starting point of the welding in order to achieve maximum joint length is not discussed.

- There is not much discussion about the elimination of end hole defect during FSW process.

➢ **Objective-4:**

Finding appropriate starting position and elimination of the end hole in FSW.

2.5 Literature-4: Modeling of FSW Process

This section includes the review of the understanding of mechanical and thermal processes during FSW. During FSW heat is generated by friction between the tool and the work-piece which results in intense plastic deformation and temperature increase within and around the stirring zone. Due to this a significant microstructural evolution, including grain size, grain boundary character, dissolution and coarsening of precipitates, breakup and redistribution of dispersoids, and texture takes place. Various models used by different researchers to study the FSW process are shown in **Table 2.4**.

Table 2.4 Models Used in Various Studies

Models	Study	References
Statistical models	Thermal history	[Liu and Ma, 2008]
	Forces	[Bitondo *et al.*, 2011]
	Relationships between grain size and hardness	[Rajakumar and Balasubramanian, 2012]
	Heat generated	[Chen, 2009]
	Relationship between process variables and mechanical properties	[Elangovan and Balasubramanian, 2007; Elangovan and Balasubramanian, 2008b; Sundaram and Murugan, 2010; Rajakumar *et al.*, 2010; Karthikeyan and Senthil Kumar, 2011; Rajakumar *et al.*, 2011a; Rajakumar and Balasubramanian, 2012; Blignault *et al.*, 2012; Davis *et al.*, 2012; Palanivel and Mathews, 2012; Liang *et al.*, 2012]
	Process parameters	[Blignault *et al.*, 2012]
Thermo mechanical model	Average grain size	[Fratini *et al.*, 2009]
	Thermal history	[Buffa *et al.*, 2010; Biswas and Mandal, 2011]
	Material flow	[Fratini *et al.*, 2010]

	Temperature distributions and the material deformations	[Zhang *et al.*, 2009]
	Heat input	[Aval *et al.*, 2011a]
	Thermo-mechanical and microstructural issues	[Aval *et al.*, 2011b]
	Tool shoulder diameter	[Arora *et al.*, 2011]
Soft computational models	Process parameters	[Kennedy and Eberhart, 1995; Fratini *et al.*, 2009; Lakshminarayanan and Balasubramanian, 2009: Tansel *et al.*, 2010]
	Power values	[Davis *et al.*, 2012]
Surrogate models	Relation between process parameters and maximum temperature	[Liao and Daftardar, 2009]
Restoring models	Microstructure and micro-texture	[Chen, 2009]
Computational fluid dynamics (CFD)	Thermal, tensile, macro-section and process force	[Lammlein *et al.*, 2009; Atharifar *et al.* 2009]

2.5.1 Statistical Models

Hwang *et al.* [2008] used a second-order polynomial equation to predict the temperature of 6061-T6 aluminium alloy workpiece during FSW process. Uniform temperature distribution was found inside the pin and heat transfer took place from the rim of the pin to the edge of the workpiece. They also found appropriate temperatures ranges for a successful welding were between 365 °C and 390 °C. The temperatures on the advancing side were slightly higher than those on the retreating side. The tensile strength and the hardness at the thermo-mechanically affected zone were about half of the base metal. Sundaram and Murugan [2010] developed regression models to predict the ultimate tensile strength (UTS) and tensile elongation (TE) of the dissimilar friction stir welded joints of aluminium alloys. The prediction performances of the models were within ±10%. They observed that the straight cylinder tool produced lowest tensile strength and tensile elongation, whereas the tapered hexagon tool produced higher pulsating effect and smooth material flow which resulted in the highest tensile strength and tensile elongation of the dissimilar FS welded joints. The tensile strength increased with the increase in the tool rev/min or welding speed to a maximum value and then decreased. The tensile elongation decreased with the increase in tool rev/min and increased with increase in the welding speed.

Bitondo *et al.* [2011] developed two sets of empirical models to predict in-plane and downward forces and yield and tensile strengths of the friction stir welded joints. They validated the models using statistical tools such as analysis of variance (ANOVA), F tests, Mallows' C_P and coefficient of determination. Palanivel and Mathews [2012] developed a linear regression model using response surface methodology (RSM) for establishing the relationship between the FSW process parameters and UTS of AA5083- H111 aluminum alloy. They considered tool rotational speed, welding speed, and axial force as the process parameters. They found satisfactory adequacy of the model by checking with ANOVA test and scatter diagrams. Rajakumar and Balasubramanian [2012] established linear regression relationships between grain size and hardness of the weld nugget and tensile strength for FSW joints of commercial grade aluminium alloy.

Using Taguchi technique, Lakshminarayanan and Balasubramanian [2008] evaluated that the tool rotational speed had 41% contribution, traverse speed had 33% contribution and axial force had 21% contribution to tensile strength of the welded joints. Karthikeyan and Kumar [2011] developed a mathematical model to establish the relationship between the different process variables and the mechanical properties of friction stir processed of AA6063-T6 aluminum alloy. They observed maximum increase of UTS, ductility and micro-hardness by 46.5%, 133% and 33.4%, respectively. Dinaharan and Murugan [2012] developed a mathematical model to predict UTS using experimental data. Experiments were conducted using a four factor, five level central composite rotatable design. They also optimized the process parameters using generalized reduced gradient method to maximize the UTS. Blignault *et al.* [2012] performed FSW experiments using response surface method and developed an empirical model to predict UTS. They found that the standard deviation between the measured and the predicted tensile strength values was around 13%. Kumar *et al.* [2012] developed empirical models to select process parameters to join AA5083 aluminum alloy using FSW. They concluded that the axial force was most affected by tool diameter, rotational speed and welding speed whereas the horizontal force by welding speed, pin diameter and interaction of tool diameter and rotational speed. Welding speed, tool diameter and rotational speed affected heat input.

2.5.2 Thermo Mechanical Models

Durdanovic *et al.* [2009] developed a mathematical model which describes heat generated during various stages of FSW process. It was concluded from the developed model that determination of precise amount of heat generated during FSW process was complicated since there were various uncertainties, assumptions and simplifications of mathematical models that describes the welding process. Fratini *et al.* [2009] combined neural network and finite element model to predict the average grain size in FSW process. They predicted final grain dimension using local numerical values of strain, strain rate, temperature and Zener-Hollomon parameter as inputs. A very good agreement between predicted values and experimental results were obtained. Arora *et al.* [2011] developed a three-dimensional heat transfer and visco-plastic flow model for the optimum tool shoulder diameter. They varied tool rev/min in three steps. They found superior tensile properties with shoulder diameter of 18 mm and tool rotational speed of 1200 rev/min. Soundararajan *et al.* [2005] developed a thermo-mechanical model to predict the stresses, three dimensional forces and transient temperature field in friction stir welding of Al 6061. This model with adaptive contact conductance at the interface of the workpiece and backing plate showed good agreement with experimental results.

Arora *et al.* [2012] studied load bearing capacity of FSW tool pin by computation of traverse force and torque using a three-dimensional heat transfer and viscoplastic material flow model. They observed a significant increase in the traverse force with increasing TPL. The maximum shear stress on tool pin increased with either increasing TPL or decreasing PnD. Colegrove *et al.* [2007] developed a translating 3D thermal model to predict the heat generation and temperature in FSW. Particularly at the high RPM, they observed a better correlation between the weld macrographs and the rotational flow diagrams obtained from the model. This is when a slip boundary condition was used at the shoulder. Buffa *et al.* [2010] developed a finite element (FE) model to analyze the FSW of corner fillet geometries. The temperature distributions predicted by the model showed a good agreement with experimental data and useful information were derived from the analysis of the deformation as well as of the forces on the welding tool. Biswas and Mandal [2011] developed a three-dimensional FE transient thermal model to study the effect of tool

geometries on the thermal history of the workpiece. They found that the tools having a concave shoulder led to lesser temperature rise. Conical tool pins exhibited somewhat lesser peak temperature compared to that of a cylindrical pin. They also found that with 100% increased in tool rotational speed, the increase in peak temperature was only about 13%. However the reduction of plunging force was more than 40%.

Arora *et al.* [2009] obtained strains and strain rates in the ranges of -10 to 5 and -9 to 9 s^{-1}, respectively during FSW of AA2524 alloy. They developed a three-dimensional coupled viscoplastic flow and heat transfer model to calculate the strains and strain rates. As per the model it was seen that the material experiences tensile and compressive strain in the welding transverse direction respectively. Fratini *et al.* [2010] developed an improved continuum FE model for the simulation of friction stir welded T joints. They used temperature, strain and strain rate dependent flow stress to model plastic behavior. They found that the developed model was able to successfully predict material flow, as well as the most relevant field variable distribution. A three-dimensional, heat transfer and materials flow model was developed by Mehta *et al.* [2011] to predict the optimal FSW tool shoulder diameter. At all the considered RPMs, the peak temperature, spindle power, and torque requirements increased with increase in SD. The optimum SD for different RPMs were 20 mm-710, 25 mm-560 and 30 mm-355 rev./min.

Song and Kovacevic [2003] developed a three-dimensional heat transfer model in a moving coordinate system. This model reduced the difficulties in determining the temperature distribution near the moving tool pin. Zhang *et al.* [2009] used a fully coupled thermo-mechanical model to study the effect of shoulder size on the temperature distributions and the material deformations in FSW of AL6061-T6 alloy. They concluded that with the increased of the shoulder size the maximum temperature can be increased and the temperature distribution under the shoulder becomes more uniform. It can also lead to the increase of the efficient power for FSW process. Manvatkar *et al.* [2015] proposed a three-dimensional heat transfer and material flow model to map peak temperatures and cooling rates for the FSW of high-carbon steels. The result concluded that the formation of martensite can only be prevented only at fairly low rate of heat generation. Based on a rectangular fixed grid finite difference method, Nandan *et al.* [2007] proposed a heat, momentum, and solute transport model for heat transfer and materials flow calculations

during FSW of dissimilar aluminum alloys. They considered the parameters like friction coefficient, the sticking, heat transfer coefficient, and the extent of viscous dissipation and found to be significant in affecting temperature fields and the torque on the tool.

Aval *et al.* [2011a] developed a three-dimensional FE model to predict welding heat input. It was observed that the frictional power had a major effect in heat generation and temperature distribution within the metal. Initial condition of the material can significantly affect the final microstructures and mechanical properties of the welded joint. The temperature in FSW was asymmetrically distributed and peak temperatures were higher on the advancing side than the retreating side. In another study De *et al.* [2014] studied the tool durability and microstructure for friction stir welding of mild steel. The developed model showed good agreement with published literatures in calculating temperature profiles and cooling rates. Tool durability enhanced with increasing RPM. Due to lower pick temperature at higher WS, the tool durability also reduces. Aval *et al.* [2011b] investigated the thermo-mechanical and microstructural issues in dissimilar FSW of AA5086-AA6061. Finer grains and large thermally affected region were found in AA6061 side compared to AA5086 side. In the AA5086 side the micro-hardness was higher than the base metal because of recrystallization and generation of fine grains in weld nugget. But in the AA6061 side, because of dissolution of the hardening phases in the TMAZ, softening was observed.

2.5.3 Soft Computational Models

During FSW heat is generated by friction between the tool and the work-piece which results in intense plastic deformation and temperature increase within and around the stirring zone. Due to this a significant microstructural evolution, including grain size, grain boundary character, dissolution and coarsening of precipitates, breakup and redistribution of dispersoids, and texture takes place. Different researchers used different modeling and optimization techniques to study and optimize the FSW process. Among them regression, thermo mechanical and mathematical models are frequently used for the analysis of thermal and mechanical properties with respect to different process parameters. The main drawbacks of these models are that they are time consuming and not reliable. So soft computation approaches for modeling the FSW weld quality and optimize the process parameters may be

beneficial. Though soft computational modeling and optimization techniques are few in application especially for FSW process, some of the relevant reviews were discussed below.

Artificial neural network (ANN) is one of the intelligent systems, which is useful in a variety of real-world application as it can deal with complex and highly interactive processes. For modeling of weld quality different types of ANN can be used, namely multilayer neural network (MLNN), radial basis function (RBF), self-organizing map (SOM), etc. These techniques can very efficiently map the non-linear relationships in the friction stir welding process. Popularly, multilayer neural network (MLNN) trained with the back-propagation error algorithm is used for weld quality modeling [Lim and Gweon, 1999; Kim *et al.*, 2003; Lightfoot *et al.*, 2005; Pal *et al.*, 2007; Okuyucu *et al.*, 2007; Ghetiya *et al.*, 2014]. Kim *et al.* [2003] developed an intelligent system for automatic determination of optimal welding parameters for each pass and welding position. Lakshminarayanan and Balasubramanian [2009] found better prediction capability of ANN model compared to response surface model. The feed forward multilayer ANN model was much more robust and accurate in estimating the tensile strength values. Pal *et al.* [2007] developed six different types of radial basis function neural network (RBFNN) models to predict welding distortion. Different research works [Fratini *et al.*, 2009; Buffa *et al.*, 2012] linked FEM with ANN to predict mechanical and microstructural properties of friction stir welded joints. A generalized feed-forward (GFF) and modular feed-forward (MFF) neural networks along with a MLNN were developed by Lightfoot *et al.* [2005] to model the weld induced deformation in ship plate. Manvatkar *et al.* [2012] developed five ANN models to predict the torque, peak temperature, traverse force, bending and maximum shear stresses exerted on tool pin during the joining of aluminium alloy by FSW process. These models are compared with a three dimensional heat and material flow model and found suitable to be used even beyond the training range.

Lim and Gweon [1999] proposed an ANN model to estimate the joint strength of spot welds during the pulsed laser spot welding process. Okuyucu *et al.* [2007] developed an ANN model to correlate the input parameters (welding speed and tool rotation speed) of FSW process with mechanical properties of aluminum butt joints. Tansel *et al.* [2010] developed a genetically optimized neural network system in order to obtain the optimal process parameters. The average estimation errors of the artificial neural networks (ANN)

were less than 0.5%.A multilevel adaptive fuzzy control (MLFC) was used to improve the weld quality [Davis *et al.*, 2012]. MLFC was able to maintain nearly constant spindle power for a wide range of process parameters even when the process was subjected to significant variations and external disturbances. Liao and Daftardar [2009] constructed two surrogate models, one linear and one non-linear to relate FSW process parameters with maximum temperature at a selected location, using simulation data generated by a thermal model. They implemented five population based metaheuristics namely ant colony optimization (ACO), differential evolution (DE), genetic algorithm (GA), harmony search (IHS) and particle swarm optimization (PSO). For loose temperature range linear model produced better optimization results where as non-linear model produced better results for tight temperature range.

2.5.4 Others

Lammlein *et al.* [2009] developed a computational fluid dynamics process model to analyze thermal, tensile, macro-section and forces. They found that the 90º tool was better than the 60º, 80 º, or 120 º tools as it retained a reasonable percentage of parent material strength (50-60%). They also found that the small cone inclusive angles required higher spindle speeds and created more flash while large angles produced larger heat affected zones. McNelley *et al.* [2008] developed two models to interpret microstructure and micro-texture data of welded joint. They concluded that recrystallization and grain refinement occurs during FSW process. Robson *et al.* [2010] adapted a microstructure model which used the Wagner and Kampmann numerical method [1991] to track the evolution of the full particle distribution for each of the precipitate phases of interest during the weld thermal cycle. They conducted multi-pass FSW of 6.4 mm thick AA7050-T7451 plates. They concluded that in the nugget, under normal welding conditions full precipitate dissolution occurs during each pass. A post-weld aging treatment was found to be ineffective in recovering weld properties at the HAZ after multiple weld passes. Wang *et al.* [2013] investigated the contact condition between the FSW tool and the workpiece. They found reduced heat generation in slip boundary condition compared to the stick model. It also produces a lower strain rate history.

Arora *et al.* [2011] used an approximate analytical technique for the calculation of three-dimensional material flow during FSW considering the motion of an incompressible fluid induced by a solid rotating disk. A mathematical model was developed by Heidarzadeh *et al.* [2012] to predict the tensile properties of friction stir welded AA6061-T4 aluminum alloy joints. They showed that the developed model can be effectively used to predict the UTS and tensile elongation of the joints at 95% confidence level. They also showed that the UTS of the joints increased with the increase of tool rotational speed, welding speed and tool axial force up to a maximum value, and then decreased. The tensile elongation of the joints increased with increase in rotational speed and axial force, but decreased by increasing of welding speed. Arora *et al.* [2009] modeled torque, power requirement and stir zone geometry during FSW of AA2524 aluminum alloy by solving the equations of conservation of mass, momentum and energy. It was concluded that due to higher heat generation rate and higher temperature the torque required for the welding decreased with increase in the tool rotation speed. The size of the TMAZ increased slightly with the increase in tool rotational speed.

The gaps and the objectives relevant to the current literature section are discussed below,

- **Gaps:**
  - Current FSW process sub-models are complex, time consuming, and difficult to be used in real time.
  - They all suffer from lack of reliability of the predicted results. This is because the physics is highly complex and the current phenomenological models do not contain any model component designed to ensure a good agreement with experimental results.
  - Use of soft computational models to study the FSW process is rare in literature.
- **Objective-5:**

  Modeling of weld quality using artificial neural network.

2.6 Literature-5: Optimization of FSW Process Parameters

The selection of optimal FSW process parameter setting is a difficult task because in this joining technique, the numbers of input parameters are more. Also the input-output relationships are non-linear, highly complex and interdependent. Dutta *et al.* [2007] developed conventional regression analysis, a back-propagation neural network (BPNN) and a genetic-neural system (GA-NN) from experimental data of tungsten inert gas (TIG) welding process to achieve the best bead geometry. Dey *et al.* [2009] proposed regression analysis to establish input-output relationships in bead-on-plate welds on austenitic stainless steel plates using electron beam welding.GA with a penalty function approach was used to determine optimal weld-based geometry. Tansel *et al.* [2010] used genetically optimized neural network systems (GONNS) to optimize the FSW process parameters. Nagesh *et al.* [2010] developed neural network model for predicting the weld bead geometry for TIG welding process and used GA for optimizing the process parameters. Teimouri and Baseri [2013] proposed fuzzy-artificial bee colony-imperialist competitive algorithm systems for the forward and backward predictions of the friction stir welding parameters which can reduce the number of experiments significantly. Dhas *et al.* [2011] used GA and PSO algorithms to determine optimal welding parameters for submerge arc welding process. Roshan *et al.* [2013] used adaptive neuro-fuzzy inference systems (ANFIS) for mapping the process parameters and output response using experimental observations. Then they used these models as objective function to find optimal FSW parameters by using of simulated annealing algorithm. Sathiya *et al.* [2012] used ANN to model the laser welding process and GA for optimizing the process parameters. From the literatures, it is found that GA was used intensively in optimization of welding processes.

Evolutionary algorithm works on natural evolutionary principles to constitute search and optimization procedures. Genetic algorithms (GAs) have been used extensively as search and optimization tools in various problem domains [Deb, 2001]. Kennedy and Eberhart **[12]** [1995] proposed an optimization algorithm inspired by the collective behavior of flocks which is particle swarm optimization (PSO). Storn and Price [1997] proposed differential evolution (DE) algorithm which is a stochastic population based real parameter optimization algorithm for challenging continuous problems. Shojaeefard *et al.* [2013] used ANN to model FSW process and multi objective particle swarm optimization for pareto optimization

of mechanical properties. Other evolutionary algorithms like PSO and DE were not tested much, although they are very efficient and fast search algorithms. It may be useful to apply these techniques to optimize FSW process.

The gaps and the objectives relevant to the current literature section are discussed below,

- **Gaps:**
  - Process parameter optimization by considering most of the parameters is not being reported.
  - Uses of non-traditional hybrid optimization techniques for FSW process are very few.
- **Objective-6:**

  Optimization of process parameters using Neuro-Evolutionary Algorithm techniques.

Apart from the literatures related to the present thesis work some other important aspects of FSW process have also been reviewed in this chapter. This is in a view to explore the complexity in understanding the physics of the process in a more detailed manner. They are in terms of different types of process defects, possible reasons and their effects on joint properties. Also various types of advanced testing methods to identify the defects both in macro and micro level have been discussed. The possible condition monitoring of FSW process was reviewed. These are discussed in the following sections.

2.7 Literature-6: Process Defects and Testing

FSW is characterized by high weld quality, but defects still exist at unsuitable joining parameters [Vijay and Murugan, 2010]. In the present review, the research status of welding defects has been introduced from the aspects of defects characterizations, affecting factors and testing methods. The defect characterizations and their affecting factors can be on the base of microstructural analysis and mechanical property. There is no liquid state for the weld pool during FSW for which the potential defects are within the weld.

A “Characteristic Defect” is a microstructural or geometric anomaly peculiar to a FSW that adversely affects form, fit or function. Defects in FSW are related to processing

temperatures, material flow patterns and joint geometry, which in turn are a function of process parameters and TG. William and Arbegast [2003] studied various types of FSW defects, its cause and its effects. Under cold processing, they observed wormhole (due to insufficient metal flow, excessive WS for given rev/min, cold weld etc.), scalloping (due to moderately cold weld and insufficient axial load) and cold lap (in lap joints due to inadequate vertical mixing) types of defects which reduced the mechanical properties and lap shear strength. Similarly in hot processing, defects like ribbon flash (due to excessive PD and thickness mismatch between AS and RS), nugget collapse (due to excessive material flow into AS, higher heat input etc.), faying surface (due to excessively hot weld and too far offset to AS), root flow defect (due to excessive metal flow within weld zone under pin tip, higher TPL and improper PnD), sheet thinning (in lap joint due to hot processing parameters pulled up faying surface). All these defects lead to reduced mechanical properties, fatigue life and lap shear strength. They [William and Arbegast, 2003] also observed geometry related defects like lack of full weld depth due to inadequate metal flow and recrystallization of weld zone. The other possible reasons are inadequate tool pin length, improper PnD and cold weld.

The non-destructive ultrasonic method [Ghidini *et al.*, 2005] has been used as a promising technique to detect and characterize any of the imperfections mentioned above. Through-hole impact test is a method to identify the presence of a root defect and zone of weakness [Thomas *et al.*, 2005]. Unintentional offsetting of the pin can cause several types of discontinuities or defects including lack of penetration or a displaced bond line developing a “stuck” or “weak” bond having no strength [Cruz, 2013]. Presently, the best methods for non-destructive evaluation (NDE) of friction stir welds include ultrasonic inspection (UT), radiographic inspection (RT) and eddy current inspection (ET) depending on individual needs. Further advanced NDE processes using a slight variation of the PAUT called Matrix Phased Array Ultrasonic Testing (MPA-UT) have been developed [Cruz, 2013; Lamarre and Moles, 2000]. It uses a series of the conventional ultrasonic elements that are grouped together to function as a unit and can be directed at various angles as they pass through the part being inspected. This results in giving a complete map of the joint area.

Santos *et al.* [2010] introduced a eddy current (EC) probe to test AA2024 welded joints. They were able to detect and sizing micro root defects on FSW joints with 60 micros depth. . Liu *et al.* [2008] evaluated the defects in friction stir welded aluminum alloy with a new ultrasonic method, which is based on multiple-incident angle reflection at joints by using spot-focused beam. Lombard *et al.* [2006] found pseudo-bond defects in the form of planar regions on the fracture surface and in the form of onion-skin defects in the FS welded 5083-H321 alloy. Occurrences of these defects were found to be a function of tensile strength and tool speed. Santos *et al.* [2007] inspected AA5083-H11 welded samples by a on-line NDT inspection integrated system employing a data fusion algorithm with fuzzy logic and fuzzy inference functions.

2.8 Literature-7: Condition Monitoring

In FSW, there is no appreciable tool consumption for many systems for which there do not seem to be any literature reports of systematic studies of tool condition. The issue of tool condition for extended processing will become an important concern especially where abrasive particles are involved since there is increasing interest in aerospace, automotive and marine system applications for advanced metal matrix composite use. Thompson and Babu [2010] used three tungsten-based tool materials namely material A (99% W-1% La_2O_3), material B (75% W-25% Re), and material C (70% W-20% Re-10% HfC) to join high strength steel. They identified the tool degradation mechanisms by studying the pre- and post-weld microstructures of the tool. They found that the grain deformation was the most significant source of tool degradation. The primary degradation mechanism of material A was deformation, for material B it was twinning and for C it was inter-granular failure. Yang *et al.* [2008] developed a monitoring algorithm to detect gaps in friction stir butt welding of aluminium alloys. Three different welding scenarios were considered. In the first one tool stirs a solid piece of material, second one consists of two sheets which are firmly pushed together such that there was no gap and then welded. For the third scenario two sheets were separated by shims such that there was a constant known gap and then welded. They concluded that the algorithm was able to detect the presence of gaps in FSW operations reliably for tool traverse speeds below 4.233 mm/s and gap sizes above 0.3048 mm.

Prado *et al.* [2003] studied the tool wear and the rate of wear in the FSW of Al 6061 aluminium alloy. They concluded that threaded tool produced a self optimized shape with no threads which continues to produce excellent welds but without any additional tool wear. The self optimized shape changed with increase in weld speed and at a constant tool rotational speed of 1000 rev/min. They also concluded that the rate of tool optimization increased with increasing weld speeds. Chen *et al.* [2003] carried out wavelet transform analysis of acoustic emission in monitoring friction stir welding of 6061 Al alloy. They detected acoustic emission (AE) signals and analyzed the possibility of applying the AE technique for the in-process monitoring of an entire FSW process. Three equally spaced gaps were made of two notches aligned along the joint line. They found a sudden change in the band energy at the moment when the pin penetrates into and pulls out of the weld joint, as well as when the shoulder makes contact with or detaches from the plates. This reflected the existence, location, and size of the weld defects. Lienert *et al.* [2003] studied tool deformation and wear by comparing critical tool dimensions for a given tool before and after each weld using an optical comparator. For defect free welds of mild steel tool load at a welding speed of 0.42 mm/s was approximately 18.7 kN, while measured torque was in 55 Nm. The peak surface temperature was close to 1000°C, measured on the tool shoulder during the process. Both metallographic and metrology techniques suggested changes in tool dimensions resulted from both rubbing wear and deformation of the tool. The greatest changes in dimensions occurred during the initial plunging stage.

2.9 Major Gaps from the Literatures

From the aforementioned literature studies following major gaps can be listed:

- The alignment of the tool travel along the joint line using the existing fixtures is difficult, which increases setup time.
- There is less study for quantification of relative contribution of all controllable process parameters on the weld qualities.
- Their is not much study on selection of an appropriate starting point and elimination of end hole to maximize the joint length in FSW process.

- Current FSW process sub-models are complex, time consuming, and difficult to be used in real time. Use of soft computational approaches for modeling of FSW process are rare.
- Uses of non-traditional hybrid optimization techniques for finding optimal process parameters considering most of the parameters in FSW are very rare.

As per the above gaps in literatures the objectives of the present research work were finalized (presented in Section 1.2, Chapter - 1). The methodologies adopted to complete the stated objectives, observations and major findings of the present work are discussed in detail in the subsequent chapters of the thesis.

Chapter 3

Experimental Setup

3.1 Introduction

For carrying out FSW in milling machine a proper fixture is required to hold the workpiece, position it correctly with respect to the tool, and support it during welding process. It should also provide ease and safety of operation, with increased productivity. The clamping system should be developed such that the plates would not move apart creating a gap at the joint line by the vertical pressure applied during the welding process. It should also prevent the motion of the workpiece along with the tool in welding direction. The difficulties with different clamping devices used and the advantages of the developed one are discussed in following sections.

3.2 L-Clamps

Initially, the welding was carried out by fixing the work piece with L-clamps. Four numbers of L-clamps were used to hold the workpiece as shown in **Fig. 3.1**. But it was seen that the gripping was insufficient to fix the workpiece rigidly in a particular position due to lesser contact area. As a result of which in most of the cases, the plates moved apart at the starting of the operation *i.e.*, during tool plunging period. Furthermore, after plunging when the tool started to travel along the joint line the workpieces has also been dragged along the direction of tool movement. So it has been found that L-clamps are not adequate for clamping during FSW process.

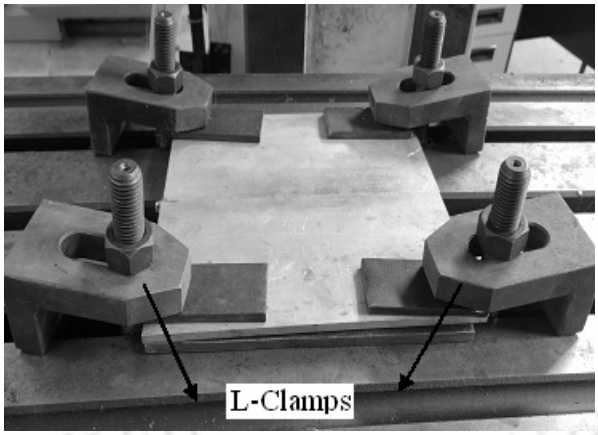

Figure 3.1 Plates fixed with L-clamps

3.3 S-Clamps

In order to improve the gripping, new types of clamps in S-shape have been fabricated in-house as shown in **Fig. 3.2**. During the use of S-clamps the workpiece movement along the tool movement direction has been eliminated. But the lateral movement *i.e.*, perpendicular to tool movement, of the workpieces during plunging still remained. Even in some cases initially it was not there but after a small tool travel the gap was developed between the plates.

The alignment of the tool travel along the joint line is difficult in both of the above cases due to which setup time is also more. Keeping in view all the possible problems a special type of fixture is designed, developed and fabricated in-house, the details of which is discussed in the following section.

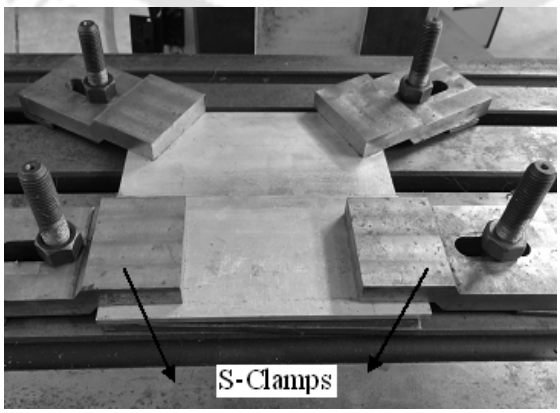

Figure 3.2 Plates fixed with S-clamps

3.4 Development of a Special Fixture

The developed fixture is highly useful for carrying out FSW operations in vertical milling machine. The fixture has four main components, namely top plate, clamps, backing plate and support plates. Each part has been fabricated individually with all appropriate features required for overcoming the above mentioned problems.

3.4.1 Top Plate

This plate is made up of mild steel of thickness 10 mm. The plate is provided with slots to slide the clamps as per the dimension of workpiece to be welded. The detail dimension and photograph of the top plate is shown in **Fig. 3.3**.

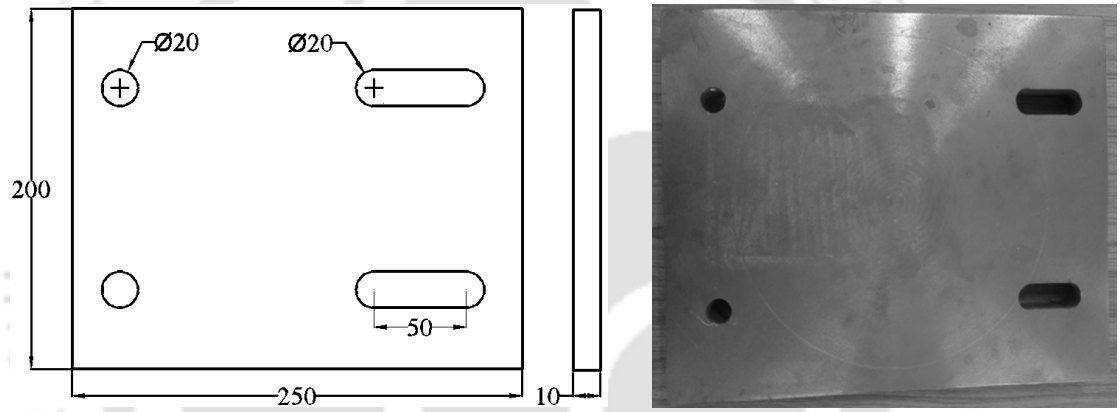

(a) (b)

Figure 3.3 (a) Detail drawing and (b) image of top plate

3.4.2 Clamp

The clamps are fitted over the machine bed along with the top plate. It has all the necessary features required for the clamping of workpiece and to arrest the lateral as well as longitudinal movement of the workpiece. It is made of mild steel. Clamp has intricate and complex design that's why it is fabricated in two pieces. After fabrication of two separate pieces in various machines, it is joined together to form single piece as shown in **Fig. 3.4**. Two M16 bolts are provided on each clamp to apply vertical tightening force. At one end of the clamp, a protruding part of 20×20 mm dimension is provided to arrest the linear movement of the workpiece along the direction of welding.

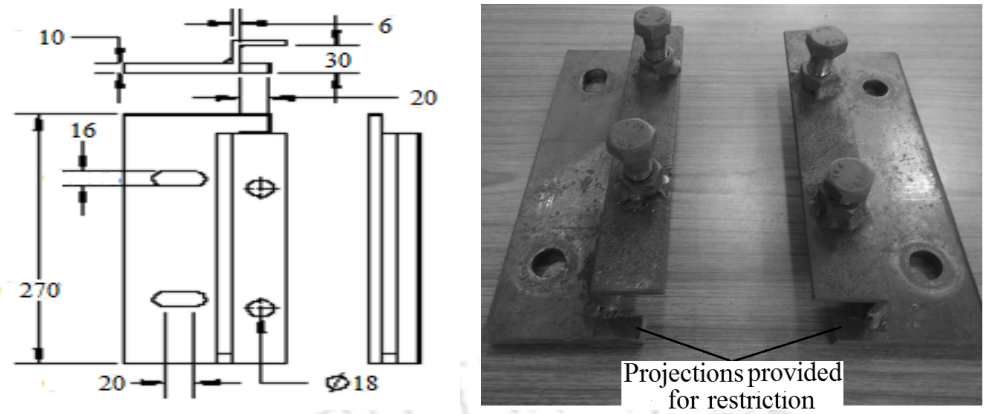

(a) (b)

Figure 3.4 (a) Detail drawing and (b) image of clamp

3.4.3 Backing Plate

It is a smooth flat plate, made up of mild steel, as shown in **Fig. 3.5**. Its main purpose is to provide support to the workpiece. During welding operation, plasticized material forged down by the tool. Backing plate will ensure that the plasticized material is retained within the welding zone. It also provides safety to the top plate in case the tool tip goes beyond the workpiece thickness.

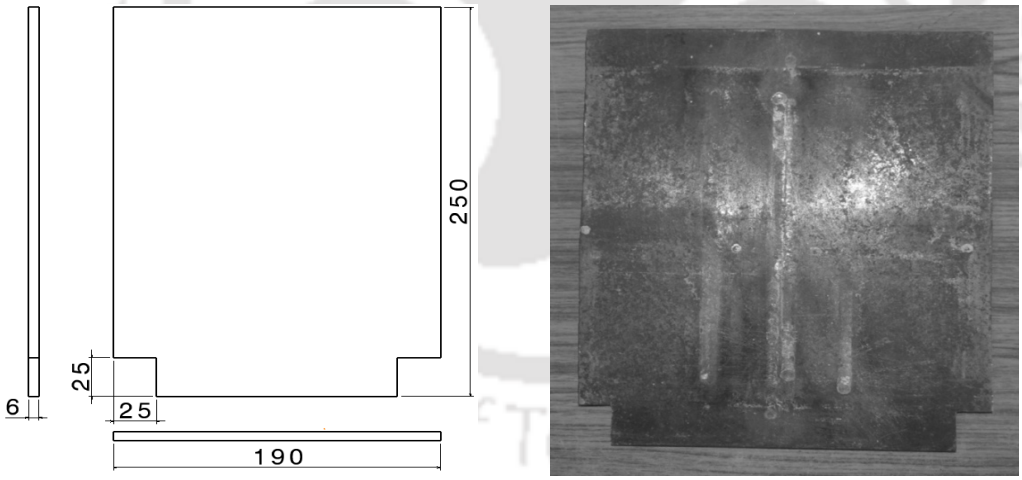

(a) (b)

Figure 3.5 (a) Detail drawing and (b) image of backing plate

3.4.4 Support Plate

It is a piece of mild steel flat, as shown in **Fig. 3.6**. It facilitates uniform distribution of the tightening force over the workpiece.

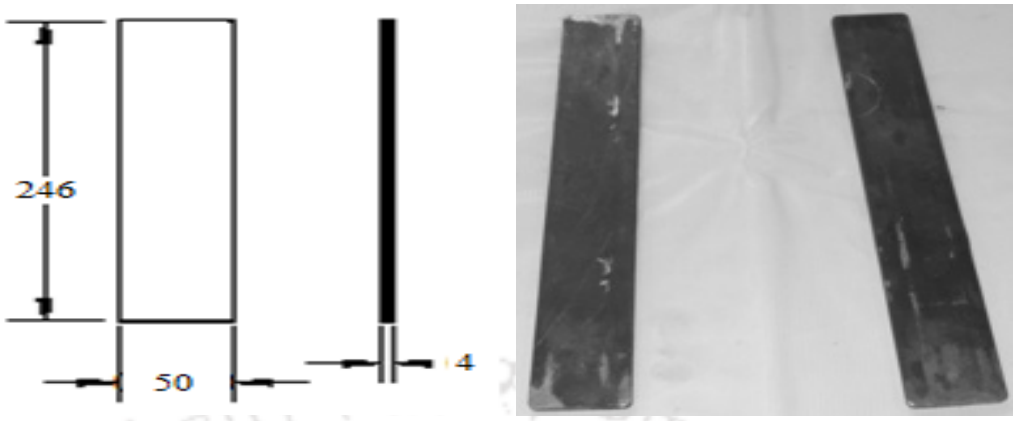

(a) (b)

Figure 3.6 (a) Detail drawing and (b) image of support plate

3.4.5 Fixture Assembly

The complete assembly of the developed fixture is shown in **Fig. 3.7**. All the parts of the fixture are assembled together with their relative positioning. It is designed in such a way that all the features required to carry out FSW operations in milling machine are facilitated. The developed fixture was found very effective for supporting and clamping the workpiece.

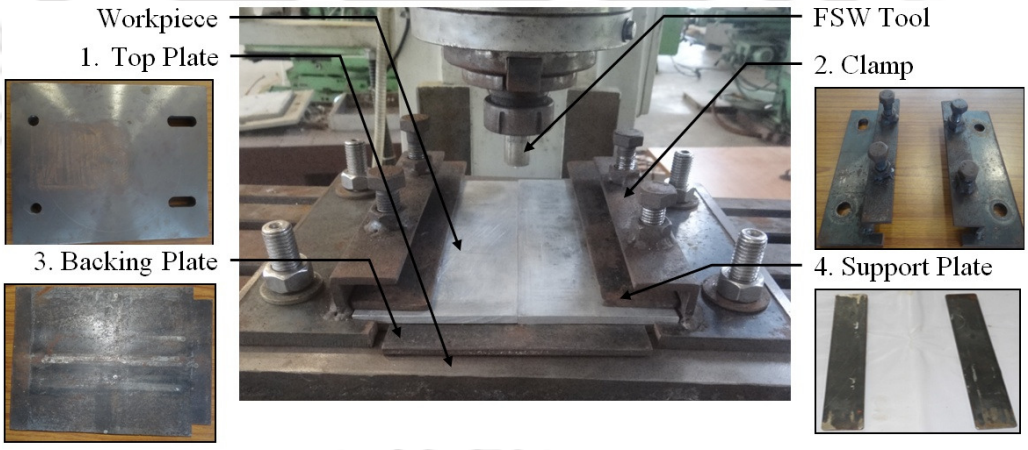

Figure 3.7 Complete fixture assembly

3.5 Workpiece and Tool Material

The workpiece material considered for the present experimental work is the commercially available 1100 series aluminium alloy without any heat treatment. The main reason behind the selection of the softer grade Al series is its popular use for general sheet metal work in chemical process plant equipment, food industry containers etc., availability,

and low cost. The rolled plates were cut and machined into rectangular pieces of 200×100×6 mm for joining purpose. Welding was carried out in butt joint configuration using FSW process. EDX (Energy-dispersive X-ray spectroscopy) was carried out to find out the composition of the aluminum alloy and the results are shown in **Fig. 3.8**. The chemical composition and mechanical properties of the plate are given in **Tables 3.1** and **3.2**, respectively.

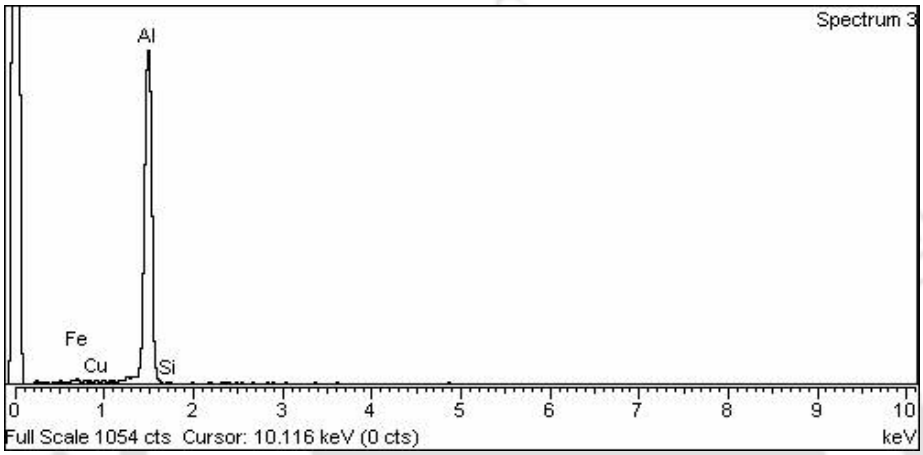

Figure 3.8 EDX spectrum of workpiece material

Table 3.1 Chemical Composition of Base Material

Elements	Cu	Si	Fe	Al
Weight (%)	0.05	0.2	0.1	Balance

Table 3.2 Mechanical Properties of Base Material

Ultimate tensile strength (MPa)	Yield strength (MPa)	% Elongation
153.05	84.93	33.04

The tool material should be such that it can withstand the vertical pressure and torque applied to it. The FSW tool should not wear out easily. Hence choosing an appropriate tool material is important for FSW application. In this work, stainless steel (Grade-310) is used as tool material because of its excellent high temperature properties with good ductility. A vertical milling machine was used to carry out the horizontal FSW experiments. The specification of the milling machine used is; Spindle speed: 12 steps [50-1500 rpm], Table feed rate: 8 steps [22-555 mm/min], Main motor power: 5.5 kW, Feed motor power: 0.75

kW. The tool was mounted using a suitable collate. The tool rotation speed and translational speed of the bed were set prior to each run of welding. Before welding the edge mismatch of the plates was checked. In order to avoid mismatch, the edges of all the workpieces are machined. Some minor cleaning of the joining surfaces by fine grade emery paper has also been done to remove atmospheric contaminations. The parameters used in the present work are shown in **Table 3.3**.

Table 3.3 Parameter Descriptions with Units Used

Parameters	Unit	Description
Plunge depth (PD)	mm	Distance moved by the shoulder from workpiece surface along the tool axis.
Tool rotational speed (RPM)	rev/min	Revolutions per minute of machine spindle.
Welding speed (WS)	mm/min	Speed of tool advancing through the workpiece.
Tool geometry (TG)	-	Straight cylindrical (SC), Tapered cylindrical (TC), Square (SQ), Threaded (THRD).
Shoulder diameter (SD)	mm	Diameter of the tool shoulder.
Pin diameter (PnD)	mm	Diameter of the tool pin.
Tool pin length (TPL)	mm	Distance between inner shoulder surface and tip of pin along tool axis.
Dwell time (DT)	second	Time between plunge sequence and weld traverse sequence.

3.6 Tool Fabrication

Welding tools were prepared from either 42 mm or 32 mm round stainless steel (Grade-310) bar. Different tool geometries that were considered in the present work are straight cylindrical (SC), tapered cylindrical (TC), square (SQ) and threaded tool (THRD). The fabricated 32 numbers of tools having different shape and dimensions are shown in **Fig. 3.9 (a-d)**. Initially all the 8 numbers of straight cylindrical tools and 8 numbers of tapered cylindrical tools were prepared using lathe machine. For preparing square and threaded tools first the tool pins were made in a straight cylindrical shape using lathe machine. Then squares of appropriate diagonal were prepared using milling machine and right handed threads having a pitch of 1mm were prepared using lathe machine.

(a) (b)

(c) (d)

Figure 3.9 Fabricated tools (a) SC (b) TC (c) SQ and (d) THRD

3.7 Temperature Measurement During Welding

For temperature measurement an Infra Red (IR) camera was implemented. It is having a spectral range of 7.5 to 14 µm, temperature measuring range (-40 to 2000°C), temperature resolution at 30°C better than 0.05 K, measurement accuracy ± 1.5 K (0-100°C), ± 2 % (< 0 and > 100°C), emissivity adjustable from 0.1 to 1.0, in increments of 0.01 (Make: INFRATEC, Model: VarioCAM-hr head). Before welding the camera was placed in an appropriate location to capture the thermal image. The complete experimental setup with IR camera is shown in **Fig. 3.10(a)**. For each experiment the straight lines as shown in **Fig. 3.10** are marked (in the advancing side) prior to the welding which is exactly at half the distance of the tool shoulder diameter from the welding line. Then the temperatures are recorded at the point which is at a distance of 120 mm away from the starting edge of the 200 mm long

workpiece. Prior to temperature measurement the IR camera is calibrated and the calibration plots for different points are shown in **Fig. 3.10 (b)**. For calibration purpose thermocouples are used and the thermal histories are compared with that of IR camera readings.

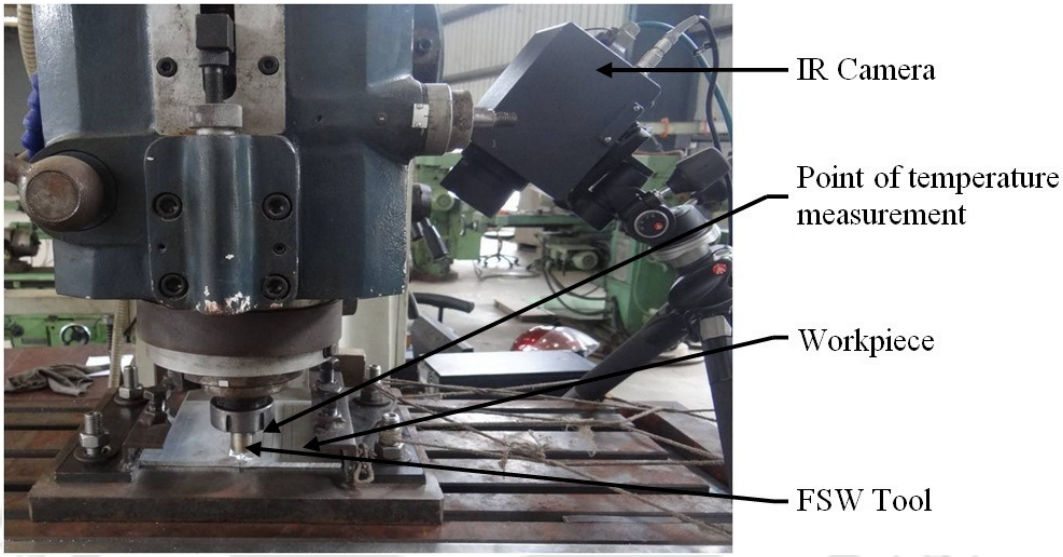

(a)

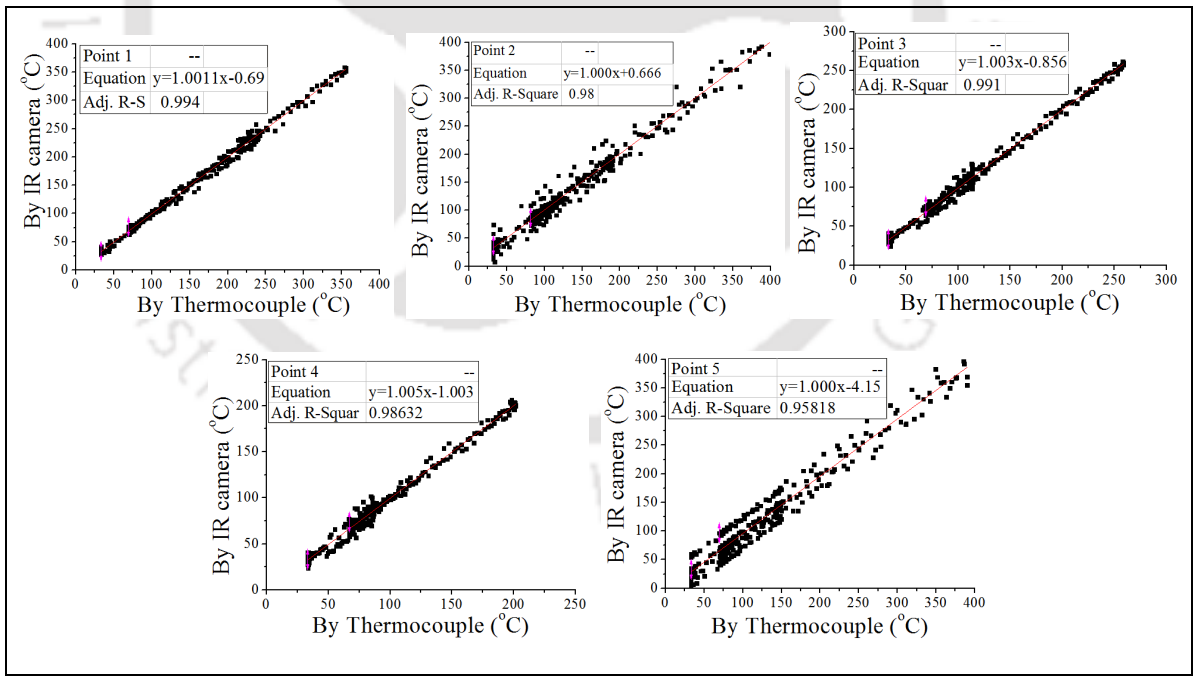

(b)

Figure 3.10 (a) Experimental setup with IR camera and (b) calibration plots for IR camera

3.8 Observations

The following observations have been made from the above developed fixture.

- The developed fixture is rigid enough to hold the workpieces securely without gap formation between the interfaces during tightening as well as FSW operation.
- It does not allow the workpiece to move along the direction of tool travel, due to horizontal force.
- As support plates are used above the workpiece, hence uniform tightening force is applied to the entire workpiece to be joined.
- It does not allow any misalignment to the workpiece.
- No need to align the tool every time before welding. Once the tool movement is aligned with the joint line then it takes very less time for the next job which will reduce the overall setup time.

3.9 Major Findings

The developed fixture has been used extensively to conduct FSW operations. From the experimentation following conclusions can be made:

a) The developed fixture is simple and cost-effective. It is rigid enough to hold the workpieces securely without gap formation and transverse movement of the workpiece.

b) The job changing and alignment time period i.e., setup time reduces significantly.

Chapter 4

Experimental Investigation and Characterization of Welds

4.1 Introduction

The present experimental investigation is divided into two phases. In first phase most number of process parameters are considered to find out their influences on output responses. Taguchi's orthogonal array design of experimental (DOE) method has been followed in this phase. Initially the significance of process parameters has been evaluated using Taguchi's technique. This technique is one of the most used methods to optimize single performance characteristics. But the real world application needs multi-response analysis process to evaluate the influence of input parameters on output responses. Therefore in next step, different theories such as grey relational analysis (GRA), utility concept (UC) and desirability function approach (DFA) were coupled with the Taguchi method. Apart from these traditional techniques one new multi objective analysis technique namely fuzzy assisted grey Taguchi (FZ-GRA) approach has been proposed and successfully applied to find the significance of different parameters on output responses. Second phase of the experiments is related to the study of the effect of significant parameters on joint quality. Full factorial DOE has been used for this experimental work. All the above mentioned experimental works and their out comings were discussed in the following sections.

4.2 Experimental Methods

4.2.1 Observations from Preliminary Experiments

In order to find out the feasible range of the selected process parameters some trial experiments were carried out. The results of the trial runs are listed in **Table 4.1**. It was seen that at all the four rotational and welding speeds the welding process can be carried out. The weld bead images obtained at different plunging depths are shown in **Fig. 4.1**. The lower plunging depth (PD) results inadequate shoulder contact throughout the welding. Even if initially the shoulder appeared to be in contact with the workpiece, after moving some distance the shoulder contact was not found till the end of the process. Higher PD value results in excess material thinning which in turn reduces the joint strength. Therefore, the working range of PD was found from 0.09 to 0.15 mm.

Table 4.1 Preliminary Experimental Observations

Sl. No	**Process Parameters**								**Remarks**
	PD	**RPM**	**WS**	**SD**	**PnD**	**TPL**	**TG**	**DT**	
1	0.06	600	63	20	5	5	SC	**05**	Due to insufficient dwell time the shoulder penetration at the starting was insufficient
2	**0.06**	600	63	20	5	5	SC	10	All the parts of the shoulder has not touched the base material along the weld line
3	0.09	600	63	20	5	5	SC	10	Weld bead was appropriate and process can be carried out
4	0.09	600	98	20	5	5	SC	10	-do-
5	0.09	600	132	20	5	5	SC	10	-do-
6	0.09	600	200	20	5	5	SC	10	-do-
7	0.09	815	63	20	5	5	SC	10	-do-
8	0.09	815	98	20	5	5	SC	10	-do-
9	0.09	815	132	20	5	5	SC	10	-do-
10	0.09	815	200	20	5	5	SC	10	-do-
11	0.09	1500	63	20	5	5	SC	10	-do-
12	0.09	1500	98	20	5	5	SC	10	-do-
13	0.09	1500	132	20	5	5	SC	10	-do-
14	0.09	1500	200	20	5	5	SC	10	-do-

15	0.15	600	63	20	5	5	SC	10	-do-
16	**0.18**	600	63	20	5	5	SC	10	Due to excess flashing material thinning takes place

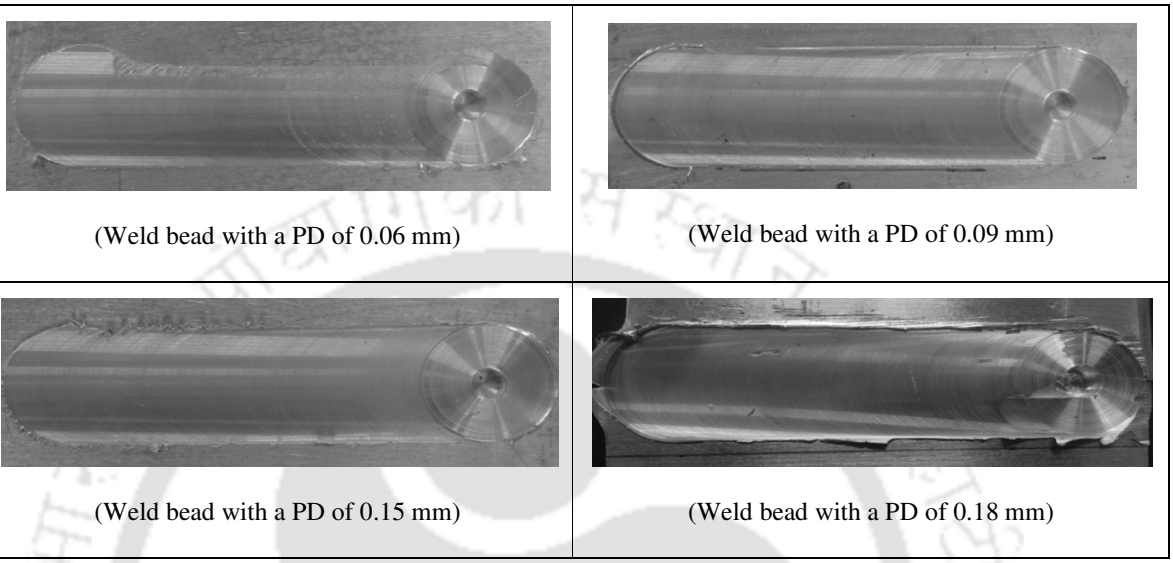

(Weld bead with a PD of 0.06 mm)

(Weld bead with a PD of 0.09 mm)

(Weld bead with a PD of 0.15 mm)

(Weld bead with a PD of 0.18 mm)

Figure 4.1 Weld bead images at different plunging depths (PD)

4.2.2 Design of Experiments

Design of experiment (DOE) implies a series of runs, or tests, in which changes are made to input variables purposefully and simultaneously and the responses are observed. It can be used to systematically investigate the process variables that influence product quality. In the present work, initially a list of all possible process parameters were prepared and narrowed to eight depending on the machine flexibility and setup limitations. As the experiments were conducted on a vertical milling machine so there is no provision to change the tilt angle. Thirty two different tools were fabricated for 32 numbers of experiments. This limited the consideration of parameter like tool hardness in order to avoid large number of tools. Again a different setup is required to carry out FSW process in liquid medium which increases the experimental complexity. Keeping in view of above mentioned limitations welding medium was also not taken into account.

The two important points that should be well thought-out prior to selecting an orthogonal array (OA) for DOE are the number of process parameters and their levels. As the number of factors (or parameters) are 8 in the present work, the OA can be chosen from

2-level, 3-level or mixed level available Taguchi designs. Furthermore, for a better study of the influence of process parameters the number of levels should be more which is considered as four in the present case. Out of all available mixed level designs L_{32} is the only OA in which one parameter can be varied in two levels and all other seven parameters in four levels [Montgomery, 2006]. Therefore, L_{32} OA has been selected in the present work. The selection of the parameter which has to be varied in two levels is important. From the initial trial runs (discussed in the Section 4.2.2), the working range of PD was found to be less due to which it has been varied in two levels.

In order to check the adequacy of the selected OA the degrees of freedom (DOF) has been verified. Each 4-level parameter has 3 DOF and 2-level parameter has 1 DOF. The required DOF for 1 factor at two levels and 7 factors each at four levels is 22. As per Taguchi's design of experiment, the total required DOF for the experiment must be less than DOF of the selected OA [Montgomery, 2006]. So L_{32} OA having 31 (total no. of experiments-1) DOF was chosen for the present study. The considered levels of each parameter and design matrix are shown in **Table 4.2** and **4.3**, respectively.

Table 4.2 Process Parameters Levels and their Values

Levels	PD	RPM	WS	TG	SD	PnD	TPL	DT
Level 1	0.09	600	63	SC	20	5	5.2	10
Level 2	0.15	815	98	TC	25	6	5.4	15
Level 3	-	1100	132	SQ	30	7	5.6	20
Level 4	-	1500	200	THRD	35	8	5.8	25

Table 4.3 Design Matrix as Per L_{32} Orthogonal Array

Sl. No.	PD	RPM	WS	TG	SD	PnD	TPL	DT
1	1	1	1	1	1	1	1	1
2	1	1	2	2	2	2	2	2
3	1	1	3	3	3	3	3	3
4	1	1	4	4	4	4	4	4
5	1	2	1	1	2	2	3	3
6	1	2	2	2	1	1	4	4
7	1	2	3	3	4	4	1	1
8	1	2	4	4	3	3	2	2
9	1	3	1	2	3	4	1	2

10	1	3	2	1	4	3	2	1
11	1	3	3	4	1	2	3	4
12	1	3	4	3	2	1	4	3
13	1	4	1	2	4	3	3	4
14	1	4	2	1	3	4	4	3
15	1	4	3	4	2	1	1	2
16	1	4	4	3	1	2	2	1
17	2	1	1	4	1	4	2	3
18	2	1	2	3	2	3	1	4
19	2	1	3	2	3	2	4	1
20	2	1	4	1	4	1	3	2
21	2	2	1	4	2	3	4	1
22	2	2	2	3	1	4	3	2
23	2	2	3	2	4	1	2	3
24	2	2	4	1	3	2	1	4
25	2	3	1	3	3	1	2	4
26	2	3	2	4	4	2	1	3
27	2	3	3	1	1	3	4	2
28	2	3	4	2	2	4	3	1
29	2	4	1	3	4	2	4	2
30	2	4	2	4	3	1	3	1
31	2	4	3	1	2	4	2	4
32	2	4	4	2	1	3	1	3

4.2.3 Specimen Preparation and Testing

Once the welding is over, the welded specimens were tested for tensile, bending and hardness properties. Also the joint macro and micro graphs were captured. The positions of extraction of samples for different tests are shown in **Fig. 4.2(a)**. The tensile specimens were prepared to the necessary dimensions as per the guidelines of ASTM E8. The specimens for tensile and bending tests are shown in **Fig. 4.2(b)** and **(c)**, respectively. Specimens for hardness, macro and micro-structural studies were cut from the welded joint as shown in **Fig. 4.2(d)**. Tensile tests and three point bend tests were carried out in a digitally controlled closed loop 10T (100KN) capacity servo hydraulic dynamic testing machine (Make: INSTRON, Model 8801). All the tensile and bending tests were carried out in term of displacement control criteria which is 2 mm/min and 5 mm/min, respectively, in the present

work. 140° bending was carried out for all the samples and bend angle was measured during the crack initiation on visual basis.

Both macro and micro graphs were taken from the same sample. After cutting the sample from the welded joint, it was polished by different grades of emery papers using a disc type polishing machine (Make: Buehler, Model: AutoMet 250) shown in **Fig. 4.3(f)**. The polishing was carried out from courser to finer grit size paper. Once the samples were made scratch free, these were polished by velvet cloth to get mirror finished surface. Then the samples were etched by Keller's reagent widely used for etching aluminum and its alloys. The composition of the etchant used is 95 mL distilled water, 2.5 mL HNO_3, 1.5 mL HCl and 1.0 mL HF. For macro-graphic tests all the welded joints were examined at low magnification (10x) using stereo zoom microscope to analyze the quality of weld nugget region. Optical microscope (Make: Carl ZEISS, Model: Imager A1m) was used to capture grains present in different weld zones and shown in **Fig. 4.3(g)**. After completing the tensile test, the fracture surface morphology of the selected specimens was examined by a Scanning Electron Microscope (SEM-Make: LEO, Model: 1430vp).

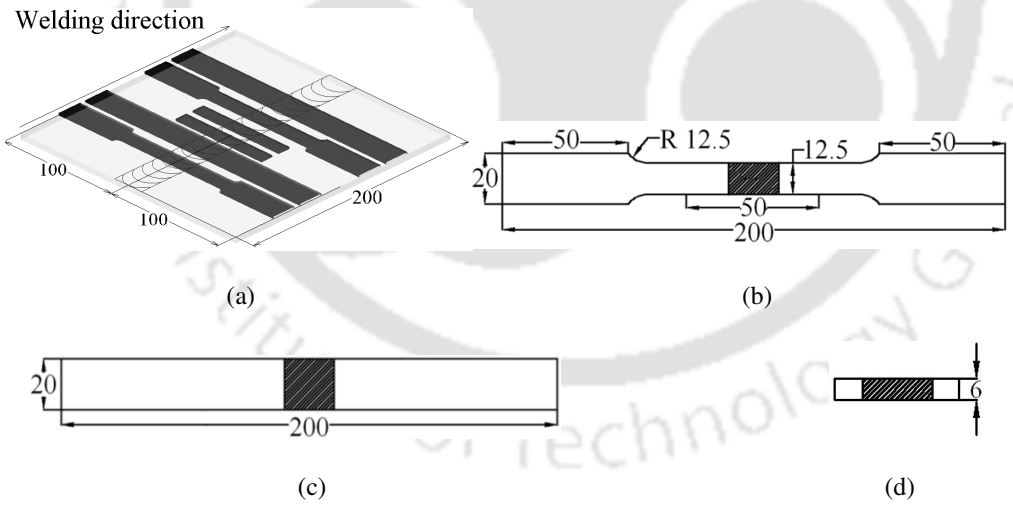

Figure 4.2 Schematic diagrams of (a) position of specimen extraction for tensile, bending, hardness and macrostructure and dimensions of (b) tensile (c) bending (d) hardness and macrostructure specimens

The tensile and bending samples with test setups are shown in **Fig. 4.3(a-c)**. The bent surfaces of a tested specimen are shown in **Fig. 4.3(d-e)**. The polishing machine and optical microscope are shown in **Fig. 4.3(f-g)**. As aluminium is a soft grade material so

microhardness test was carried out using Vicker's micro hardness tester (Make: Omni Tech). The load applied in the present study was 500 gm-f for a time period of 10 seconds. The samples with test setup are shown below in **Fig. 4.3(h)** and **(i)**. Before taking the micro-hardness readings all the samples were polished upto mirror finish similar to microstructure samples. Here for hardness values, the readings were taken from the weld centre in 1 mm incremental distance basis both in advancing and retreating side. Total 15 points were considered for NZ hardness. Then the average value was considered.

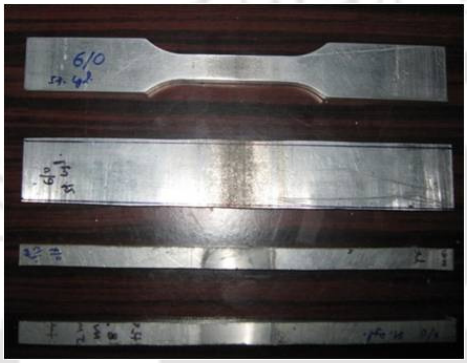

(a)

(b)

(c)

(d)

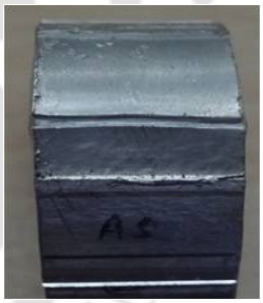

(e)

(f)

(g)

(h) (i)

Figure 4.3 (a) Prepared test specimens, (b) tensile testing, (c) three point bending test in instron machine, tested bending specimens for (d) good and (e) defective joint, (f) polishing machine, (g) optical microscope, (h) hardness specimens and (i) test setup for hardness measurement

4.3 Identification of Significant Process Parameters

4.3.1 Evaluation of Signal to Noise Ratio

Signal is a factor, with a range of settings, which is controlled by the user to make use of its intended function. Noise is the factor that cause variability in the performance of a system or product, but cannot be controlled during production or product use. The signal to noise (SN) ratio is a measure of robustness used to identify control factors that reduce variability in a product or process by minimizing the effects of uncontrollable factors. To access the influence of factors on the response, the SN ratios for each control factor should be calculated. In the present investigation the ultimate tensile strength (UTS), yield strength (YS), bending angle (BA), percentage elongation (%Elng.), weld bead thickness (WBT), nugget zone hardness (HRD) and shoulder-workpiece interface temperature were measured and analyzed to determine the effect of FSW process parameters on the measured weld qualities. The experimental results were then transformed into means and SN ratio. As in a joint the primary objective is to increase the strength and ductility simultaneously, so to maximize the response, larger-the better SN ratio criteria is chosen. The SN ratio (η_j) was calculated using **Eq. 4.1** [Koilraj *et al.*, 2012].

$$\eta_j = -10log\left(\frac{1}{n}\sum\frac{1}{Q_{ij}^2}\right) \quad (4.1)$$

where, n is the number of tests and Q_{ij} is the response of the i^{th} quality characteristics in the j^{th} experiment.

4.3.2 Analysis of Variance

The purpose of analysis of variance (ANOVA) is to find the statistical significance of the factors and their levels on the responses. It gives a detail picture of how far the process parameters affect the response and the level of significance of the factors considered. It separates the total variability of the response (sum of squared deviations about the grand mean) into contributions rendered by each of the parameter and the error. Thus,

$$SS_T = SS_F + SS_e \tag{4.2}$$

where,

$$SS_T = \sum_{j=1}^{p} (\gamma_j - \gamma_m)^2 \tag{4.3}$$

And SS_T Total sum of squared deviations about the mean,

γ_j Mean response for j^{th} experiment,

γ_m Grand mean of the response,

p Number of experiments in the orthogonal array,

SS_F Sum of squared deviations due to each factor,

SS_e Sum of squared deviations due to error.

In ANOVA table mean square deviation can be defined as:

$$MS = \frac{SS\ (Sum\ of\ squared\ deviation)}{DF\ (Degree\ of\ freedom)} \tag{4.4}$$

The F-test named after Fisher was also carried out to study the significance of the process parameters. The high F value (Fisher's ratio or variance ratio) shows that the factor is highly significant in affecting the response of the process. It is given by:

$$F = \frac{MS\ for\ a\ term}{MS\ for\ the\ error\ term} \tag{4.5}$$

Depending on F-value, P-value (probability of significance) is then calculated. The P-value depends upon the extent of confidence level e.g. at 95% confidence level if the P-value for a term appears less than 0.05 then it can be concluded that, the effect of the factor is significant on the selected response.

4.3.3 Grey Relational Analysis

GRA method analyzes a process that has unknown or incomplete information about the effect of parameters on the responses. Among many statistical analysis techniques the most popular technique used in engineering problems is the Taguchi method. But the limitation of the method is that it can optimize only single quality characteristic. So the Taguchi method coupled with GRA can be used for analyzing the complicated interrelationships among the multi-responses. A number of steps have to be followed one by one in order to perform GRA which are listed below.

STEP-1: Grey relational generation i.e. normalization of the measured output responses from 0 to 1.

STEP-2: Calculation of grey relational coefficient from the normalized data to represent the correlation between the desired and actual experimental data.

STEP-3: Determination of grey relational grade (GRG) by averaging the grey relational coefficients corresponding to selected responses.

STEP-4: Overall evaluation of the multiple performance characteristics based on the calculated GRG. This converts a multiple response analysis problem into a single response analysis situation.

STEP-5: Analyzing the results using Taguchi method.

Three different criteria, such as larger the better, smaller the better and nominal the best, can be used for normalization of responses. In a welded joint the primary objective is to increase the strength, ductility, weld bead thickness and hardness simultaneously. So to maximize these responses, larger the better normalization criterion is chosen which is defined as:

$$x_i^*(k) = \frac{x_i(k) - \min x_i(k)}{\max x_i(k) - \min x_i(k)} \tag{4.6}$$

where, k = 1 to m, i = 1 to 32, m is the performance characteristic and i is the trial number, $x_i^*(k)$ is the value after grey relational generation, $x_i(k)$ is the response for the k^{th} performance characteristics of i^{th} experiment, $\min x_i(k)$ and $\max x_i(k)$ are the smallest and largest value of $x_i(k)$, respectively.

Then the grey relational coefficient $\xi_i(k)$ can be calculated as follows:

$$\xi_i(k) = \frac{\Delta_{\min} + \zeta\Delta_{\max}}{\Delta_{0i}(k) + \zeta\Delta_{\max}} \tag{4.7}$$

where, $\Delta_{0i}(k) = \|x_0^*(k) - x_i^*(k)\|$, $\Delta_{\min}(k) = \min_{\forall j \in i}\min_{\forall k} \| x_0^*(k) - x_j^*(k) \|$ and $\Delta_{\max}(k) = \max_{\forall j \in i}\max_{\forall k} \| x_0^*(k) - x_j^*(k) \|$. $\Delta_{0i}(k)$ is the deviation sequence of the reference sequence $x_0^*(k)$ and comparability sequence $x_i^*(k)$, $\zeta \in [0-1]$ is the distinguishing coefficient and the value of 0.5 is widely accepted. In this study, the distinguishing coefficients (ζ) were set to a value of 0.5. After calculating grey relational coefficients, the grey relational grade is obtained as follows:

$$\gamma_i = \frac{1}{m}\sum_{k=1}^{m} \xi_i(k) \tag{4.8}$$

where, m = number of process responses.

4.3.4 The Utility Concept

Utility of a product measures its usefulness in reference to the customer satisfaction. A product is evaluated on the basis of a number of different quality characteristics. The overall usefulness of a product or process is the sum of utilities of each of the quality characteristics. This can be combined to give a composite index termed as utility of a process or product.

Thus, if Z_i is the measure of effectiveness of a quality characteristic i (1 to m) evaluating the outcome space, then the overall utility function can be expressed [Derek, 1982] as:

$$U(Z_1, Z_2, \ldots\ldots, Z_m) = f\big(U_1(Z_1), U_2(Z_2), \ldots\ldots, U_m(Z_m)\big) \tag{4.9}$$

where, $U_i(Z_i)$ is the utility of the i^{th} attribute. Assuming that all the performance parameters are independent and have no interaction between themselves and the overall utility is a linear function of sum of individual utilities, and then the overall utility function can be written as:

$$U(Z_1, Z_2, \ldots\ldots, Z_m) = \sum_{i=1}^{m} U_i(Z_i) \tag{4.10}$$

Depending upon the relative performance importance, the attributes may be assigned different weights. The general form of weighted overall utility function can be written as:

$$U(Z_1, Z_2, \ldots\ldots, Z_m) = \sum_{i=1}^{m} W_i U_i(Z_i) \quad (4.11)$$

where, W_i is the weight assigned to the performance parameters and the sum of the weights for all the performance parameters should be equal to 1 [Rahim *et al.*, 2012]. The condition is given as:

$$\sum_{i=1}^{m} W_i = 1 \quad (4.12)$$

$$\sum W_i = W_{UTS} + W_{YS} + W_{\%\,Elng} + W_{WBT} + W_{HRDNS} \quad (4.13)$$

where, W_{UTS}, W_{YS}, $W_{\%\,Elng}$, W_{WBT}, W_{HRDNS} are the weights assigned to the responses of performance parameters. In this study equal importance has been given to all the quality parameters. Therefore $W_{UTS} = W_{YS} = W_{\%\,Elng} = W_{WBT} = W_{HRDNS} =$ 0.2 and the overall utility can be calculated as:

$$U = \sum_{i=1}^{m} W_i P_i \quad (4.14)$$

To determine the utility value for each performance characteristic a preference scale is constructed. The preference numbers are set between 0 (for minimum acceptable factor) and 9 (for the best factor).In a logarithmic scale, the preference number P_i is given as [Gupta and Murthy, 1982]:

$$P_i = A log \frac{Z_i}{Z_i'} \quad (4.15)$$

where, Z_i and Z_i' are the observed and the minimum acceptable values of the i^{th} performance characteristic, and A is a constant for i^{th} attribute. The value of A can be found by the condition that if $Z_i = Z^*$(where Z^* is the optimum value of Z_i), then P_i= 9. The criteria for signal-to-noise ratio associated with the utility value is higher the better type. Therefore if the overall utility is maximized, the performance characteristics considered for its evaluation will automatically be optimized (maximized or minimized whichever the case may be).

4.3.5 Desirability Function Approach

Derringer and Suich [1980] proposed a multiple response analysis method called desirability. In general practice, industrial applications is based on the idea that a product or process should satisfy multiple quality characteristics. Desirability function approach is a useful method to analyze the multiple responses simultaneously at one best setting of

process variables. It can be used to transform several response variables into a desirability function.

Let X_{ij} is a measure of performance of i^{th} alternative with respect to j^{th} criteria. For each output response, the desirability function assigns a number d_{ij} that varies over the range $0 \leq d_{ij} \leq 1$. When d_{ij}=0, the desirability for that response is completely unacceptable and when $d_{ij} = 1$, that quality characteristic has an ideal value. The transformation of criteria values into desirability function can be done by using either one-sided or two-sided transformation. In the present case one-sided transformation [Murphy *et al.*, 2005; Costa *et al.*, 2011] of d_{ij} is used which can be formulated as:

$$d_{ij} = \begin{cases} 0 & \text{if} \quad X_{ij} \leq L_i \\ \left[\frac{X_{ij}-L_i}{T_i-L_i}\right]^p & \text{if} \quad L_i \leq X_{ij} \leq T_i \\ 1 & \text{if} \quad X_{ij} \geq T_i \end{cases} \tag{4.16}$$

where, L_i is the lower specification limit, selected just below the minimum value for larger-the-better (LB) criteria and just above the maximum value for smaller-the-better (SB). T_i is a target value and would take a maximum value for LB and minimum value for SB criteria, unless other specific target value is defined. The value of p is a weight used to determine scale of desirability and equals to 0.2 in this work.

Finally a single valued composite desirability (D) can be formed by combining individual desirability index of all the output responses which is given by:

$$D = (d_1 \times d_2 \times \dots\dots\dots d_m)^{\frac{1}{m}} \tag{4.17}$$

where, m is the number of output responses. After considering weights corresponding to different quality characteristics the above equation can be rewritten as [Derringer and Suich, 1980]:

$$D = \left(d_1^{w_1} \times d_2^{w_2} \times \dots\dots\dots d_m^{w_m}\right)^{\frac{1}{m}} \tag{4.18}$$

where, w_1, w_2 ...are the weights associated with different output responses and m is the numbers of outputs.

4.3.6 Fuzzy Assisted Grey Relational Analysis

The GRA, UC and DFA (discussed in the Section 4.3.3-4.3.5), all these theories aggregate many quality characteristic parameters into one integrated quality parameter which can easily be optimized using Taguchi method. However in such aggregation procedure, the relative importance/weight of each quality characteristic parameter is required to be assigned [Walia *et al.*, 2006; Pal *et al.*, 2009; Aydin *et al.*, 2010; Prasanna *et al.*, 2013; Kumar *et al.*, 2013; Karande *et al.*, 2013]. Assignment of equal weights to all quality parameters may not be a good decision. In practice, all the quality characteristics of a product may not be of equal importance. The relative priorities depend on application area and functional requirements. The assignment of different weights to each quality characteristic depends on the judgment of the decision maker which may lead to uncertainty as well as indistinctness in the optimum solution. Moreover, aforementioned methods are based on the assumption that the quality characteristic parameters are uncorrelated. While in practice any change in one parameter remarkably affects another parameter. Therefore, to overcome the above mentioned difficulties, a fuzzy [Zadeh, 1965] assisted grey Taguchi method has been proposed in this work to optimize the FSW process parameters. The steps for this approach are depicted in **Fig. 4.4** and described later in the following sub-sections. The first step of the approach includes experimentation by DOE method. Then from the measured output responses the grey relational coefficient values were calculated by the methodology mentioned in Section 4.3.3. Finally the analysis of process parameters was done by the fuzzy inference system.

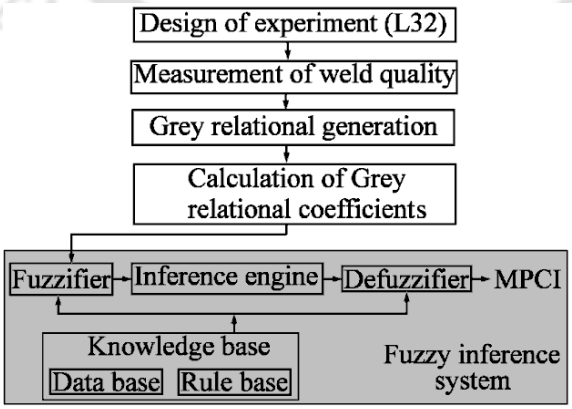

Figure 4.4 Functional blocks of the proposed fuzzy grey model

4.3.6.1 Fuzzy Inference System

The concepts of fuzzy sets and the principles of fuzzy algorithms were originally proposed by Zadeh in the mid 1960s [Zadeh, 1965]. Mamdani and Assilian [1975] then extended the concepts into what became the fuzzy logic system. After that, the fuzzy logic system has become one of the most active research topics and has successfully been implemented in many industrial and service areas. The detailed theory on fuzzy logic may be consulted in [Zadeh, 1965; Mamdani and Assilian, 1975]. In this work, the analysis of process parameters based on a fuzzy system comprises four main components, which are, fuzzification, fuzzy rule base, fuzzy inference and defuzzification. Computer programs for the fuzzy system were developed using the C programming language. **Figure 4.5** shows the fuzzy model used in this research. All these steps are briefly described in the following paragraphs.

***STEP-1:* Fuzzification**

Fuzzification comprises the process of transforming crisp values into grades of membership for linguistic terms of fuzzy sets. The membership function is used to associate a grade to each linguistic term. All the input variables, *i.e.*, grey relational coefficients of the measured quality characteristics are divided into three linguistic terms or fuzzy levels, namely low (L), medium (M) and high (H) quality. The output variable, i.e., multi-performance characteristic index (MPCI) is divided into nine fuzzy levels, namely very very low (VVL), very low (VL), low (L), between low and medium (LM), medium (M), between medium and high (MH), high (H), very high (VH) and very very high (VVH). The output of the fuzzification process is given by $\mu_{Sj}(x_i)$, where the symbol $\mu_S(x)$ is the membership function. Its value on the unit interval [0, 1] measures the degree to which element belongs to the fuzzy set S, x_i is the i^{th} variable and S_j is the j^{th} linguistic label or fuzzy set of the x_i variable. In the present work, triangular membership functions are used as membership functions because of their simplicity and computational efficiency. The triangular membership function is specified by a set of three parameters {a, b, c} as

$$\mu_S(x) = Max\left(Min\left(\frac{x-a}{b-a}, \frac{c-x}{c-b}\right), 0\right) \tag{4.19}$$

where, a and c $(c > a)$ are feet of the triangle and b is the peak of the triangle. The membership functions of input and output variables are shown in **Figs. 4.5** and **4.6**, respectively.

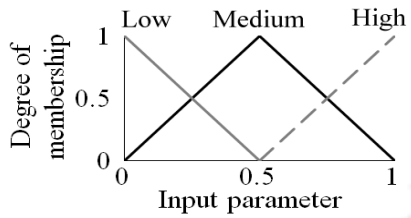

Figure 4.5 Membership functions of input parameters

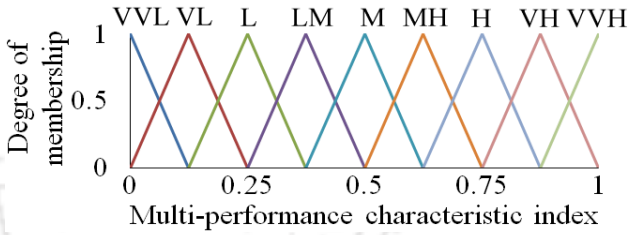

Figure 4.6 Membership functions of multi-performance characteristic index

***STEP-2:* Fuzzy Rule Base**

A fuzzy rule base consists of rules and each rule, in its turn, is obtained from properties expressed by linguistic variables and using logical connectives. It represents the relationships between input and output variables. A fuzzy rule base is essential to perform the inference operation. Usually, *IF-THEN* rules are subjectively specified by humans who are experienced and knowledgeable in the problem. A fuzzy *IF-THEN* rule (i^{th} rule) can expressed as:

$$R_i: \textit{IF UTS is L and YS is L and \% Elong is L and WBT is M and NZH is M THEN MPCI is VL} \quad (4.20)$$

i.e., from the above rule (**Eq. 4.20**) we can say that IF ultimate tensile strength belongs to fuzzy set low, yield strength belongs to fuzzy set low, percentage elongationbelongs to fuzzy set low, weld bead thickness belongs to fuzzy set medium and nugget zone hardness belongs to fuzzy set medium THEN the multi-performance characteristic index is fuzzy set very low. In this rules the conditions of the IF part must be met simultaneously in order for the result of the THEN part to occur. The fuzzy rules are derived based on the fact that the larger the grey relational coefficient is, the better the MPCI value. The conditions of the IF part of the rules are connected by fuzzy AND operator. Because to produce good weld joints, all the quality characteristics parameters (*i.e.*, UTS, yield strength, percentage elongation, weld bead thickness and nugget zone hardness) have to be maximum simultaneously. There are five input parameters and three fuzzy subsets for each parameter. Therefore, a total of 3^5 *i.e.*, 243 rules are derived. It is considered that if all the quality characteristics parameters belong

to fuzzy set low or only one parameter belongs to fuzzy set medium and all other are in fuzzy set low then MPCI belongs to fuzzy set very very low. If any two parameters are in medium and all other in low or any one in high and all other in low then MPCI is very low. If any three parameters are in medium and all other in low or one in high and one in medium and all other in low then MPCI is low. Similarly, if all are in high or one in medium and all other in high then MPCI is very very high. Few rules are shown in **Table 4.4**; the complete rule base is given in Appendix I.

Table 4.4 Fuzzy Rule Base

Rule No.	Antecedent Part					Consequent (Rule Output)
	UTS	YS	% Elng.	WBT	HRD	
1	Low	Low	Low	Low	Low	Very very low
3	Low	Low	Low	Low	High	Very low
6	Low	Low	Low	Medium	High	Low
9	Low	Low	Low	High	High	Between low and medium
18	Low	Low	Medium	High	High	Medium
27	Low	Low	High	High	High	Between medium and high
54	Low	Medium	High	High	High	High
215	High	Medium	High	High	Medium	Very high
234	High	High	High	High	High	Very very high

***STEP-3:* Fuzzy Inference Machine**

Fuzzy inference is sometimes called fuzzy reasoning or approximate reasoning. It is used in a fuzzy rule to determine the rule outcome from the given rule input information. When specific information is assigned to input variables in the rule antecedent, fuzzy inference is needed to calculate the outcome for output variable(s) in the rule consequent. For instance, the output of the rule in **Eq. 4.20** after inference operation is given by:

$$w_i = min\big(\mu_L(UTS), \mu_L(YS), \mu_L(\%\, Elong), \mu_M(WBT), \mu_M(NZH)\big) \qquad (4.21)$$

where, w_i is called the firing strength of the i^{th} rule.

***STEP-4:* Defuzzification**

Defuzzification or aggregation of rules outputs is a mathematical process by which the fuzzy sets that represent the outputs of each rule are combined into a single real number or

crisp value. In this work, centre of gravity method is adopted in the defuzzification process. The defuzzification value, called a multi-performance characteristic index, was calculated using **Eq. 4.22**.

$$MPCI = \frac{\sum_{i=1}^{R} A_i^j f_i^j}{\sum_{i=1}^{R} A_i^j} \tag{4.22}$$

where, A_i^j is the area of the output's j^{th} membership function at i^{th} rule, f_i^j is the centre of the area and R is the total number of rules.

4.4 Results and Discussions

4.4.1 From Taguchi's Single Response Analysis Technique

The measured weld quality values of each welding condition corresponding to the parameter settings mentioned in **Table 4.3** are given in **Table 4.5**. The main effects plots for SN ratios obtained from Taguchi single response analysis technique for different outputs are shown in **Fig. 4.7(a-g)**. Here each response has been analyzed for calculating the percentage influence of input parameters for that particular output. The ANOVA and the response tables for SN ratios of different factors are given in **Tables 4.6** to **4.15**.

Table 4.5 Measured Output Responses Corresponding to the Parameter Settings Mentioned in Table 4.6

Exp. No.	UTS (MPa)	YS (MPa)	% Elng.	BA (°)	WBT (mm)	HRD (HV)	Interface Temp. (°C)
1	112.08	70.52	9.26	55	5.59	51.01	488.61
2	99.75	58.69	8.72	45	5.62	47.77	484.36
3	116.90	65.65	8.86	60	5.84	52.11	484.13
4	120.28	62.57	21.68	140	5.79	47.06	485.12
5	120.54	62.62	14.66	140	5.45	46.23	489.18
6	114.11	74.58	5.82	140	5.53	50.39	481.66
7	117.19	69.81	7.54	66	5.63	51.78	481.50
8	133.20	63.24	14.60	140	5.79	53.82	481.75
9	94.38	58.61	3.96	45	5.49	49.17	480.33
10	63.28	53.41	3.00	50	5.54	47.75	485.18
11	136.90	72.35	14.80	140	5.56	51.24	485.23
12	112.74	64.25	9.82	10	5.54	46.55	484.82
13	16.01	14.59	0.86	5	5.36	49.79	480.03

14	1.93	1.76	0.76	5	5.75	47.26	488.25
15	138.51	64.47	23.78	140	5.54	55.91	481.04
16	91.72	61.29	4.14	21	5.46	46.33	485.21
17	102.86	69.54	5.60	15	5.54	54.29	484.58
18	94.34	62.74	5.68	25	5.45	50.24	480.56
19	131.00	69.52	17.50	140	5.54	52.33	482.77
20	50.52	49.85	4.34	15	5.78	52.23	488.11
21	64.26	51.72	4.68	10	5.60	51.61	483.08
22	85.09	70.43	3.34	15	5.65	52.84	485.31
23	122.07	57.25	19.28	140	5.56	48.61	484.55
24	117.29	60.76	17.04	140	5.54	51.20	483.94
25	123.68	63.14	10.00	40	5.48	48.56	480.32
26	132.64	63.24	18.26	140	5.52	54.29	484.37
27	91.78	63.54	4.00	10	5.53	54.11	486.21
28	61.52	54.70	1.94	10	5.53	51.65	483.66
29	124.12	63.69	17.46	53	5.58	46.83	483.77
30	126.77	64.09	19.36	140	5.65	53.19	485.71
31	2.48	1.69	0.70	5	5.75	47.26	487.80
32	25.50	66.97	1.30	5	5.80	46.65	482.63

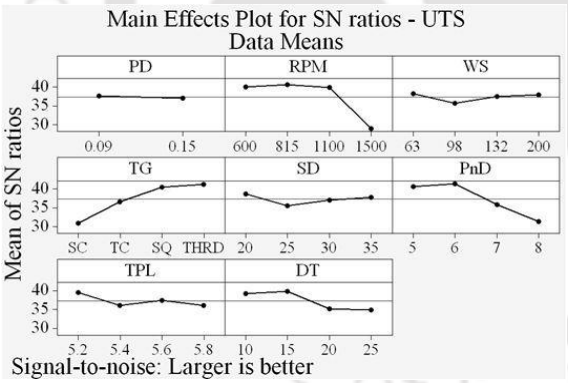

(a)

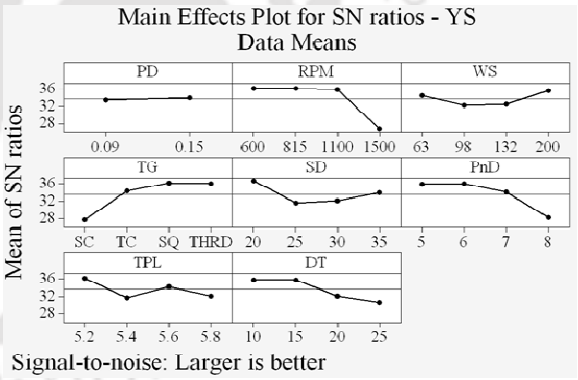

(b)

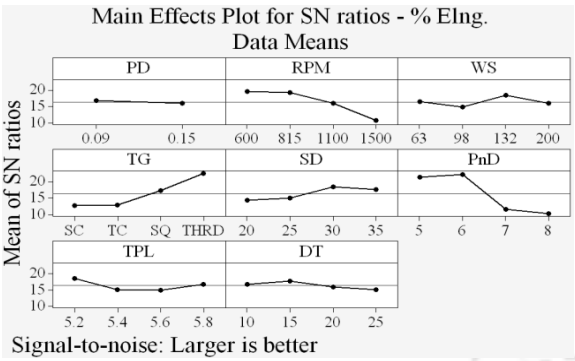

(c)

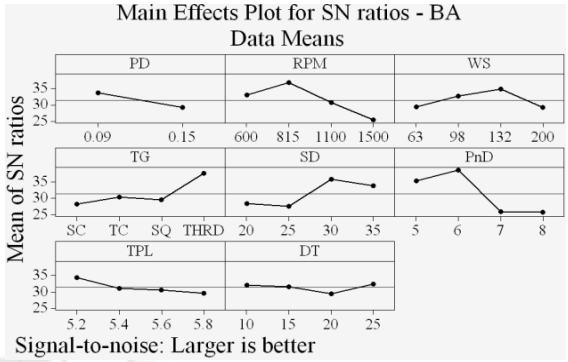

(d)

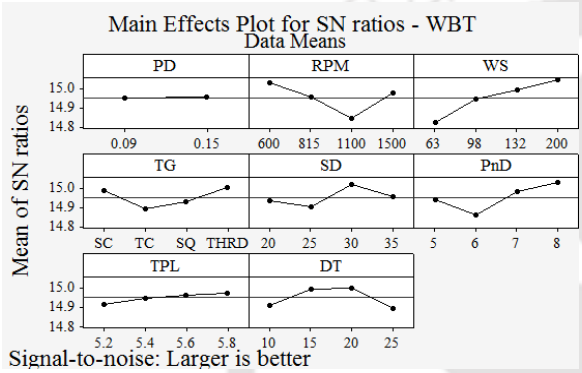

(e)

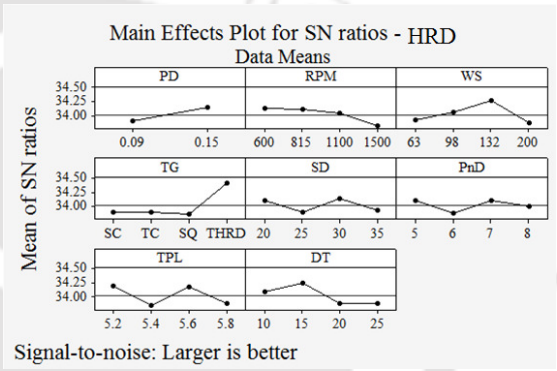

(f)

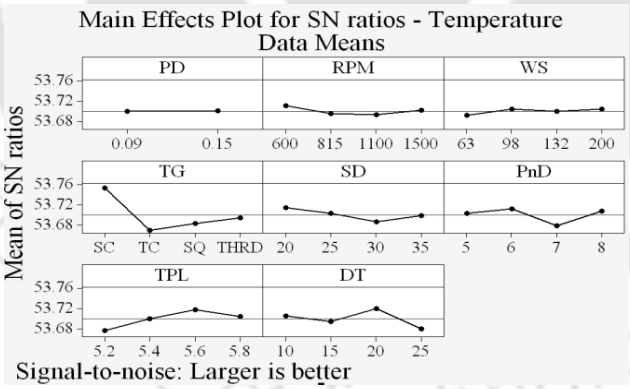

(g)

Figure 4.7 Main effect plots for (a) UTS, (b) YS, (c) % Elongation, (d) BA, (e) WBT, (f) HRD and (g) temperature

Table 4.6 ANOVA Table for SN ratios for UTS

Source	DF	SS	MS	F	P
PD	1	2.21	2.209	0.05	0.828
RPM	3	748.79	249.595	5.66	0.019

WS	3	32.43	10.812	0.25	0.863
TG	3	551.54	183.847	4.17	0.042
SD	3	44.15	14.716	0.33	0.802
PnD	3	531.83	177.277	4.02	0.045
TPL	3	60.51	20.169	0.46	0.719
DT	3	155.18	51.726	1.17	0.373
Residual Error	9	397.10	44.122		
Total	31	2523.73			

DF-Degrees of Freedom, SS-Sum of Squares, MS-Mean Square, F-Fisher Ratio, P-Probability that Exceeds 95 % Confidence Level

Table 4.7 ANOVA Table Values of SN Ratios for YS, % Elng. And BA

	YS			**% Elng.**			**BA**		
Source	**SS**	**F**	**P**	**SS**	**F**	**P**	**SS**	**F**	**P**
PD	1.78	0.05	0.82	6.97	0.18	0.68	158.35	2.20	0.17
RPM	515.74	5.27	0.02	403.17	3.50	0.06	554.98	2.57	0.12
WS	64.13	0.66	0.60	55.06	0.48	0.71	176.12	0.82	0.52
TG	377.02	3.85	0.05	515.67	4.48	0.04	425.37	1.97	0.19
SD	125.87	1.29	0.34	87.95	0.76	0.54	385.62	1.78	0.22
PnD	325.64	3.33	0.07	954.34	8.30	0.01	1000.10	4.63	0.03
TPL	99.80	1.02	0.43	71.02	0.62	0.62	99.87	0.46	0.72
DT	154.24	1.58	0.26	29.71	0.26	0.85	44.01	0.20	0.89
Residual error	293.69			345.09			648.27		
Total	1957.89			2468.98			3492.7		

Table 4.8 ANOVA Table Values of SN Ratios for WBT, HRD and Interface Temperature

	WBT			**HRD**			**Interface Temperature**		
Source	**SS**	**F**	**P**	**SS**	**F**	**P**	**SS**	**F**	**P**
PD	0.00	0.00	0.97	0.45	2.30	0.16	0.000011	0.02	0.90
RPM	0.15	1.14	0.39	0.50	0.85	0.50	0.00165	0.87	0.49
WS	0.21	1.65	0.25	0.72	1.24	0.35	0.000808	0.43	0.74
TG	0.06	0.49	0.70	1.72	2.95	0.09	0.032755	17.34	0.00
SD	0.06	0.44	0.73	0.35	0.60	0.63	0.003095	1.64	0.25
PnD	0.12	0.94	0.46	0.27	0.46	0.72	0.005555	2.94	0.09
TPL	0.02	0.12	0.94	0.81	1.39	0.31	0.007141	3.78	0.05
DT	0.07	0.57	0.65	0.74	1.26	0.35	0.006903	3.65	0.06

Residual error	0.38	1.75	0.005668
Total	1.07	7.30	0.063587

Table 4.9 Response Table for SN Ratios for UTS

Level	PD	RPM	WS	TG	SD	PnD	TPL	DT
1	37.61	40.01	38.29	30.87	38.79	40.71	39.52	39.25
2	37.08	40.56	35.68	36.59	35.6	41.45	36.18	39.82
3		39.83	37.44	40.60	37.09	35.87	37.54	35.29
4		28.98	37.97	41.32	37.90	31.34	36.14	35.02
Delta	0.53	11.58	2.61	10.45	3.19	10.12	3.38	4.8
Rank	8	1	7	2	6	3	5	4

Table 4.10 Response Table for SN Ratios for YS

Level	PD	RPM	WS	TG	SD	PnD	TPL	DT
1	33.39	36.03	34.34	27.82	36.72	36	36.19	35.77
2	33.86	36.04	32.17	34.34	31.65	36.11	31.78	35.75
3		35.76	32.4	36.27	32.16	34.12	34.32	32.23
4		26.68	35.59	36.07	33.98	28.27	32.21	30.76
Delta	0.47	9.37	3.43	8.44	5.07	7.83	4.41	5.01
Rank	8	1	7	2	4	3	6	5

Table 4.11 Response Table for SN Ratios for % Elongation

Level	PD	RPM	WS	TG	SD	PnD	TPL	DT
1	16.85	19.61	16.49	12.69	14.44	21.45	18.62	16.74
2	15.92	19.21	14.72	12.92	15.08	22.18	15.19	17.71
3		15.97	18.37	17.39	18.38	11.66	14.89	15.99
4		10.74	15.95	22.53	17.63	10.24	16.83	15.09
Delta	0.93	8.87	3.64	9.84	3.94	11.94	3.74	2.62
Rank	8	3	6	2	4	1	5	7

Table 4.12 Response Table for SN Ratios for BA

Level	PD	RPM	WS	TG	SD	PnD	TPL	DT
1	33.68	33.04	29.35	28.26	28.51	35.26	34.37	32.18
2	29.23	36.82	32.66	30.36	27.61	38.58	31.11	31.69
3		30.62	34.70	29.55	35.79	26.05	30.67	29.48
4		25.34	29.09	37.63	33.89	25.92	29.65	32.46

Delta	4.45	11.48	5.61	9.37	8.19	12.65	4.72	2.98
Rank	7	2	5	3	4	1	6	8

Table 4.13 Response Table for SN Ratios for WBT

Level	**PD**	**RPM**	**WS**	**TG**	**SD**	**PnD**	**TPL**	**DT**
1	14.95	15.03	14.82	14.99	14.94	14.94	14.92	14.91
2	14.95	14.95	14.95	14.89	14.9	14.86	14.95	15
3		14.84	14.99	14.93	15.02	14.98	14.96	15
4		14.98	15.04	15	14.95	15.03	14.97	14.89
Delta	0	0.18	0.22	0.11	0.12	0.17	0.06	0.1
Rank	8	2	1	5	4	3	7	6

Table 4.14 Response Table for SN Ratios for HRD

Level	**PD**	**RPM**	**WS**	**TG**	**SD**	**PnD**	**TPL**	**DT**
1	33.90	34.12	33.91	33.90	34.11	34.11	34.19	34.09
2	34.14	34.11	34.05	33.89	33.90	33.88	33.84	34.23
3		34.04	34.25	33.86	34.14	34.10	34.17	33.87
4		33.81	33.87	34.42	33.93	34.00	33.88	33.88
Delta	0.24	0.31	0.39	0.56	0.23	0.22	0.34	0.36
Rank	6	5	2	1	7	8	4	3

Table 4.15 Response Table for SN Ratios for Interface Temperature

Level	**PD**	**RPM**	**WS**	**TG**	**SD**	**PnD**	**TPL**	**DT**
1	53.7	53.71	53.69	53.75	53.71	53.7	53.68	53.71
2	53.7	53.69	53.7	53.67	53.7	53.71	53.7	53.69
3		53.69	53.7	53.68	53.69	53.68	53.72	53.72
4		53.7	53.7	53.69	53.7	53.71	53.71	53.68
Delta	0	0.02	0.01	0.08	0.03	0.03	0.04	0.04
Rank	8	6	7	1	5	4	2	3

The portion of the total variation observed in the experiment attributed to each significant factor is known as the percentage of contribution. It is a function of the sum of squares for each significant item. The percentage influence of the considered process parameters on the measured outputs were shown in **Fig. 4.8 (a-g)**. **Table 4.16** contains a ranking of significant effects (numbered "1" is the largest effect) for each response.

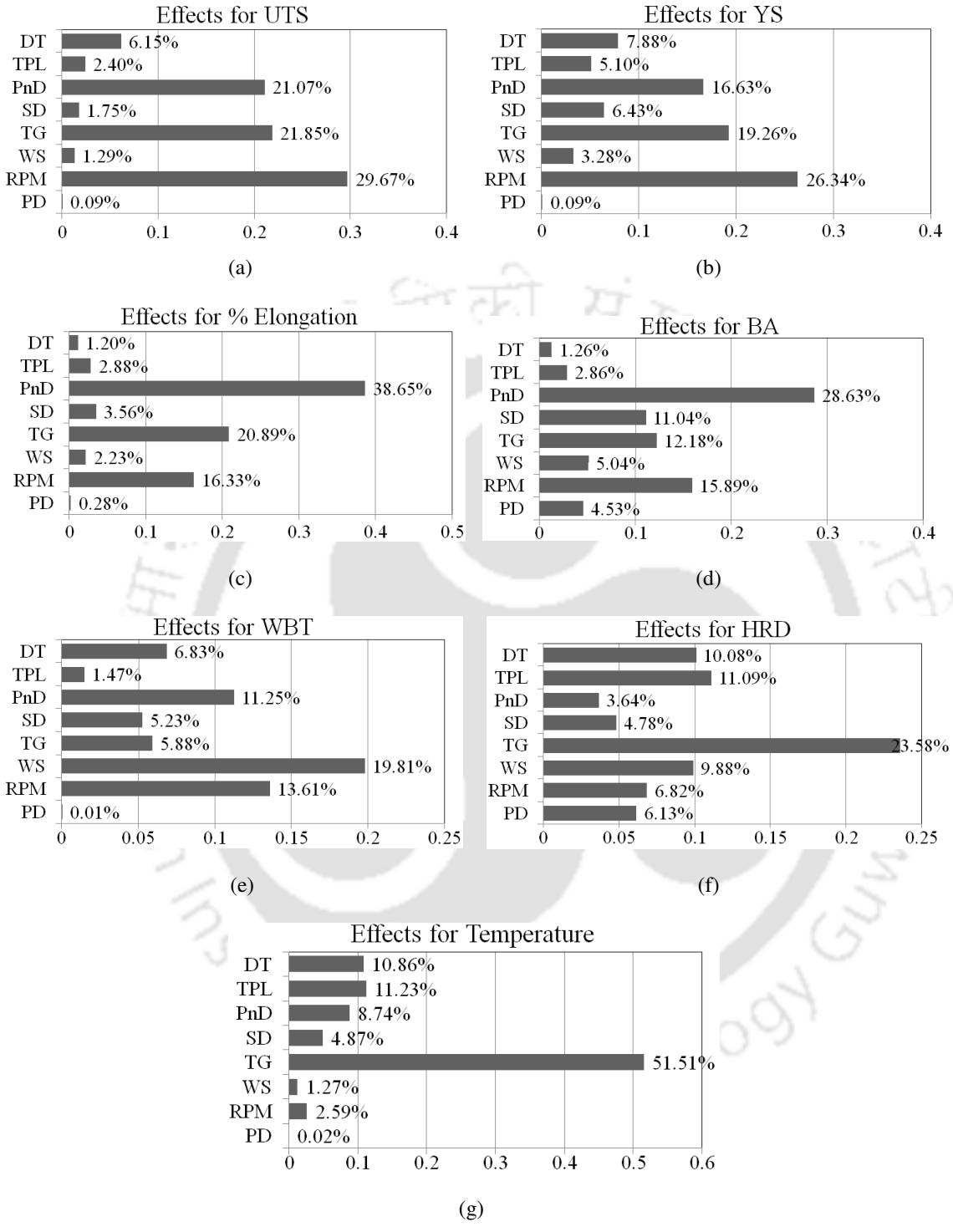

Figure 4.8 Percentage contribution plots for (a) UTS, (b) YS, (c) % Elongation, (d) BA, (e)WBT, (f) HRD and (g) temperature

Table 4.16 Ranking of Significant Factors for Each Response, One being the Most Significant

	Responses						
Factors	**UTS**	**YS**	**% Elongation**	**BA**	**WBT**	**HRD**	**Interface Temperature**
PD	-	-	-	-	-	-	-
RPM	1	1	3	2	2	-	-
WS	-	-	-	-	1	-	-
TG	2	2	2	3	-	1	1
SD	-	-	-	-	-	-	-
PnD	3	3	1	1	3	-	-
TPL	-	-	-	-	-	2	2
DT	-	-	-	-	-	3	3

From the results of single response analysis it was found that except interface maximum temperature and HRD all other measured responses were significantly influenced by RPM, TG and PnD. RPM has strong influence on rate of heat generation. In this work, the temperature of shoulder-workpiece interface was measured which did not vary much. However, the temperature of nugget zone may have varied in different welding conditions that could not be measured using IR sensor. As RPM is responsible for rate of heat generation, overall material mixing in surface level as well as in thickness direction of the workpiece, it was the most influencing factor for UTS having 29.67% weightage. TG and PnD were responsible for the material mixing along the workpiece thickness direction, these were the next influencing factors having 21.85% and 21.07% influence, respectively. For the defect free joints such as exp. 8, 11, 15, 19 etc. the joints showed higher mechanical properties. The weld specimens failed under ductile overloading due to the increasing applied load. The joints having large defects such as exp. 13, 14, 31 etc. shown the least joint properties. The joints though having very small defects showed moderate mechanical properties e.g. exp. 2, 9, 16 etc. For both of these cases when loads are applied the defect locations acted as the location for stress risers. This leads to the failure of the specimens at the defect location. Similarly for YS the influence of the above three parameters are 26.34%, 19.26% and 16.63% respectively. Bending angle was measured at the time of visible crack initiation. All the good joints were bent upto an angle of 140° without any crack. PnD controls the size and location of the defects like tunnels at the root and pin-hole at the

different places. So it was found to be the most influencing factor for BA as well as ductility having influence of 28.63% and 38.65%, respectively. RPM and TG were found to be the next influencing factors for both the responses. From the above analysis it was seen that out of seven considered output responses five responses are significantly effected by RPM, TG and PnD.

4.4.2 From Different Multi Response Analysis Techniques

4.4.2.1 From Grey Relation Analysis

First different measured responses were normalized using **Eq. 4.6**. After normalization, the GRC were calculated using **Eq. 4.7**. The next step is to convert the multiple performance characteristics into GRG values. Finally, the GRG values were calculated as per **Eq. 4.8**. The GRG of each experimental condition are shown in **Table 4.17**. From OA experimental design, it is possible to separate out the effect of each process parameter at different levels. For example, the mean grey relational grade for the PD at levels 1 and 2 can be calculated by averaging the grey relational grades from the experiments 1-16 and 17-32, respectively. The mean grey relational grades corresponding to different levels of the other parameters can also be computed in a similar manner.

Table 4.17 Calculated GRG, UV, DV and MPCI values

Exp. No.	Grey Relational Grade(GRG)	Overall Utility Values(UV)	Overall Desirability Value (DV)	MPCI Values
1	0.6493	6.64	0.9231	0.5948
2	0.5325	5.83	0.8509	0.4717
3	0.7118	7.51	0.9292	0.7014
4	0.7137	6.97	0.8888	0.5632
5	0.5635	5.21	0.7259	0.5039
6	0.6063	5.80	0.8692	0.6649
7	0.6269	6.54	0.9031	0.6078
8	0.7547	7.82	0.9584	0.6505
9	0.4991	5.09	0.8198	0.4835
10	0.4564	4.75	0.7810	0.7177
11	0.6904	6.56	0.9227	0.5774
12	0.5486	5.44	0.8014	0.4531
13	0.3691	2.56	0.5965	0.6110

14	0.4173	2.03	0.4027	0.7828
15	0.8455	7.30	0.9583	0.3219
16	0.4838	4.54	0.7181	0.4515
17	0.6236	6.31	0.8864	0.5948
18	0.5186	5.27	0.8358	0.4717
19	0.6892	6.68	0.9297	0.7014
20	0.5547	6.49	0.8560	0.5632
21	0.4999	5.79	0.8472	0.5039
22	0.5980	6.26	0.8671	0.6649
23	0.6127	6.15	0.8930	0.6078
24	0.6141	6.40	0.9120	0.6505
25	0.5671	5.53	0.8563	0.4835
26	0.7075	6.85	0.9346	0.7177
27	0.5790	6.00	0.8629	0.5774
28	0.4862	5.08	0.8000	0.4531
29	0.6139	5.97	0.8499	0.6110
30	0.7103	7.27	0.9507	0.7828
31	0.4174	2.08	0.4237	0.3219
32	0.5487	5.02	0.7093	0.4515

4.4.2.2 From Utility Concept

In utility theory, the initially preference scales were constructed for each quality characteristic by using **Eq. 4.15**. Then based on importance the weights were assigned to various quality characteristics such that it should satisfy **Eq. 4.12**. Here equal weights have been assigned to all the output responses as all were assumed to be of equal important quality characteristics. Finally the utility values for each trial condition of the experiment were calculated using **Eq. 4.14**. The calculated utility values based on responses are given in **Table 4.17**. Then these calculated values were considered as a response of the trial conditions of the selected OA and analyzed using Taguchi method.

4.4.2.3 From Desirability Function Approach

First a number was assigned for each weld quality characteristic ranging between 0 and 1 by desirability function. Then the criteria values were transformed into desirability function by using one-sided transformation using **Eq. 4.16**. For each trial condition of the experiment the desirability values were calculated using **Eq. 4.17**. Finally the overall

desirability value (DV) was calculated with appropriate weights using **Eq. 4.18**. The calculated values are shown in **Table 4.17**. After calculating DV, the results were analyzed using Taguchi method for finding out the significant process parameters.

4.4.2.4 From Fuzzy Assisted Grey Relational Analysis

From OA experimental design used for FZ-GRA technique, it is possible to separate out the effect of each process parameter at different levels. For example, the MPCI values for the plunge depth at levels 1 and 2 can be calculated by averaging the MPCI values from the experiments 1-16 and 17-32, respectively. The mean MPCI values corresponding to different levels of the other parameters can also be computed in a similar manner. The MPCI value of different selected process parameters at different levels is shown in **Table 4.17**.

4.4.2.5 Comparison between GRA, UC, DFA and FZ-GRA

The main effect plots for GRA, UC, DFA and MPCI are shown in **Fig. 4.9 (a-d)**, respectively. From these plots the influence of various parameters and their levels can be marked out. Irrespective of the quality characteristic chosen for a particular response, a greater GRG or utility or desirability or MPCI value corresponds to better quality characteristic. Therefore, the level having the greatest value indicates optimal level of the process parameter. The mean values of GRG, utility, desirability and MPCI are given in **Table 4.18-21**, respectively.

Based on the mean GRG values, the optimal parametric combination for this multi-objective analysis problem is found to be at levels 1, 1, 3, 4, 3, 1, 1 and 2 of factors plunging depth, rotational speed, welding speed, tool geometry, shoulder diameter, pin diameter, tool pin length and dwell time, respectively. Both for UC and DFA, the optimal parameter levels are found to be at levels 2, 1, 3, 4, 3, 1, 1 and 2. For FZ-GRA it is 2, 2, 3, 4, 3, 1, 1 and 2.

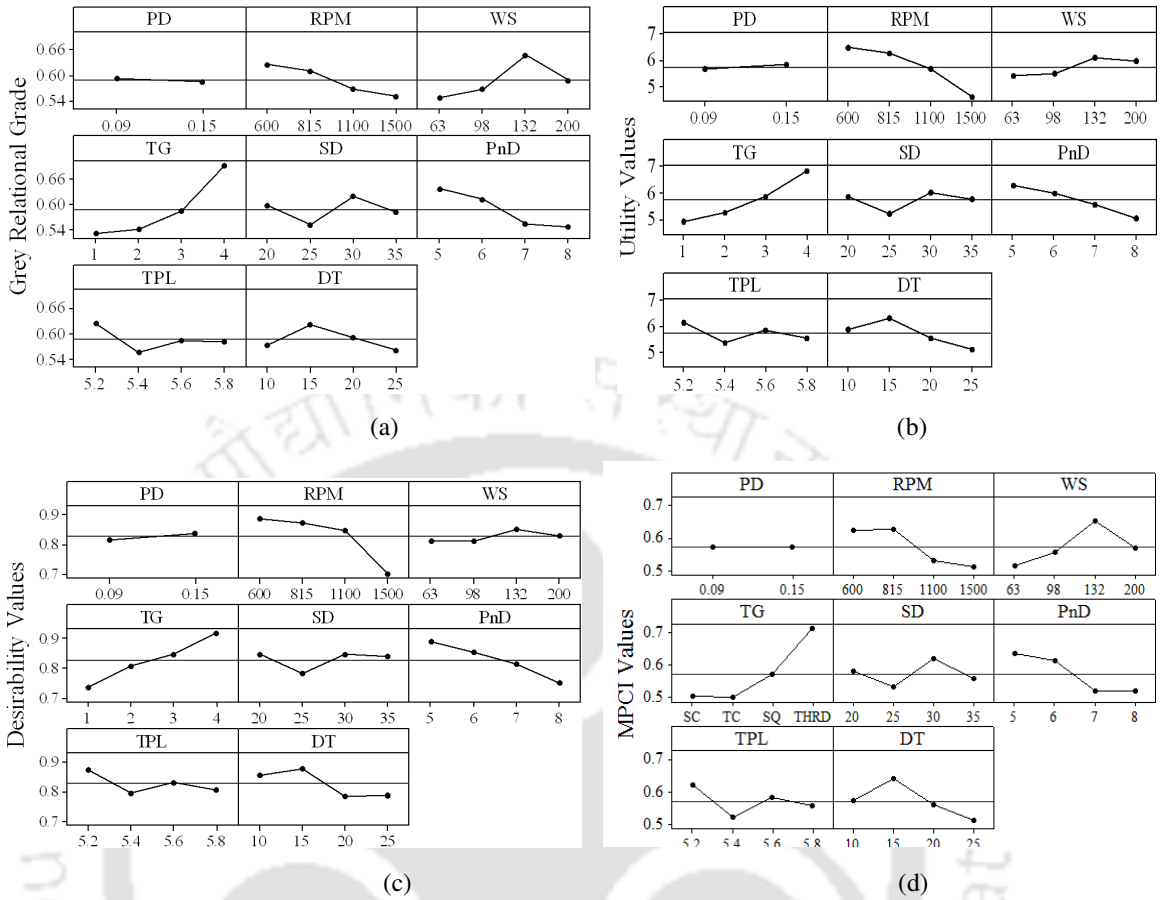

Figure 4.9 Main effects plots for (a) grey relational grade, (b) utility values, (c) overall desirability value and (d) MPCI Values

Table 4.18 The Mean GRG Values for Different Process Parameters at Different Levels

Level	PD	RPM	WS	TG	SD	PnD	TPL	DT
1	0.5918	0.6242	0.5482	0.5315	0.5974	0.6368	0.6262	0.5753
2	0.5838	0.6095	0.5684	0.5430	0.5515	0.6119	0.5560	0.6222
3		0.5668	0.6466	0.5836	0.6205	0.5548	0.5855	0.5917
4		0.5508	0.5881	0.6932	0.5819	0.5478	0.5835	0.5621
Delta	0.0080	0.0734	0.0984	0.1617	0.0689	0.0890	0.0702	0.0601

Table 4.19 The Mean Utility Values for Different Process Parameters at Different Levels

Level	PD	RPM	WS	TG	SD	PnD	TPL	DT
1	5.663	6.463	5.387	4.949	5.892	6.329	6.138	5.912
2	5.821	6.247	5.509	5.276	5.25	6.004	5.377	6.344
3		5.663	6.103	5.884	6.041	5.591	5.869	5.565

4		4.596	5.970	6.859	5.785	5.045	5.585	5.148
Delta	0.158	1.867	0.716	1.910	0.791	1.284	0.761	1.197

Table 4.20 The Mean Desirability Values for Different Process Parameters at Different Levels.

Level	PD	RPM	WS	TG	SD	PnD	TPL	DT
1	0.8156	0.8875	0.8131	0.7359	0.8449	0.8885	0.8745	0.8566
2	0.8384	0.8720	0.8115	0.8086	0.7804	0.8555	0.7960	0.8779
3		0.8473	0.8528	0.8451	0.8449	0.8150	0.8310	0.7853
4		0.7012	0.8305	0.9184	0.8379	0.7490	0.8065	0.7881
Delta	0.0228	0.1864	0.0413	0.1825	0.0645	0.1396	0.0785	0.0926

Table 4.21 The Mean MPCI Values for Different Process Parameters at Different Levels

Level	PD	RPM	WS	TG	SD	PnD	TPL	DT
1	0.5718	0.6245	0.5120	0.5042	0.5818	0.6346	0.6237	0.5732
2	0.5723	0.6254	0.5544	0.4992	0.5305	0.6125	0.5209	0.6412
3		0.5297	0.6530	0.5710	0.6188	0.5205	0.5855	0.5606
4		0.5085	0.5688	0.7137	0.5571	0.5205	0.5581	0.5132
Delta	0.0006	0.1169	0.1410	0.2145	0.0883	0.1141	0.1028	0.1280

GRA showed lower PD where as UC, DFA and FZ-GRA showed higher PD value as the optimum parametric level. All other parameters for GRA, UC and DFA are same at the optimum settings. Similarly in case of FZ-GRA method except rotational speed (in second level *i.e.* 815 rev./min) all other optimal parameter setting is same as in case of utility and desirability function approaches. But for all the analysis techniques lower values of RPM and PnD showed better joint properties. Because pin hole type of defects occur [Rajakumar *et al.*, 2010; Rajakumar and Balasubramanian, 2012a; Rajakumar and Balasubramanian, 2012b]at very higher RPM values due to the increase in turbulence of the plasticized metal and also due to excessive heat input tunnel and groove type of defects are likely to be formed at higher pin diameter [Rajakumar *et al.*, 2010; Rajakumar and Balasubramanian, 2012a]. Compared to all other tool geometries, threaded tool showed best joint properties for all the analysis techniques. The presence of threads in the tool causes an additional material flow in the thickness direction. This results in better material mixing along the plate transverse as well as the through thickness directions. Too low traverse speed results higher heat generation while higher traverse speed leads to unavailability of time required for

material mixing. So there is an appropriate welding speed for obtaining good welded joints. DT is required to plasticize the material initially and increase the temperature of the workpiece to a level at which the joining process can be started. So, lesser DT caused inadequate heat generation whereas too much of DT resulted excessive heat generation. Both these cases resulted in lower joint quality.

4.4.2.6 ANOVA Analysis and Confirmation Experiments

In order to analyze the significance and the contribution of each parameter to the GRG, utility, desirability and MPCI value ANOVA was carried out. The influences of different parameters obtained from different techniques are shown in **Table 4.22**. From the ANOVA analysis, it is found that for all the three traditional theories the contributions of tool geometry, tool rotational speed and tool pin diameter on affecting the multiple performance characteristics are more compared to other considered parameters. The newly proposed FZ-GRA technique has also shown similar result. This is because heat generation and overall material mixing is greatly influenced by the tool RPM in surface level as well as in thickness direction of the workpiece whereas TG and PnD are responsible for the material mixing along the workpiece thickness direction. The tool pin diameter also controls the defects like tunnels at the root and pin-hole at the different places. Though straight cylindrical tool is the simplest FSW tool geometry, use of square and threaded tools have their own advantages. Square tool has a pulsating stirring action which provides appropriate heat generation and material mixing. Threaded tool is having an additional material flow beside the tool pin in the workpiece thickness direction. This results in adequate material mixing which ensure defect free welds. As per GRA and FZ-GRA theory the tool geometry is the most significant factor having an influence of 33.01% and 27.95% respectively. RPM was found to be the most influencing parameter according to UC and DFA having percentage influence of 30.49% and 31.71%, respectively. The parameter setting and corresponding values (GRG, UV, DV and MPCI) for initial best condition is given in **Table 4.23**.

After obtaining the optimal parameter settings, there is need for prediction and verification of the enhancement of joint quality characteristics using the optimal parametric combinations for different techniques. The prediction of the corresponding GRG, UV, DV and MPCI values ($\hat{\Gamma}$) can be calculated from **Eq. 4.23** as given below.

$$\hat{\Gamma} = \Gamma_m + \sum_{i=1}^{o}(\overline{\Gamma}_i - \Gamma_m) \quad (4.23)$$

where, Γ_m is the total mean GRG/UV/DV/MPCI values, $\overline{\Gamma}_i$ is the mean GRG/UV/DV/MPCI value at the optimal level and o is the number of process parameters that affect the joint quality characteristics. **Table 4.23** contains the predicted GRG, UV, DV and MPCI values at optimal parameter setting obtained from GRA, UC, DFA and FZ-GRA, respectively.

Table 4.22 % Influence of Factors for Various Analysis Techniques

	% Influence			
Factors	**GRA**	**UC**	**DFA**	**FZ-GRA**
PD	0.00	0.65	0.69	0.37
RPM	**11.23**	**30.49**	**31.71**	**18.07**
WS	10.65	2.99	1.02	9.40
TG	**33.01**	**22.67**	**22.73**	**27.95**
SD	6.04	3.30	3.59	4.34
PnD	**14.06**	**13.90**	**15.94**	**13.76**
TPL	5.53	4.41	5.10	5.18
DT	4.81	10.68	9.68	9.93

Table 4.23 Initial Best, Optimal Parameter Settings and Corresponding Predicted GRG/UV/DV/MPCI values

Methods	**Cases**	**Parameter setting**	**Corresponding values (GRG / UV / DV / MPCI)**
GRA	Initial best	PD1 RPM4 WS3 TG4 SD3 PnD1 TPL1 DT2	0.8455
	Predicted (Optimal)	PD1 RPM1 WS3 TG4 SD3 PnD1 TPL1 DT2	0.9468
UC	Initial best	PD1 RPM2 WS4 TG4 SD3 PnD3 TPL2 DT2	7.82
	Predicted (Optimal)	PD2 RPM1 WS3 TG4SD3 PnD1 TPL1 DT2	9.90
DFA	Initial best	PD1 RPM2 WS4 TG4 SD3 PnD3 TPL2 DT2	0.9584
	Predicted (Optimal)	PD2 RPM1 WS3 TG4SD3 PnD1 TPL1 DT2	1.1940
FZ-GRA	Initial best	PD1 RPM2 WS4 TG4 SD3 PnD3 TPL2 DT2	0.9144
	Predicted (Optimal)	PD2 RPM2 WS3 TG4 SD3 PnD1 TPL1 DT2	1.0787

To verify the improvement of the weld quality characteristic, confirmation experiments were performed by using the optimal parameter combinations (shown in **Table 4.23**) which were obtained from GRA, UC, DFA and FZ-GRA methods. In the conformation experiment, the plunging depth, rotational speed, transverse speed, tool geometry, shoulder

and pin diameter, tool pin length and dwell time were set at 0.09 mm, 600 rpm, 132 mm/min, threaded tool geometry, 30 mm, 5 mm, 5.2 mm and 15 second, respectively, for GRA method. Both for UC and DFA methods, only the PD was set at 0.15 mm keeping all other parameters at same level as in the case of GRA. For FZ-GRA method, only RPM was changed to be set at 815 rev/min keeping all other parameters at same level as in case of UC and DFA. The weld qualities of the confirmation experiments for UTS, YS, % Elng., WBT and HRD are given in **Table 4.24**.

Table 4.24 Output Values Obtained from Confirmation Runs

Weld Quality Characteristic	Analysis Methods		
	GRA	UC and DFA	FZ-GRA
UTS	133.43	124.66	130.68
YS	55.09	66.87	69.94
% Elng.	19.87	15.7	16.26
WBT	5.60	5.47	5.57
HRDNS	57.91	57.28	56.87

From the conformational test results, it can be seen that the tensile strength and ductility value is higher for the joints produced at the optimal parameter setting obtained from grey relational analysis as compared to all other methods. This is due to the lower plunging depth used for GRA. But the yield strength is the lowest for the experiment in case of GRA and also there was no significant difference between the measured hardness values for all the methods. As in the present investigation thickness of the weld bead was considered as one of the output parameter, defect free joints with higher weld bead thickness were expected to have higher mechanical properties. For all the analysis theories except PD (0.09 for GRA and 0.15 for UC, DFA and FZ-GRA) and RPM (600 rev./min for GRA, UC and DFA and 815 rev./min for FZ-GRA) other parameter levels are same. Higher PD leads to increase the material flashing from the weld zone. As a result of which material thinning takes place. So even though the joint quality is good, the phenomenon of material thinning reduced the strength and consequently the elongation. For a good joint all the output values should be improved. So from the present experimental investigation it is really difficult to conclude any of the four above mentioned methods to be the best one for multi-objective analysis of FSW process. However if the UTS, ductility and weld bead thickness values are taken into

account then GRA method is better than all other methods. But if the overall mechanical properties will be considered then FZ-GRA method is better having highest yield strength compared to GRA, UC and DFA methods. The predicted optimal corresponding values (GRG, UV, DV and MPCI) for all the multi-response techniques were also improved as compared to initial best values.

In the present study, for recording the temperature variation of the workpiece, Infra Red camera was used during the experiments. From the experimental results it could be seen that the change in maximum interface temperature was not significant. It was found that the variation of maximum interface temperature was about 9° C (480.32°C to 489.18°C) among all the 32 experiments. So, the information about the weld quality cannot be extracted from the interface temperature. The temperature generated during the FSW process is from 70-85% of the melting temperature of the base material [Thomas *et al.*, 1991]. Here the interface temperature was measured which is nothing but the temperature of the plasticized material around the shoulder periphery. Once the material got plasticized, the workpiece flow stress falls rapidly as the solidus is approached, so that heating of the nugget at the tool/workpiece interface limits the available heat generation by reducing the torque, because of this temperature variation is insignificant. But still if it is considered as an output parameter then TG was found to be the most influencing factor having 51.51% weightage. This was due to the larger area of contact for straight cylindrical tools, pulsating effect of squared tool and a material flow along the tool axis due to the threaded tool. TPL was found to be the next influencing factor due to the effect of its depth of penetration inside the workpiece. DT was another factor which was responsible for temperature generation as it decides the time held in the plunged stage of the joining.

In the above mentioned temperature study surprisingly RPM was found to be insignificant in interface temperature generation. To cross verify the influence of RPM on interface temperature generation some more number of experiments were carried out with different RPM keeping all other parameters constant. The detail experimental layout is presented in **Table 4.25**. The interface temperature profile and peak temperatures recorded during the experiments are represented in **Figs. 4.10(a)** and **(b)**, respectively. From the temperature profiles it can be seen that the effect of RPM on shoulder workpiece interface temperature generation is not significant.

Table 4.25 Process Parameter Values and their Levels

Sl. No.	RPM	TG	WS
Exp. 1	600	SC	63
Exp. 2	815	SC	63
Exp. 3	1100	SC	63
Exp. 4	1500	SC	63

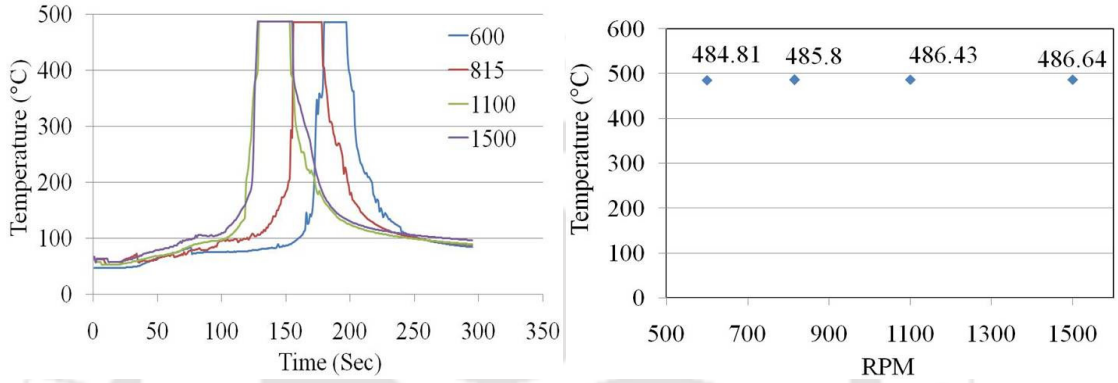

(a) (b)

Figure 4.10 (a) Temperature profile and (b) peak temperatures with respect to RPM

4.4.2.7 Macrostructure

The macrographs of the joint cross-sections for all the joints are shown in **Fig. 4.11**. The abbreviations AS and RS stands for advancing side and retreating side, respectively. The traces of material flow can be observed for good joints like Exp. no. 11, 15, 26, 30 etc. Samples like 14 and 31 showed maximum defects which may be due to the simultaneous combination of higher levels of process parameters like RPM, DT, PD and PnD which governs the amount of heat input to the weld. The defect for a particular joint (no. 20) is a tunnel type of defect. The location of the defect was on advancing side and the possible reason behind this is poor plasticization of material. The location and size of the other defects can also be observed from the macrographs which can further state the possible reason of defect formation.

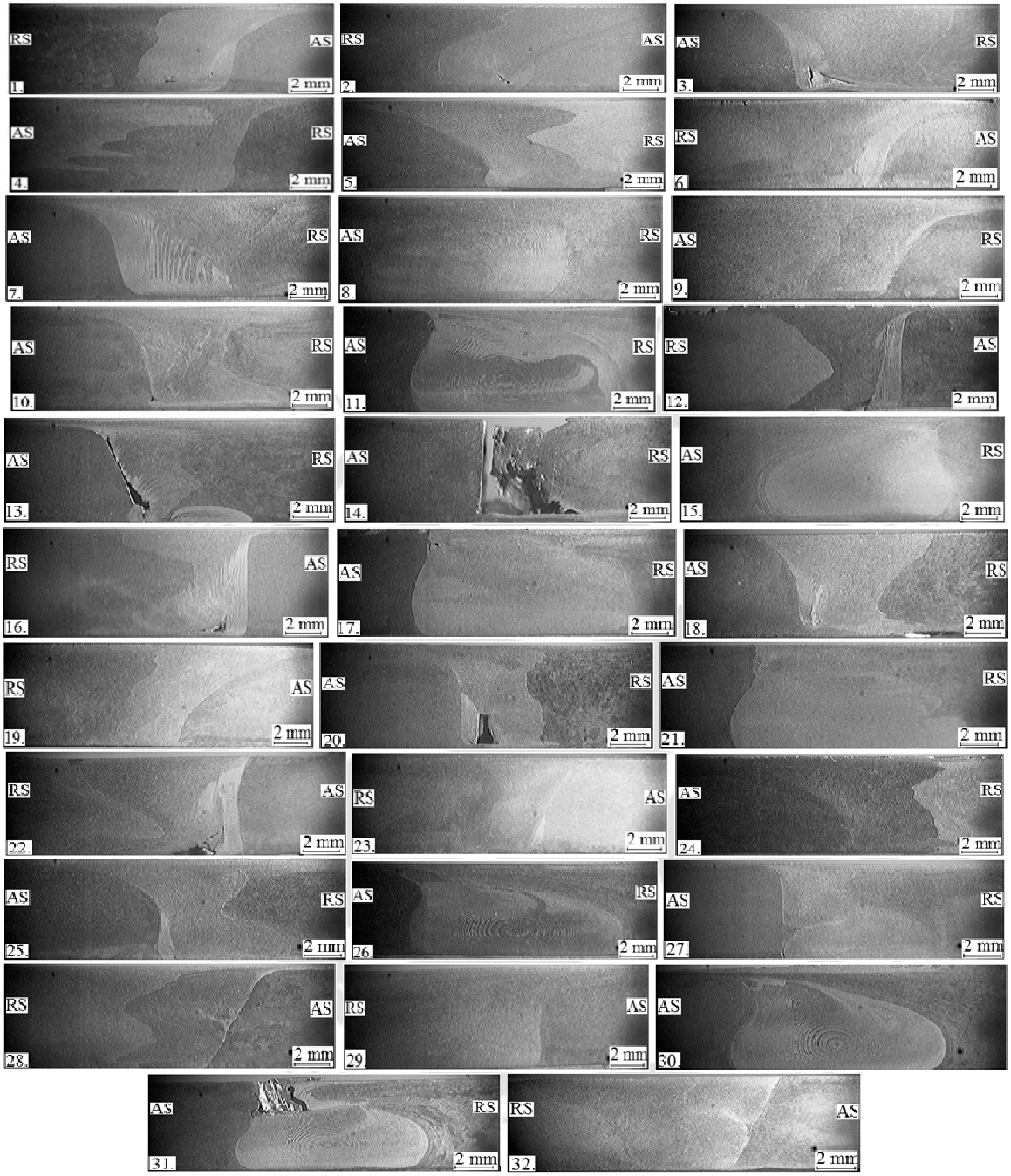

Figure 4.11 Macro graphs of joint cross-sections for Exp. 1 to 32

4.4.2.8 Fractrography

To understand the failure patterns, the fractographs of the fractured tensile tested specimens for base material and good joint were studied under SEM and are presented in **Figs. 4.12(a)** and **(b),** respectively. The fractured surfaces of both the base material and

good joint were invariably characterized by fine dimples with micro-void coalescence. This generally occurs in ductile mode of fracture indicating extensive plastic deformation. For a defective sample two SEM images were taken at two different locations. **Figures 4.12(c)** and **(d)** represent the fractrograph of a defective sample at two different locations. The location in **Fig. 4.12(c)** showed a trans-granular fracture mode. Such mode of fracture demonstrates high roughness and high crack deflection angles. Also the evidence of striations was found. The arrow marks shown in the figure represents the direction of crack propagation. This type of fracture surface was mainly seen nearby the defect region. **Figure 4.12(d)** type of fractrograph was taken away from defect region where the joints seemed to be appropriate. For the above stated reason these fracture surfaces showed dimples with tearing edges full of micro pores which is an indication of ductile mode of failure.

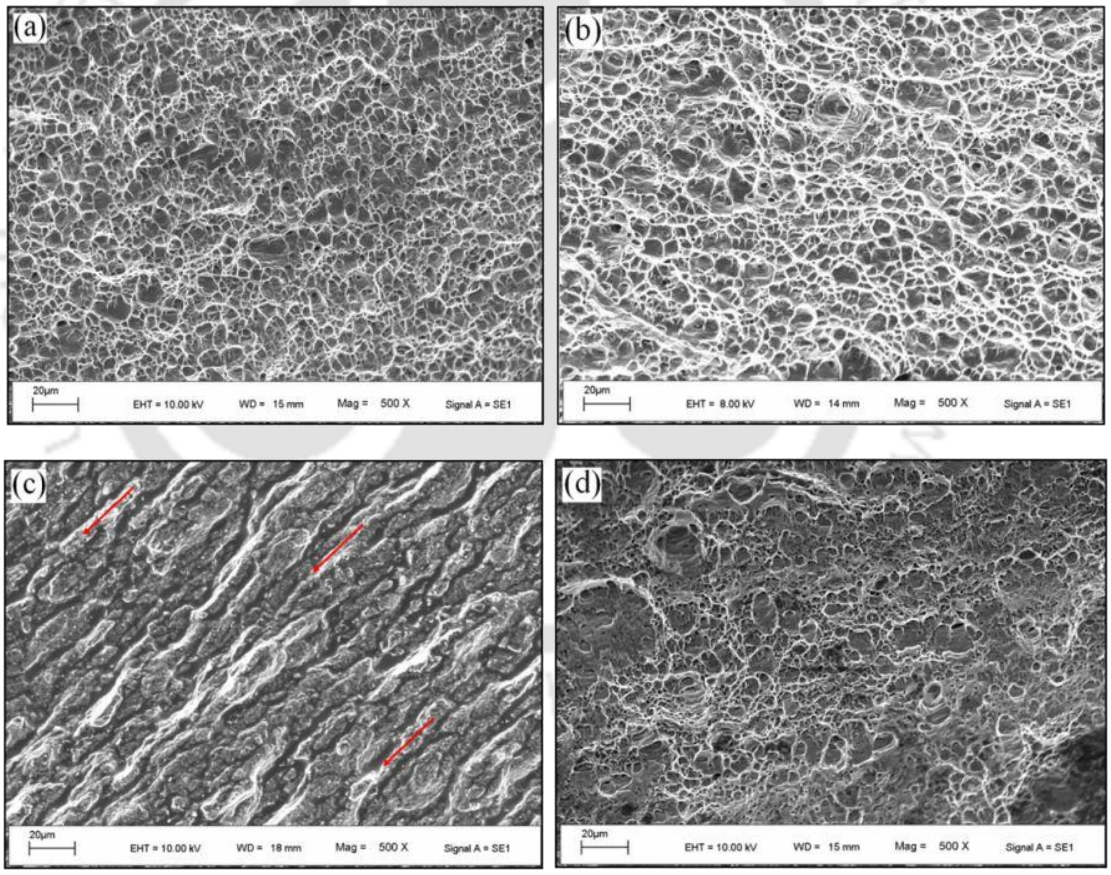

Figure 4.12 Fractographs of (a) base material, (b) good joint (c) at the defect location (d) upper part of the defect

4.4.3 From Full Factorial Design of Experiments to Study the Effect of Significant Process Parameters on Joint Properties

In this phase of experiments a full factorial design matrix is prepared. The three most significant parameters obtained from the first phase of the experimental investigation (discussed in Section 4.4.2.6) are varied in three levels which constitute a design matrix containing twenty seven numbers of experiments. The considered parameters and their values are given in **Table 4.26**. Nine numbers of tools of different shape and dimensions are fabricated to carry out all the 27 experiments. The fabricated tools are shown in **Fig. 4.13**. After welding the specimens for weld quality characterization are prepared as discussed in Section 4.2.6. Two specimens are prepared for each test to minimize the error. The test results are discussed in a detailed manner in the following sections.

Table 4.26 Considered Process Parameter Values for Full Factorial Design

Parameters	Value
Tool Rotational Speed (rev/min)	600, 815 and 1100
Tool Geometry	Straight cylindrical, Tapered cylindrical and Threaded tool pin with flat shoulder
Pin Diameter (mm)	5,6 and 7
Welding Speed (mm/min)	98
Plunging Depth (mm)	0.09
Shoulder Diameter (mm)	25
Tool Pin Length (mm)	5.7
Dwell Time (sec)	15

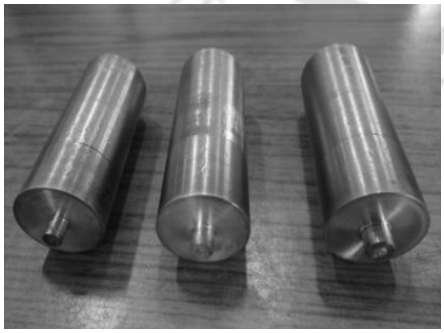

(a)

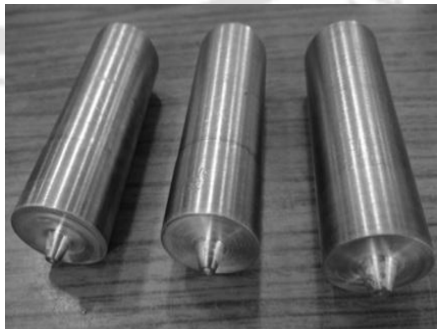

(b)

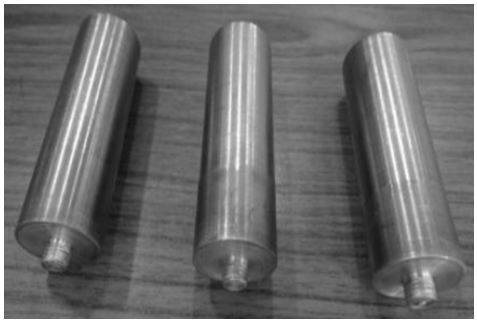

(c)

Figure 4.13 Fabricated tools (a) straight cylindrical (b) tapered cylindrical and (c) threaded

4.4.3.1 Tensile Test

Tensile tests were performed as described in Section 4.2.6. During tensile test properties namely, UTS, YS and % Elongation are measured in the present work. The complete experimental layout for 27 numbers of experiments and the measured output values are given in **Table 4.27**. All the joints are found to be defect free on macro as well as microscopic point of view. The effects of RPM, TG and PnD on UTS, YS and ductility were shown in **Fig. 4.14-16** along with the error bars.

Table 4.27 Experimental Layout with Measured Outputs

Exp. No.	RPM	TG	PnD	UTS (MPa)		YS (MPa)		% Elng.		BA (°)		HRD
				S1	S2	S1	S2	S1	S2	RB	FB	
1	600	SC	5	111.56	116.19	57.23	62.09	10.25	11.07	140	140	57.80
2	815	SC	5	120.46	116.54	67.44	65.69	11.98	12.12	140	140	56.37
3	1100	SC	5	119.87	123.06	71.92	67.10	14.21	12.27	140	140	55.29
4	600	SC	6	126.12	122.45	66.38	74.81	13.40	12.02	140	140	54.57
5	815	SC	6	124.14	127.42	71.72	77.70	11.93	15.83	140	140	58.40
6	1100	SC	6	131.19	128.68	78.41	77.30	14.15	16.77	140	140	50.94
7	600	SC	7	124.53	130.43	77.53	72.61	14.36	13.66	140	140	57.31
8	815	SC	7	123.98	127.03	69.99	76.11	15.23	14.93	140	140	53.27
9	1100	SC	7	118.19	115.13	65.24	61.15	15.03	14.01	140	140	53.32
10	600	TC	5	129.55	125.79	78.36	73.09	11.82	8.70	140	140	56.11
11	815	TC	5	127.58	131.66	74.14	83.79	13.08	14.84	140	140	53.27
12	1100	TC	5	130.49	135.62	82.51	87.97	15.73	15.07	140	140	50.93
13	600	TC	6	125.77	130.83	80.86	78.97	15.84	14.04	140	140	56.13
14	815	TC	6	130.28	133.79	80.52	86.21	15.96	15.20	140	140	50.32

15	1100	TC	6	135.18	137.26	86.33	87.92	15.48	16.82	140	140	53.56
16	600	TC	7	128.26	134.95	80.21	88.12	15.02	13.66	140	140	57.93
17	815	TC	7	135.23	132.54	82.83	90.81	14.79	15.57	140	140	49.93
18	1100	TC	7	131.49	125.55	79.01	78.59	13.99	14.93	140	140	55.38
19	600	THRD	5	126.11	135.25	82.42	78.29	14.53	15.31	140	140	58.55
20	815	THRD	5	131.29	135.91	83.15	88.15	15.40	15.00	140	140	57.47
21	1100	THRD	5	140.24	139.22	90.15	88.35	16.24	16.06	140	140	58.10
22	600	THRD	6	127.82	134.80	83.82	84.39	15.71	14.41	140	140	56.09
23	815	THRD	6	134.82	137.00	93.36	88.12	16.11	15.61	140	140	57.61
24	1100	THRD	6	145.16	139.29	101.87	109.81	16.96	15.76	140	140	62.76
25	600	THRD	7	129.84	134.59	88.20	86.99	13.90	15.35	140	140	57.64
26	815	THRD	7	137.25	132.95	87.23	91.27	15.19	15.81	140	140	59.17
27	1100	THRD	7	127.38	133.67	97.43	89.38	14.87	15.61	140	140	54.07

S1 = Sample 1, S2 = Sample 2, RB = Root Bend and FB = Face Bend

From **Fig. 4.14 (a), 4.15 (a)** and **4.16 (a)** it can be seen that at lower tool pin diameters the tensile properties increases with increase in tool rotational speed for all the tool geometries. But once the pin diameter value reaches 7 mm the properties diminishes with further increase in RPM. Tool rotational speed is a parameter which is responsible for material mixing in both surface level and thickness direction of the joint. So the tensile properties increase with increasing RPM. When the tool pin travels in forward direction, the void formed behind the tool gets filled by the rotating material coming from front side of the workpiece. At higher PnD this void size increased whereas the volume of material available to fill it remains the same due to constant shoulder diameter. This decreases the material density at the joint decreasing the corresponding tensile properties in terms of UTS and YS. So there is an optimum value of pin diameter beyond which the joint properties deteriorates.

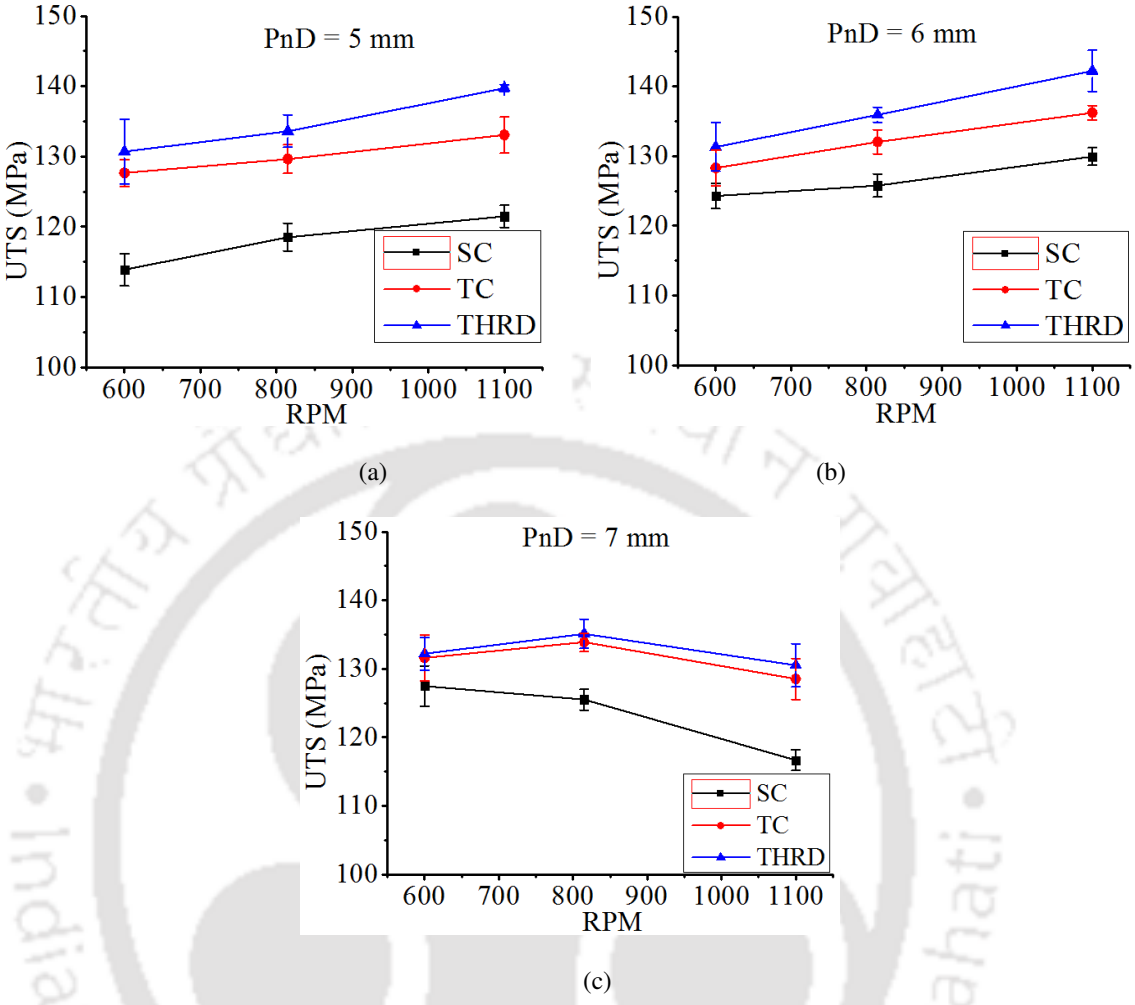

Figure 4.14 UTS values for different TG at different RPM for a PnD of (a) 5, (b) 6 and (c) 7 mm

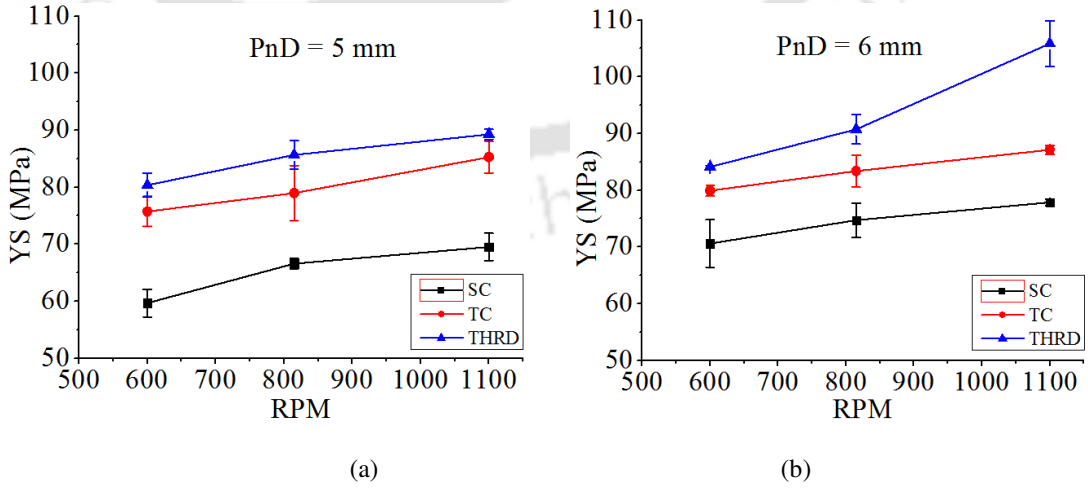

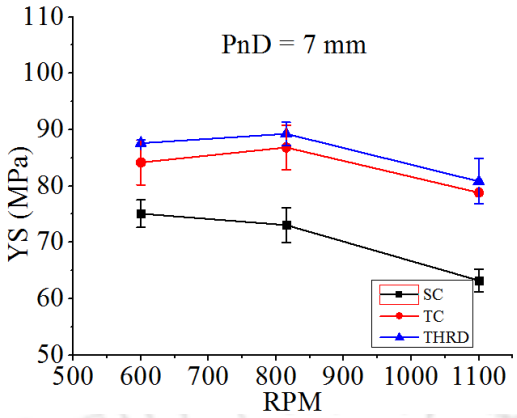

(c)

Figure 4.15 YS values for different TG at different RPM for a PnD of (a) 5, (b) 6 and (c) 7 mm.

Particularly for SC tools the drop in tensile properties at higher PnD is significant. This is because, THRD tools induces an addition material flow adjacent to the tool pin in material thickness direction with the help of threads which pushes the nearby material in downward direction while rotating. For this reason joint produced with threaded tool of 6 mm PnD at 1100 RPM showed best tensile properties. TC tools have varying tool pin diameter from root of the pin to tip. This lefts smaller size of voids to be filled at the root of the joints. Where as in case of SC tools there is no additional material flow and the size of the void to be filled is same both at the top and root of the joint. This leads to decrease in tensile properties for SC tools at higher PnD. From the % Elng. plots shown in **Fig. 4.16(a-c)** similar trends were observed as in case of UTS and YS. At higher PnD the ductility shown by both SC and TC tools were nearly equivalent whereas THRD tool showed better elongation property than these tools.

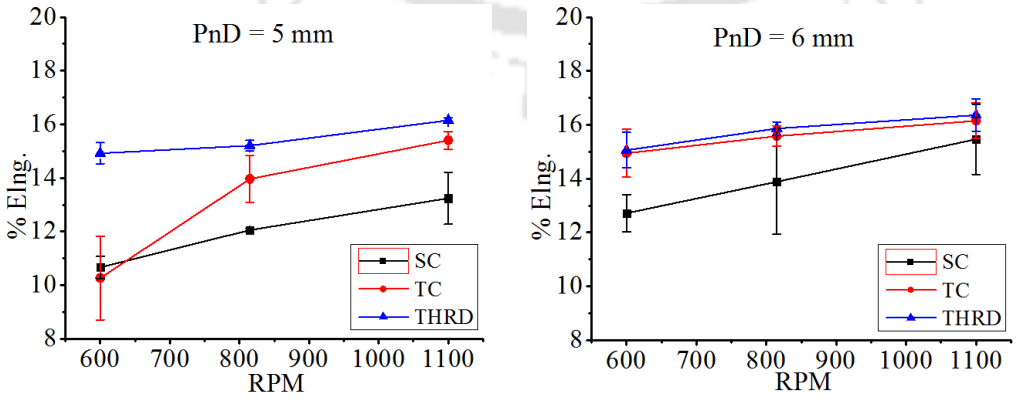

(a) (b)

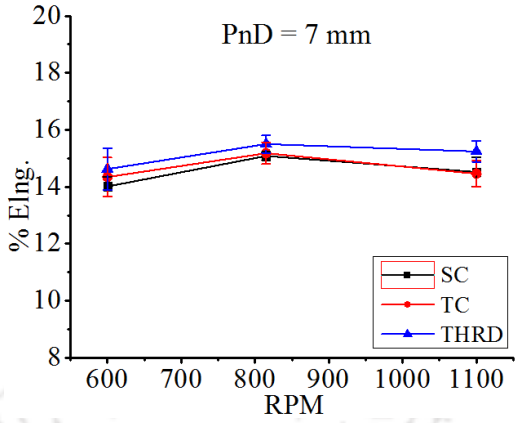

(c)

Figure 4.16 % Elng. values for different TG at different RPM for a PnD of (a) 5, (b) 6 and (c) 7 mm

4.4.3.2 Bending Test

With the available bending test setup the maximum angle that can be bent is 140°. So all the bending tests were carried out upto an angle of 140° both for root and face bend tests. As all the joints are defect free, both the roots and faces of all the samples were bent upto an angle of 140° without any visible crack on the bent surface. The images of the bent specimens before and after testing were shown in **Fig. 4.17(a)** and **(b)** respectively. After two types of bend test the images of the bent surfaces were captured and shown in **Fig. 4.17(c)** and **(d)**. From the images it can be observed that both the face and root of the joint are defect free.

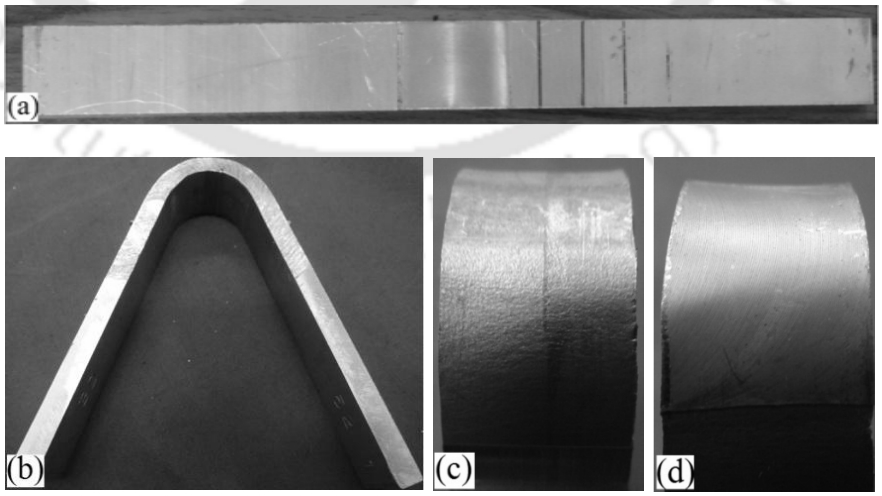

Figure 4.17 Images of (a) bending specimen, (b) tested specimen (c) joint root and (d) joint face after bending

4.4.3.3 Hardness Test

The Vickers microhardness values are measured during the hardness test. The values at all the points were recorded as per the mapping shown in **Fig. 4.18.** The hardness readings were taken from the weld centre in 1 mm (for NZ) and 2mm (for TMAZ, HAZ and BM) incremental distance basis both in advancing and retreating side. Here the values were measured at three different layers across the material thickness direction at 1 mm, 2.5 mm and 4 mm distance from the top surface of the weld. 15 points were considered for NZ hardness, 12 and 9 points each on advancing side (AS) and retreating side (RS) of the weld for thermo mechanically affected zone (TMAZ) and heat affected zone (HAZ), respectively. The average value for each zone was calculated and taken into consideration for comparison. To measure hardness of workpiece material 45 different readings were taken from a sample and average value was considered. The hardness plots at different experimental conditions are shown in **Fig. 4.19 (a-c)**.

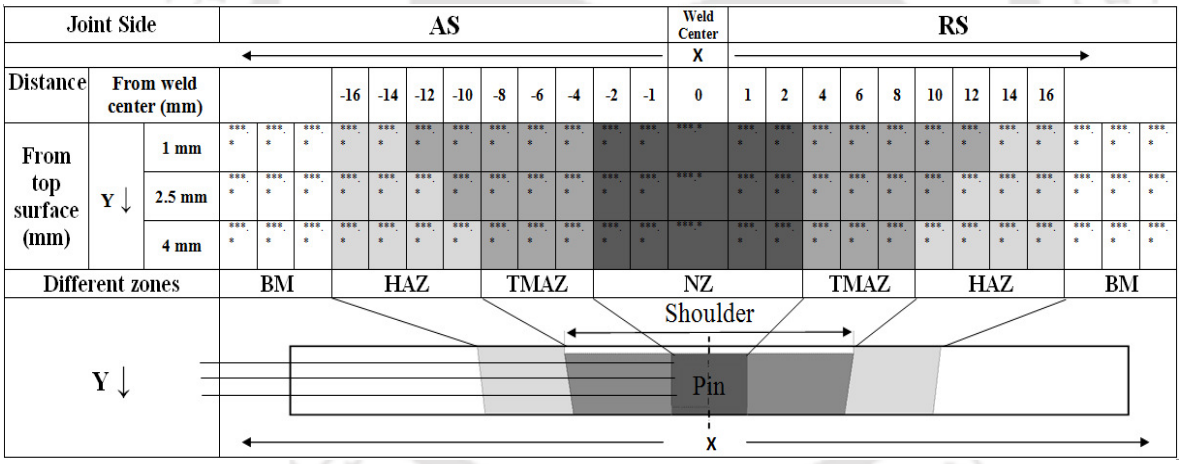

Figure 4.18 Layout for microhardness values recorded from a joint

Here the initial comparison was made between different tool geometries for the best parameter setting obtained from tensile test i.e. for 1100 RPM and 6 mm pin diameter. Threaded tool showed highest NZ hardness compared to other TG. This is due to better material mixing and more refined grains at the NZ. The NZ hardness value for THRD tools was also found to be higher than all other zones. Similarly the second plot (**Fig. 4.19 (b)**) shows the condition for varying rotational speed from 600 to 1100 RPM. Due to better material mixing and dynamic recrystallization process at higher RPM, the NZ hardness

value increases with the increase in tool rotation speed for a particular TG and PnD. The NZ hardness value increases with increase in PnD from 5 mm to 6 mm then decreases for a PnD of 7 mm. This is due to the decreased material density at NZ at higher PnD.

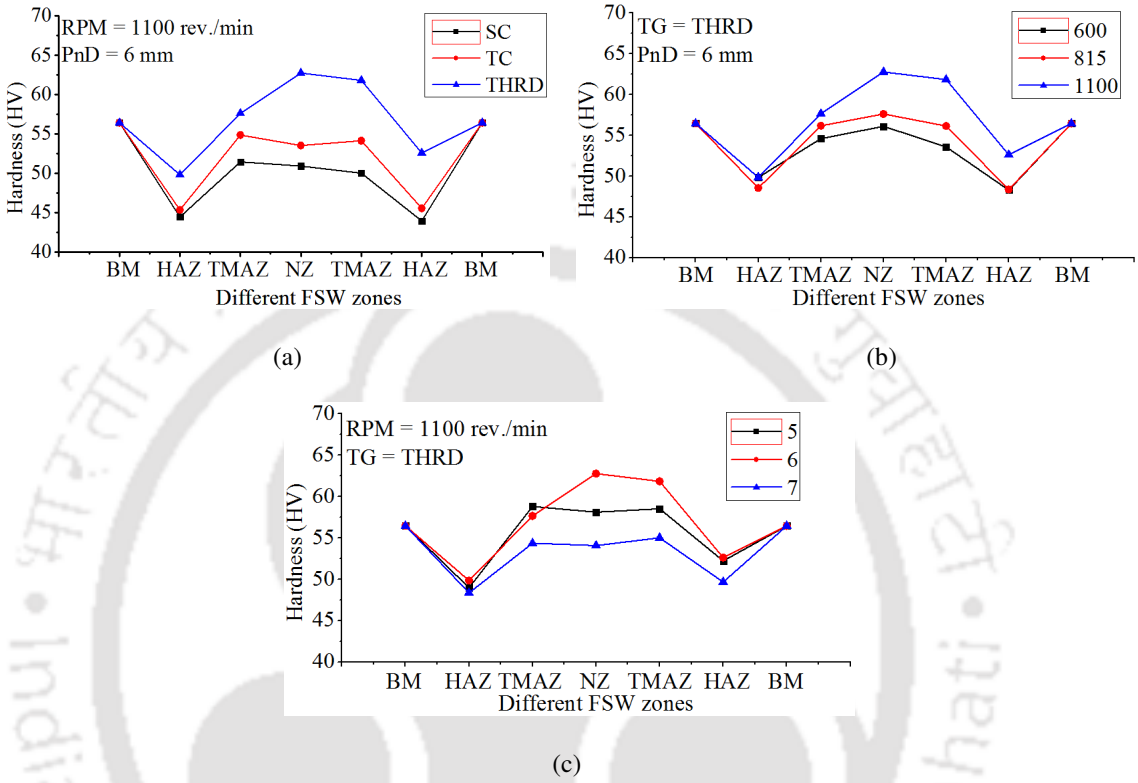

Figure 4.19 Hardness plots for different experimental conditions such as (a) varying TG, (b) varying RPM and (c) varying PnD

4.4.3.4 Macrostructure

The macrographs of the joint cross-sections for all the welded joint are shown in **Fig. 4.20 (a)**. From the macrograph the usual basin shape can be seen which was formed due to the microstructural changes occurred during the FSW process. The dimensions of different zones formed during FSW process for a sample are shown in **Fig. 4.20 (b)**. The upper part of the basin is the result of rotating shoulder and lower part due to tool pin. All the joints shown defect free macrographs. The weld zone in FSW process is not symmetrical which can be observed from **Fig. 4.20 (c)**.

(a)

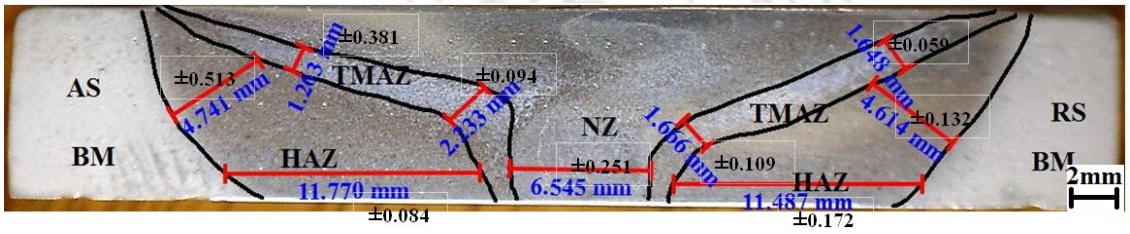

(b)

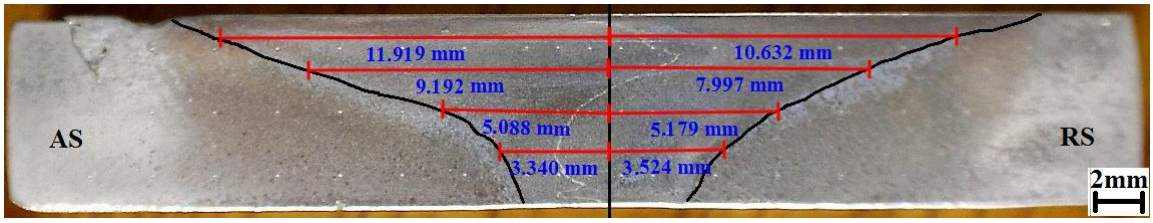

(c)

Figure 4.20 (a) Macro graphs of joint cross-sections for Exp. 1 to 27, (b) dimensions of different zones and (c) dimension of weld nugget

4.4.3.5 Microstructure

The micrographs of workpiece material (BM) and HAZ are shown in **Figs. 4.21(a)** and **(b),** respectively. The grains in HAZ are larger than the BM. This is due to the expansion of grains at HAZ which has undergone a thermal cycle. The TMAZ and NZ microstructure for a welded sample are shown in **Figs. 4.21(d)** and **(e),** respectively. It can be seen from the transition zone micro graph shown in **Fig. 4.21(c)** that there is a change in grain structure and density from TMAZ to NZ as a result of stirring of material under the rotating FSW tool. TMAZ contains elongated grains as the zone is subjected to both thermal and mechanical cycle. The grains are in deformed state due to the stirring action of the material. The stir zone or NZ consists of fine equiaxed grains due to phenomena of dynamic recrystallization. The NZ grain size is finer and more uniform compared to all other zones which lead to enhanced joint properties.

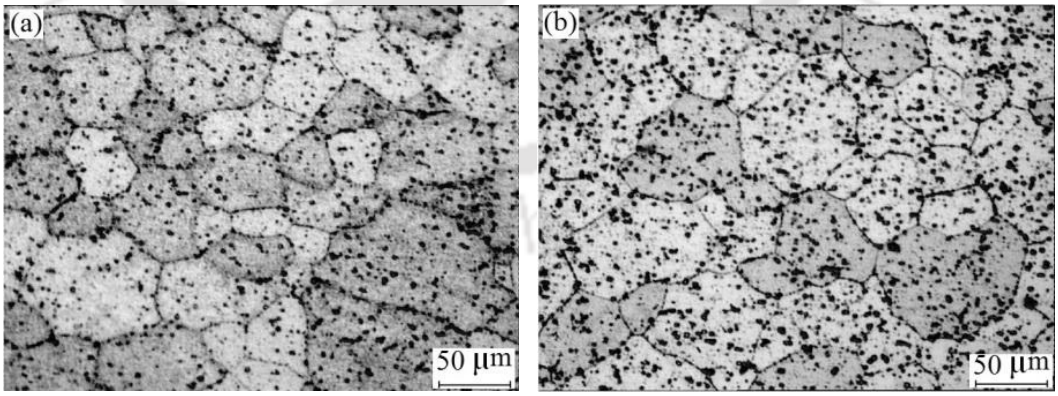

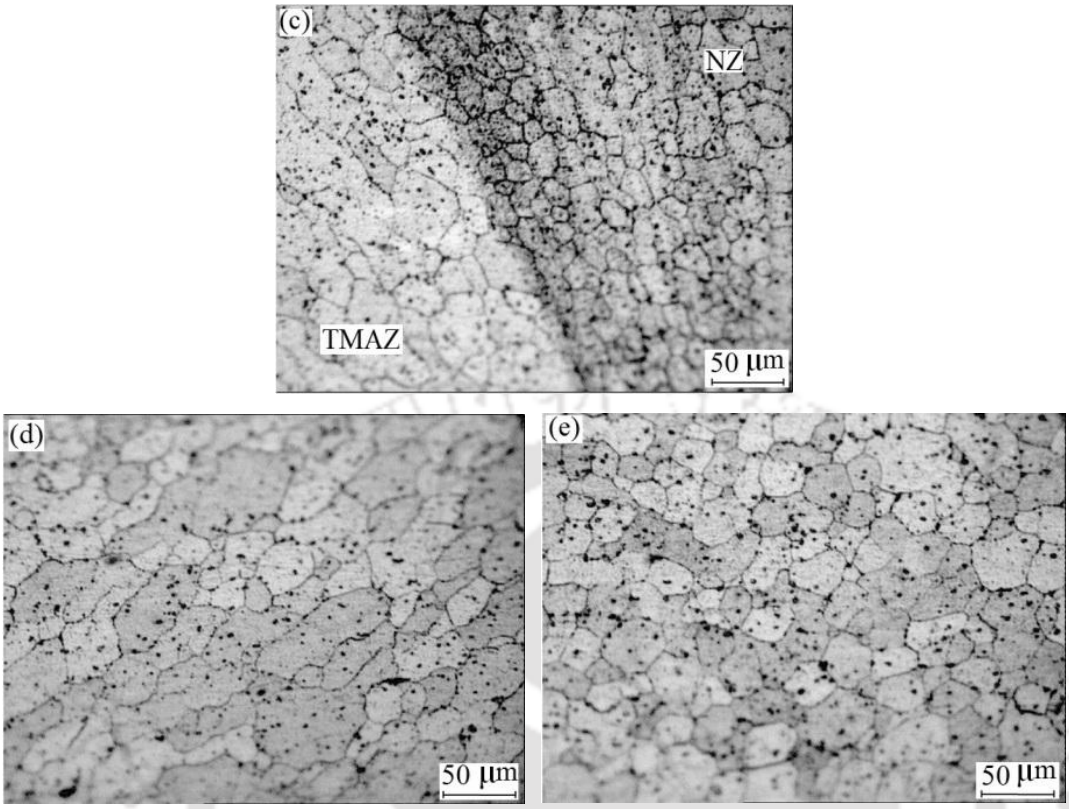

Figure 4.21 Microstructure of (a) base material, (b) HAZ, (c) transition zone, (d) TMAZ and (e) NZ

4.5 Observations

The observations of the aforementioned studies are listed below:

- Spindle speed, TG, and PnD were the three most significant process parameters of the FSW process as obtained from Taguchi's single response analysis technique.
- UTS and YS were most affected by RPM; TG and PnD had secondary effects.
- Ductility was most affected by PnD, followed by TG and RPM.
- BA is most affected by PnD, followed by RPM, TG and SD.
- The traditional multi-objective techniques namely GRA, UC and DFA also showed similar results.
- The newly proposed FZ-GRA technique was found to be another efficient method for multi-response analysis of a process. The results obtained were also agreed to the results from above techniques.
- Though the temperature variation was not significant, the tool shoulder and

workpiece interface temperature was most affected by TG, followed by TPL and DT.

- Shoulder workpiece interface temperature cannot be used as an indicator for weld quality.
- Fractrographic sample showed ductile fracture for good welded joints where as defective joints shown a mixed mode of fracture.
- The tensile properties increased with increasing RPM for all the tool geometries especially at lower PnD. But it decreases with RPM at higher PnD.
- THRD and SC tools showed best and least mechanical properties. Best tensile and hardness properties were observed for the joints produced by THRD tool pin geometry of 6 mm pin diameter at 1100 RPM.
- NZ hardness value was also found to be highest for the above parameter setting. The HRD value increased with RPM for a particular TG and PnD.
- The microstructure revealed the phenomena of dynamic recrystallization in NZ, deformed grains in TMAZ and expanded grains in HAZ.

4.6 Major Findings

- From the single as well as different multi response analysis techniques, the three most significant factors of the FSW process are found to be spindle speed, tool pin geometry and tool pin diameter.
- The proposed fuzzy assisted grey Taguchi method is suitable for selecting the optimal process parameter setting for the FSW process.
- Due to insignificant variation of shoulder workpiece interface temperature, it cannot be used as an indicator for weld quality.
- Good joints showed ductile mode of fracture where as defective ones shown a mixed mode of fracture.
- Tool with threaded and straight cylindrical pin geometry showed best and least joint properties.
- From the microstructure the phenomena of dynamic recrystallization in NZ, deformed grains in TMAZ and expanded grains in HAZ are observed.

Chapter 5

Finding Appropriate Starting Position and Elimination of the End Hole in FSW

5.1 Introduction

One of the limitations of the FSW process is that end hole remains at the end of the joint and some offset distance need to be provided at the start of the joint. The present Chapter focuses on different approaches in finding an appropriate starting position and to eliminate the end hole type of defect in FSW process. It is based on several distinct experimental trials. These trial runs consist of numbers of different cases of start and end locations. The main aim of these case studies is to achieve maximum joint length and minimum material wastage while joining two materials by FSW process. All the process parameters like rotational speed, welding speed, plunging depth, tool geometry and dwell time were kept constant during the trial runs.

5.2 Methodology

In the usual practice, the FSW process is being carried out as shown in **Figs. 5.1(a)** and **(b)**. It can be seen that some offset distance, gap between edge of the plates and actual weld, is provided both at start and end of the joint for effective welded joint. As a result of which some volume of material need to be removed both from the start as well as end part of the joint. This reduces the effective joint length which is approximately equal to the sum of two

offset distances and the tool shoulder diameter. Therefore, to ensure a certain weld length, higher workpiece dimension has to be considered and post welding operation has also to be carried out, both these increase production cost.

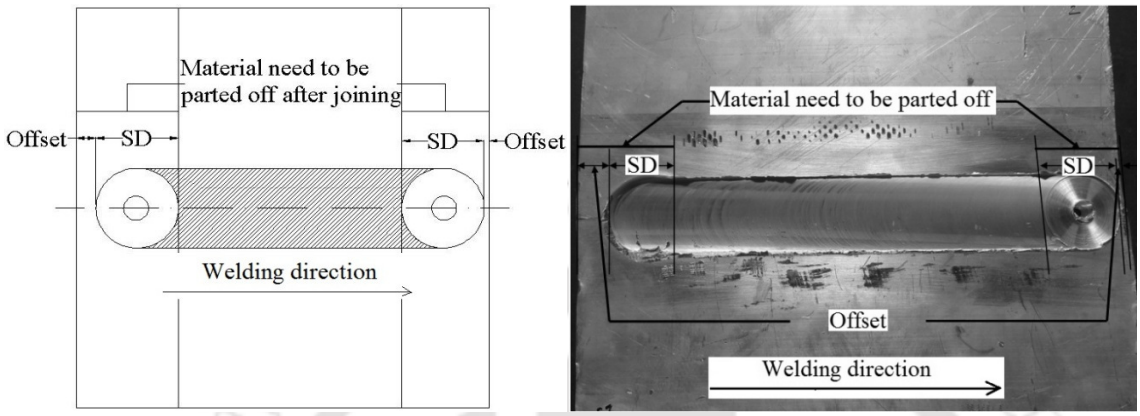

(a) (b)

Figure 5.1 (a) Schematic diagram of welding by usual practice and (b) welded plate

The above mentioned offsets are provided to avoid outward material flow at both the positions. It occurs when the welding starts and finishes exactly by aligning the tool shoulder with the starting and ending edges of the workpiece material as shown in **Fig. 5.2(a)**. The material deformation occurs due to the movement of some volume of plasticized material from the weld zone. **Figure 5.2(b)** shows the as welded image of outward material flow. Other major limitation of the process is the end hole remains at the end of the joint. The end hole at the end of the weld is due to the removal of the FSW tool from the workpiece as the final step of welding, leaving a hole of diameter equal to tool pin. Altogether the above discussed issues reduce the joint length leading to wastage of material.

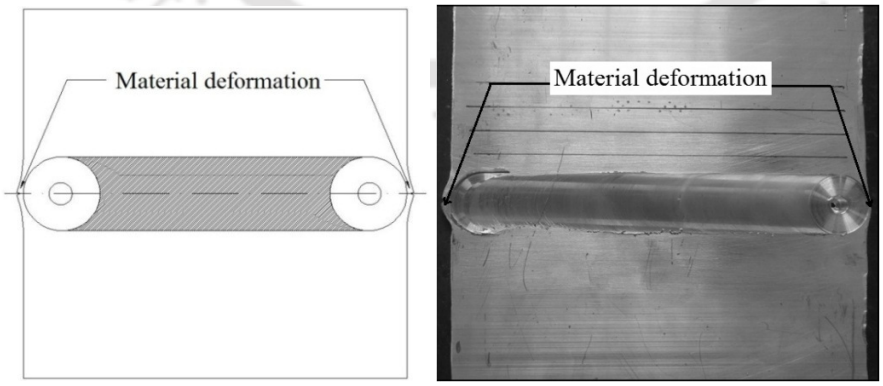

(a) (b)

Figure 5.2 (a) Schematic diagram of material deformation at start and end and (b) image of welded specimen with edge deformations

Several possible ideas or experimental cases were prepared methodically to find out an appropriate starting location and eliminate the end hole, which are described below in details. The process parameters considered for studying these cases are presented in **Table 5.1**.

Table 5.1 Parameters Settings Used in the Experiments

Parameters	Value
Plunging Depth (mm)	0.09
Tool Rotational Speed (rev./min)	1100
Welding Speed (mm/min)	98
Tool Geometry	Threaded straight cylindrical pin with flat shoulder as shown in **Fig. 5.3**
Shoulder Diameter (mm)	25
Pin Diameter (mm)	7
Dwell Time (sec)	15

Figure 5.3 FSW tool

Case-1

This is regular practice for carrying out FSW at the usual start and stop positions as shown in **Fig. 5.1**. In this case some offset distance was provided both at the starting and ending of the joint. It avoids material deformation at both the ends or edges. This case is considered as reference to compare all other considered cases.

Case-2

In this case the welding was started and stopped exactly by aligning the tool shoulder with the starting and ending edges of the workpiece. It is shown in **Fig. 5.4**. This case was carried out without any restriction at the starting and end faces of the workpiece.

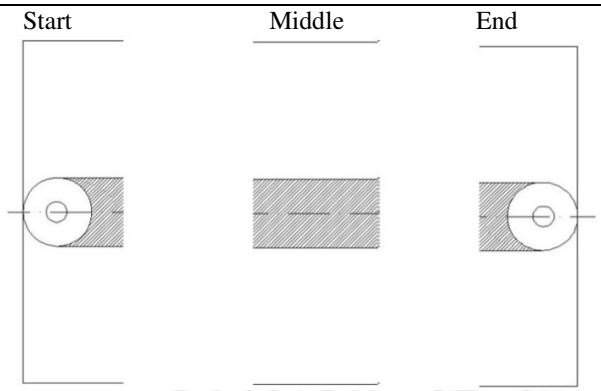

Figure 5.4 Case-2

Case-3

The welding was started and stopped exactly by aligning circumference of the tool pin with the starting and ending edges of the workpiece material. No restriction was provided either at the start or at the end of the weld as shown in **Fig. 5.5**.

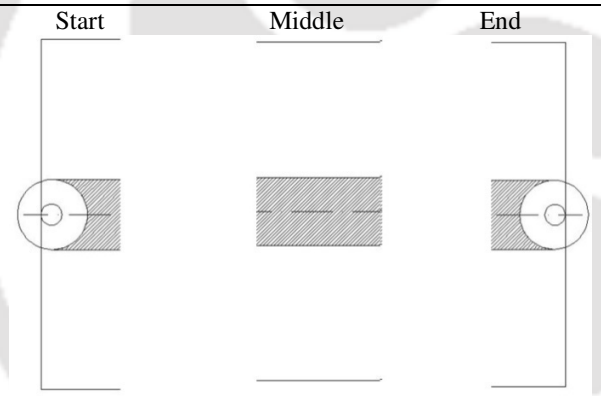

Figure 5.5 Case-3

Case-4

This includes implementation of restriction both at the start and end of the weld. The plates used for restriction are made of mild steel having slightly lesser thickness than the workpiece material. Again the tool shoulder was aligned with the starting and ending edges of the workpiece material as shown in **Fig. 5.6**. The restrictions are maintained in such a way that there should not be visible air gap between the mild steel and aluminium plates both at the start and end.

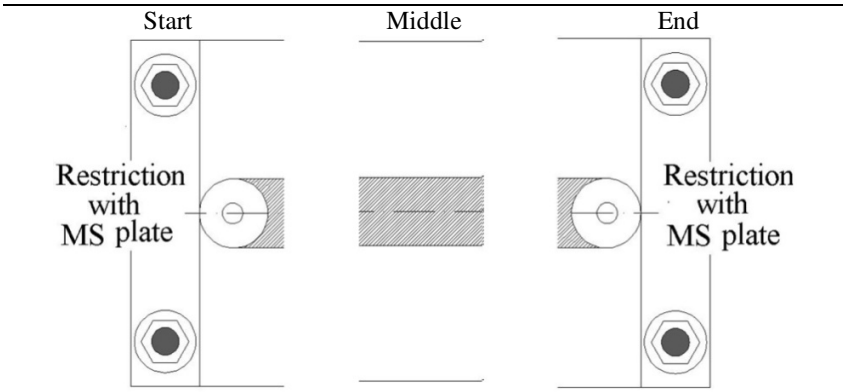

Figure 5.6 Case-4

Case-5

Same restriction was provided as of Case-4. The welding neither be started nor ended by exactly aligning the circumference of the tool pin with the edges of the workpiece material. This may lead to tool wear by rubbing with the restriction plate. So the welding was started and stopped at a distance of 1 mm away both from the starting and ending edges of the workpiece material as shown in **Fig. 5.7**.

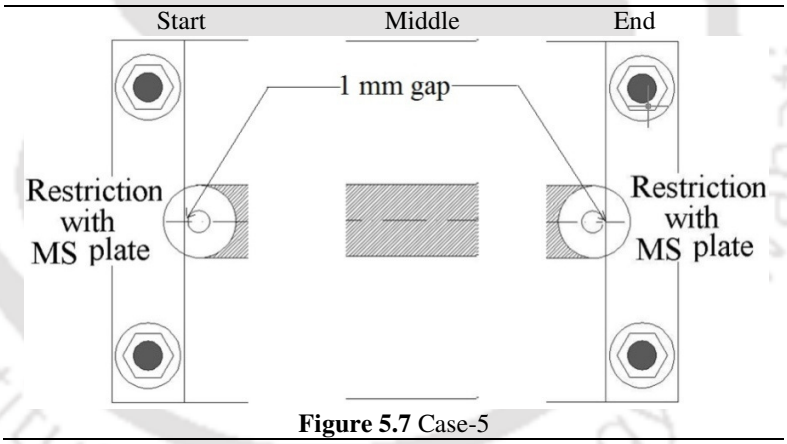

Figure 5.7 Case-5

Case-6

In this case two slots were provided, one at the start and another at the end of the plates. The slots were made in the restriction plates. The size of the slots is slightly higher than the tool pin diameter and packed with aluminium powder. The welding was carried out from the starting slot to the end slot. The detail arrangement is shown in **Fig. 5.8**.

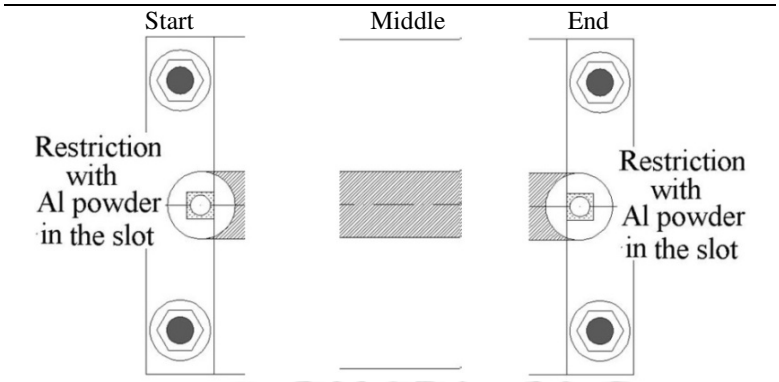

Figure 5.8 Case-6

Case-7

In this case, all the arrangements are similar to Case-6 except the aluminium powder in the slots was replaced by solid rectangular aluminium blocks as shown in **Fig. 5.9**. The blocks were fitted in the slots in such a manner that there was no visible air gap between the side walls of the slot and aluminium blocks.

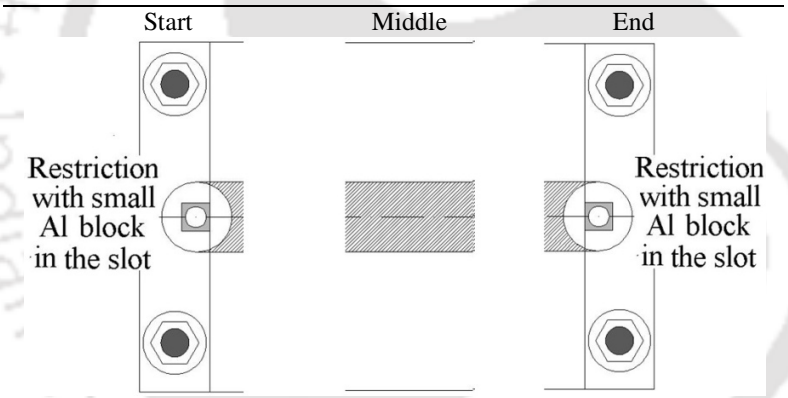

Figure 5.9 Case-7

Case-8

In this case the starting condition was kept the same as in Case-7. But the lengths of the end slot as well as the aluminium block were increased as shown in **Fig. 5.10**. This is in view to move the tool completely outside the workpiece.

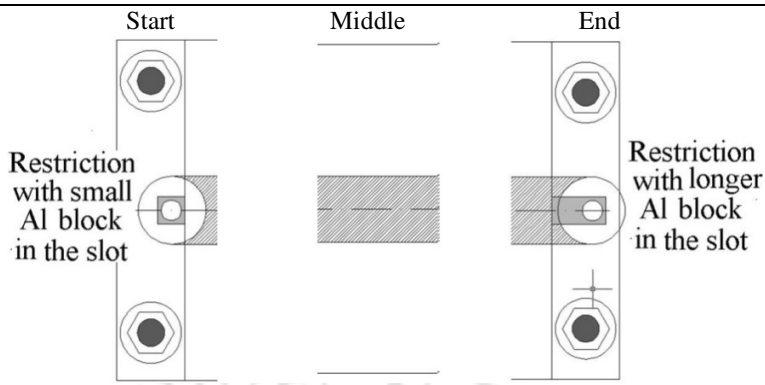

Figure 5.10 Case-8

Case-9

In this case solid aluminium pieces were provided at the start and end of the plates. These pieces act as the restricting plate and the size of the pieces are larger than the size of the tool shoulder with thickness same as the workpiece thickness. Also the tool pin was aligned with the start and end edges of the workpiece in such a way that the pin will be outside the workpieces. The complete arrangement is shown in **Fig. 5.11**. Instead of stopping the tool exactly at the interface of tool pin circumference and outside edge of the workpiece it has been moved slightly some distance away. This is to avoid the chance of formation of minute defects at the trailing side of the end hole as shown in **Fig. 5.23(b)**.

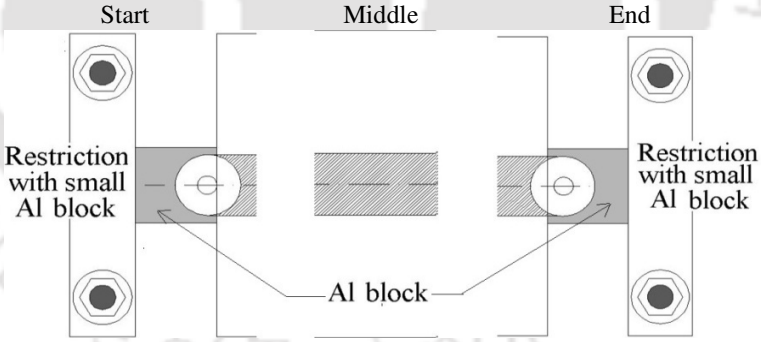

Figure 5.11 Case-9

Case-10

All the arrangements are similar to Case-9 except the tool shoulder was aligned with the start and end edges of the workpiece in such a way that the complete tool shoulder will be outside the workpieces as shown in **Fig. 5.12**.

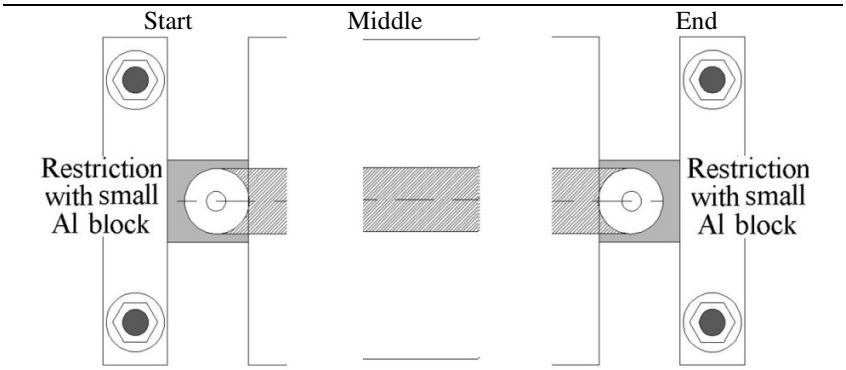

Figure 5.12 Case-10

Case-11

This case also includes the restriction of workpieces by means of aluminium pieces at both the ends. But the size of the plates is bigger than the previous case. Also the welding operation was started and stopped at some distance away from the edges of the workpiece. The complete arrangement is shown in **Fig. 5.13**.

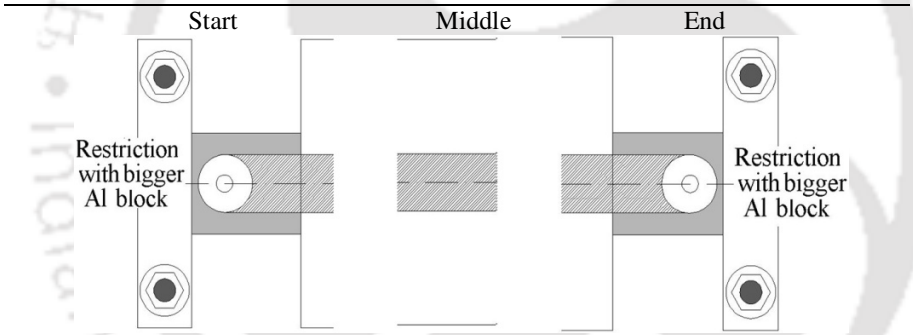

Figure 5.13 Case-11

In addition to the above mentioned 11 cases some more experimental cases were considered. These are the extended cases of Case-5 in which the distance of the tool pin circumference from the start edge of the workpiece was varied from 2 mm to 7 mm (Case-12 to Case-17). This is to check the optimum distance of the tool pin circumference from the start edge of the workpiece that can be considered for good joining.

The workpieces to be joined were rigidly clamped to completely restrict its movement under both plunging and translational forces of the FSW tool. The tool rotation speed and traverse speed of the bed were set prior to each experimental run. For temperature measurement an Infrared (IR) camera was used. The specifications are given in Chapter 4, Section 4.2.5. Before welding the camera was mounted in an appropriate location to capture

thermal images. The complete experimental setup with IR camera is shown in **Fig. 5.14**. From each welded sample three tensile specimens were prepared one from the start, one at the middle and one at the end of the weld as shown in **Fig. 5.15**. The tensile specimens were prepared as per the ASTM E8 guidelines, details are given in Chapter 4, Section 4.2.6. The temperature histories at a distance of 20 mm away from the joint line in the advancing side (shown in **Fig. 5.15**) were also recorded for all the three positions. Each experiment was repeated two times to minimize the experimental error.

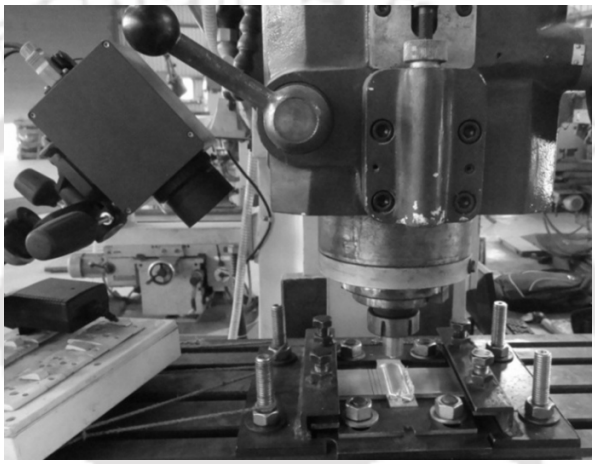

Figure 5.14 Experimental set up with IR camera.

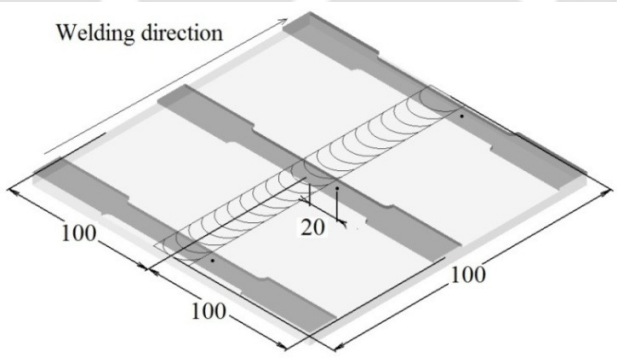

Figure 5.15 Schematic diagrams of position of specimen extraction for tensile tests (All the above mentioned dimensions are in mm)

5.3 Results and Discussions

The appearance of weld bead at the start and end portion of the joint for different cases are shown in **Table 5.2**. The weld beads of extended cases of Case-5 are shown in **Table 5.3**. Being the usual practice there was no outward material flow for Case-1 both at start

and end. This is shown in **Fig. 5.16(a)** and **(b)**. For Case-2 and Case-3 as no restriction was provided the plasticized material tends to flow out from the weld zone both at the start and end position as shown in **Figs. 5.17-18**. Case-4 and Case-5 are similar to Case-2 except being provided with restrictions both at start and end of the weld. So the outward material flow at start and end portion is at the top surface only. It is shown in **Figs. 5.19-20**. For Case-6 to Case-8, slots of different sizes are provided in the restriction plate both at start and end. In all these cases welding was started and finished outside the workpiece material. It can be seen from **Figs. 5.21-23** that in all the three cases there were material flashing at the surface level as the shoulder of the rotating tool tries to push the plasticized material behind the tool. Case-9 showed defect free weld on visual basis both at start and end position which can be seen from **Fig. 5.24**. Cases-10 and 11 showed defects particularly at the transition portions between the extra material and workpiece both at the start and end part of the joint. These are showed in **Figs. 5.25-26**.

Table 5.2 Weld Bead Appearance for Different Cases

Cases	**Weld bead appearance**	
	Start portion of the weld	**End portion of the weld**
Case-1	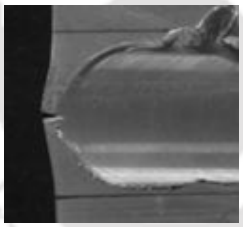	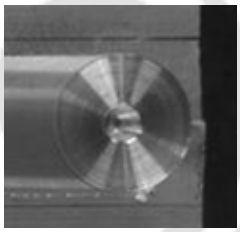
	Figure 5.16 (a) Start	**Figure 5.16** (b) End
Case-2	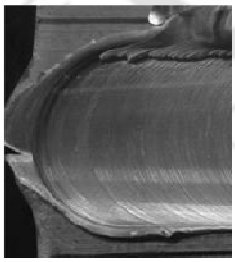	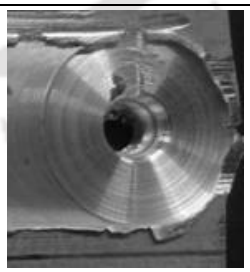
	Figure 5.17 (a) Start	**Figure 5.17** (b) End

Case-3

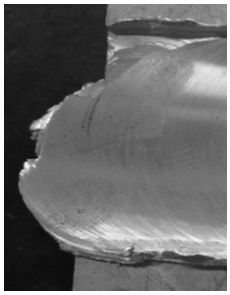

Figure 5.18 (a) Start (top)

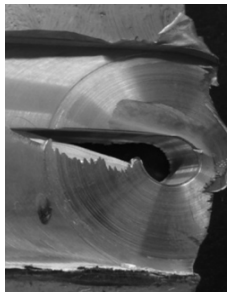

Figure 5.18 (b) End (top)

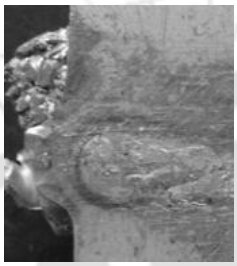

Figure 5.18 (c) Start (bottom)

Figure 5.18 (d) End (bottom)

Case-4

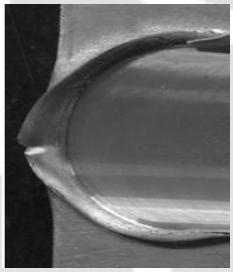

Figure 5.19 (a) Start

Figure 5.19 (b) End

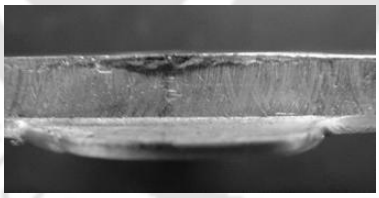

Figure 5.19 (c) Start (side)

Figure 5.19 (d) End (side)

Case-5

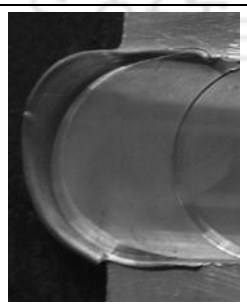

Figure 5.20 (a) Start

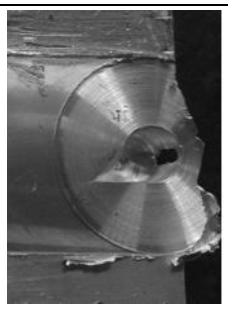

Figure 5.20 (b) End

Case-6

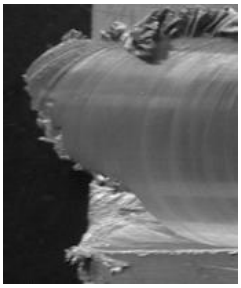

Figure 5.21 (a) Start

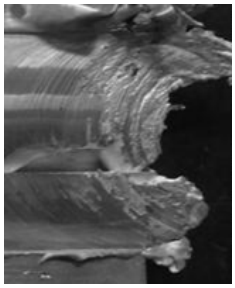

Figure 5.21 (b) End

Case-7

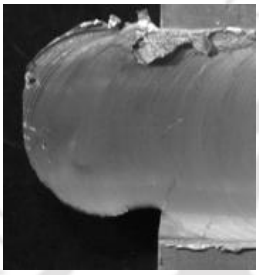

Figure 5.22 (a) Start (top)

Figure 5.22 (b) End (top)

Figure 5.22 (c) Start (bottom)

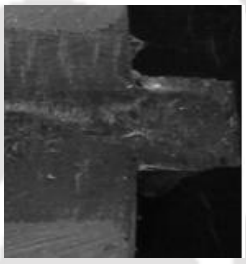

Figure 5.22 (d) End (bottom)

Case-8 -

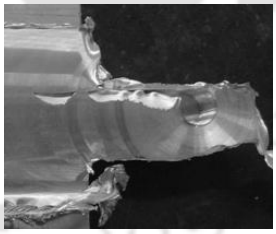

Figure 5.23 (a) End (top)

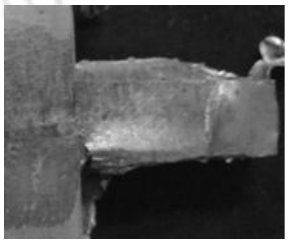

Figure 5.23 (b) End (bottom)

Case-9	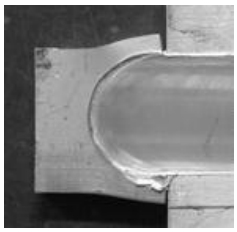 **Figure 5.24** (a) Start	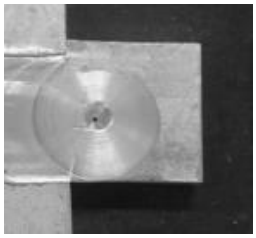 **Figure 5.24** (b) End
Case-10	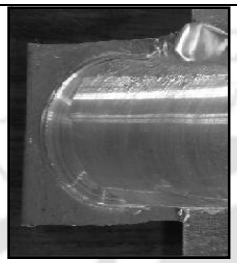 **Fig. 5.25(a)** start	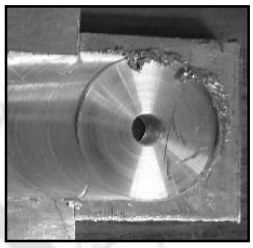 **Fig. 5.25(b)** end
Case-11	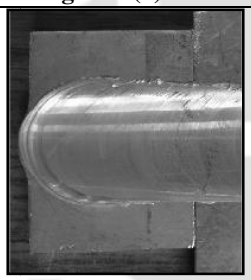 **Fig. 5.26(a)** start	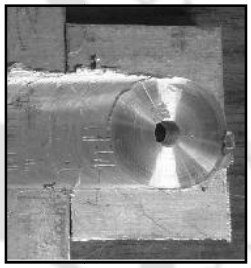 **Fig. 5.26(b)** end

Table 5.3 Weld Bead Appearance for Extended Cases of Case-5

Weld Bead Appearance at Start		
Case-12	Case-13	Case-14
 **Figure 5.27** Start	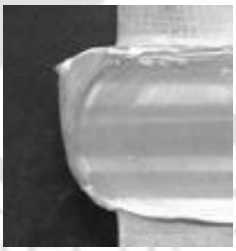 **Figure 5.28** Start	 **Figure 5.29** Start
Case-15	Case-16	Case-17
 **Figure 5.30** Start	 **Figure 5.31** Start	 **Figure 5.32** Start

Each experimental case was repeated two times and the average tensile properties (ultimate tensile strength, yield strength and ductility) at three different positions namely, start, middle and end of the joint are given in **Table 5.4-5.6**. From the tested joints, it was seen that for usual practice i.e. Case-1 the presence of offset distance at both start and end locations lowers the weld strength at the respective positions. As the workpiece materials within the offset distance are not plasticized by the joining process, the strengths are low in these regions. Due to absences of restrictions for both Case-2 and Case-3 the plasticized material at start and end edges escape from the weld region as shown in **Fig. 5.17(a-b)** and **Fig. 5.18(a-d)**, respectively. It leads to defect at both the positions with an additional keyhole at the end. Therefore in these two cases, the strengths at the start and end of the joint were low. From the recorded temperature data as shown in **Fig. 5.33(a)**, it can be seen that the peak temperature at the start position is little lower in Case-1 compared to other two cases due to the presence of offset distance. But the thermal histories at the end position shown in **Fig. 5.33(b)** are almost similar.

Table 5.4 Measured Ultimate Tensile Strength at Different Positions of a Joint for Different Cases

Cases	Start			Middle			End		
	Trial 1	**Trial 2**	**Avg.**	**Trial 1**	**Trial 2**	**Avg.**	**Trial 1**	**Trial 2**	**Avg.**
Case-1	54.21	43.65	48.93	139.15	129.25	134.2	51.09	43.21	47.15
Case-2	25.29	31.37	28.33	135.58	139.26	137.42	29.04	35.74	32.39
Case-3	36.6	30.46	33.53	140.41	137.11	138.76	11.62	6.7	9.16
Case-4	97.38	84.88	91.13	134.73	144.67	139.7	77.8	89.92	83.86
Case-5	136.42	145.28	**140.85**	138.9	144.62	141.76	59.19	48.95	54.07
Case-6	55.18	63.8	59.49	81.6	97.66	**89.63**	25.1	17.44	21.27
Case-7	92.48	110.6	101.54	131.81	133.09	132.45	103.88	109.48	106.68
Case-8	101.86	106.56	104.21	139.59	129.85	134.72	100.03	94.31	97.17
Case-9	132.7	129.84	**131.27**	130.25	134.39	132.32	127.4	137.5	**132.45**
Case-10	138.19	133.52	**135.85**	137.80	134.01	135.09	142.74	129.98	**136.36**
Case-11	123.09	140.37	**131.73**	135.20	129.23	132.26	137.62	138.10	**137.86**
Extended cases of Case-5									
Case-12	144.19	138.45	141.32						
Case-13	135.95	141.23	138.59						
Case-14	138.27	142.53	140.4						
Case-15	140.97	131.61	136.29						

Case-16	100.5	105.7	103.1
Case-17	94.22	107.58	100.9

Table 5.5 Measured Yield Strength at Different Positions of a Joint for Different Cases

Cases	Start			Middle			End		
	Trial 1	**Trial 2**	**Avg.**	**Trial 1**	**Trial 2**	**Avg.**	**Trial 1**	**Trial 2**	**Avg.**
Case-1	45.12	37.05	41.08	69.73	74.00	71.87	41.02	39.87	40.44
Case-2	22.35	24.95	23.65	78.14	67.92	73.03	22.88	27.34	25.11
Case-3	24.01	27.04	25.52	70.01	77.01	73.51	5.26	8.19	6.73
Case-4	59.84	52.80	56.32	68.95	78.76	73.85	47.95	59.44	53.69
Case-5	71.42	77.11	**74.27**	66.91	82.28	74.60	39.34	46.54	42.94
Case-6	41.19	48.61	44.90	58.60	52.96	**55.78**	20.01	16.19	18.10
Case-7	62.95	57.20	60.08	71.08	71.39	71.23	61.80	62.06	61.93
Case-8	66.81	55.27	61.04	68.51	75.59	72.05	60.94	56.06	58.50
Case-9	72.14	69.48	**70.81**	70.13	72.25	71.19	72.55	69.91	**71.23**
Case-10	69.58	73.27	**71.42**	74.30	70.51	72.40	63.91	74.45	**69.20**
Case-11	66.20	70.01	**68.12**	72.87	77.05	74.96	75.50	70.10	**72.80**
Extended Cases of Case-5									
Case-12	74.99	73.88	74.44						
Case-13	70.91	75.99	73.45						
Case-14	68.43	79.78	74.10						
Case-15	78.79	66.45	72.62						
Case-16	60.01	61.27	60.64						
Case-17	54.64	65.05	59.84						

Table 5.6 Measured Ductility at Different Positions of a Joint for Different Cases

Cases	Start			Middle			End		
	Trial 1	**Trial 2**	**Avg.**	**Trial 1**	**Trial 2**	**Avg.**	**Trial 1**	**Trial 2**	**Avg.**
Case-1	4.65	6.27	5.46	12.89	13.77	13.33	3.98	5.01	4.50
Case-2	2.95	3.66	3.30	11.99	11.42	11.71	5.28	7.25	6.27
Case-3	5.17	5.56	5.37	10.87	14.14	12.51	6.21	8.3	7.25
Case-4	8.002	7.70	7.85	14.68	14.00	14.34	5.99	7.79	6.89
Case-5	15.24	14.80	**15.00**	12.90	16.04	14.47	4.90	7.70	6.30
Case-6	3.02	4.92	3.97	8.219	7.602	**7.911**	1.99	2.52	2.25
Case-7	7.68	9.12	8.40	12.05	10.39	11.22	5.88	7.20	6.54
Case-8	7.01	8.22	7.62	14.29	16.5	15.40	8.89	9.00	8.94

Case-9	12.59	12.3	**12.5**	13.03	10.98	12.00	12.00	10.4	**11.2**
Case-10	14.18	11.59	**12.89**	10.69	13.52	12.10	9.76	12.23	**10.99**
Case-11	13.03	11.31	**12.17**	11.78	15.61	13.70	11.42	14.10	**12.76**
Extended Cases of Case-5									
Case-12	14.19	16.50	15.30						
Case-13	14.86	13.30	14.10						
Case-14	15.99	16.70	16.40						
Case-15	15.01	20.1	17.6						
Case-16	14	15.4	14.7						
Case-17	7.01	5.72	6.36						

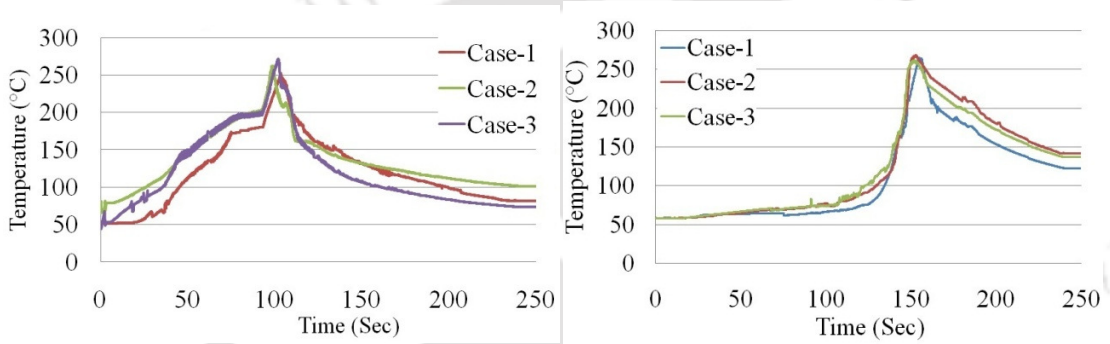

(a) (b)

Figure 5.33 Thermal histories at (a) start and (b) end position of the joints for Case-1 to 3

As the restriction was provided both for Case-4 and Case-5, the plasticized material could not escape from the weld zone which can be seen in **Figs. 5.19 (c)** and **(d)**. Due to less material flows out, sufficient heat generation and proper material mixing the strength at the starting portion of the joint in Case-5 was good. Although, the material flashing was low and heat generation was slightly higher in Case-4 as compared to Case-5, the strength of the starting portion was low. This is because in Case-4, the welding was started by aligning the periphery of the tool shoulder with the starting edge of the workpiece, which mixes the material in the surface level only. The material mixing in the thickness direction was inadequate. The strength of the end part in both the cases was poor due to improper material mixing and the presence of keyhole. The recorded thermal histories at start and end positions are shown in **Fig. 5.34 (a)** and **(b)** respectively. The plot showed almost equal trend.

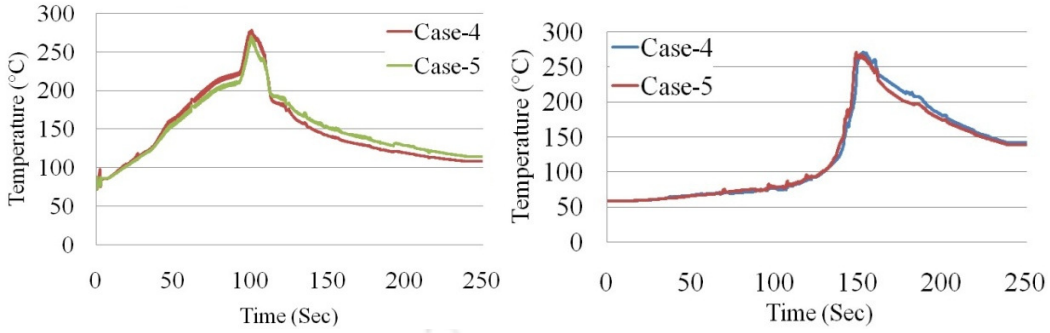

Figure 5.34 Thermal histories at (a) start and (b) end position of the joints for Case-4 and 5

The next three cases (Cases 6, 7 and 8) are based on starting and stopping of the process outside the workpiece material. The welding was started in a slot provided in the restriction plate and filled with aluminum (Al powder for Case-6 and Al blocks for Case 7 and 8). Similar provisions were provided at the end position except for Case-8 in which the length of the block was more. In Case-6 it was seen that the Al powder in the slot tried to come out both at the start and end of the joint. Specifically it was more at the starting point due to the plunging of the rotating tool. This leads to lesser heat generation and inadequate material availability at the start as well as at the end of the joint which leads to poor weld strength at both the ends. Also due to inadequate heat generation, defect formation starts lowering the strength at the middle portion of the joint. In Case-7 and Case-8 the Al powder was replaced by small rectangular Al blocks in a view to improve the heat generation and material availability. The sizes of the blocks were slightly bigger than the size of the tool pin. These rectangular blocks were of same size at the start for both the cases but smaller and longer at the end for Case-7 and Case-8, respectively. The thermal histories recorded at start and end positions of Case-6 to Case-8 are shown in **Fig. 5.35 (a)** and **(b)** respectively. Though in both the cases the weld strength was improved but due to the outward material flow at the surface levels both at the start and end, weld strength was lower than the middle portion. This is due to the flashing out of material around the open spaces available at the start and end other than the size of the block. These open spaces are available at start and end because the tool was plunged into a material which size is just larger than the tool pin diameter. The temperature plots at middle position of the joints for all the cases from Case-1 to Case-11 are shown in **Fig. 5.35 (c)**. From the plot it can be seen that except Case-6 all other cases

peak temperature variation was not noticeable. Due to the lack of material availability both at the start and end the heat generation was less for Case-6.

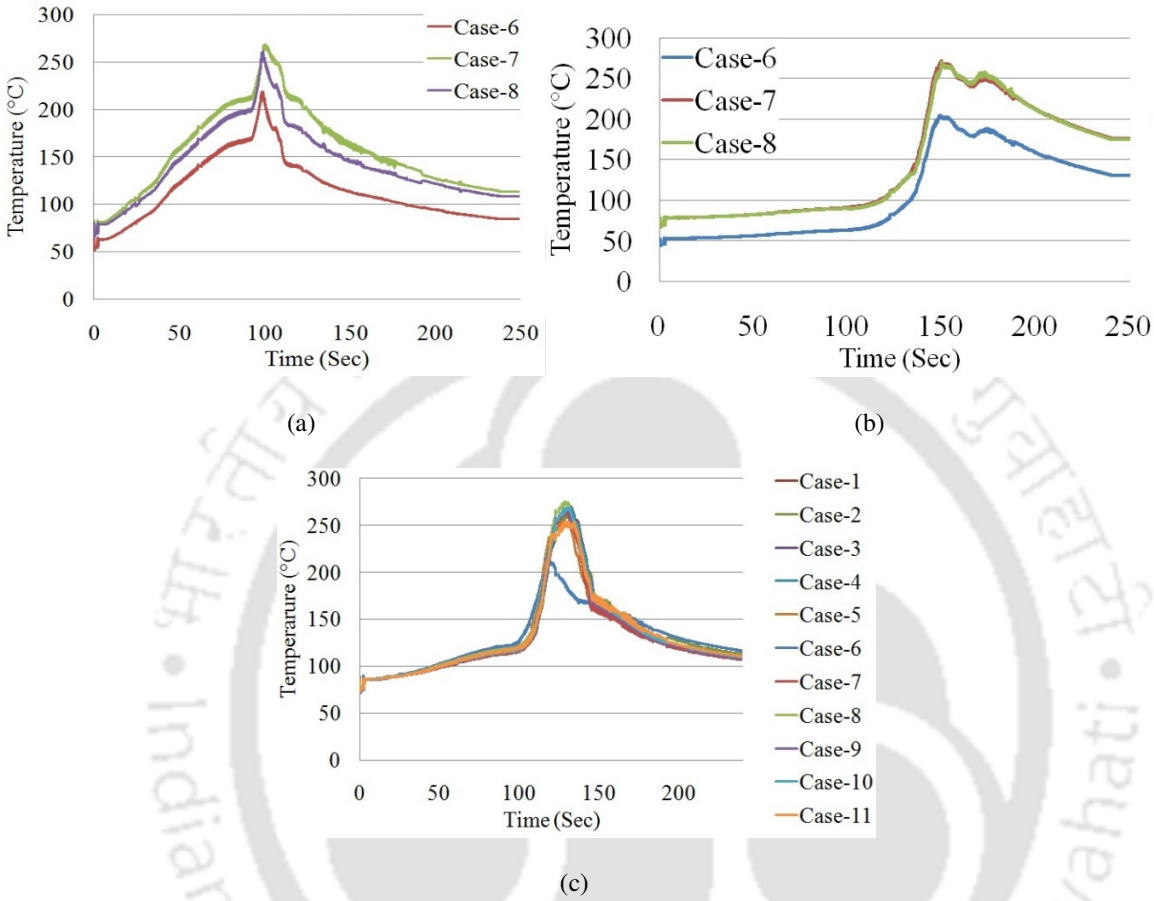

Figure 5.35 Thermal histories at (a) start, (b) end position of the joints for Case-6 to 8 and (c) mid position of the joints for Case-1 to 11

For Case-9 and Case-10 the size of the rectangular Al blocks were increased from tool pin size to slightly bigger than the size of the shoulder. Case-9 was found to be another appropriate condition to start the process. In this case the end part of the joint is also having good weld strength. The process was started by aligning the periphery of the tool pin with the starting edge of the workpiece in such a way that the tool pin will be outside the workpiece. Only the tool pin was moved by a little distance from the end edge keeping the shoulder above the transition zone (from base plate to run-off plate). This results in adequate amount of heat generation and the material at the end of the joint gets sufficient time to mix. Also for both the Case-10 and Case-11 the joint strength was found to be adequate at start as

well as at the end of the welding. But particularly for these two cases the matching surface preparation both for the workpiece and the tab material is an important issue. All the matching surfaces should be machined and polished by emery paper thoroughly. Also there must not be any visible air gap present between the matching surfaces of the workpiece and tab material at start and end positions. The presence of gap may lead to the formation of defects particularly at the transition positions at start and end. Because the tool enters and exits the workpiece in the rotation condition for both the above cases. From **Fig. 5.36 (a)** it can be seen that the heat generation at start position is almost constant for three cases. But at end the temperature in Case-9 is slightly higher than the two other cases as shown in **Fig. 5.36 (b)**. This is due to stopping the joining process when the tool was at the transition zone itself.

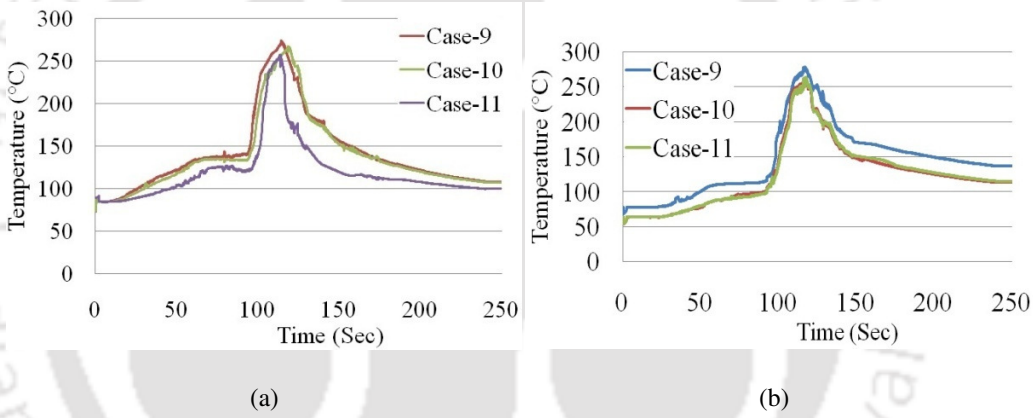

Figure 5.36 Thermal histories at (a) start and (b) end position of the joints for Case-9 to 11

From the aforementioned case studies (Case 2 to Case 11), it is found that only Case 5 and Case 9 give almost equal weld strength to that of middle part of the joint. Therefore, any of these two cases can be considered as an appropriate starting condition. In Case 9, a solid aluminium block is used as restricting plate which became integral part of the workpiece. After the welding the block has to be separated from the workpiece using some machining operation. Both the use of aluminium block and separation from the workpiece will increase production time and cost. Therefore, Case 5 is relatively better as a starting condition. In Case 5, the circumference of the tool pin was aligned with the edge of the workpiece material. In order to find out the range of exact starting location that can be considered for Case-5, six more cases (Case-12 to Case-17) were investigated. These cases are considered to check whether there is any flexibility to choose a starting location. In Case-12 to Case-17, the

welding was started at a distance varying from 2 mm to 7 mm from the starting edge in an increment of 1 mm, respectively. The thermal plots are shown in **Fig. 5.37 (a)**. From the tensile test data, given in **Table 5.4**, it can be seen that up to a distance of 5 mm from the starting edge of the workpiece to the tool pin circumference, the joint strength is adequate. Then the strength decreases as shown in **Fig. 5.37 (b)**. This is due to inadequate material plasticization at the starting edge.

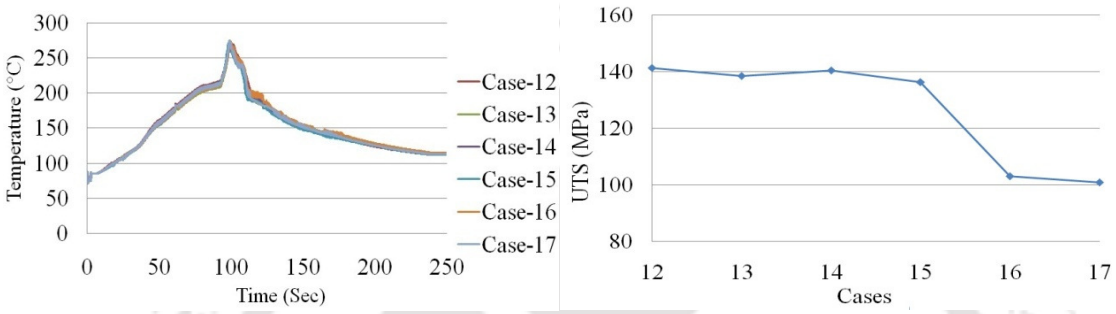

(a) (b)

Figure 5.37 (a) Thermal histories and (b) strengths at start for Case-12 to 17

5.4 Observations

The following observations have been made from the above experimental studies.

- From the experimental results it was seen that both Case-5, 9, 10 and 11 can be implemented to resolve the starting position issue. Case-9 to 11 can be used for elimination of end hole type of defect.
- Out of all the cases, Case-9 was found to be the better approach to overcome the end hole limitations in FSW. Because though insignificant but the tab size and the welding time can be reduced in Case-9 as compared to Case-10 and 11.
- The thermal histories at the middle of the joints showed similar trend except in Case-6 which was a defective joint. Case-6 was also shown a lesser heat generation at both start and end position.
- The appropriate distance from which the welding can be started was found to be from 1 mm to 5 mm, beyond which the joint strength diminishes. It was found that the starting issue can be resolved only by providing a proper restriction without adding any extra material.

- This can eliminate post welding machining work and material wastage. The end hole can be eliminated by providing a small rectangular piece with a size of bigger than the shoulder diameter and by moving the tool pin at some distance away from the end edges of the workpiece.

5.5 Major Findings

From the above experimentation and results following major conclusions can be made:

a) The welding can be started with in a distance of 1 mm to 5 mm from the starting position in a view to use the start portion as a joint beyond which the joint quality diminishes. So the starting issue can be resolved only by providing a proper restriction without adding any extra material which can eliminate post welding machining work and material wastage.

b) The end hole limitation can be solved by providing a small rectangular piece of size bigger than the tool shoulder diameter. This can be achieved by moving the tool pin at some distance away from the end edges of the workpiece.

Chapter 6

Modeling of FSW Process

6.1 Introduction

During FSW heat is generated by friction between the tool and the work-piece which results in intense plastic deformation and temperature increase within and around the stirring zone. Due to this a significant microstructural evolution, including grain size, grain boundary character, dissolution and coarsening of precipitates, breakup and redistribution of dispersoids, and texture takes place. To study the FSW process researchers developed and used a numbers of different models namely regression models, thermo mechanical and mathematical models, surrogate, restoring and computational fluid dynamics (CFD) models. A detailed literature review on modeling of FSW process is given in Chapter 2, Section 2.5.3.

It has been seen that current FSW process sub-models are complex, time consuming and difficult to use in real time. And also they all suffer from lack of reliability of the predicted results. This is because the physics is highly complex and the current phenomenological models do not contain any model component designed to ensure a good agreement with experimental results. Apart from using physical knowledge to derive or build a model, one could also apply numerical interpolation or approximation of discrete data. The models resulting from these techniques are called black box models. A very important advantage of black box modeling techniques is that one can in principle obtain a quasi-static model of any

required accuracy by providing a sufficient amount of (sufficiently accurate) discrete data and without any physical knowledge of the process. One of the most popular black box modeling techniques is ANN. But the use of ANN models for FSW process is very rare. Therefore in the present work, a multilayer feed-forward neural network with back propagation training algorithm, commonly known as back propagation neural network (BPNN), and radial basis function network (RBFN) have been used for modeling of FSW process.

6.2 Artificial Neural Network

Artificial neural network is a biologically inspired computational method useful in a variety of real-world application. It deals with complex and highly interactive processes, like pattern recognition, speech recognition, finance, medicine, sales forecasting, weather forecasting, and monitoring and control of manufacturing processes. ANN's important characteristics include a number of processing elements called neurons which is used to determine input output relationships of a complex process, its generalization and learning ability (by which it produces reasonable outputs for inputs not encountered during learning), distributed computation and adaptability, intrinsic relative information processing and low energy consumption. For modeling of weld quality different types of ANN can be used, namely BPNN, RBFN, self-organizing map (SOM), etc. In the present work, computer programs for BPNN and RBFN models are developed using 'C' programming language for modeling of FSW process.

6.3 Back Propagation Neural Network

Depending upon the direction of information flow ANNs can be divided into two categories: (i) feed-forward and (ii) feed-back (or recurrent) networks. In the first one the information is passed into one direction starting from the input layer towards the output layer through the hidden layers without forming any cycle or loop. Whereas in the second case information is passed in both the directions namely feed-forward and feed-back. Typically, the multilayer neural network consists of a set of input neurons that form the input layer, one or more numbers of hidden layers of computational neurons and an output layer of computational neurons. Two types of passes exist in back propagation learning, which is most commonly used to train ANN models. In the first one i.e. forward pass the

information is received by the input layer from an external source, which is subsequently multiplied by the interconnection weights between it and the adjacent hidden layer. Then the products are summed up and modified by an activation function. These values become the output signal for the first hidden layer and subsequently the input signal for the next layer. Finally the signal reaches the output layer, where it is terminated at the external receptor node(s). The interconnection weights are updated by the error-correction delta rules based on the gradient descent search method during the backward pass. These two passes are repeated until a desired level of training of the network is achieved. The basic structure of the multilayer neural network and the back propagation learning algorithms used in this work are explained in the following subsections.

6.3.1 Structure of BPNN

Figure 6.1 shows a schematic representation of a fully connected multi-neuron, multi-layer ANN architecture. The network consists of three layers a) an input layer with L_I number of input neurons/parameters, b) a hidden layer with L_H number of hidden neurons and c) an output layer with L_O number of output neurons/parameters. As the network is fully connected type so all the neurons of a layer are connected to all the neurons in the adjacent layers. The activation function used in the hidden and output layers is chosen as a logistic sigmoid function. In the diagram (**Fig. 6.1**), Y_i is the i^{th} input data to the input layer, O_i is the output of i^{th} neuron of the output layer, V_{ij} is the connection weight between the i^{th} input neuron and the j^{th} hidden neuron, W_{jk} is the connection weight between the j^{th} hidden neuron and the k^{th} output neuron, b_H is the bias at the hidden layer, b_O is the bias at the output layer.

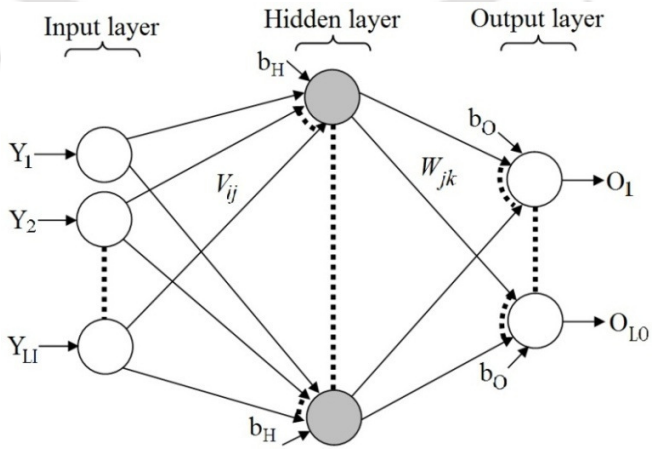

Figure 6.1 A schematic diagram of a back propagation neural network

6.3.2 BPNN Model Development Steps

The development procedure for BPNN model consists following steps:

STEP-1: **Definition**

The architecture of the network is defined in terms of the values for L_I, L_H and L_O. Among the three, L_I and L_O values are fixed for a particular problem. L_H is an integer value and can be varied. Then values of the learning rate (η), the momentum co-efficient (α) and an activation function (logistic sigmoid in the present work) are assigned. Learning rate and momentum coefficient are chosen in the range of 0.05 to 0.95.

STEP-2: **Initialization**

In this step the weights and biases are initialized. The connection weights V_{ij} and W_{jk} are randomly initialized between -0.9 to +0.9, with the biases b_H=b_O=1.

STEP-3: **Presentation of the training patterns**

The process of network modification by updating its weights, biases and other parameters, if any is known as training. The training may be in sequential mode or batch mode. In sequential mode the network is modified utilizing the training scenarios sent one after another in a sequence. In batch mode which is used for network training in the present work, the whole training data set consisting of a large number of scenarios, is passed through the network and an average error in predictions is determined. Then it is propagated back to update the weights and bias values of the network so that it can predict more accurately.

STEP-4: **Normalization of the dataset**

To train a neural network model sometimes the raw training data is required to be scaled in which the range of target values is constrained to remain within the range of activation function. In this case logistic sigmoid function is used which is given by,

$$S(y) = \frac{1}{(1+e^{-ay})} \tag{6.1}$$

where, a is constant and y is the input to the activation function S. For a BPNN model with above mentioned activation functions, the target value must be within, say, [0.1 to 0.9], instead of the usual range [0, 1] as it maps the range of y to [-∞,∞]. It prevents the algorithm from driving some of the connection weights to infinity and thus slowing down the training process. The range of each input is linearly scaled to the range of the activation function. This allows the connection weights to have the same magnitude. So, the input and output parameters for all the datasets are normalized in the range of 0.1 to 0.9 as follows:

$$y_{norm} = 0.1 + 0.8\left(\frac{y - y_{max}}{y_{max} - y_{min}}\right) \tag{6.2}$$

where, y_{max} and y_{min} are the maximum and minimum values of any parameter in the dataset under consideration, y is the actual value of the parameter and y_{norm} is the corresponding normalized value.

STEP-5: **Forward pass**

After applying the activation function to the weighted sum from a neuron the output from it can be calculated and this becomes the input for the next layer. The same process can be carried out for each hidden node and then output node. The output from the j^{th} hidden neuron and k^{th} output neuron for p^{th} pattern is calculated using the following equations:

$$O_{jH}^{p}(n) = \frac{1}{1+exp\left\{-\left(\sum_{i=1}^{L_I} V_{ij}(n) Y_i^p + b_H\right)\right\}} \tag{6.3}$$

$$O_{kO}^{p}(n) = \frac{1}{1+exp\left\{-\left(\sum_{j=1}^{L_H} O_{jH}^{p}(n) Y_i^p + b_O\right)\right\}} \tag{6.4}$$

where, $O_{jH}^{p}(n)$ is the output of j^{th} hidden neuron for p^{th} pattern at the n^{th} iteration, $O_{kO}^{p}(n)$ is the output of k^{th} output neuron for p^{th} pattern at the n^{th} iteration, V_{ij} is the connection weight between the i^{th} input neuron and the j^{th} hidden neuron at the n^{th} iteration, W_{jk} is the connection weight between the j^{th} hidden neuron and the k^{th} output neuron at the n^{th} iteration, Y_i^p is the value of the i^{th} input neuron for the p^{th} pattern.

STEP-6: **Error calculation**

By comparing the calculated output from the k^{th} output neuron $O_{kO}^{p}(n)$, with the target output T_k^p for p^{th} pattern at the n^{th} iteration, the error can be calculated by following equation:

$$E_k^p(n) = \frac{1}{2}\left(O_{kO}^{p}(n) - T_k^p\right)^2 \tag{6.5}$$

STEP-7: **Setting the stopping criteria for training**

The aim of training of the BPNN model is to reach a point where mean square error (MSE) for all the training patterns declines to a sufficiently small value. The MSE can be determined by,

$$MSE(n) = \frac{1}{2PL_O}\sum_{p=1}^{P}\sum_{k=1}^{L_O}(O_{kO}^{p}(n) - T_k^p)^2 \tag{6.6}$$

where, *MSE(n)* is the MSE at the n^{th} iteration and *P* is the total number of training patterns. Generally the back propagation learning algorithm cannot be shown to converge under all conditions and there are no well-defined criteria for stopping the network training [Haykin, 2004]. The problem of over-fitting or over-learning of the network is often observed which may be due to the presence of noise in the training dataset. To record the trend of over-fitting MSE for the testing patterns is also determined after each iteration of training. Then training is stopped when MSE for testing dataset keeps on increasing even though it decreases training dataset.

STEP-8: **Backward pass**

The updatation of all the connection weights is as per the gradient descent algorithm by using the following equations:

$$\Delta V_{ij}(n) = \frac{1}{2PL_O}\sum_{p=1}^{P}\sum_{k=1}^{L_O}\eta\left(T_k - O_{kO}^{p}(n)\right)O_{kO}^{p}(n)\left(1 - O_{kO}^{p}(n)\right)O_{jH}^{p}(n)$$

$$\left(1 - O_{jH}^{p}(n)\right)V_{jk}(n-1)Y_i + \{\alpha\Delta V_{jk}(n-1)\} \tag{6.7}$$

$$\Delta W_{jk}(n) = \frac{1}{2PL_O}\sum_{p=1}^{P}\sum_{k=1}^{L_O}\eta\left(T_k - O_{kO}^{p}(n)\right)O_{kO}^{p}(n)\left(1 - O_{kO}^{p}(n)\right)O_{jH}^{p}(n)$$

$$\left(1 - O_{jH}^{p}(n)\right) + \{\alpha\Delta V_{jk}(n-1)\} \quad (6.8)$$

where, η and α are learning rate and momentum coefficient, respectively.

STEP-9: **Iteration**

Until the stopping criterion for learning is reached Steps 4 to 7 are repeated. The flowchart for the back propagation learning algorithm is shown below in **Fig. 6.2**.

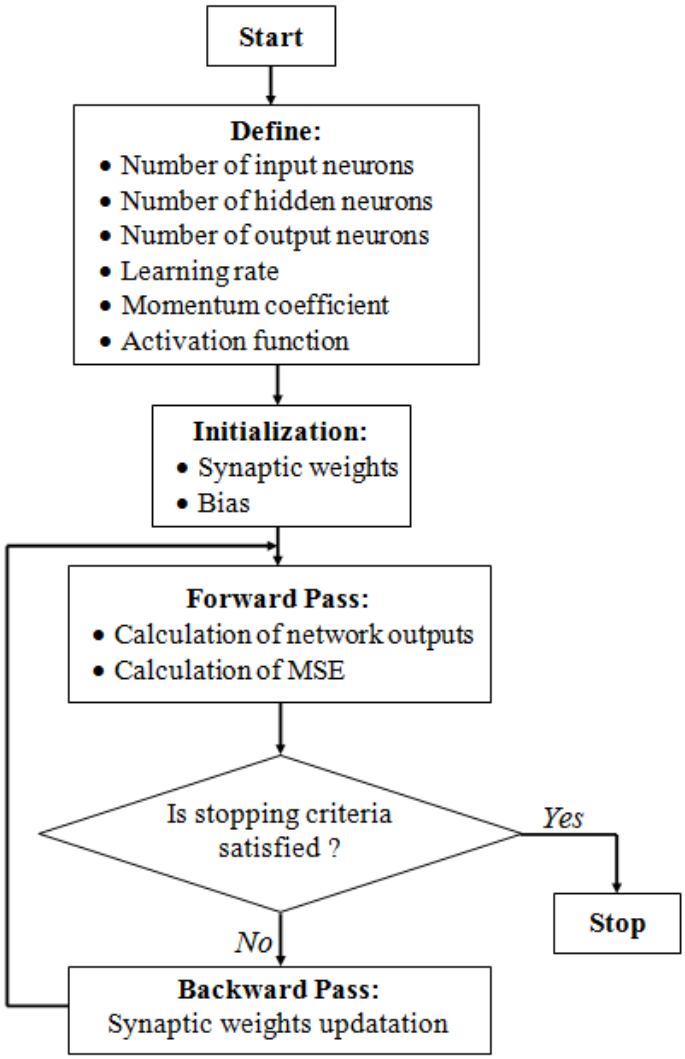

Figure 6.2 Flowchart of BPNN training algorithm

6.4 Radial Basis Function Network

Radial basis function network (RBFN) is a three-layered special class of multi-layer feed forward network [Haykin, 2004]. This network provides an alternative to BPNN as a tool for classification and function approximation. Apart from function approximation the technique can be used for the problems related to time-series forecasting, classification, clustering, recognition of hand written characters etc. Though both BPNN and RBFN are good in universal approximation for nonlinear input-output mapping, they are different from each other in several aspects [Haykin, 2004], which are as follows:

- For BPNN, the nonlinear transformations are usually performed by both hidden and output layer whereas only the hidden layer of RBFN performs this task using some nonlinear function known as radial basis functions (RBF).
- A RBF network consists of single hidden layer which can be more than one in case of BPNN.
- RBFN uses exponentially decaying nonlinear function (e.g., Gaussian function) to construct local approximations of nonlinear input-output mappings while BPNN construct global approximations.
- Though both the networks have almost the same learning capability, RBFN has a simpler structure and is computationally less expensive compared to BPNN.

6.4.1 Structure of RBFN

It uses a special type of function (Radial basis function), whose response increases or decreases monotonically with its distance from a central point. The network mainly consists of three layers having different tasks for different layers. The input layer connects the network to its environment. The only hidden layer i.e. the second layer applies a non-linear transformation from the input space to the hidden space [Cover's theorem, Cover, 1965]. There are no connection weights between the input layer and the hidden layer. Among various activation functions Gaussian function is the most popular. The output layer is generally linear, but may be nonlinear [Taghi, 2004] and supplies the response of the network to the activation pattern. In this work, nonlinear activation function is used in the

output layer. The performance of this network depends upon the number of hidden neurons, their centers and radii. The basic structure of a RBFN is shown in **Fig. 6.3**.

6.4.2 RBFN Model Development Steps

The development procedure for RBFN model consists following steps:

STEP-1: **Definition**

The RBFN architecture is defined, i.e., values for number of input and output neurons are selected, which depend on the given problem. The number of basis functions, i.e., the number of hidden neurons, was varied in the range of 5 to 30 in step of one. Gaussian activation function was used in the hidden layer for this research. Learning rate was chosen in the range of 0.05 to 0.5.

STEP-2: **Initialization**

Initially the centers of RBF are chosen randomly from the input space. The connection weights (V_{jk}) between hidden and output layers are randomly initialized between -0.9 to +0.9.

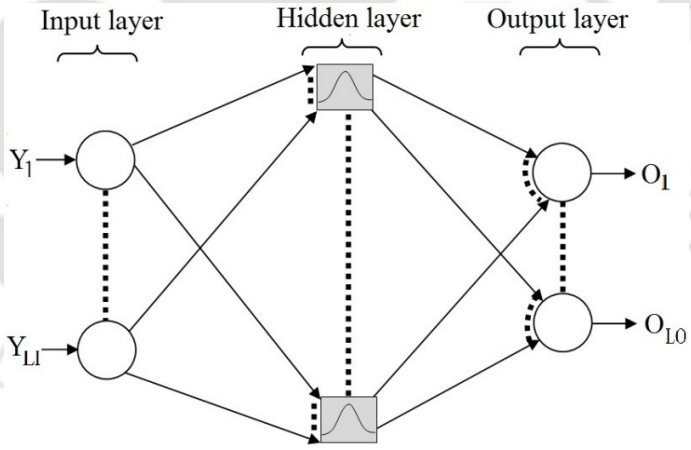

Figure 6.3 A schematic diagram of a radial basis function network

Step-3: **Presentation of the training patterns**

For this network also the training patterns are normalized in the range of 0.1 to 0.9, and presented to the network in batch mode.

STEP-4: **Forward pass calculation**

The output from j^{th} hidden neuron and k^{th} output neuron for p^{th} pattern are calculated as follows:

Output of hidden neuron: The output of j^{th} hidden neuron is given by,

$$R_j^i(n) = e^{-\left(\frac{\left\|Y_i - C_j(n)\right\|^2}{2(\sigma_j(n))^2}\right)} \tag{6.9}$$

where, $R_j^i(n)$is the output of j^{th} hidden neuron of Y_i input pattern at the n^{th} iteration,$C_j(n)$is the is the j^{th} centre of the Gaussian function at the n^{th} iteration, $\left\|Y_i - C_j(n)\right\|^2$is a Euclidean norm and $\sigma_j(n)$is width of theGaussian function at the n^{th} iteration which is given by,

$$\sigma(n) = \frac{d_{max}(n)}{\sqrt{2H}}, \tag{6.10}$$

And $d_{max}(n)$ is the maximum distance between chosen centers at the n^{th} iteration. The dimension of C_j is same as that of Y.

Output of output neuron: The output from k^{th} output neuron for i^{th} input pattern at the n^{th} iteration was calculated using sigmoid activation function:

$$O_{kO}^i(n) = \frac{1}{(1+e^{-S_{kO}^i(n)})} \tag{6.11}$$

and

$$S_{kO}^i(n) = \sum_{j=0}^{H} V_{jk}(n) R_j^i(n) \tag{6.12}$$

where, $O_k^i(n)$ is the output from k^{th} output neuron with i^{th} input pattern in the n^{th} iteration, $S_{kO}^i(n)$ is the weighted sum of the k^{th} output neuron with i^{th} input pattern in the n^{th} iteration, $V_{jk}(n)$ is the connection weight between the j^{th} hidden neuron and the k^{th} output neuron at the n^{th} iteration.

STEP-5: **Training algorithms**

The network training for RBFN is done by updating center of the RBF, width of Gaussian function and the weight between hidden and output neurons of the

network. In the present work full training algorithm is used in which all the above parameters were updated through back propagation algorithm and at same time scale. The updatation of the centers (see Appendix II) is as follows:

$$C_j(n) = C_j(n) - \eta_1 \frac{\partial \xi(n)}{\partial C_j(n)} \tag{6.13}$$

The spread of Gaussian function was updated (see Appendix II) using

$$\sigma_j(n) = \sigma_j(n) - \eta_2 \frac{\partial \xi(n)}{\partial \sigma_j(n)} \tag{6.14}$$

and weights were updated (see Appendix II) using

$$V_{jk}(n) = V_{jk}(n) - \eta_3 \frac{\partial \xi(n)}{\partial V_{jk}(n)} \tag{6.15}$$

In **Eqs. 6.13** to **6.15**, η_1, η_2 and η_3 are learning rates in the range 0 to 1.

STEP-6: **Setting the stopping criteria for training**

All the parameters of RBFN model are updated at same time. When MSE for all the training patterns, given below in **Eq. 6.16**, reaches to a sufficiently small value, the training of the network stops.

$$MSE(n) = \xi(n) = \frac{1}{2Nl_O} \sum_i^N \sum_k^{lo} \left(T_k^i - O_{kO}^i(n)\right)^2 \tag{6.16}$$

STEP-7: **Iteration**

Till the stopping criterion for learning is met Steps 4 to 6 are repeated. The flowchart for training of RBF network is shown in **Fig.6.4**.

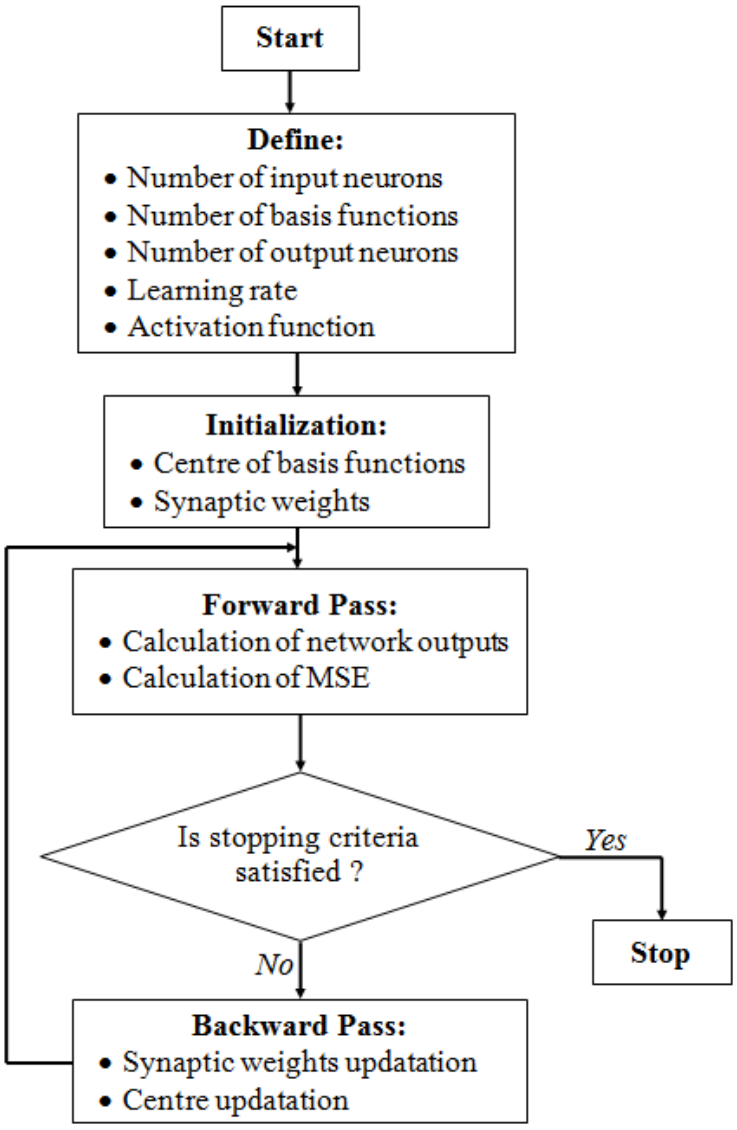

Figure 6.4 Flowchart of RBFN training algorithm

6.5 Results and Discussions

The complete data set used for training, testing and validation of the developed model is given below in **Table 6.1**. The Table consists of 59 experimental conditions with measured weld quality parameters. Among these 32 numbers of experiments were conducted using Taguchi's L_{32} OA and 27 numbers of experiments using full factorial DOE.

Table 6.1 Complete Experimental Data Set Used for Modeling

Exp. No.	PD	RPM	WS	TG	SD	PnD	TPL	DT	UTS	YS	% Elong.	BA	HRD
1	0.09	600	63	1	20	5	5.2	10	112.08	70.52	9.26	55	51.01
2	0.09	600	98	2	25	6	5.4	15	99.75	58.69	8.72	45	47.77
3	0.09	600	132	4	30	7	5.6	20	116.90	65.65	8.86	60	52.11
4	0.09	600	200	3	35	8	5.8	25	120.28	62.57	21.68	140	47.06
5	0.09	815	63	1	25	6	5.6	20	120.54	62.62	14.66	140	46.23
6	0.09	815	98	2	20	5	5.8	25	114.11	74.58	5.82	140	50.39
7	0.09	815	132	4	35	8	5.2	10	117.19	69.81	7.54	66	51.78
8	0.09	815	200	3	30	7	5.4	15	133.20	63.24	14.60	140	53.82
9	0.09	1100	63	2	30	8	5.2	15	94.38	58.61	3.96	45	49.17
10	0.09	1100	98	1	35	7	5.4	10	63.28	53.41	3.00	50	47.75
11	0.09	1100	132	3	20	6	5.6	25	136.90	72.35	14.80	140	51.24
12	0.09	1100	200	4	25	5	5.8	20	112.74	64.25	9.82	10	46.55
13	0.09	1500	63	2	35	7	5.6	25	16.01	14.59	0.86	5	49.79
14	0.09	1500	98	1	30	8	5.8	20	1.93	1.76	0.76	5	47.26
15	0.09	1500	132	3	25	5	5.2	15	138.51	64.47	23.78	140	55.91
16	0.09	1500	200	4	20	6	5.4	10	91.72	61.29	4.14	21	46.33
17	0.15	600	63	3	20	8	5.4	20	102.86	69.54	5.60	15	54.29
18	0.15	600	98	4	25	7	5.2	25	94.34	62.74	5.68	25	50.24
19	0.15	600	132	2	30	6	5.8	10	131.00	69.52	17.50	140	52.33
20	0.15	600	200	1	35	5	5.6	15	50.52	49.85	4.34	15	52.23
21	0.15	815	63	3	25	7	5.8	10	64.26	51.72	4.68	10	51.61
22	0.15	815	98	4	20	8	5.6	15	85.09	70.43	3.34	15	52.84
23	0.15	815	132	2	35	5	5.4	20	122.07	57.25	19.28	140	48.61
24	0.15	815	200	1	30	6	5.2	25	117.29	60.76	17.04	140	51.20
25	0.15	1100	63	4	30	5	5.4	25	123.68	63.14	10.00	40	48.56
26	0.15	1100	98	3	35	6	5.2	20	132.64	63.24	18.26	140	54.29
27	0.15	1100	132	1	20	7	5.8	15	91.78	63.54	4.00	10	54.11
28	0.15	1100	200	2	25	8	5.6	10	61.52	54.70	1.94	10	51.65
29	0.15	1500	63	4	35	6	5.8	15	124.12	63.69	17.46	53	46.83
30	0.15	1500	98	3	30	5	5.6	10	126.77	64.09	19.36	140	53.19
31	0.15	1500	132	1	25	8	5.4	25	2.48	1.69	0.70	5	47.26
32	0.15	1500	200	2	20	7	5.2	20	25.50	66.97	1.30	5	46.65
33	0.09	600	98	1	25	5	5.7	15	113.88	59.66	10.66	140	57.80
34	0.09	1100	98	1	25	5	5.7	15	121.47	69.51	13.24	140	55.29

35	0.09	1100	98	3	25	6	5.7	15	142.23	105.84	16.36	140	62.76
36	0.09	600	98	3	25	5	5.7	15	130.68	80.36	14.92	140	58.55
37	0.09	1100	98	1	25	6	5.7	15	129.94	77.85	15.46	140	50.94
38	0.09	1100	98	1	25	7	5.7	15	116.66	63.19	14.52	140	53.32
39	0.09	600	98	2	25	6	5.7	15	128.30	79.91	14.94	140	56.13
40	0.09	815	98	1	25	7	5.7	15	125.51	73.05	15.08	140	53.27
41	0.09	815	98	2	25	7	5.7	15	133.89	86.82	15.18	140	49.93
42	0.09	600	98	1	25	6	5.7	15	124.28	70.59	12.71	140	54.57
43	0.09	815	98	2	25	5	5.7	15	129.62	78.97	13.96	140	53.27
44	0.09	1100	98	2	25	5	5.7	15	133.05	85.24	15.40	140	50.93
45	0.09	600	98	1	25	7	5.7	15	127.48	75.07	14.01	140	57.31
46	0.09	815	98	2	25	6	5.7	15	132.04	83.37	15.58	140	50.32
47	0.09	815	98	1	25	5	5.7	15	118.50	66.57	12.05	140	56.37
48	0.09	600	98	2	25	7	5.7	15	131.60	84.17	14.34	140	57.93
49	0.09	815	98	1	25	6	5.7	15	125.78	74.71	13.88	140	58.40
50	0.09	1100	98	2	25	7	5.7	15	128.52	78.80	14.46	140	55.38
51	0.09	600	98	2	25	5	5.7	15	127.67	75.73	10.26	140	56.11
52	0.09	815	98	3	25	5	5.7	15	133.60	85.65	15.20	140	57.47
53	0.09	1100	98	3	25	5	5.7	15	139.73	89.25	16.15	140	58.10
54	0.09	600	98	3	25	6	5.7	15	131.31	84.10	15.06	140	56.09
55	0.09	815	98	3	25	6	5.7	15	135.91	90.74	15.86	140	57.61
56	0.09	1100	98	2	25	6	5.7	15	136.22	87.13	16.15	140	53.56
57	0.09	600	98	3	25	7	5.7	15	132.21	87.59	14.62	140	57.64
58	0.09	815	98	3	25	7	5.7	15	135.10	89.25	15.50	140	59.17
59	0.09	1100	98	3	25	7	5.7	15	130.53	93.41	15.24	140	54.07

6.5.1 Prediction of Joint Quality using BPNN Model

The performance of a BPNN model depends on number of hidden neurons (NHN), learning rate (η) and momentum coefficient (α). Therefore, several combinations should be tried out to choose an optimal combination. In this work, single hidden layer was tried. Learning rate and momentum coefficient were varied between 0.05 to 0.95 in the step of 0.05. The considered outputs are UTS, YS, % Elng., BA and HRD. The optimal combination of network parameters was selected separately for each output. Out of fifty nine datasets (see **Table 6.1**), forty datasets were used for training and nine for testing the network and remaining ten for validation of the developed model. With the increasing

number of iterations the MSE for training patterns tends to decrease continuously. Also there is no significant change in MSE values for large number of iterations. The trend of MSE for testing patterns decreased initially and then increased, this is due to the over fitting of the network [Haykin, 2004]. So the selection of the best ANN architecture on the basis of the minimum training error is not possible. To avoid this, the testing dataset are used to check the model behavior when presented with previously unseen data. The best model in this case is chosen on the basis of the minimum MSE in training and testing both.

The variations of MSE of training and testing datasets with the number of hidden neurons (2 to 30) for five different outputs are shown in **Figs. 6.5**. It has been seen that MSE of training sometimes decreases at higher NHN, but the MSE of testing increases. This implies the convergence nature of the network towards local minima at higher NHN [Haykin, 2004]. It was also observed that the convergence rate was faster with higher number of hidden neurons. **Figure 6.6** show the variation in mean square training and testing errors with learning rates (η from 0.05 to 0.95) of the BPNN model for five different outputs. It can be seen that the MSE does not vary significantly at higher learning rates. Similarly, the variations of MSE of training and testing with the momentum coefficients (α from 0.05 to 0.95) for different outputs are shown in **Fig. 6.7**. The different pattern was observed for all different output.

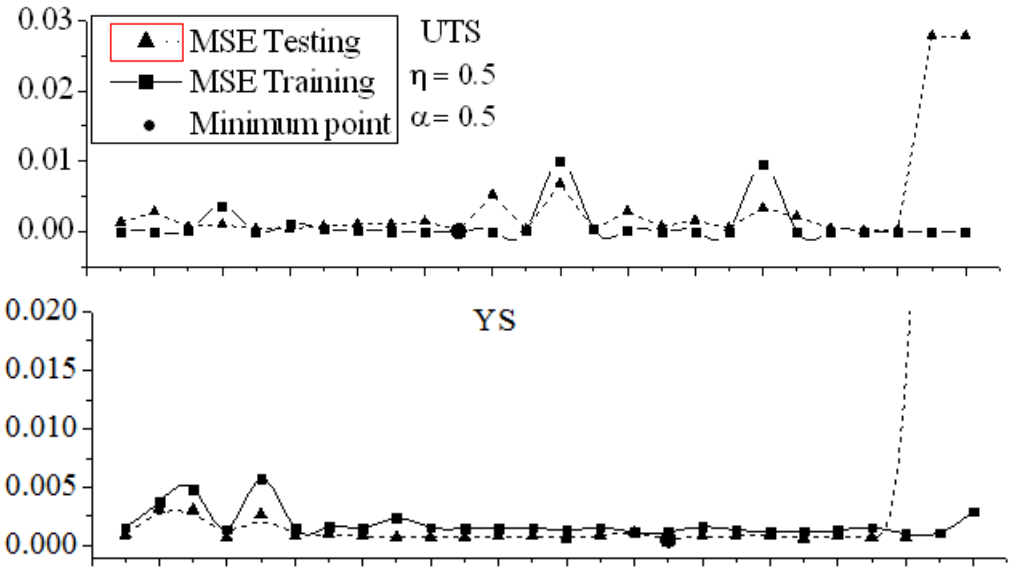

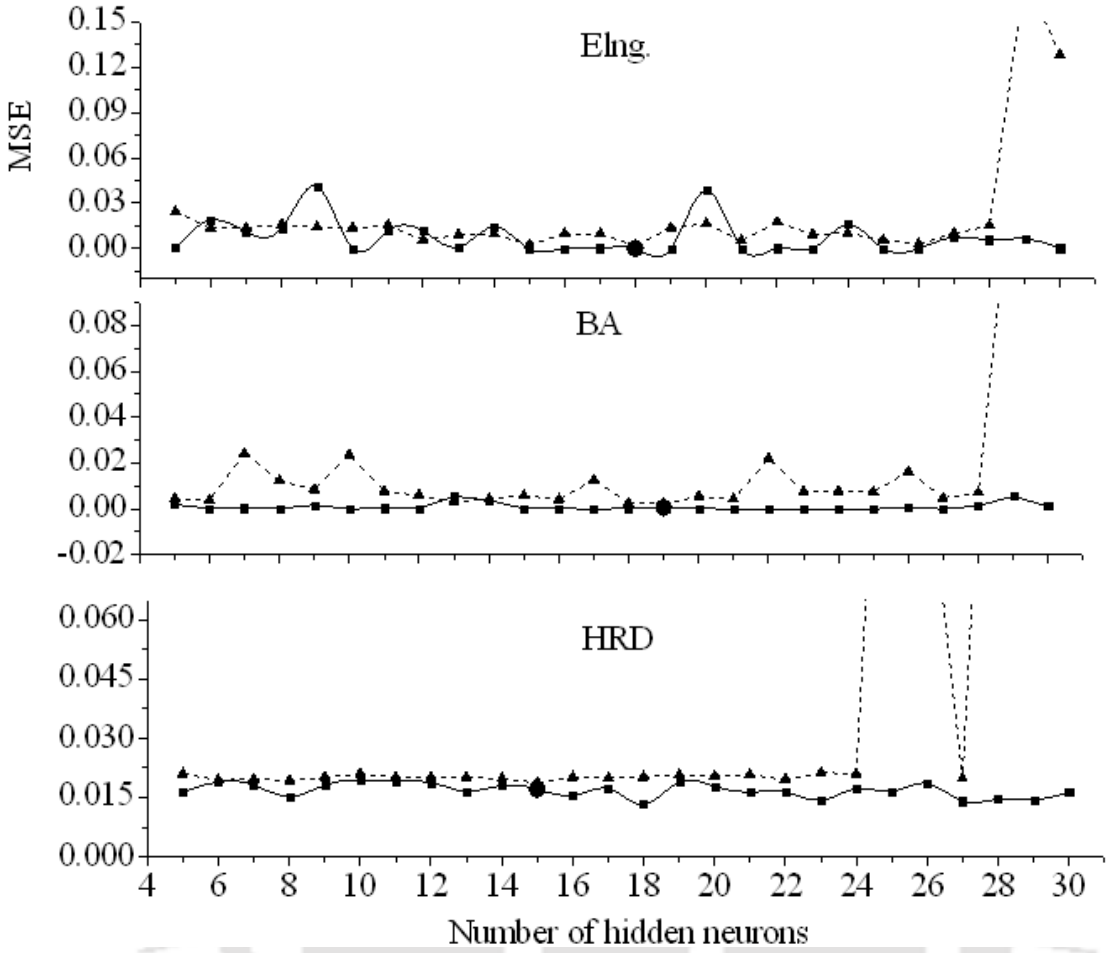

Figure 6.5 Number of hidden neurons vs. MSE of training and testing datasets

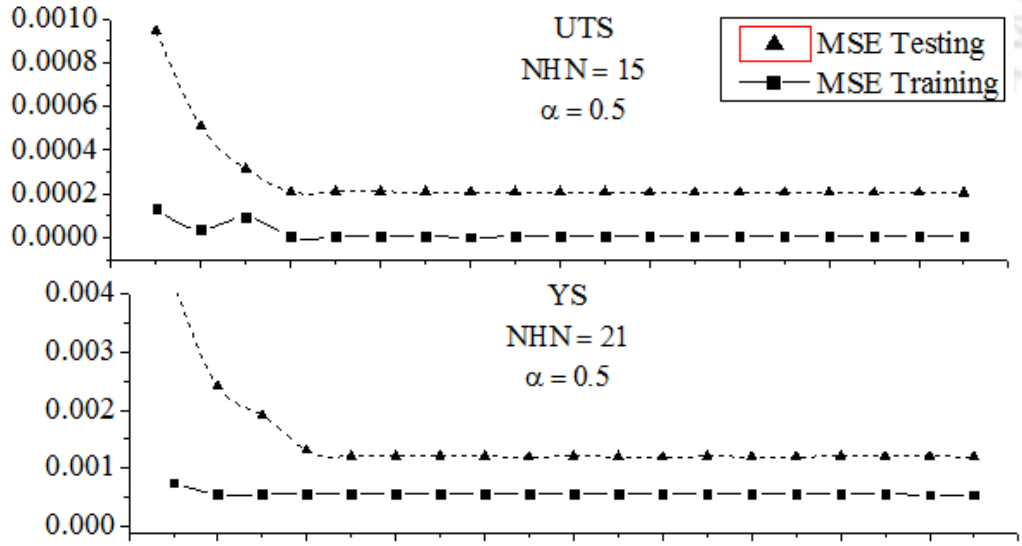

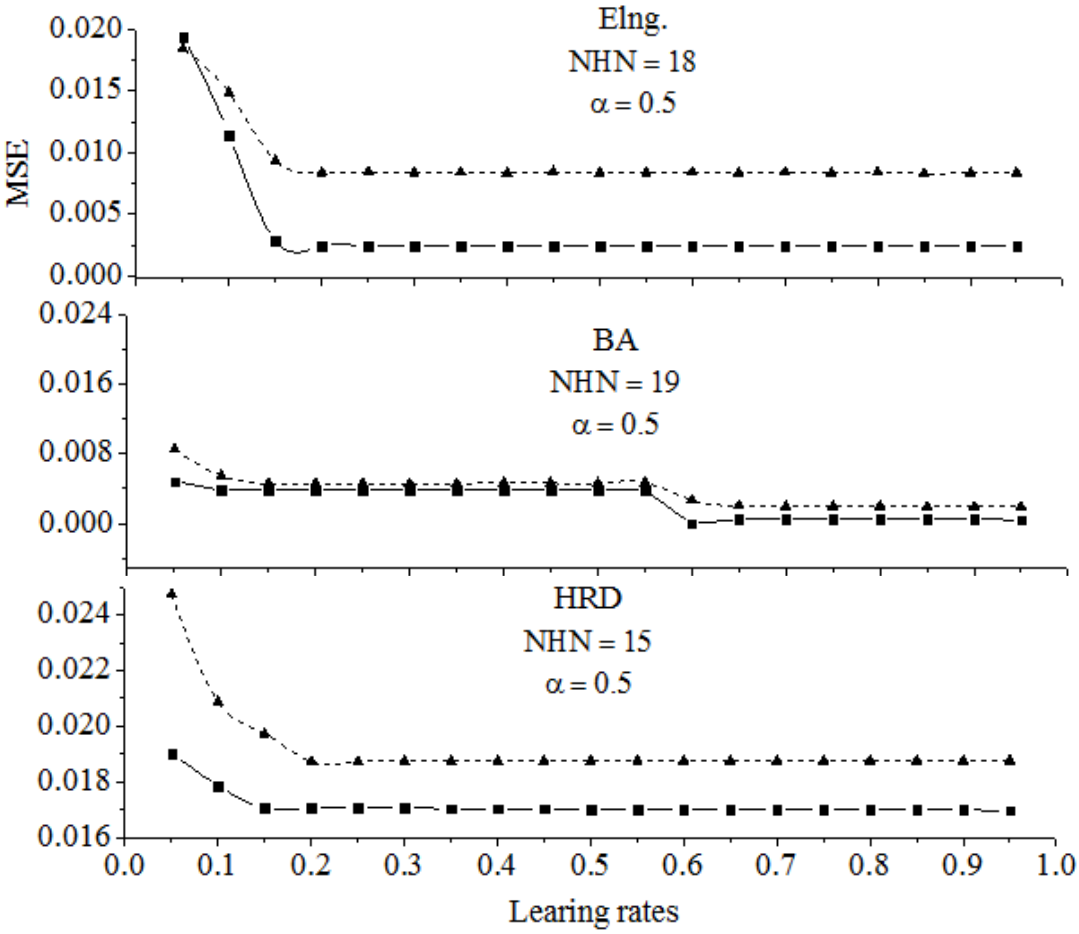

Figure 6.6 Variation of MSE with learning rate for different outputs

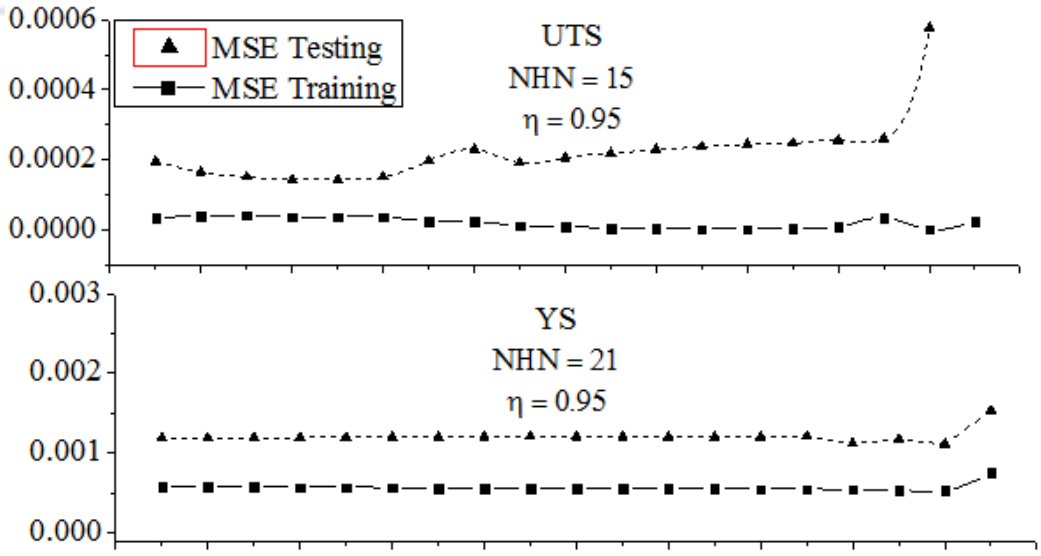

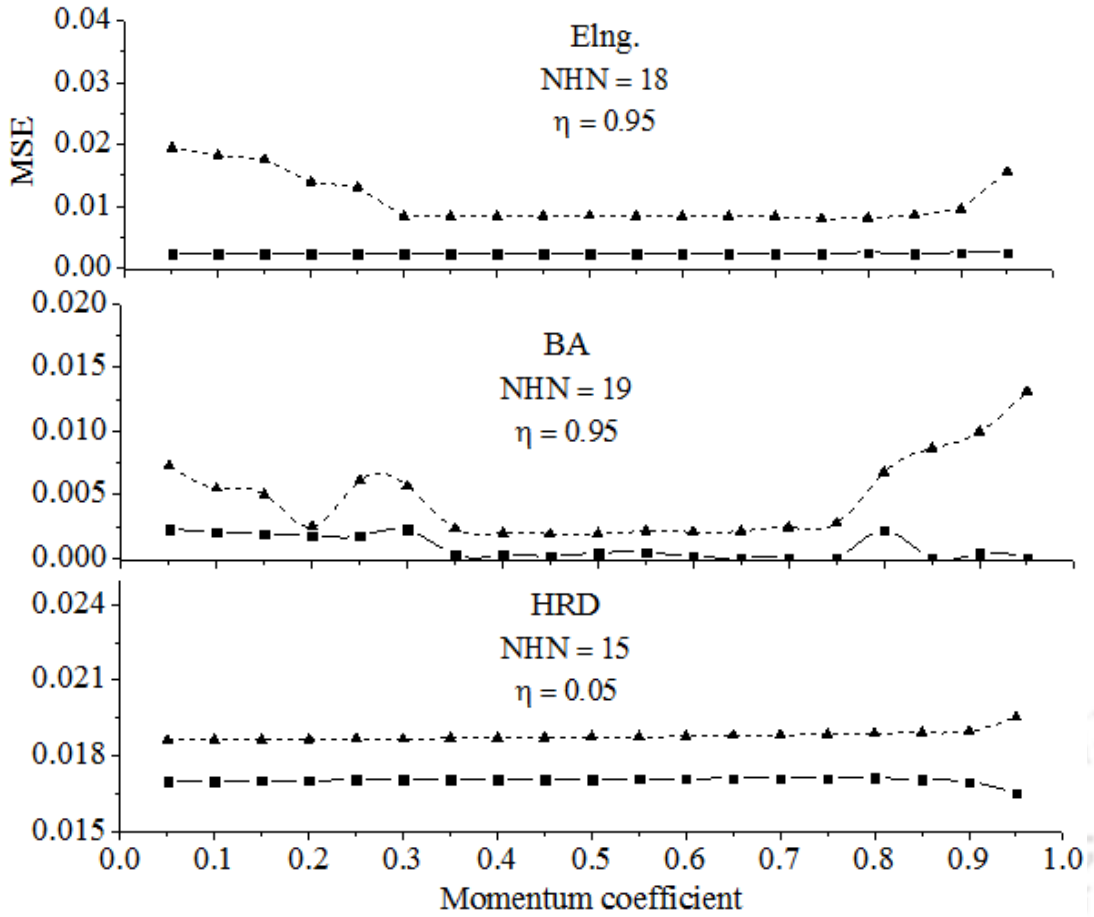

Figure 6.7 Variation of MSE with momentum coefficient for different outputs

From the aforementioned studies, the best BPNN model for UTS prediction among all the networks considered in this analysis was found to be the 8-15-1 architecture with learning rate and momentum coefficient values 0.95 and 0.20, respectively. The best BPNN architecture with number of hidden neurons, learning rate and momentum coefficient for all the five outputs are shown in **Table 6.2**.

Table 6.2 Optimized Network Parameters for BPNN models

Sl. No.	Network Parameters	Optimized Network Parameters				
		UTS	YS	% Elng.	BA	HRD
1	Number of Hidden Neurons (NHN)	15	21	18	19	15
2	Learning Rate(η)	0.95	0.95	0.95	0.95	0.05
3	Momentum Coefficient(α)	0.2	0.9	0.7	0.45	0.05

6.5.2 Prediction of Joint Quality using RBFN Model

The performance of a RBFN model depends on the dimension of the hidden space, i.e., the number of neurons in the hidden layer, learning rate and the momentum coefficient. Therefore, several combinations should be tried out to choose an optimal combination. In this work, the number of neurons in the hidden layer was varied from5 to 30 (in the step of 1). Learning rate was varied between 0.05 to 0.95 (in the step of 0.05), and the momentum coefficient was kept constant at zero. This process was carried out separately for each output. Similar to BPNN model out of 59, 40 and 9 datasets were used for training and testing of the network. The remaining 10 were used for validation of the developed model. The variations of MSE of training and testing datasets with the number of hidden neurons (2 to 30) for five different outputs are shown in **Figs. 6.8**. It has been seen that at higher NHN, MSE of training sometimes decreases, but the MSEs of testing increases significantly. This implies the convergence tendency of the network towards local minima at higher NHN [Haykin, 2004]. It was also observed that the convergence rate was faster with higher number of hidden neurons. The variation in mean square training and testing errors with different learning rates (η from 0.05 to 0.95) of the RBFN model for five different outputs are shown in **Figs. 6.9** to **6.11**. It can be seen that the for all the three learning rates (η_1-for weight, η_2- for center, η_3-for spread of Gaussian function) MSE does not vary significantly at higher learning rates.

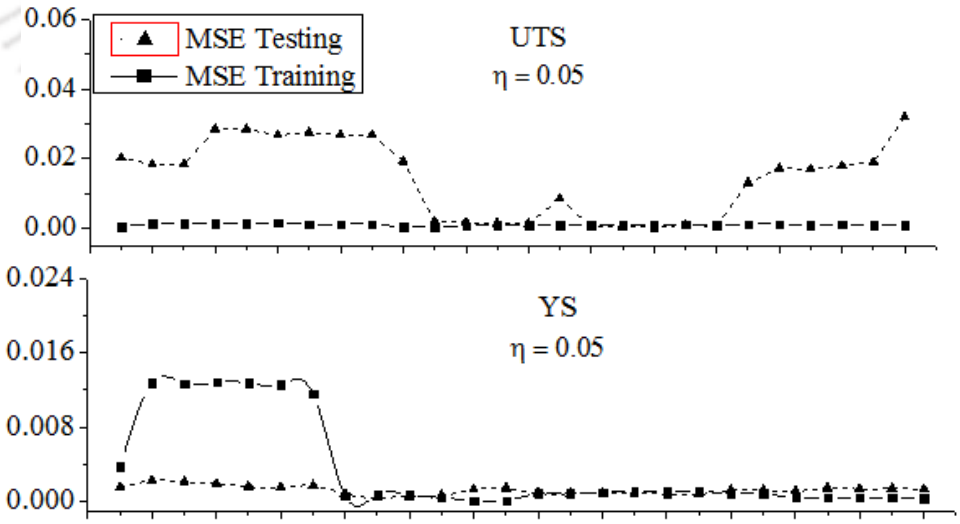

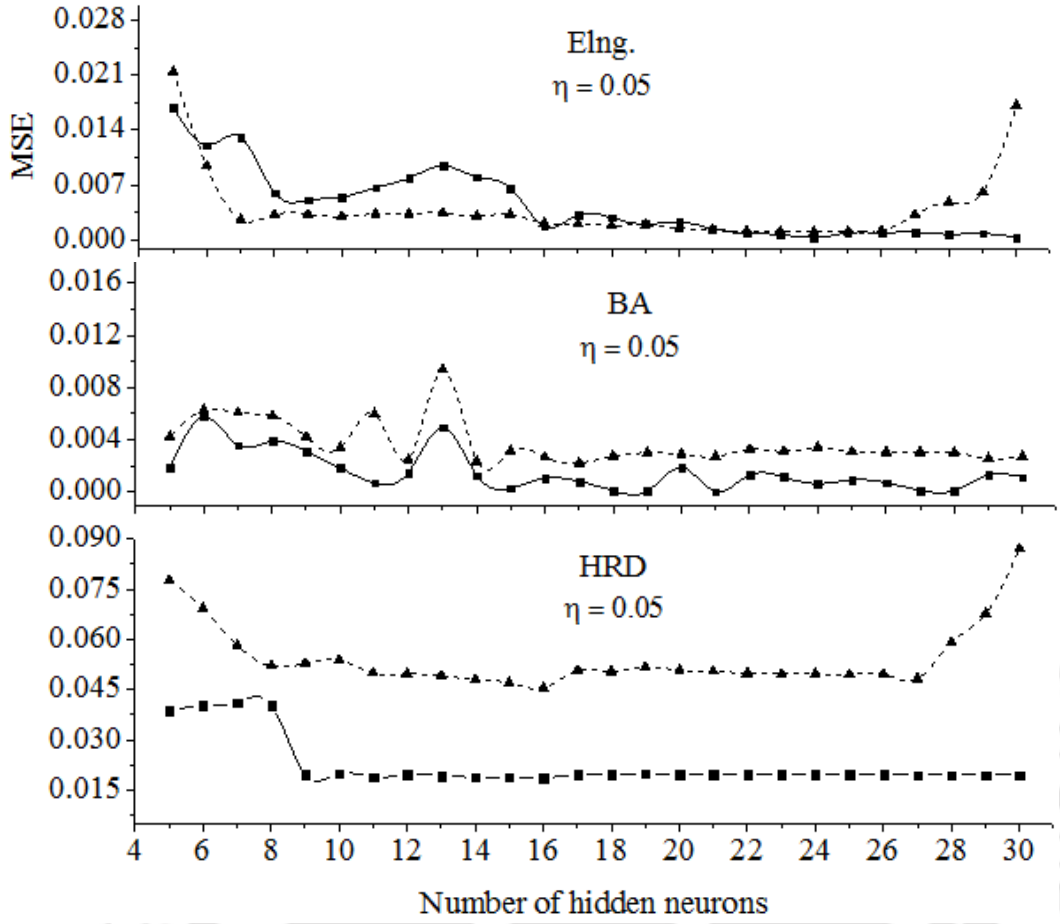

Figure 6.8 Number of Hidden Neurons vs. MSE Training and Testing

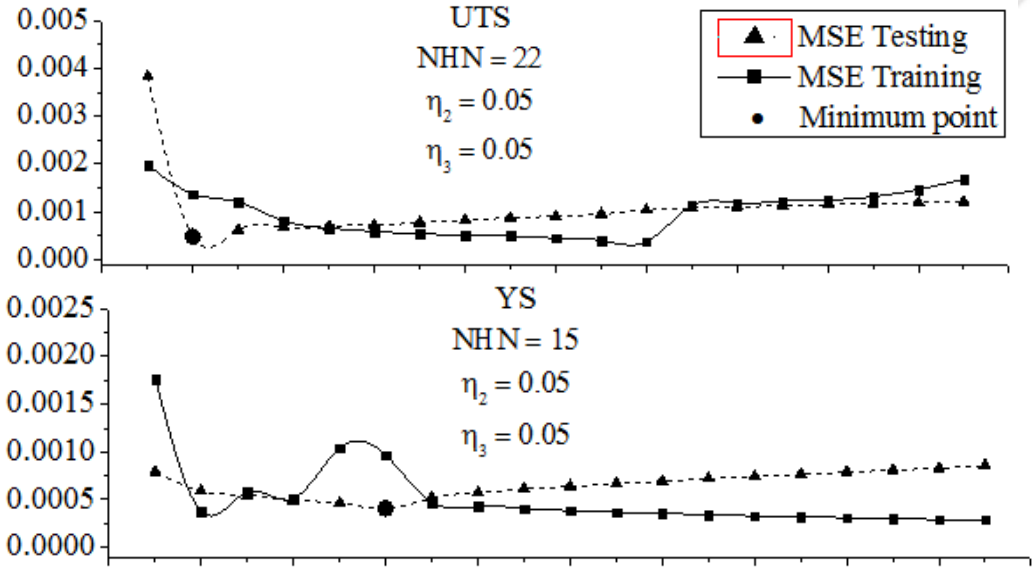

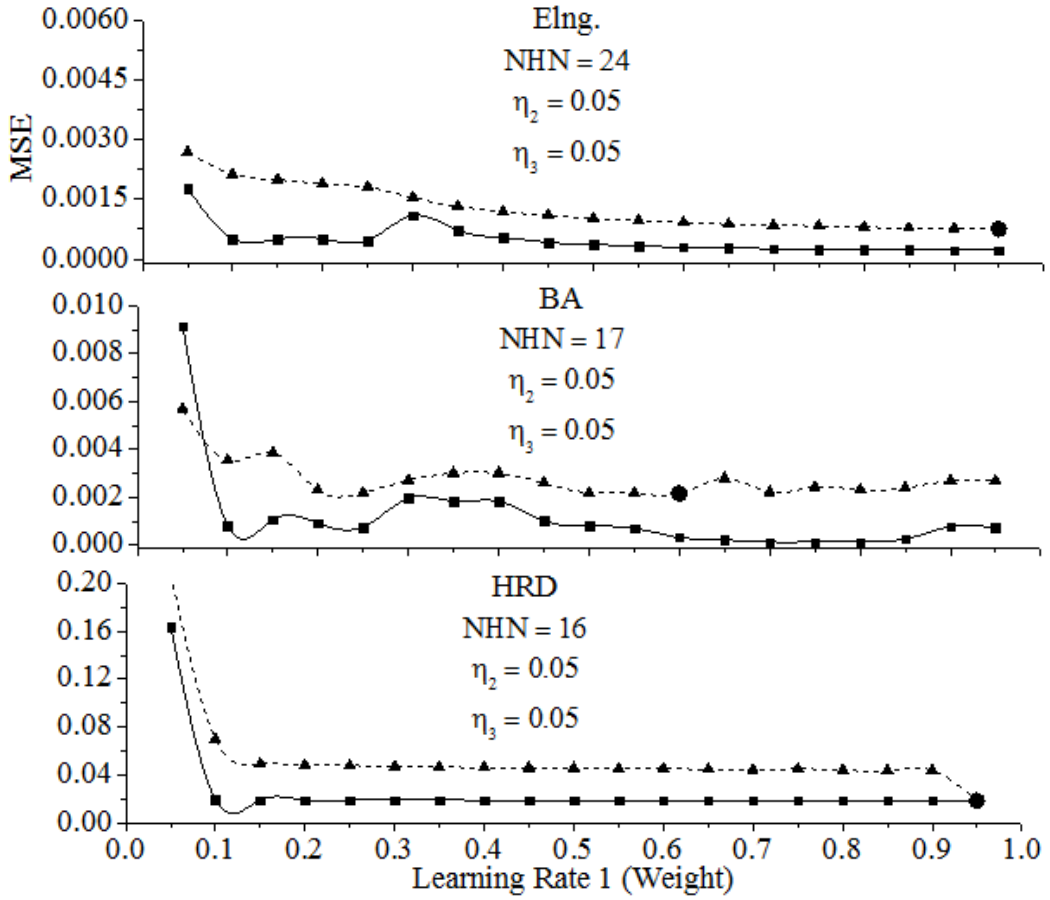

Figure 6.9 Variation of MSE with learning rate 1 (Weight) for different outputs

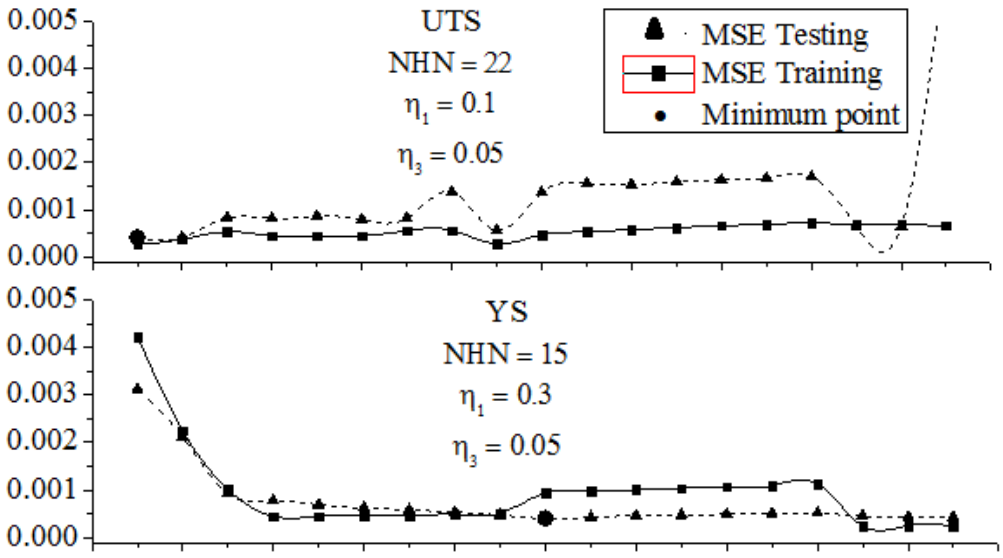

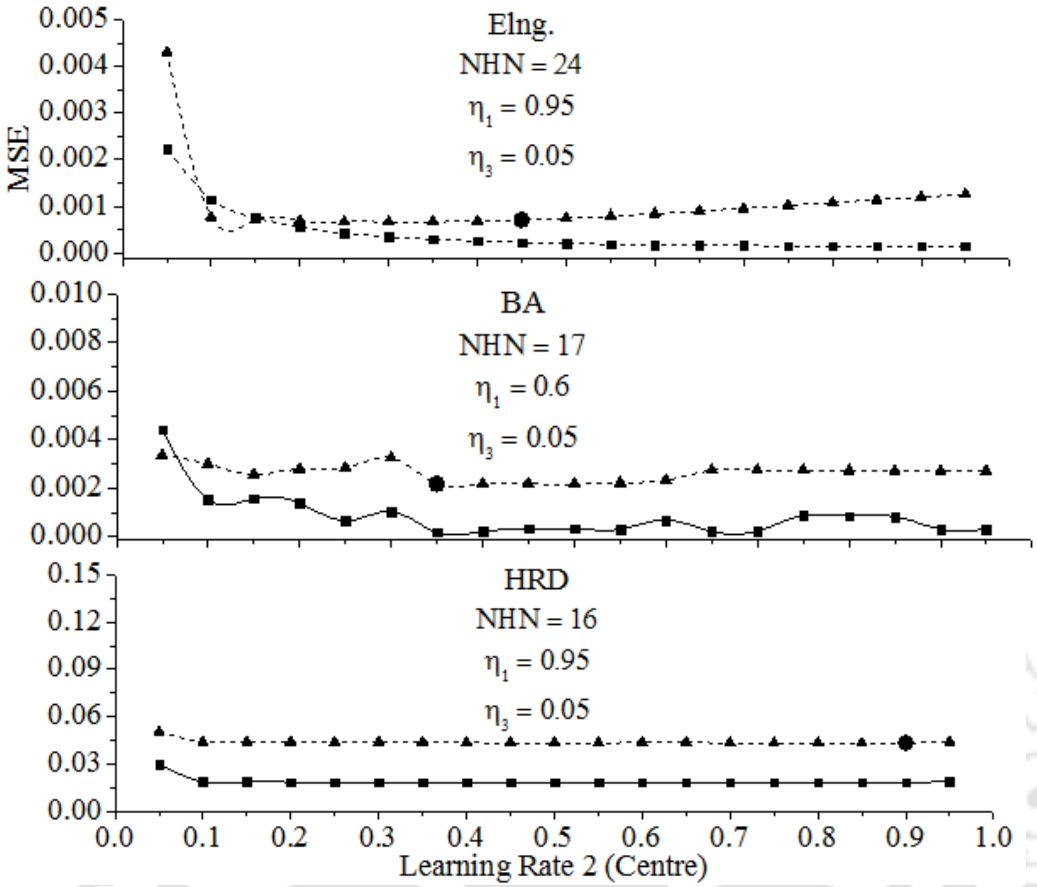

Figure 6.10 Variation of MSE with learning rate 2 (Center) for different outputs

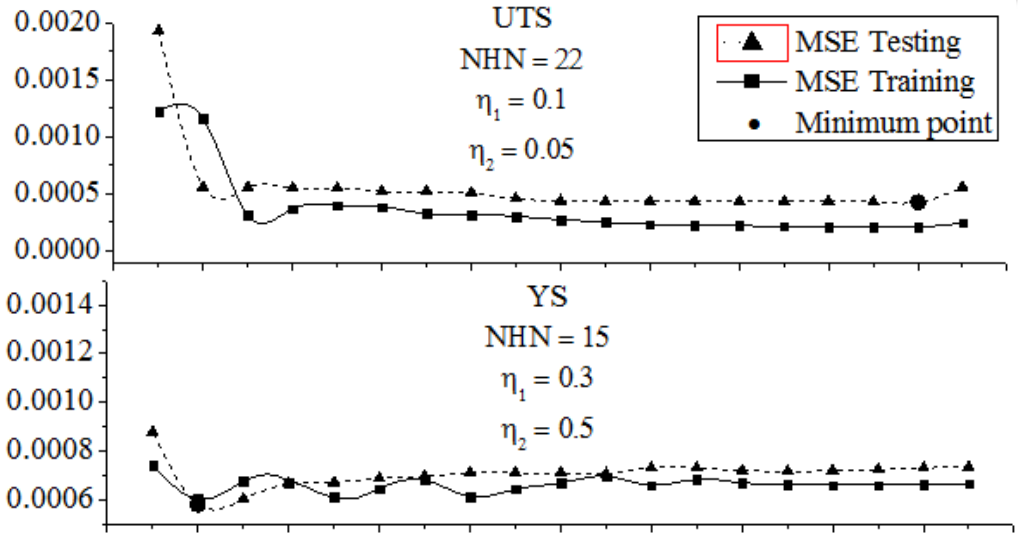

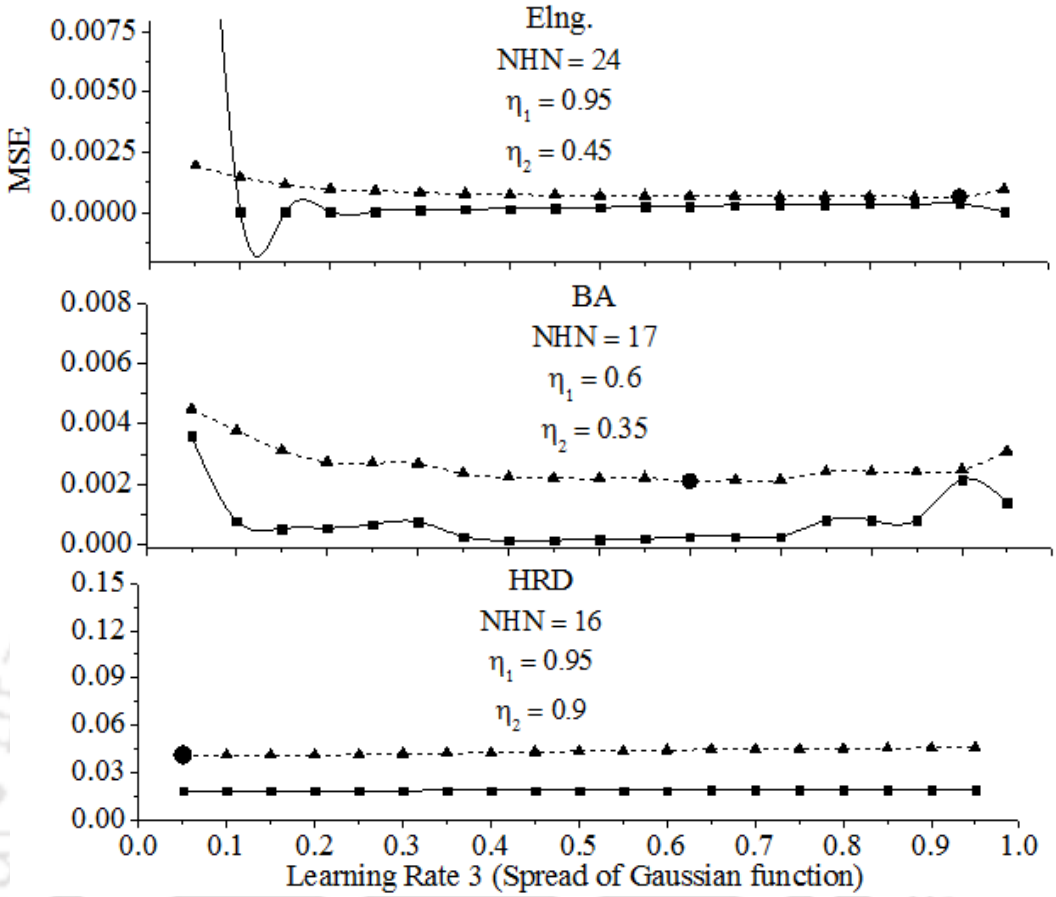

Figure 6.11 Variation of MSE with learning rate 3 (Spread of Gaussian function) for different outputs

From the aforementioned studies, the best RBFN model for UTS prediction among all the networks considered in this analysis was found to be the 8-22-1 architecture with learning rates for weight, centre and spread of Gaussian function are of 0.1, 0.05 and 0.9, respectively. The best RBFN architectures with learning rates for all models are shown in **Table 6.3**.

Table 6.3 Optimized Network Parameters for RBFN models

Sl. No.	Different Network Parameters	Optimized Network Structure				
		UTS	YS	% Elng.	BA	HRD
1	Number of Hidden Neurons	22	15	24	17	16
2	Learning Rate 1 (Weight)	0.1	0.3	0.95	0.6	0.95
3	Learning Rate 2 (Centre)	0.05	0.5	0.45	0.35	0.9
4	Learning Rate 3 (Spread of Gaussian function)	0.9	0.1	0.9	0.6	0.05

6.5.3 Validation of the Developed ANN Models

The above mentioned models were developed using training and testing patterns. Therefore, it is difficult to evaluate whether a developed model correlates the input-output relationship appropriately or not on the basis of the prediction performance of testing patterns. The generalization capability of the developed models can be checked by using an entirely new set of experimental data which are unknown to the model. These are called validation patterns and were used for evaluation of the weld quality prediction performance. The error statistics or prediction performance of the best BPNN and RBFN models for validation patterns for all weld quality parameters are shown in **Table 6.4** and **6.5**, respectively. It can be observed that the mean absolute percentage errors for both the models in case of all the output responses are below 10%.

Table 6.4 Actual and BPNN Predicted Values of Prediction Dataset with % Error

Exp.	UTS			YS			% Elng.			BA			HRD		
No.	Actl.	Pred.	Err.	Actl.	Pred.	Err.	Actl.	Pred.	Err.	Actl.	Pred.	Err.	Actl.	Pred.	Err.
50	128.5	131.33	2.18	78.8	85.96	9.09	14.46	13.24	-8.45	140	140.25	0.18	55.38	58.66	5.92
51	127.7	121.25	-5.03	75.73	69.73	-7.92	10.26	12.60	22.85	140	123.66	-11.67	56.11	57.06	1.69
52	133.6	134.54	0.70	85.65	93.36	9.00	15.2	15.94	4.86	140	147.50	5.36	57.47	58.88	2.46
53	139.7	138.01	-1.23	89.25	104.46	17.04	16.15	17.00	5.29	140	151.23	8.02	58.1	58.43	0.57
54	131.3	132.07	0.58	84.1	89.20	6.06	15.06	15.71	4.34	140	143.67	2.63	56.09	59.05	5.27
55	135.9	138.09	1.61	90.74	98.84	8.93	15.86	16.06	1.27	140	144.42	3.16	57.61	60.39	4.82
56	136.2	139.93	2.72	87.13	99.46	14.16	16.15	15.63	-3.22	140	141.64	1.17	53.56	56.36	5.22
57	132.2	129.85	-1.79	87.59	85.77	-2.08	14.62	13.89	-4.98	140	141.59	1.13	57.64	57.57	-0.12
58	135.1	133.95	-0.85	89.25	91.29	2.28	15.5	13.25	-14.50	140	136.37	-2.59	59.17	59.89	1.22
59	130.5	134.38	2.95	93.41	95.57	2.31	15.24	12.30	-19.29	140	127.44	-8.97	54.07	61.80	14.29
Mean Absolute %Errors			**1.9641**			**7.8872**			**8.9054**			**4.4879**			**4.1587**

Actl.=Actual Value, Pred.= Predicted Value and Err.= % Error

Table 6.5 Actual Values and RBFN Predicted Values of Prediction Dataset with % Error

Exp.	UTS			YS			% Elng.			BA			HRD		
No.	Actl.	Pred.	Err.	Actl.	Pred.	Err.	Actl.	Pred.	Err.	Actl.	Pred.	Err.	Actl.	Pred.	Err.
50	128.5	125.49	-2.36	78.8	89.39	13.44	14.46	13.44	7.056	140	142.76	1.97	55.38	54.31	-1.93
51	127.7	121.40	-4.91	75.73	72.69	-4.01	10.26	11.78	14.8	140	127.91	-8.64	56.11	57.29	2.11

52	133.6	133.44	-0.12	85.65	85.75	0.12	15.2	13.76	9.45	140	138.94	-0.76	57.47	56.71	-1.32
53	139.7	138.04	-1.21	89.25	93.08	4.29	16.15	14.74	8.73	140	137.05	-2.11	58.1	59.92	3.13
54	131.3	131.26	-0.04	84.1	86.20	2.50	15.06	16.56	9.993	140	146.41	4.58	56.09	59.49	6.07
55	135.9	137.13	0.90	90.74	95.39	5.13	15.86	15.90	0.272	140	146.76	4.83	57.61	59.75	3.71
56	136.2	132.60	-2.66	87.13	91.98	5.57	16.15	14.73	8.766	140	147.97	5.70	53.56	58.39	9.03
57	132.2	133.50	0.98	87.59	89.16	1.80	14.62	16.18	10.661	140	141.14	0.81	57.64	51.63	-10.42
58	135.1	136.44	0.99	89.25	97.86	9.65	15.5	15.49	0.043	140	140.44	0.32	59.17	55.97	-5.41
59	130.5	133.05	1.93	93.41	104.01	11.35	15.24	14.76	3.128	140	133.29	-4.80	54.07	59.70	10.41
Mean Absolute % Errors			**1.6087**			**5.7858**			**7.2899**			**3.4488**			**5.353**

The best BPNN and RBFN models' performances for the training, testing and validation patterns for all weld quality parameters are shown in **Figs. 6.12** and **6.13**, respectively. From the scatter diagram (**Figs. 6.12 (a)** to **(e)** and **6.13 (a)** to **(e)**) between the actual and ANNs predicted output values, it can be seen that the deviation for training, testing as well as validation data sets are well within 10% for both the ANN models. The two lines drawn adjacent to the central line shows the range for ±10% deviation. In case of BPNN models, only 3.7% cases error is more than 10% whereas in RBFN models 7.4% cases error is more than 10%. Therefore, it can be argued that the developed models are well generalized and they can be reliably used for representing input-output relationships of weld quality parameters.

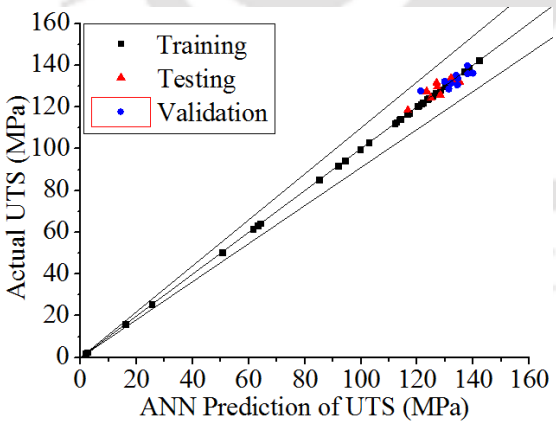

(a)

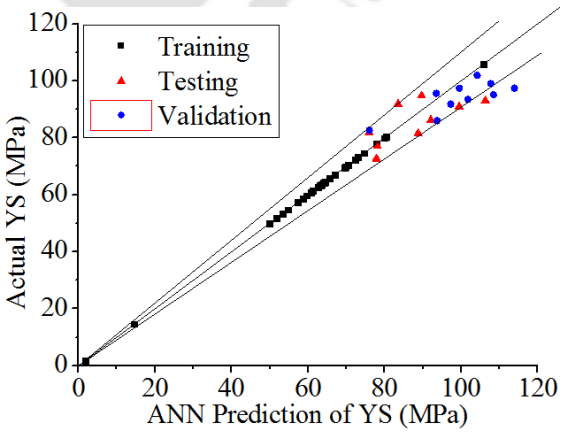

(b)

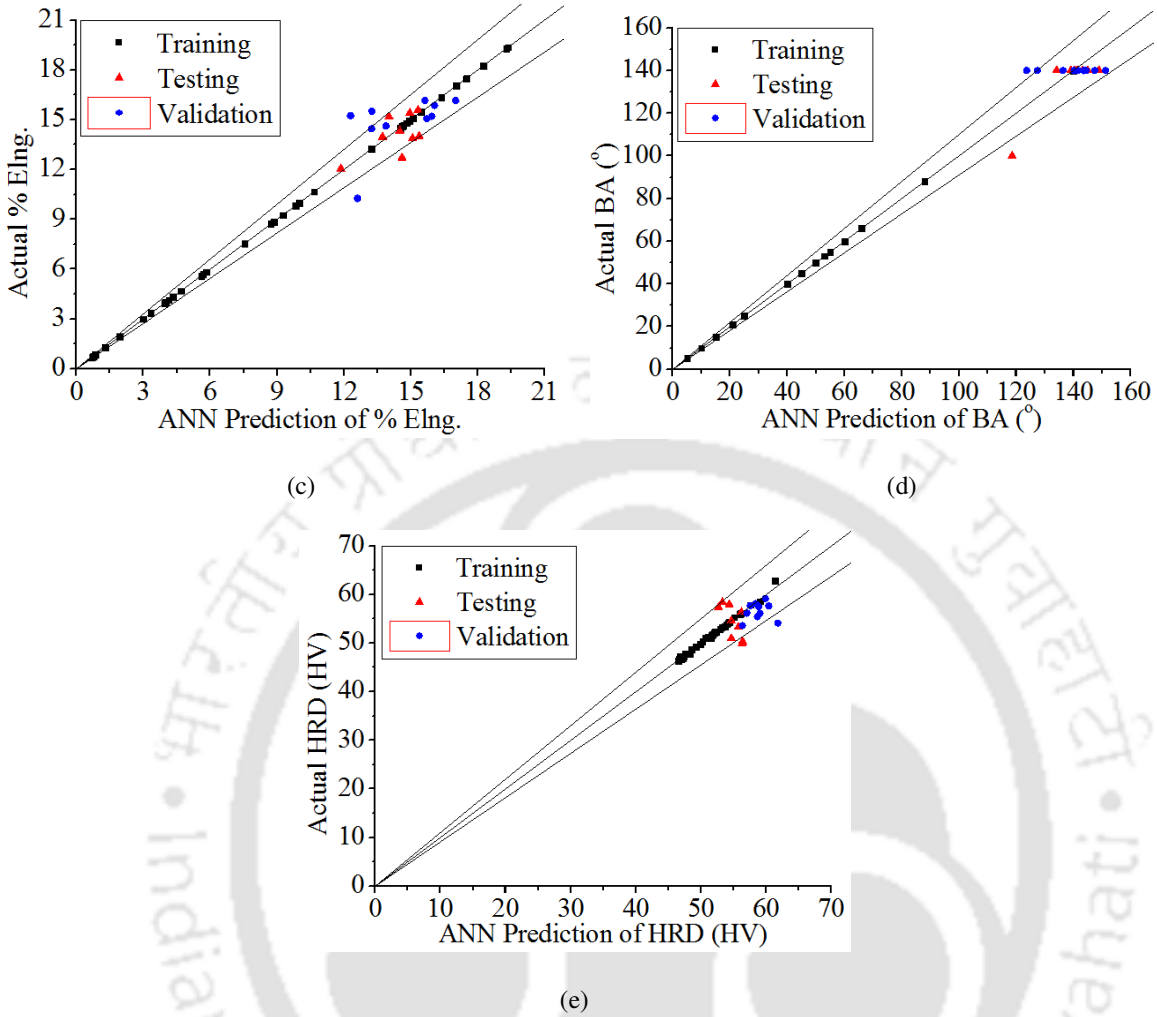

Figure 6.12 Scatter diagram of ANN prediction Vs. (a) actual UTS, (b) actual YS, (c) actual % Elng. (d) actual BA and (e) actual HRD for training, testing and validation data sets by BPNN

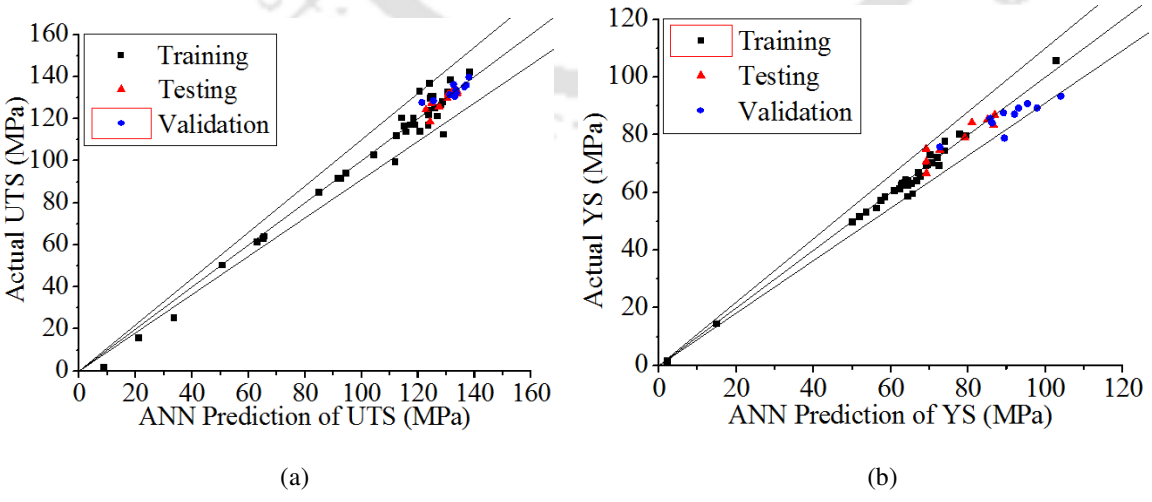

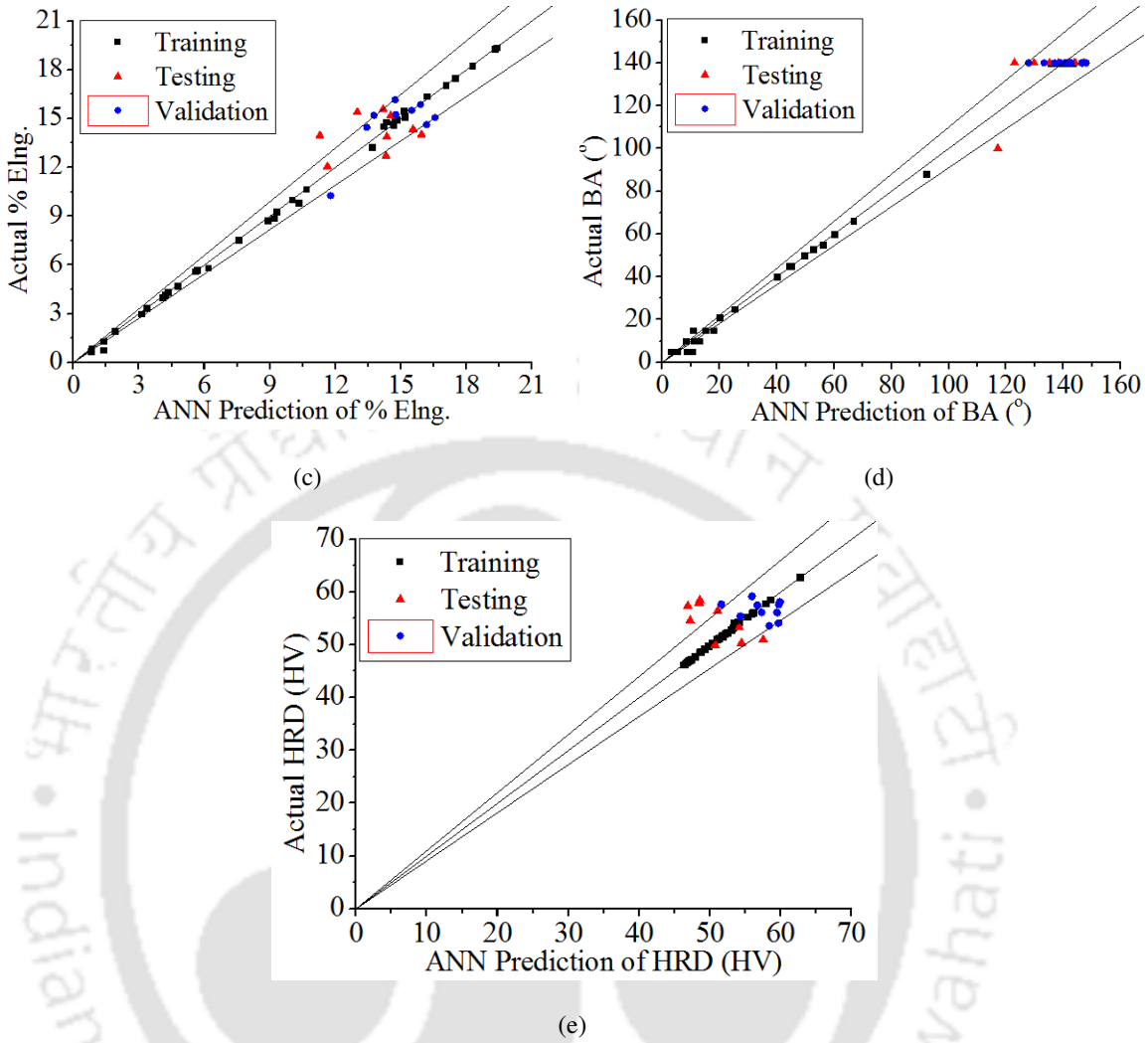

Figure 6.13 Scatter diagram of ANN prediction Vs. (a) actual UTS, (b) actual YS, (c) actual % Elng. (d) actual BA and (e) actual HRD for training, testing and validation data sets by RBFN

6.6 Observations

The following observations have been found from the aforementioned studies:

- In case of BPNN model, the network with 15-0.95-0.2 i.e., number of hidden neurons-learning rate-momentum coefficient, gives the lowest prediction error for UTS modeling. Similarly, 21-0.95-0.9, 18-0.95-0.7, 19-0.95-0.45 and 15-0.05-0.05 networks give lowest prediction errors for YS, % Elng., BA and HRD, respectively.
- In case of RBFN model, the network with 22-0.1-0.05-0.9 i.e., number of hidden neurons-learning rate 1 (learning rate for weight) -learning rate 2 (learning rate for

center) -learning rate 3 (learning rate for spread of Gaussian function), gives the lowest prediction error for UTS. Similarly for YS, % Elng., BA and HRD, the 15-0.3-0.5-0.1, 24-0.95-0.45-0.9, 17-0.6-0.35-0.6 and 16-0.95-0.9-0.05 networks give lowest prediction errors, respectively.

- In cases of UTS, YS, % Elng. and BA modelling, RBFN models produced better prediction as compared to BPNN models. On the other hand, in HRD, BPNN models gave superior prediction as compared to RBFN models.
- It was also seen that the average errors in prediction of joint properties from both BPNN and RBFN models are within 10%. So the developed models can be used effectively for prediction of weld quality in FSW process.

6.7 Major Findings

From the above mentioned modeling techniques and results, following major conclusions can be made:

a) The prediction performance of RBFN models was found to be better in case of UTS, YS, % Elng. and BA, as compared to BPNN models whereas, for HRD, BPNN models gave superior prediction than RBFN models.

b) The average errors in prediction of joint properties using best models (i.e., RBFN model for UTS, YS, % Elng. and BA and BPNN model for HRD) are within 5% which indicates that the developed models can be used effectively for joint quality prediction in FSW process.

c) For overall joint properties, the prediction capabilities of RBFN models are found to be better as compared to BPNN models.

Chapter 7

Neuro-EA Optimization of Process Parameters

7.1 Introduction

The quality of a welded joint can be evaluated from many characteristics, such as strength, ductility, hardness *etc*. and these characteristics depend upon different process parameters. Therefore, to get the best of friction stir welding process, the selection of an optimal welding parameter setting is very vital. This will not only ensure better joint quality but also enhance the productivity by eliminating further experimentation. But this is not an easy task as the relationships between the process parameters and the output parameters are non-linear, highly complex and interdependent. The mathematical models showed their inefficiency to explain the nonlinear properties existing between the input and output parameters of FSW. So intelligent systems, such as artificial neural network (ANN) have been used in the present work to correlate the input-output parameters of FSW process using experimental data (discussed in **Chapter 6**). Then four different optimization techniques were applied on the developed ANN models to get the optimum input parameters settings. The used techniques are binary-coded genetic algorithm (BCGA), real-coded genetic algorithm (RCGA), differential evolution (DE) and particle swarm optimization (PSO) algorithms. Two cases were considered in the present work, the first one was the maximization of mechanical properties of the welded joint and the other one was the optimization of desired weld quality

parameters. In this chapter, short introductions to all the proposed techniques are given and their application for the optimization of FSW process is described subsequently.

7.2 Optimization Procedures

7.2.1 Genetic Algorithms

Genetic algorithm (GA) based techniques are mainly used in welding to get the optimum process parameter setting. These are population based probabilistic search and optimization procedures motivated by the principles of natural genetics and natural selection and derived from the theory of evolution given by Charles Darwin. Some fundamental ideas of genetics are borrowed and used artificially to construct search algorithms that are robust and require minimal problem information. These algorithms maintain a collection of potential solutions, which evolve according to a measure reflecting the quality of solutions. John Holland [1975] and group contributed much to the initiation and development of this field in the year of 1965. Further development can be credited to Goldberg [1989]. Different types of GAs are BCGA, gray-coded GA, RCGA, micro GA, visualized interactive GA etc. Present work includes two types of GA *i.e.* BCGA and RCGA. The working principle of a BCGA is elaborated in the following steps.

STEP-1: **Generation of population of solutions**

In binary GA the input parameters of the optimization problem are represented as binary strings comprised of 0 and 1. This binary codification is randomly generated over the search space, where each individual represents a possible problem solution. To make sure that the population satisfies the problem bounds, the **Eq. 7.1** is applied.

$$x_i = {x_i}^{min} + \frac{{x_i}^{max} - {x_i}^{min}}{2^{l_i}-1} V_D(s_i) \tag{7.1}$$

where, l_i is the string length used to code the i^{th} parameter and $V_D(s_i)$ is the decoded value of the string s_i. l_i can be calculated from the following relation with desired accuracy (ε):

$$l_i = \log_2\left(\frac{{x_i}^{max} - {x_i}^{min} + 1}{\varepsilon}\right) \tag{7.2}.$$

STEP-2: **Evaluation of goodness value**

The next necessary procedure is to evaluate the goodness or fitness value of each solution in the population in order to decide the survival of each individual. This is by means of the objective and constraint functions. In absence of constraints, the fitness is made equal to the objective function value which was made by using weighted sum method in this work. The weighted sum method scalarizes a set of objectives into single objective by pre-multiplying each objective with a user defined weight. The weight of an objective is usually chosen in proportion to the relative importance in the problem. Since the objectives in the present study have the same rank, there is no need for scaling. The objective function considered in the present work is defined as follows:

$$f_i = 0.25UTS_i + 0.25YS_i + 0.2Elong_i + 0.15BA_i + 0.15HRD_i \quad (7.3)$$

where, f_i is the fitness of the i^{th} individual in the population; UTS_i, YS_i, $Elong_i$, BA_i and HRD_i are the ultimate tensile strength, yield strength, % elongation, bending angle and nugget zone hardness values at the i^{th} individual in the population, which were obtained from the pre-trained ANN models.

STEP-3: **Reproduction**

After the evaluation of the fitness values the population is then modified using different operators. This is because all the solutions in a population may not be equally good in terms of their fitness values [Pratihar, 2009]. These operators are namely reproduction, crossover and mutation. In the reproduction step the good solutions are selected from the population of strings based on their goodness value. Out of different reproduction schemes [Deb, 2001] the tournament selection has better or equivalent convergence and computational time complexity properties. In this work tournament selection method was used with tournament size of 5.

STEP-4: **Crossover**

After selection, crossover is made on the selected individuals in which there is an exchange of properties between the parents. This results in creation of new

children solutions and gives the GA its exploration ability. Different types of crossover schemes are single point crossover, two point crossover, multi point crossover and uniform crossover. The value of crossover probability is usually varies between 0.5 to 0.95. Uniform crossover was applied in the present work which is found to be better for a large search space [Pratihar, 2009]. In this type of crossover scheme each bit of the first parent string has a 0.5 probability of swapping with the corresponding bit of the second parent string. The scheme of uniform crossover is shown in **Fig. 7.1**.

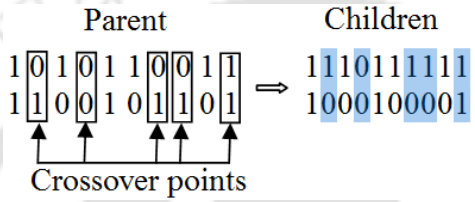

Figure 7.1 Uniform crossover

STEP-5: **Mutation**

It is considered as a method to recover the lost genetic material as well as for randomly distributing genetic information. It is a simple search operator and prevents the algorithm from falling into a local minimum. The mutation probability is usually kept low (e.g. 0.1) to avoid random search. It is performed by flipping a bit *i.e.* changing 0 to 1 and vice-versa as shown in **Fig. 7.2**.

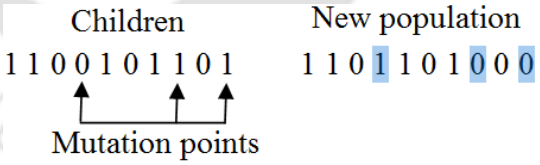

Figure 7.2 Mutation

Real values are used directly instead of binary strings in case of RCGA. Although the same reproduction operators described in BCGA can be used, the difference lies in using efficient crossover and mutation operators. Different crossover procedures which can be used in RCGA are linear crossover, blend crossover (BLX), simulated binary crossover (SBX). SBX crossover and random mutation operators were used in this work. **Figure 7.3** shows the flow chart of the neuro-GA model.

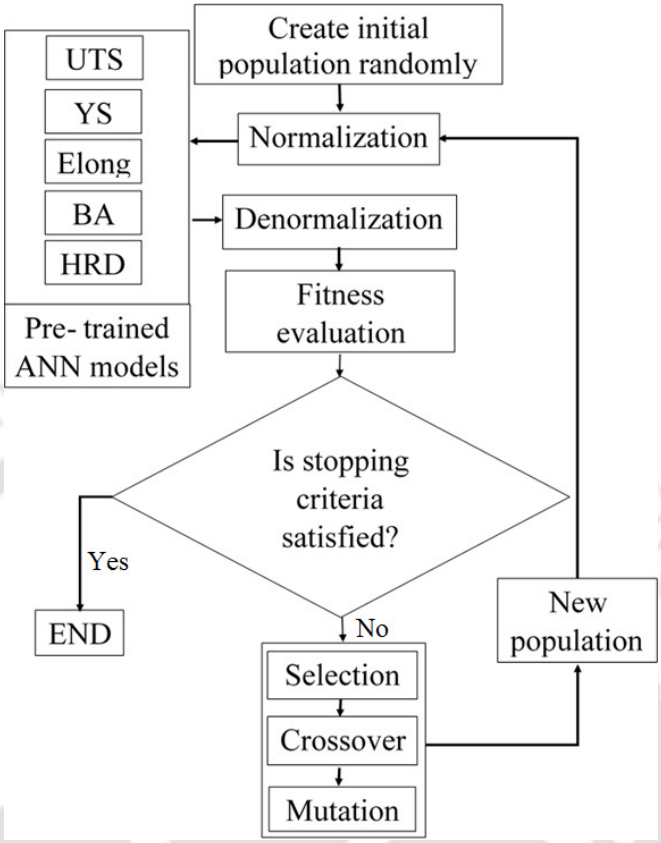

Figure 7.3 The neuro-GA flow chart

7.2.2 Differential Evolution

Differential evolution (DE) is a population based stochastic search algorithm [Storn and Price, 1997]. Similar to GA, DE also starts with a random population and performs operators like crossover, mutation and selection. It uses a vector population where the stochastic perturbation of the population vectors can be done independently. DE's self-organizing scheme takes the difference vector of two randomly chosen population vectors to perturb an existing vector. The different steps of DE are discussed below.

STEP-1: **Creation of population of solutions**

Initially a vector population is randomly created which should cover the entire search space.

STEP-2: **Mutation**

In mutation operator, DE generates new parameter vectors by adding the weighted difference between two population vectors to a third vector. The mutated vector's parameters are then mixed with the parameters of another predetermined vector, called the target vector. For all the target vectors x_i, the mutant vector v_i is calculated by using the **Eq. 7.4**.

$$v_i = x_{r_1} + F\left(x_{r_2} - x_{r_3}\right) \tag{7.4}$$

where, x_{r_1}, x_{r_2} and x_{r_3} are randomly chosen vectors and F is a constant factor $\in [0\ 2]$,

Another way to create the mutant vector is to replace x_{r_1} by x_{best} which the best vector is obtained so far. To increase diversity, two difference vectors are used in the present work as given in **Eq. 7.5**.

$$v_i = x_{best} + F\left(x_{r_1} - x_{r_2} + x_{r_3} - x_{r_4}\right) \tag{7.5}$$

where, $x_{r_1}, x_{r_2}, x_{r_3}$ and x_{r_4} are randomly chosen vectors.

STEP-3: **Crossover**

In DE parameter mixing is often referred to as crossover which is done by generating trial vectors $u_{ij,G+1} = (u_{1i,G+1}, u_{2i,G+1}, \dots \dots u_{ji,G+1})$. If the trial vector yields a better fitness function value than the target vector, then the trial vector replaces the target vector in the following generation. Crossover procedure is shown in **Eq. 7.6**.

$$u_{ij,G+1} = \begin{cases} u_{ij,G+1} & if\ r \le pc \quad or\ j = \delta \\ x_{ij,G} & if\ r > pc \quad or\ j \ne \delta \end{cases} \tag{7.6}$$

where, r is a random number $\in [0\ 1]$, $\delta \in \{1,2, \dots \dots, n\}$ randomly chosen index of any individual and pc is the crossover rate.

.***STEP-4:*** **Selection**

The selection scheme depends on the probability of all solutions in the population to have the same chance of being selected as parents. After the mutation and

crossover operations the new produced vectors are evaluated. To decide whether or not it should become a member of generation G+1, the trial vector $u_{i,G+1}$ is compared to the target vector $x_{i,G}$ using the greedy criterion. If vector $u_{i,G+1}$ yields a better fitness function value than $x_{i,G}$ then $x_{i,G+1}$ is set to $u_{i,G+1}$, otherwise, the old value $x_{i,G}$ is retained. The flow chart of DE is shown in **Fig. 7.4**.

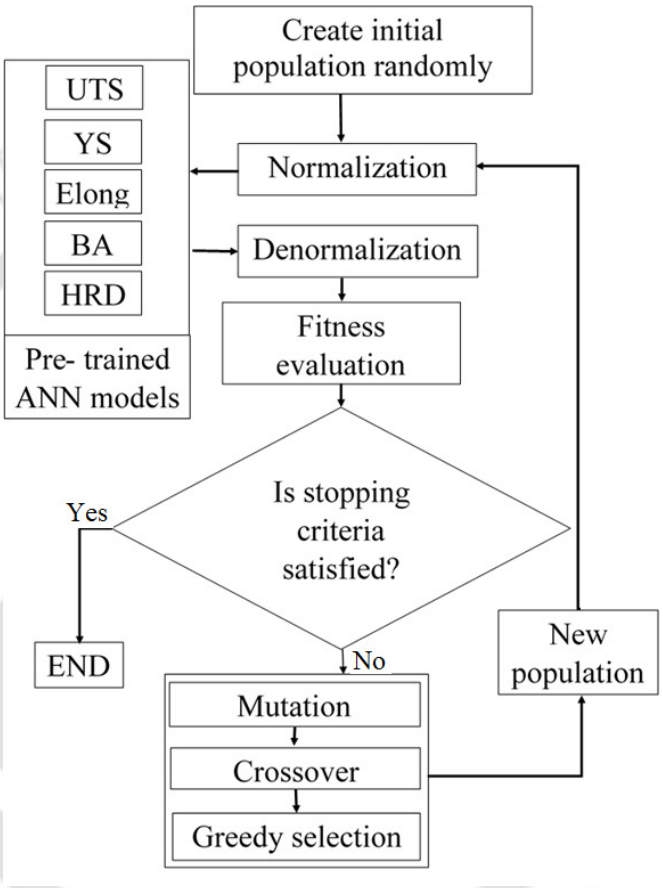

Figure 7.4 The neuro-DE flow chart

7.2.3 Particle Swarm Optimization

Particle swarm optimization (PSO) is a population based parallel search technique inspired by social behavior of bird flocking or fish schooling [Kennedy and Eberhart, 1995]. The potential solutions, called particles are conceptual entities, which fly through the multi-dimensional search space. At any particular instant, each particle has a position and a velocity. In every iteration, each particle is updated by two other best particles namely p-best (the best solution or particle which has been achieved so far) and g-best (is the best

value obtained so far by any particle in the population). The particle updates its velocity and positions after finding these two best values. The PSO scheme has different algorithmic parameters namely an inertia factor (ω), two uniformly distributed random numbers r_1 and r_2 that respectively determine the influence of p-best and g-best on the velocity updatation formula and two constant multiplier terms c_1 and c_2 known as self-confidence and swarm confidence, respectively.

After initialization of all particles the position and velocity of particle are updated using following equations. **Figure 7.5** shows the neuro-PSO flow chart.

$$par_i^{(t+1)} = par_i^{(t)} + v_i^{(t+1)} \tag{7.7}$$

$$v_i^{(t+1)} = \omega_i v_i^{(t)} + c_1 r_1 \left(pbest^{(t)} - par_i^{(t)}\right) + c_2 r_2 \left(gbest^{(t)} - par_i^{(t)}\right) \tag{7.8}$$

where, par_i^t is the i^{th} particle at the t^{th} iteration, $v_i^{(t)}$ is the velocity of the i^{th} particle at the t^{th} iteration, ω_i is the inertia added to the i^{th} particle, $c_1 \& c_2$ are acceleration coefficients and $r_1 \& r_2$ are random numbers $\in$ [0 1].

In the velocity updatation rule (**Eq. 7.8**), the three terms characterize the local behaviors of the particles. The first term represents the inertial velocity or momentum of the particle which serves as a memory of the previous flight direction. It prevents the particle from drastically changing direction. The second and the third term are called cognitive and social components respectively. The cognitive component models the tendency of particles to return to previously found best positions whereas the social component quantifies the performance of a particle relative to its neighbors. It represents a group norm or standard that should be attained.

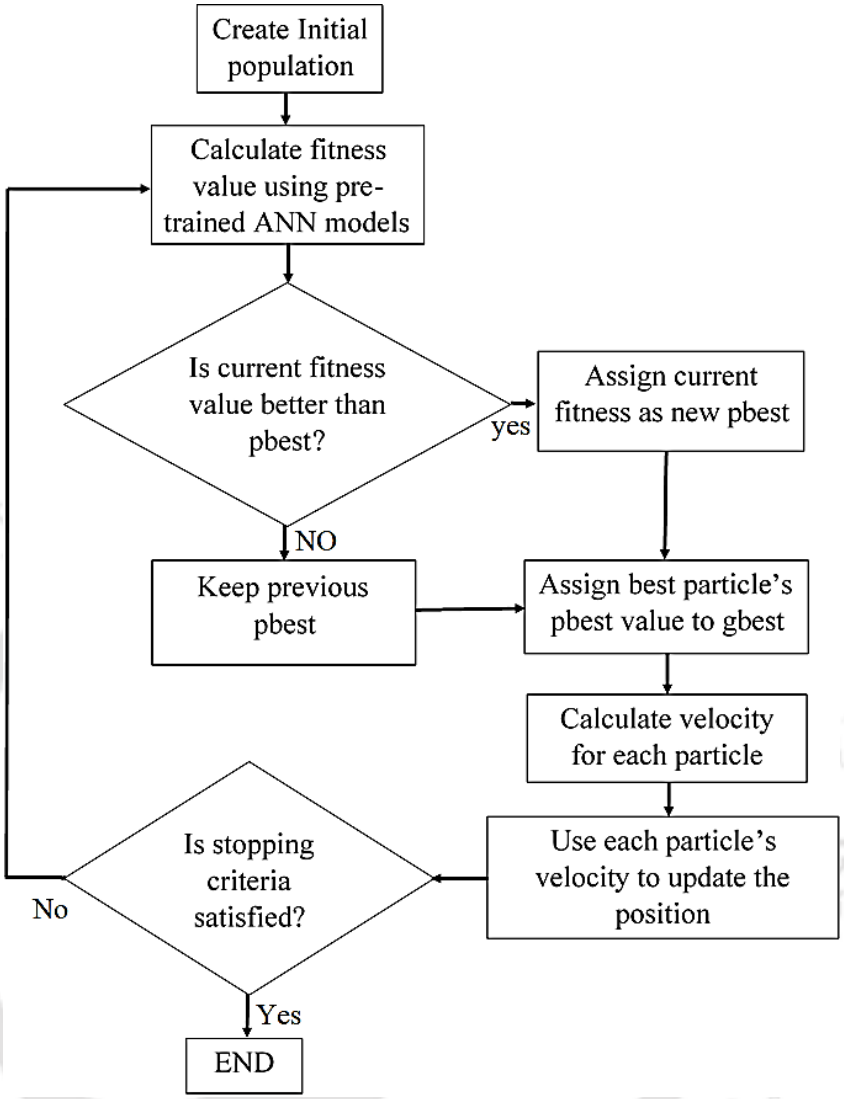

Figure 7.5 The neuro-PSO flow chart

7.3 Results and Discussion

7.3.1 Determination of Optimum Input Parameter Setting for Maximization of Weld Qualities

Initially random population of solutions was created inside the search space of the experiment. Then the normalization between [0.1-0.9] was done before feeding it as input to the pre-trained ANN models. The response characteristics were computed inside the ANN models. The denormalized values were fed to the four evolutionary algorithms mentioned in Section 7.2. Different operators were used to generate a new population in each algorithm.

The new population was again fed to the ANN models and the response characteristics were again computed and fed to each algorithm. The process was continued until the optimal quality characteristics were obtained. The objective of these algorithms was to find out an optimal process parameter setting for higher weld quality characteristics.

In BCGA, 2 bits were chosen to represent four tool geometries (SC, TC, SQ and THRD) and 5 bits string for the tool rotation speed. The number of bits in each string of the input parameters with accuracy $\varepsilon = 0.001$ and the bounds of the input parameters and the parameters of BCGA computations are given in **Table 7.1** and **7.2** respectively.

Table 7.1 Bounds and Number of Bits used in BCGA

Parameters	Lower Bound	Upper Bound	No. of Bits in a String
Plunging depth (mm)	0.09	0.15	11
Tool rotation speed (rpm)	600	1500	5
Welding speed (mm/sec)	63	200	18
Tool geometry	1	4	2
Shoulder diameter (mm)	20	35	14
Pin diameter (mm)	5	8	12
Tool pin length (mm)	5.2	5.8	11
Dwell time (sec)	10	25	14

Table 7.2 Parameters of BCGA Computations

Operators	
Population size	50 to 500 in steps of 50
Selection process	Tournament selection
Crossover	Uniform crossover with probability between 0.1- 0.95 in a step of 0.1
Mutation	Global mutation with probability between 0-0.95 in a step of 0.05

In GA, the performance of the algorithm is influenced by population size, crossover and mutation probability. A large population size allows better exploration of the search space and reduces the chances of sticking in local optima. The variations of the maximum objective function values with different population sizes and different crossover rates are shown in **Fig. 7.6(a)** and **(b),** respectively. It can be seen from the figure that population size of 200 or more and crossover rates higher than 0.5 are giving better objective function values.

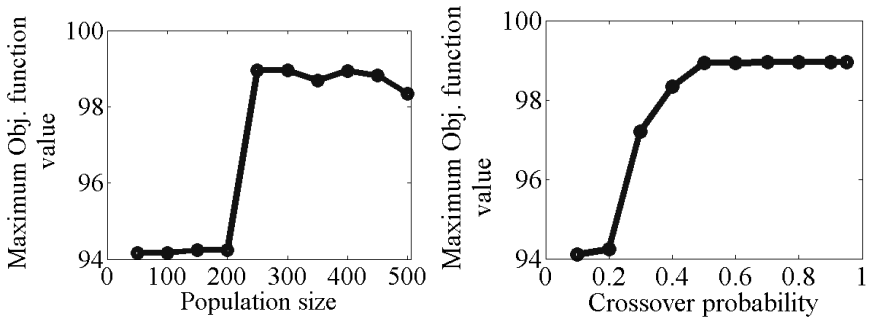

(a) (b)

Figure 7.6 Variation of maximum objective function value with (a) population size and (b) crossover rate in BCGA

Too high probability of mutation leads to much random perturbation, and the individuals of the next generation will lose the good features of the parents. On the other hand too low value results in continuing the fitter individuals to survive without any change. This causes poor exploration of the solution space. The variation of maximum objective function value with different mutation probabilities is shown in **Fig. 7.7(a)**. It can be seen that the mutation rates between 0.1 and 0.25 gave the better objective function values. The convergence of the objective function value to the optimal solution with 200 population size, 0.9 crossover rate and 0.2 mutation rate is shown in **Fig. 7.7(b)**.

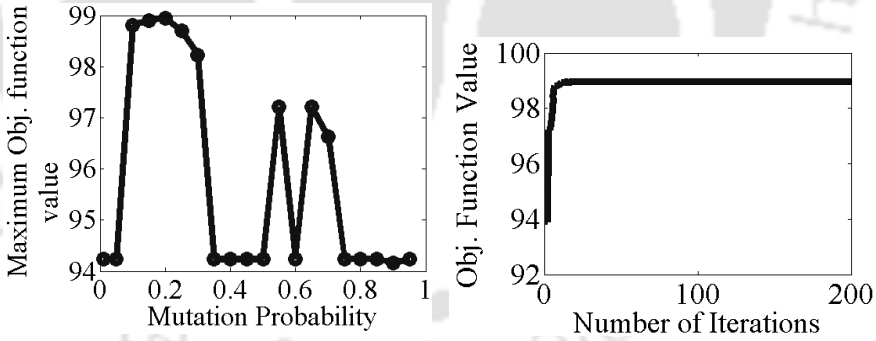

(a) (b)

Figure 7.7 Variation of maximum objective function value with (a) mutation rate and (b) number of generation in BCGA

Similar analysis was made in case of RCGA. The parameters of RCGA computations are shown in **Table 7.3**. The variations of the maximum objective function values with population sizes, crossover rates and mutation probabilities are shown in **Figs. 7.8(a-c)**, respectively. It can be seen that population size with 300 individuals or more, crossover

rates higher than 0.8 and mutation rates between 0.15 and 0.3 are giving better results. The convergence of the objective function value to the optimal solution with 400 population size, 0.95 crossover rate and 0.2 mutation rate is shown in **Fig. 7.8(d)**.

Table 7.3 Parameters of RCGA Computations

Operators	
Population size	50 to 1000 in steps of 50
Selection process	Tournament selection
Crossover	SBX crossover with probability between 0.1- 0.95 in a step of 0.1
Mutation	Random mutation with probability between 0-0.95 in a step of 0.05

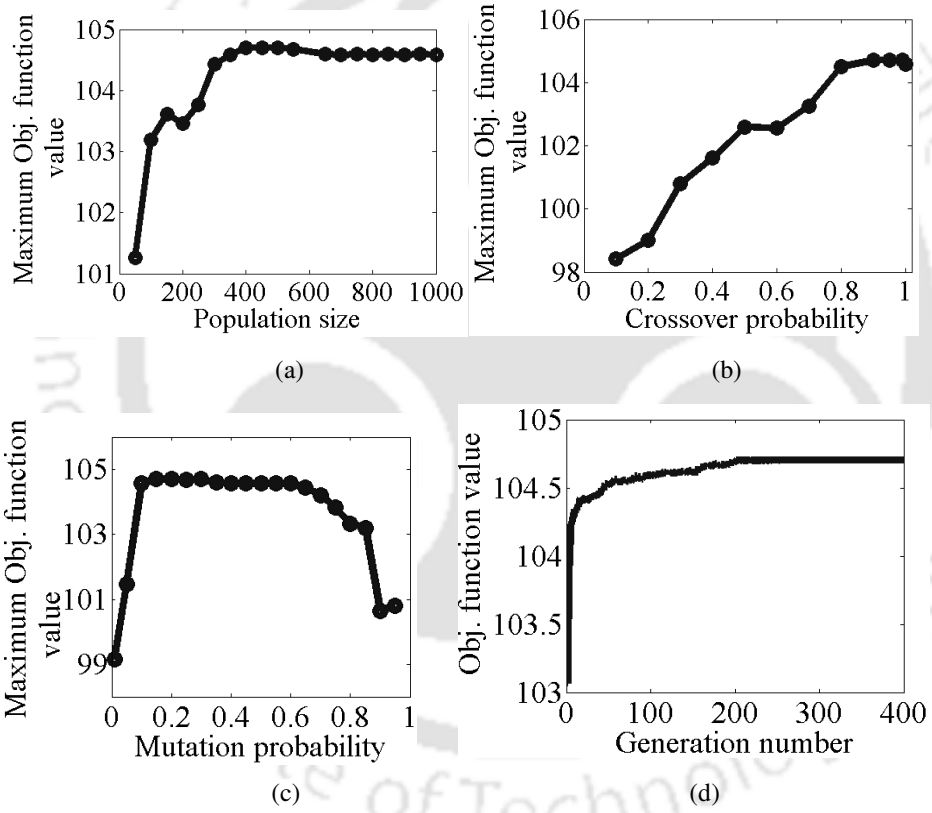

Figure 7.8 Variation of maximum objective function value for (a) different population sizes, (b) crossover rates, (c) mutation rates and (d) the number of generations by using RCGA.

In PSO, the population size, inertia component *w* and acceleration coefficients *c1* and *c2* have influence on the algorithm performance. A population size with 150 particles and more was found to give the best objective function values. The variations of maximum objective function values with population sizes are shown in **Fig. 7.9(a)**. By changing the values of the inertia component between 0 and 2 with a 0.1 step, it can be seen from the **Fig. 7.9(b)**

that values of ω less than 1.5 give better objective function values. From **Fig.7.9(c)** and **(d)**, values of *c1* higher than 1 and values of *c2* between 0.5 and 3.5 give the best maximum objective function values. By running the algorithm with ω equals to 0.9, 2 for *c1* and *c2*, 150 population size and 200 iterations, the convergence of the objective function value to the optimal solution is shown in **Fig. 7.9(e)**.

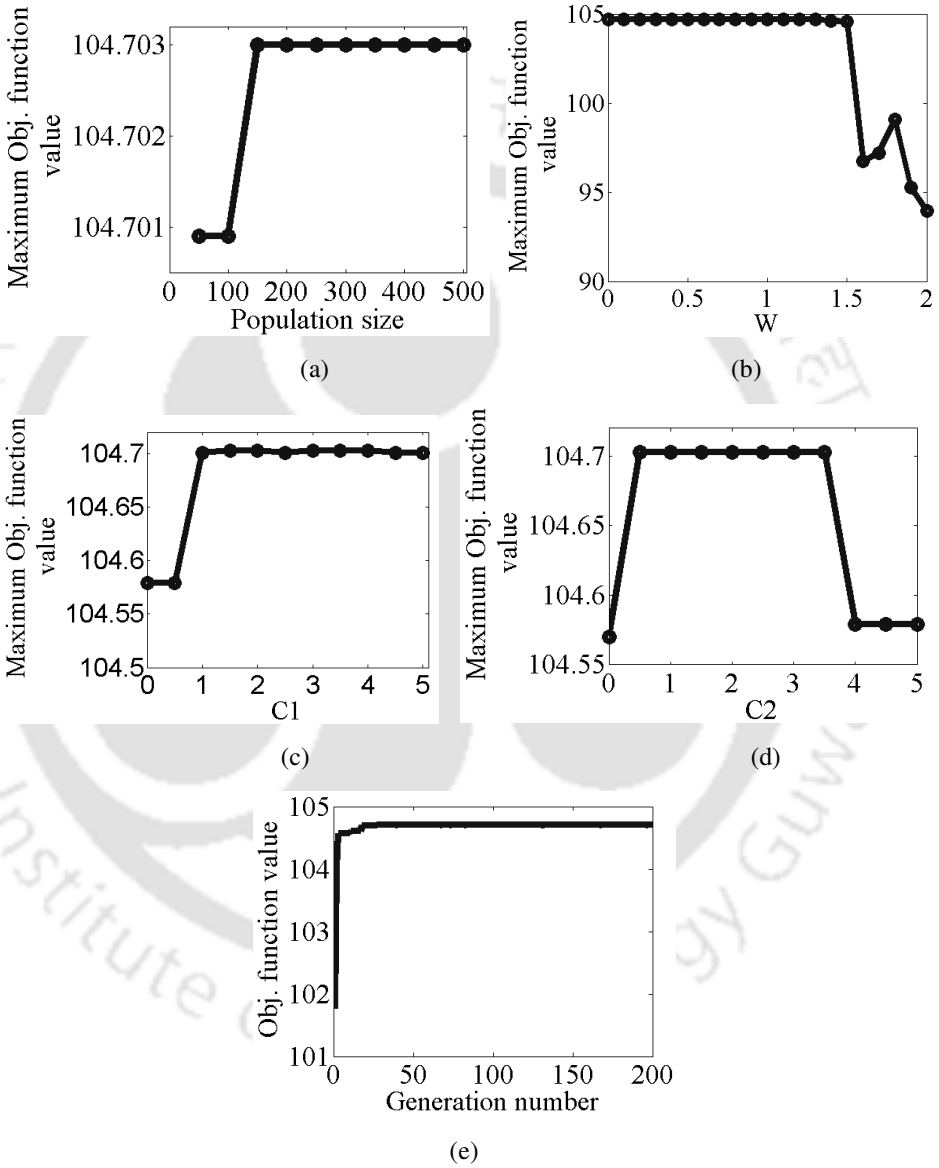

Figure 7.9 Objective function values vs (a) population size, (b) inertia component value (ω), (c) acceleration coefficient c1, (d) acceleration coefficient c2 and (e) number of generation by using PSO

The performance of DE algorithm was checked by varying population size, F factor and crossover rate. The maximum objective function value versus population size is shown in

Fig. 7.10(a). The population size was varied from 50 to 500 by a step of 50 and it can be seen that that population size more than 150 is sufficient. The factor F was varied from 0 to 2 with a step of 0.1 (shown in **Fig. 7.10(b)**) to find the best F value which will give the best objective function value. It was found that the value of 0.3 and values between 0.5 and 1.7 seem to give best results. From **Fig. 7.10(c)** it can be observed that crossover rate higher than 0.5 gives better objective function value. The convergence of DE algorithm with crossover rate of 0.5, F factor of 1.5 and population size of 150, is shown in **Fig. 7.10(d)**.

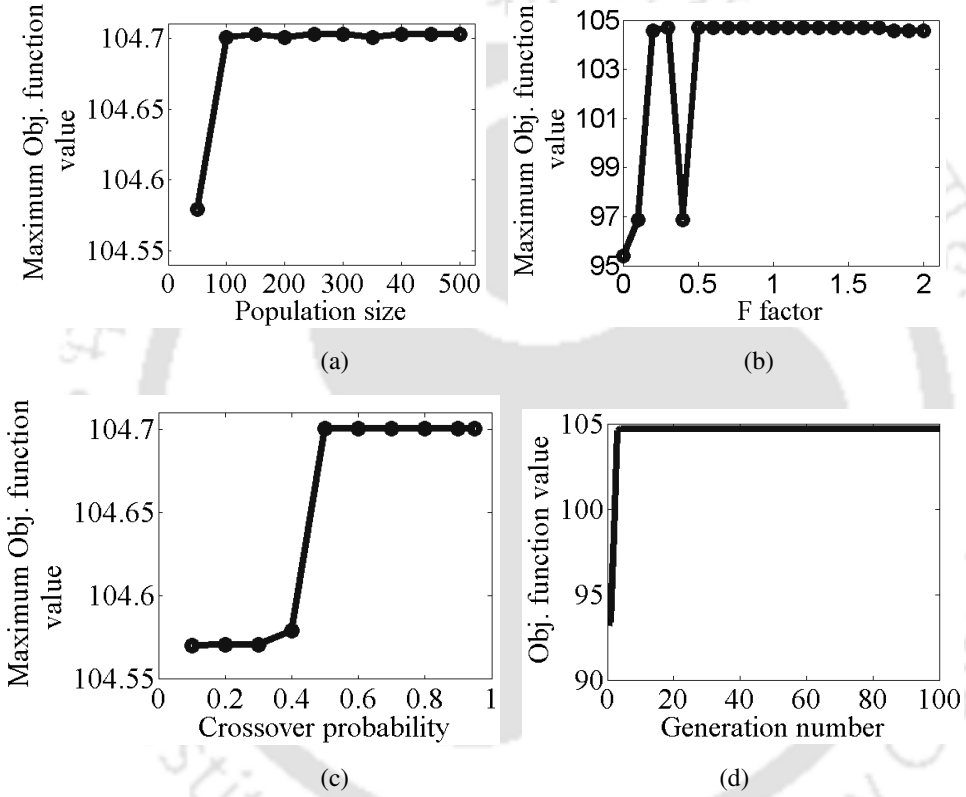

Figure 7.10 Variation of maximum objective function value with (a) population size, (b) F factor, (c) crossover rate and (d) number of iteration by using DE

The comparative results of all the techniques used in the present study are shown in **Table 7.4**. From the tabulated result it was observed that RCGA, PSO and DE algorithms gave better weld characteristics than BCGA. Moreover, PSO gives the near optimal solution with a relatively low population size and iteration number, or in other words less computation cost. Results obtained from RCGA, DE and PSO are approximately same. One confirmation experiment was conducted to confirm the best model predicted outputs. The optimum process parameters settings were rounded to near possible parameters in the FSW

machine. The measured weld quality values are 145.38 MPa (UTS), 99.25 MPa (YS), 19.98 (% Elong.), 140° (BA) and 64.1 HV (HRD). Mean absolute percentage error between models predicted and experimentally measured weld quality values was 8.89 %. Even though the error is a little bit high, the experiment gave good confirmation to the model predicted values.

Table 7.4 Results Obtained from Maximization of Weld Quality Parameters

	Parameter	BCGA	RCGA	DE	PSO
Optimum Input Parameters	Plunging depth	0.09	0.09	0.09	0.09
	RPM	1035	1500	1500	1500
	Welding speed	89.20	65.91	65.97	65.91
	Toll geometry	SQ	THRD	THRD	THRD
	Shoulder diameter	20.36	35	35	35
	Pin diameter	7.53	5	5	5
	Toll pin length	5.78	5.8	5.8	5.8
	Dwell time	17.21	11.90	11.88	11.89
Model Predicted Outputs	UTS	151.31	158.84	158.84	158.85
	Yield stress	105.10	110.37	110.37	110.35
	Elongation	15.34	24.68	24.68	24.69
	Bending angle	152.14	153.70	153.70	153.70
	Hardness	59.70	62.75	62.75	62.74
	Objective function value	98.9458	104.703	104.703	104.703

7.3.2 Determination of Optimum Input Parameters Setting for Desired Weld Quality Parameters

In the previous case (discussed in the Section 7.3.1) optimum process parameters settings were determined for maximum weld quality characteristics. Other than maximization of weld quality parameters sometime desired weld quality values are also required. Therefore, for finding the optimum process parameters setting for desired (target) weld quality characteristics following objective function was considered.

$$O_f(i) = w_1\left(\frac{UTS_t - UTS(i)}{UTS_t}\right)^2 + w_2\left(\frac{YS_t - YS(i)}{YS_t}\right)^2 + w_3\left(\frac{\%\,Elong_t - \%\,Elong(i)}{\%Elong_t}\right)^2 + w_4\left(\frac{BA_t - BA(i)}{BA_t}\right)^2 + w_5\left(\frac{HRD_t - HRD(i)}{HRD_t}\right)^2 \quad (7.9)$$

where, $O_f(i)$ is the value of the objective function of the i^{th} individual in the population; $UTS_t, YS_t, \%\,Elong_t, BA_t \text{ and } HRD_t$ are the target or desired value for the tensile strength, yield strength, elongation, bending angle and hardness of the welded joint respectively; $UTS(i), YS(i), \%\,Elong(i), BA(i) \text{ and } HRD(i)$ are the values of tensile strength, yield strength, % elongation, bending angle and nugget zone hardness for the i^{th} individual in the population respectively; w_1, w_2, w_3, w_4 and w_5 are the weights that give different status or importance to each response. The weights assigned in the present work were on the basis of importance of the response. The most important response is the UTS, followed by the yield strength, elongation, bending angle and hardness. So the weights were 0.25 for UTS and yield strength, 0.2 for elongation and 0.15 both for bending angle and nugget zone hardness.

In this case, two target values were considered. Target value 1 was the best quality parameters which were obtained from the maximization of FSW process using RCGA, PSO and DE. Target value 2 was arbitrary desired weld quality parameters. These desired weld quality parameters are shown in **Table 7.5**.

Table 7.5 Desired Weld Quality Parameters

	Desired Quality Parameters				
Parameters	**UTS (MPa)**	**YS(MPa)**	**Elong. (%)**	**BA (°)**	**HRD**
Target Values 1	158.84	110.37	24.68	153.70	62.75
Target Values 2	130	100	20	140	50

Similar procedure that was used for the first objective function (*i.e.*, maximization of quality parameters) was used to obtain best parameters for each of the proposed algorithm. For BCGA 300 population size, 0.9 crossover rate and 0.2 mutation rate were found the best parameters. The objective function (**Eq. 7.9**) value versus the iteration number is shown in **Fig. 7.11(a)**. The variation of objective function value for RCGA with 400 population size,

0.95 crossover rate and 0.2 mutation rate is shown in **Fig. 7.11(b)**. Similarly, the variation of objective function values for DE and PSO are shown in **Figs. 7.11(c)** and **(d)**, respectively. The optimum input parameter settings and the model predicted outputs corresponding to target value 1 and target value 2 are shown in **Table 7.6** and **7.7**, respectively. In both the cases RCGA, DE and PSO were able to find approximately the same near optimum weld characteristics which are better than BCGA.

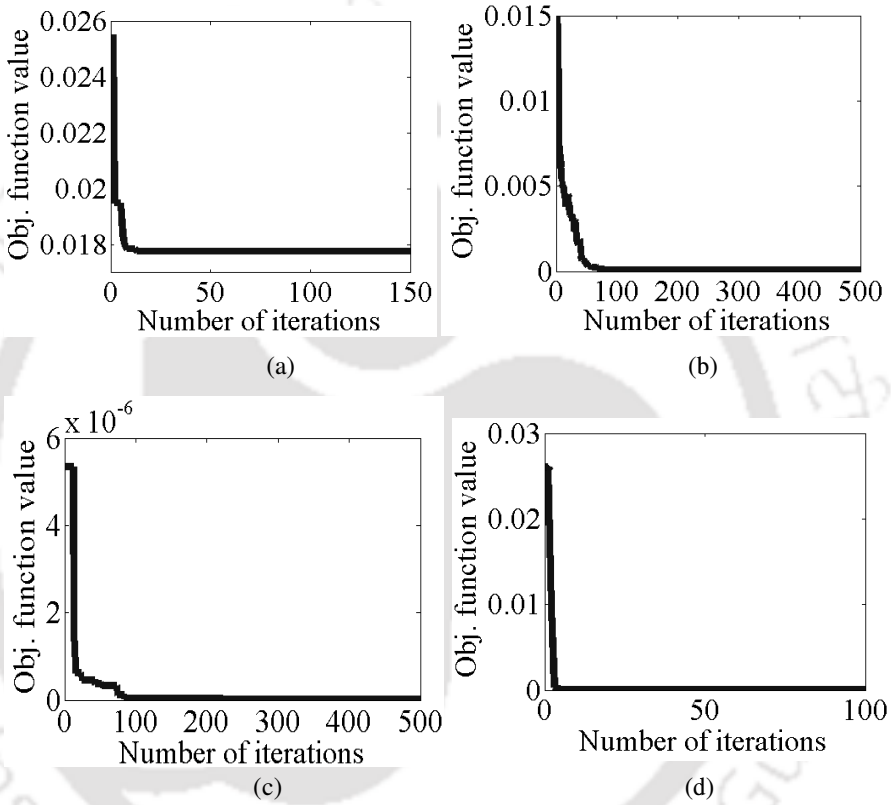

Figure 7.11 The objective function value vs. the iteration number for (a) BCGA, (b) RCGA, (c) DE and (d) PSO

Table 7.6 Optimized Parameter Settings with Model Predicted Weld Quality for Target Value 1

	Parameter	BCGA	RCGA	DE	PSO
Optimum Input Parameters	Plunging depth	0.0962	0.0908	0.09	0.09
	RPM	1245	1487	1500	1500
	Welding speed	79.7694	64.8569	65.99	65.8718
	Tool geometry	SQ	THRD	THRD	THRD
	Shoulder diameter	21.1641	33.9686	34.9714	35
	Pin diameter	7.8975	5.0411	5	5
	Tool pin length	5.8	5.7856	5.8	5.8

	Dwell time	17.15	10.2057	11.8718	11.8974
Model Predicted Outputs	UTS	150.324	157.8858	158.8359	158.8537
	Yield stress	101.9072	109.551	110.3636	110.3494
	Elongation	16.8488	24.6158	24.6793	24.6809
	Bending angle	141.5896	153.7778	153.6955	153.6913
	Hardness	60.8579	63.6864	62.7532	62.7367
	Objective function value	0.018	5.76E-05	1.74E-09	1.31E-08

Table 7.7 Optimized Parameter Settings with Model Predicted Weld Quality for Target Value 2

	Parameter	**BCGA**	**RCGA**	**DE**	**PSO**
Optimum Input Parameters	Plunging depth	0.0959	0.1012	0.1041	0.1039
	RPM	832.2581	601	600	600
	Welding speed	82.5395	63.4215	63	63
	Toll geometry	THRD	SQR	SQR	SQR
	Shoulder Diameter	25.8925	20.4008	20.1143	20
	Pin diameter	5.1406	7.2748	7.0064	7.0336
	Toll pin length	5.5071	5.7934	5.8	5.8
	Dwell time	13.838	22.7782	22.8014	22.9076
Model Predicted Outputs	UTS	132.8219	133.9478	129.896	130.4584
	Yield stress	94.6741	98.4154	100.585	100.55
	Elongation	18.261	19.7293	19.8631	19.9867
	Bending angle	129.8933	140.8372	138.7833	138.8176
	Hardness	56.9566	50.814	51.3287	51.2923
	Objective function value	0.006	2.76E-04	1.35E-04	1.22E-04

7.3.3 Confirmation Test Results

To check the adequacy of the modelling and optimization procedure, four confirmation experiments were conducted. The input parameters were taken from **Table 7.6** and **7.7** and rounded to the near possible parameters in the FSW machine. The first experiment was performed for checking the optimum solution of BCGA for the target value 1. The second one was for checking the value obtained from RCGA, DE and PSO result for target value 1. The third and fourth experiments were for checking the target value 2 for BCGA and RCGA, DE and PSO results, respectively. Experimental weld characteristics with corresponding model predicted outputs and percentage errors are shown in **Table 7.8**. Although experimental results for target value 1 were good, the error was relatively high.

This is because of the error in prediction of ANN models and limitation of FSW machine to give input parameter setting exactly as predicted ones. Also the bending test machine can't test more than 140° bending angle. For target value 2, error was lower and the experiments gave good confirmation of the predicted values. The reason behind this is the predicted input parameter settings were very close to that possible in FSW machine.

Table 7.8 Comparison between Experimental and Model Predicted Weld Characteristics

Cases	Optimization Techniques		UTS	YS	% Elong	BA (°)	HRD	Mean Absolute Errors
Target Value 1	BCGA	Predicted Values	151.31	105.10	15.34	152.14	59.70	10.82%
		Experimental values	139.26	86.34	12.32	140.00	57.70	
		% Error	-8 %	-17 %	-17.8%	-8 %	-3.3 %	
	RCGA, DE and PSO	Predicted Values	158.83	110.36	24.68	153.69	62.75	9.85%
		Experimental values	145.38	99.25	19.98	140	64.1	
		% Error	-8.2 %	-10 %	-20 %	-8.9 %	+2.15 %	
Target Value 2	BCGA	Desirable Values	130	100	20	140	50	8.49%
		Experimental values	130.38	93.02	17.16	140	60.5	
		% Error	+0.29 %	-6.98 %	-14.2 %	0 %	+21 %	
	RCGA, DE and PSO	Desirable Values	130	100	20	140	50	6.58%
		Experimental values	121.706	92.38	16.5	140	50.7	
		% Error	-6.38 %	-7.62 %	-17.5 %	0 %	+1.4 %	

7.4 Observations

The following observations have been made from the above optimization studies.

- The Neuro-EA approach could be a powerful tool in welding process optimization with a relatively small number of experiments.
- BCGA gave an optimal input parameter setting of PD-0.09 mm, RPM-1035 rev/min, WS-89.20 mm/min, TG-SQ, SD-20.36 mm, PnD-7.53 mm, TPL-5.77 mm and DT-17.21 with a predicted output response values of UTS-151.31 MPa, YS-105.09 MPa,

% Elng.-15.34, BA-152.14° and HRD-59.7 HV and objective function value of 98.94.

- Whereas RCGA, PSO and DE algorithms gave an optimal input parameter setting of PD-0.09 mm, RPM-1500 rev/min, WS-66.50 mm/min, TG-THRD, SD-35 mm, PnD-5 mm, TPL-5.8 mm and DT-11.89 with a predicted output response values of UTS-150.40 MPa, YS-118.62 MPa, % Elng.-26.55, BA-154.04° and HRD-62.76 HV and objective function value of 104.703.
- The neuro-EA techniques were found to be suitable both for determining optimum parameter setting for maximization of weld qualities and for desired weld quality parameters.
- RCGA, PSO and DE algorithms gave better optimal FSW weld characteristics than BCGA.
- PSO gives the optimal solution with a relatively low population size and iteration number, or in other words less computation cost.
- The mean absolute error values for target value 1 and 2 are 10.8% and 8.49%, respectively, in case of BCGA. The error values are 9.85% and 6.58% for target values 1 and 2, respectively, for RCGA, PSO and DE.
- For both the target values, mean absolute error was found to be less than 10% and the experiments gave good confirmation of the predicted values.

7.5 Major Findings

From the aforementioned optimization studies and conformational tests following major conclusions can be made:

a) Out of the four hybrid optimization techniques PSO method gave better optimal process parameters leading to improved friction stir welded joint quality. It gave the optimal solution with a relatively low population size and iteration number lowering the computational cost.

b) The proposed Neuro-EA techniques can not only be used for determining optimum parameter setting for maximization of weld qualities but also for desired weld quality parameters with a mean absolute error value of less than 10%.

Chapter 8

Conclusions and Future Scopes of Investigation

8.1 Conclusions of the Present Work

Welding is a prominent area in joining of materials. Its wide range of applications in almost every industrial sector made it the most effective joining technique. The quality of a weld is a key issue, and in many cases a weld must fulfill some specific quality requirements. Among all, FSW is a solid state welding technique developed to join especially light weight structural materials like Al, Mg etc. The main limitation in adopting this technique in small scale industrial sectors lies in the requirement of a high cost sophisticated FSW machine. Alternatively, milling machine can be used for FSW operations but it needs a special type of fixture. The purpose of an appropriate fixture is to hold the workpiece rigidly against the vertically downward force and traverse force exerted by the FSW tool during the welding process. Though every process has a number of parameters, for successful implementation there is a need to know the most influencing parameters and their effect on process outputs. Development of a reliable technique for modeling of FSW process to predict the joint quality will be helpful. These models can be applied to optimize the process to obtain the best input parameter setting for the optimum or desired product (or process) quality. This will lead to reduce the material wastage and overall production time.

In the present work a low cost clamping device to carry out welding operations on a conventional milling machine has been developed and fabricated. A detailed experimental

investigation was carried out considering most number of FSW process parameters with the help of Taguchi's design of experiment approach. Significant input parameters were identified on the basis of Taguchi's single response as well as Taguchi coupled multi response analysis techniques. A newly developed fuzzy assisted grey relational analysis (FZ-GRA) technique for finding out the optimal FSW parameter setting is also proposed. Effect of significant process parameters on joint properties have been studied using full factorial design of experiments. The solutions to FSW process limitations such as appropriate starting point and remaining end hole were provided. ANN models have been developed to predict the weld quality. Finally, hybrid Neuro-evolutionary optimization techniques are used to obtain the optimum process parameters settings.

The conclusions that can be drawn from the present research work are listed as follows:

- The developed fixture was successful to carry out FSW operations in milling machine. It is simple and significantly reduces setup time.
- Among all the considered parameters, the three most significant parameters of the FSW process are spindle speed, tool geometry and pin diameter.
- The starting issue can be resolved by using an appropriate restriction plate and commence the welding 1 to 5 mm away for the starting edge of the workpiece.
- The end hole defect can be eliminated by providing a suitable solid Al piece.
- The prediction performance of the developed ANN models are good and it is less than an average error of 5% for the best models (i.e., RBFN model for UTS, YS, % Elng. and BA and BPNN model for HRD). The prediction capabilities of RBFN models are found to be better as compared to BPNN models for overall joint properties.
- Out of four hybrid optimization techniques, RCGA, PSO and DE algorithms gave better optimal weld characteristics than BCGA. But PSO gives the optimal solution with a relatively low population size and iteration number *i.e.* in less computational cost. The proposed techniques can not only be used for maximization of joint but also for required weld quality parameters with a mean absolute error value of less than 10%.

8.2 Scopes for Future Work

Based on this work, the following areas are suggested for further research:

- Since the time of invention a great deal of progress has been made in implementing FSW in production of aluminum structures. This process is most suitable for components which are flat and long (plates and sheets) used in present work, but can be adapted for pipes and hollow sections welding.
- A third material at the joint could be introduced in the form of powder or sheet to improve the joint properties especially in case of aluminium joints.
- Some hybrid FSW techniques in which external heat sources like plasma, high frequency induction heating or electrical heating etc. can be used to increase the welding speed significantly.
- The present research concentrates only on aluminium workpiece of 6 mm thickness. But various materials of different thicknesses are joined by FSW in different manufacturing industries. So, the joint quality prediction for different materials of different thicknesses should be incorporated into the proposed models.
- In this work, BPNN and RBFN models have been used for weld quality prediction. Other ANN models like, support vector machine, Bayesian network etc. can be used and newer models can be compared with the present model. Similarly, NSGA-III (non-dominated sorting genetic algorithm) and multi-objective PSO can also be used for optimization of weld quality parameters.
- Other quality parameters, like, toughness, grain sizes etc. and other metallurgical properties of the joint can be incorporated in the proposed models.

References

Acerra, F., Buffa, G., Fratini, L. and Troiano, G. (2010), Int. J. Adv. Manuf. Techno.: On the FSW of AA2024-T4 and AA7075-T6 T-joints: An industrial case study, Vol. 48, pp. 1149-1157.

Adamowski, J. and Szkodo, M. (2007), Journal of Achievements in materials and Manufacturing Engineering: Friction stir welds (FSW) of aluminum alloy AW6082-T6, Vol. 20, pp. 403-406.

Ahmed, M. M. Z., Wynne, B. P., Rainforth, W. M. and Threadgill, P. L. (2011), Scripta. Mater.: Through-thickness crystallographic texture of stationary shoulder friction stir welded aluminium, Vol. 64, pp. 45-48.

Ahmed, M. M. Z., Wynne, B. P., Rainforth, W. M. and Threadgill, P. L. (2012), Mater. Charact.: Microstructure, crystallographic texture and mechanical properties of friction stir welded AA2017A, Vol. 64, pp. 107-117.

Allen, C. D. and Arbegast, W. J. (2005), SAE International: Evaluation of friction spot welds in aluminium alloys, SAE technical paper no. 2005-01-1252, Warrendale, PA, USA.

Aonuma, M. and Nakata, K. (2012), Mater. Sci. Eng. B: Dissimilar metal joining of ZK60 magnesium alloy and titanium by friction stir welding, Vol. 117, pp. 543-548.

Arici, A. and Selale, S. (2007), Sci. Technol. Weld. Joi.: Effects of tool tilt angle on tensile strength and fracture locations of friction stir welding of polyethylene, Vol. 6, pp. 536-539.

Arora, A., Deb, A. and DebRoy, T. (2011), Scripta. Mater.: Toward optimum friction stir welding tool shoulder diameter, Vol. 64, pp. 9-12.

Arora, A., DebRoy, T. and Bhadeshia, H. K. D. H. (2011), Acta. Materialia.: Back-of-the-envelope calculations in friction stir welding-Velocities, peak temperature, torque, and hardness, Vol. 59, pp. 2020-2028.

Arora, A., Mehta, M., De, A. and DebRoy, T. (2012), Int. J. Adv. Manuf. Technol.: Load bearing capacity of tool pin during friction stir welding, Vol. 61, pp. 911-920.

Arora, A., Nandan, R., Reynolds, A. P. and DebRoy, T. (2009), Scripta. Mater.: Torque, power requirement and stir zone geometry in friction stir welding through modeling and experiments, Vol. 60, pp. 13-16.

Arora, A., Zhang, Z., De, A. and DebRoy, T. (2009), Scripta. Mater.: Strains and strain rates during friction stir welding, Vol. 61, pp. 863-866.

Arora, K. S., Pandey, S., Schaper, M. and Kumar, R. (2010), Int. J. Adv. Manuf. Techno.: Effect of process parameters on friction stir welding of aluminum alloy 2219-T87, Vol. 50, pp. 941-952.

Arora, K. S., Pandey, S., Schaper, M. and Kumar, R. (2010), J. Mater. Sci. Technology: Microstructure evolution during friction stir welding of aluminum alloy AA2219, Vol. 26, pp. 747-753.

Atharifar, H., Lin, D. and Kovacevic R. (2009), JMEPEG: Numerical and experimental investigations on the loads carried by the tool during friction stir welding, Vol. 18, pp. 339-350.

Attallah, M. M., Claire, L. D. and Strangwood, M. (2007), J. Mater. Sci.: Microstructure-microhardness relationships in friction stir welded AA525, Vol. 42, pp. 7299-7306.

References

Aval, H. J., Serajzadeh, S. and Kokabi, A. H. (2011a), Int. J. Adv. Manuf. Techno.: Theoretical and experimental investigation into friction stir welding of AA 5086, Vol. 52, pp. 531-544.

Aval, H. J., Serajzadeh, S. and Kokabi, A. H. (2011b), J. Mater. Sci.: Thermo-mechanical and microstructural issues in dissimilar friction stir welding of AA5086–AA6061, Vol. 46, pp. 3258-3268.

Aval, K. H. J., Serajzadeh, S., Kokabi, A. H. and Loureiro, A. (2011c), Sci. Technol. Weld. Joi.: Effect of tool geometry on mechanical and microstructural behaviors in dissimilar friction stir welding of AA 5086-AA 6061, Vol. 16, pp. 597-604.

Aydin, H., Bayram, A., Esme, U., Kazancoglu, Y. and Guven, O. (2010), Materials and Technology: Application of grey relation analysis (GRA) and Taguchi method for the parametric optimization of friction stir welding (FSW) process, Vol. 44, pp. 205-211.

Aydin, H., Tutar, M., Durmus¸ A., Bayram, A. and Sayaca, T. (2012), T. Indian I. Matals.: Effect of welding parameters on tensile properties and fatigue behavior of friction stir welded 2014-T6 aluminum alloy, Vol. 65, No. 1, pp. 21-30.

Azimzadegan, T. and Serajzadeh, S. (2010), J. Mater. Eng. Perform.: An investigation into microstructures and mechanical properties of aa7075-t6 during friction stir welding at relatively high rotational speeds, Vol. 19, No. 9, pp. 1256-1263.

Baghel, P. K. (2012), Innovative Systems Design and Engineering: Design and development of Fixture for Friction Stir Welding, Vol. 12, pp. 40-47.

Bakavos, D., Chen, Y., Babout, L. and Prangnell, P. (2011), Metall. Mater. Trans. A: Material interactions in a novel pinless tool approach to friction stir spot welding thin aluminum sheet, Vol. 42, No. 5, pp. 1266-1282.

Balasubramanian, V. (2008), Mater. Sci. Eng. A: Relationship between base metal properties and friction stir welding process parameters, Vol. 480, pp. 397-403.

Barcellona, A., Buffa, G., Fratini, L. and Palmeri, D. (2006), J. Mater. Process. Tech.: On microstructural phenomena occurring in friction stir welding of aluminium alloys, Vol. 177, pp. 340-343.

Barlas, Z. and Ozsarac, U. (2012), Weld. J.: Effects of FSW parameters on joint properties of $AlMg_3$ Alloy, Vol. 91, pp. 16-22.

Barnes, S. J., Bhatti, A. R., Steuwer, A., Johnson, R., Altenkirch, J. and Withers, P. J. (2012), Metall. Mater. Trans. A: Friction stir welding in HSLA-65 steel: Part I. influence of weld speed and tool material on microstructural development, Vol. 43, No. 7, pp. 2342-2355.

Biswas, P. and Mandal, N. R. (2011), Weld. J.: Effect of tool geometries on thermal history of FSW of AA1100, Vol. 90, pp. 129-135.

Bitondo, C., Prisco, U., Squilace, A., Buonadonna, P. and Dionoro, G. (2011), Int. J. Adv. Manuf. Techno.: Friction-stir welding of AA 2198 butt joints: mechanical characterization of the process and of the welds through DOE analysis, Vol. 53, pp. 505-516.

Bitondo, C., Prisco, U., Squillace, A., Giorleo, G., Buonadonna, P., Dionoro, G. and Campanile, G. (2010), Int. J. Mater. Form.: Friction stir welding of AA 2198-T3 butt joints for aeronautical applications, Vol. 3, pp. 1079-1082.

Blignault, C., Hattingh, D. G. and James, M. N. (2012), J. Mater. Eng. Perform.: Optimizing friction stir welding via statistical design of tool geometry and process parameters, doi: 10.1007/s11665-011-9984-2.

Boz, M. and Kurt, A. (2004), Mater. Design.: The influence of stirrer geometry on bonding and mechanical properties in friction stir welding process, Vol. 25, pp. 343-347.

Bozkurt, Y. (2012), Mater. Design.: The optimization of friction stir welding process parameters to achieve maximum tensile strength in polyethylene sheets, Vol. 35, pp. 440-445.

Bozkurt, Y. and Bilici, M. K. (2013), Mater. Design.: Application of Taguchi approach to optimize of FSSW parameters on joint properties of dissimilar AA2024-T3 and AA5754-H22 aluminum alloys, Vol. 51, pp. 513-521.

Brown, R., Tang, W. and Reynolds, A. P. (2009), Mater. Sci. Eng. A: Multi-pass friction stir welding in alloy 7050-T7451: Effects on weld response variables and on weld properties, Vol. 513-514, pp. 115-121.

Buffa, G., Fratini, L. and Micari, F. (2012), J. Manuf. Process.: Mechanical and microstructural properties prediction by artificial neural networks in FSW processes of dual phase titanium alloys, Vol. 14, pp. 289-296.

Buffa, G., Fratini, L. and Ruisi, V. (2009), Int. J. Mater. Form.: Friction stir welding of tailored joints for industrial applications, Vol. 2, pp. 311-314.

Buffa, G., Fratini, L., Arregi, B. and Penalva, M. (2010), Int. J. Mater. Form.: A new friction stir welding based technique for corner fillet joints: Experimental And numerical study, Vol. 3, pp. 1039-1042.

Cabibbo, M., McQueen, H. J., Evangelist, E., Spigarelli, S., Paol, M. D. and Falchero, A. (2007), Journal of Mater. Sci. Eng. A: Microstructure and mechanical property studies of AA6056 friction stir welded plate, Vol. 460-461, pp. 86-94.

Çam, G., Mistikoglu, S. and Pakdil, M. (2009), Weld. J.: Microstructural and mechanical characterization of friction stir butt joint welded 63% Cu-37% Zn brass plate, Vol. 11, pp. 225-232.

Cavaliere, P., Squillace, A. and Panell, F. (2008), J. Mater. Process. Tech.: Effect of welding parameters on mechanical and microstructural properties of AA6082 joints produced by friction stir welding, Vol. 200, pp. 364-372.

Cerri, E. and Leo, P. (2009), Journals for Mater. Design.: Warm and room temperature deformation of friction stir welded thin aluminum sheets, Vol. 31, pp. 1392-1402.

Cerri, E., Leo, P., Wang, X. and Embury, J. D. (2010), Metall. Mater. Trans. A: Mechanical properties and microstructural evolution of friction-stir-welded thin sheet aluminum alloys, Vol. 42, No. 5, pp. 1283-1295.

Ceschini, L., Boromei, I., Minak, G., Morri, A. and Tarterini, F. (2007), Composites Part A: Applied Science and Manufacturing : Microstructure, tensile and fatigue properties of AA6061/20 vol.% Al_2O_3p friction stir welded joints, Vol. A 38, No. 4, pp. 1200-1210.

Chao, Y. J., Wang, Y. and Miller, K. W. (2001), Weld. J.: Effect of friction stir welding on dynamic properties of AA2024-T3 and AA7075-T7351, Vol. 8, pp. 196-200.

Chen, C., Kovacevic, R. and Jandgric, D. (2003), Int. J. Mach. Tool Manu.: Wavelet transform analysis of acoustic emission in monitoring friction stir welding of 6061 aluminum, Vol. 43, pp. 1383-1390.

Chen, J., Fujii, H., Sun, Y., Morisada, Y. and Ueji, R. (2013), Mater. Sci. Eng.A: ne grained Mg-3Al-1Zn alloy with randomized texture in the double-sided friction stir welded joints, Vol. 580, pp. 83-91.

Chen, J., Fujii, H., Sun, Y., Morisada, Y., Kondoh, K. and Hashimoto, K. (2012), Mater. Sci. Eng. A: Effect of grain size on the microstructure and mechanical properties of friction stir welded non-combustive magnesium alloys, Vol. 549, pp. 176-184.

Chen, K. E., Gan, W., Okamoto, K., Chung, K. and Wagoner, R. H. (2011), Matall. Mater. Trans. A: The Mechanism of Grain Coarsening in Friction-Stir-Welded AA5083 after Heat Treatment, Vol. 42, No. 2, pp. 488-507.

Chen, T. (2009), J. Mater. Sci.: Process parameters study on FSW joint of dissimilar metals for aluminum–steel, Vol. 44, pp. 2573-2580.

Chien, C. H., Lin, W. B. and Chen, T. (2011), J. Chin. Inst. Eng.: Optimal FSW process parameters for aluminum alloys AA5083, Vol. 34, pp. 99-105.

Cho, H. H., Han, H. N., Hong, S. T., Park, J. H., Kwon, Y. J., Kim, S. H. and Steel, R. J. (2011), Mater. Sci. Eng. A: Microstructural analysis of friction stir welded ferritic stainless, Vol. 528, pp. 2889 - 2894.

Cho, H. H., Kang, S. H., Kim, S. H., Oh, K. H., Kim, H. J., Chang, W. S. and Han, H. N. (2012), Mater. Design.: Microstructural evolution in friction stir welding of high-strength linepipe steel, Vol. 34, pp. 258-267.

Colegrove, P. A., Shercliff, H. R. and Zettler, R. (2007), Science and Technology of Welding & Joining: A model for predicting the heat generation and temperature in friction stir welding from the material properties, Vol. 12, No. 4, pp. 284-297

Colligan, K. (1999), Weld. J.: Material flow behavior during friction stir welding of aluminum, Vol. 7, pp. 229-237.

Colligan, K. J., Xu, J. and Pickens, J. R. (2003), Proceedings of a Symposium; TMS Annual Meeting: Welding tool and process parameter effects in friction stir welding of aluminum alloys friction stir welding and processing II, pp. 181-190.

Costa, N. R., Lourenco, J. and Pereira, Z. L. (2011), Chemometr Intell Lab Syst.: Desirability function approach: A review and performance evaluation in adverse conditions, Vol. 107, pp. 234-44.

Cruz, J. (2013), EWI: Detecting flaws in FSW can be a tough proposition.

Cui, L., Fujii, H., Tsuji, N. and Nogi, K. (2007), Scripta. Mater.: Friction stir welding of a high carbon steel, Vol. 56, pp. 637-640.

Cui, L., Yang, X., Zhou, G., Xu, X. and Shen, Z. (2012), Mater. Sci. Eng. A: characteristics of defects and tensile behaviors on friction stir welded AA6061-T4 T-joints, Vol. 543, pp. Pages 58-68.

D'Urso, G. and Giardini, C. (2010), Int. J. Mater. Form.: The influence of process parameters and tool geometry on mechanical properties of friction stir welded aluminum lap joints, Vol. 3, pp. 1011-1014.

Dalder, E., Pastrnak, J. W., Engel, J., Forrest, R. S., Kokko, E., Mcternan, K. and Waldron, D. (2008), Weld. J.: Friction stir welding of thick-walled aluminum pressure vessels, Vol. 4, pp. 40-44.

Datta, S., Bandyopadhyay, A. and Pal, P. K. (2008), Int. J. Adv. Manuf. Techno.: Grey-based Taguchi method for optimization of bead geometry in submerged arc bead-on-plate welding, Vol. 39, pp. 1136-1143.

David. P. Yan, Guy Littlefair, Zhan. and W. Chen (2010), The 11th MPMD Global Innovations Symposium: Global Innovations in Manufacturing of Aerospace Materials: Material flow forming the shoulder flow zone using scroll shoulder tool during friction stir welding of thick section aluminum alloys, pp. 323-329.

Davis, T. A., Ngo, P. D. and Shin, Y. C. (2012), Int. J. Adv. Manuf. Techno.: Multi-level fuzzy control of friction stir welding power, Vol. 59, pp. 559-567.

Davis, T. A., Shin, Y. C. and Yao, B. (2010), IEEE/ASME Transactions on Mechatronics: Observer based adaptive robust control of friction stir welding axial force, Vol. 16, No. 6, pp. 1032-1039.

De, A., Bhadeshia, H. K. D. H. and DebRoy, T. (2014), Material Science and Technology: Friction stir welding of mild steel - tool durability and steel microstructure, Vol. 30, pp. 1050-1056.

De, A., Bhadeshia, H. K. D. H. and DebRoy, T. (2014), Materials Science and Technology: Friction Stir Welding of Mild Steel - Tool Durability and Steel Microstructure, Vol. 30, pp. 1050-1056.

Deb, K. (1996), Optimization for engineering design, New Delhi: Prentice hall of India (p) ltd., 1st Edition.

Deb, K. (2001), Multi-objective optimization using evolutionary algorithms, New Delhi: Wiley India, 1st Edition.

DebRoy, T., De, A., Bhadeshia, H. K. D. H. Manvatkar, V. D. and Arora, A. (2015), Proc. R. Soc. A: To ol durability maps for friction stir welding of an aluminium alloy.

Deqing, W. and Shuhua, L. (2004), J. Mater. Sci.: Study of friction stir welding of aluminum, Vol. 39, pp. 1689-1693.

Derek, W. B. (1982), Analysis of Optimal Decisions: John Wiley and Sons, New York.

Derringer, G, and Suich, R, (1980), J. Qual. Technol.: Simultaneous optimization of several response variables, Vol.4, pp. 214-219.

Dey, V., Pratihar, D. K., Datta, G. L., Jha, M. N., Saha, T. K. and Bapat, A. V. (2009), J. Mater. Process. Tech.: Optimization of bead geometry in electron beam welding using a genetic algorithm, Vol. 209, pp. 1151-1157.

Dhas, J. E. R. and Kumanan, S. (2011), Appl. Soft. Comput.: Optimization of parameters of submerged arc weld using non-conventional techniques, Vol. 11, No. 8, pp. 5198-5204.

Dinaharan, I. and Murugan, N. (2012), Mater. Sci. Eng. A: Effect of friction stir welding on microstructure, mechanical and wear properties of AA6061/ZrB_2 in situ cast composites, Vol. 543, pp. 257-266.

Dinaharan, I. and Murugan, N. (2012), Met. Mater. Int.: Optimization of friction stir welding process to maximize tensile strength of AA6061/ZrB_2 In-Situ composite butt joints, Vol. 18, pp. 135-142.

Ding, R. J. and Oelgoetz, A. (1996), US patent no. 5,893,507, US Government through the National Aeronautics and Space Administration, Greenbelt, MD, USA. The hydraulic controlled auto adjustable pin tool for friction stir welding.

Donati, L., Tomesani, L. and Morri, A. (2009), Int. J. Mater. Form.: Structural T-joint produced by means of friction stir welding (FSW) with filling material, Vol. 2, pp. 295-298.

Dumont, M., Steuwer, A., Deschamps, A., Peel, M. and Withers, P.J. (2006), Acta Materialia: Microstructure mapping in friction stir welds of 7449 aluminium alloy using SAXS, Vol. 54, pp. 4793-4801.

Durdanovic, M. B., Mijajloric, M. M., Milcic, D. S. and Stamenkovic, D. S. (2009), Tribology in Industry: Heat generation during friction-stir-welding (FSW) process, Vol. 31, pp. 8-14.

D'Urso, G., Ceretti, E., Giardini, C. and Maccarini, G. (2009), Int. J. Mater. Form.: The effect of process parameters and tool geometry on mechanical properties of friction stir welded aluminum butt joints, Vol. 2, pp. 303-306.

Dutta, P. and Pratihar, D. K. (2007), J. Mater. Process. Tech.: Modeling of TIG welding process using conventional regression analysis and neural network-based approaches, Vol. 184, pp. 56-68.

Eberl, I., Hantrais, C., Ehrtsrom, J. C. and Nardin, C. (2010), Sci. Technol. Weld. Joi.: Friction stir welding dissimilar alloys for tailoring properties of aerospace parts, Vol. 15, pp. 699-705.

El Rayes, M. M., El Danaf, E. A. and Soliman, M. S. (2011), Mater. Design.: High-temperature deformation and enhanced ductility of friction stir processed-7010 Aluminum Alloy, Vol. 32, pp. 1916-1922.

Elangovan, K. and Balasubramanian, V. (2007), Mater. Sci. Eng. A: Influences of pin profile and rotational speed of the tool on the formation of friction stir processing zone in AA2219 aluminium alloy, Vol. 459, pp. 7-18.

Elangovan, K. and Balasubramanian, V. (2008a), Mater. Design.: Influences of tool pin profile and tool shoulder diameter on the formation of friction stir processing zone in AA6061 aluminium alloy, Vol. 29, pp. 362-373.

Elangovan, K. and Balasubramanian, V. (2008b), International J. Mater. Process. Tech.: Influences of tool pin profile and welding speed on the formation of friction stir processing zone in AA2219 aluminium alloy, Vol. 200, pp. 163-175.

Elangovan, K., Balasubramanian, V., Valliappan, M. (2008c), Int. J. Adv. Manuf. Tech.: Influences of tool pin profile and axial force on the formation of friction stir processing zone in AA6061 aluminium alloy, Vol. 38, pp. 285-295.

El-Danaf, E. A., El-Rayes, M. M. and Soliman, M. S. (2010), Mater. Design.: Friction stir processing: An effective technique to refine grain structure and enhance ductility, Vol. 31, pp. 1231-1236.

El-Hafez, H. (2011), J. Mater. Eng. Perform. : Mechanical properties and welding power of friction stirred AA2024-T35 joints, Vol. 20, No. 6, pp. 839-845.

El-Rayesa, M. M. and El-Danaf, E. A. (2012), J. Mater. Process. Tech.: The influence of multi-pass friction stir processing on the microstructural and mechanical properties of Aluminum Alloy 6082, Vol. 212, pp. 1157-1168.

Feifei Liu, Songping Liu, Enming Guo and Legand Li (2008), 17th World Conference on Nondestructive Testing, Shanghai, China: Ultrasonic evaluation of friction stir welding, pp.25-28

Firouzdor, V. and Kou, S. (2009), Weld. J.: Al to Mg friction stir welding: Effect of positions of Al and Mg with respect to the welding tool, Vol. 8, pp. 213-224.

Fonda, R. W. and Bingert, J. F. (2004), Matall. Mater. Trans. A : Micro-structural evolution in the heat-affected zone of a friction stir weld, Vol. 35A, pp. 1487-1499.

Fonda, R. W., Knipling, K. E. and Bingert, J. F. (2007), Scripta. Mater.: Microstructural evolution ahead of the tool in Al friction stir welds, Vol. 58, pp. 343-348.

Fonda, R. W., Wert, J. A., Reynolds, A. P. and Tang, W. (2007), Mater. Sci. Tech. Ser.: Initial microstructural evolution during friction stir welding, pp. 175-177.

Forcellese, A., Gabrielli, F. and Simoncini, M. (2012), Mater. Design.: Mechanical properties and microstructure of joints in AZ31 thin sheets obtained by friction stir welding using ‘‘pin’’ and ‘‘pinless’’ tool configurations, Vol. 34, pp. 219-229.

Fratini, L., Buffa, G. and Monaco, L. L. (2010), Sci. Technol. Weld. Joi.: Improved FE model for simulation of friction stir welding of different materials, Vol. 15, pp. 199-207.

Fratini, L., Buffa, G. and Palmeri, D. (2009), Comput. Struct.: Using a neural network for predicting the average grain size in friction stir welding processes, Vol. 87, pp. 1166-1174.

Fratini, L., Micari, F., Buffa, G. and Ruisi, V. F. (2010), CIRP Ann. Manuf. Technol.: A new fixture for FSW processes of titanium alloys, Vol. 59, pp. 271-274.

Fu, R. D., Ji H. S., Li, Y. J. and Liu, L. (2012), Sci. Technol. Weld. Joi.: Effect of weld conditions on microstructures and mechanical properties of friction stir welded joints on AZ31B magnesium alloys, Vol. 17, pp. 174-179.

Fu, R., Xu, H., Luan, G., Dong, C., Zhang, F. and Li, G. (2012), Mater. Charact.: Top surface microstructure of friction-stir welded AA2524-T3 aluminum alloy joints, Vol. 65, pp. 48-54.

Fujii, H., Chung, Y. D. and Sun, Y. F. (2013), Sci. Technol. Weld. Joi.: Friction stir welding of AISI 1080 steel using liquid CO_2 for enhanced toughness and ductility, Vol. 18 (6), pp. 500-506.

Fujii, H., Cui, L., Maeda, M., Nogi, K. (2006), Mater. Sci. Eng. A: Effect of tool shape on mechanical properties and microstructure of friction stir welded aluminum alloys, Vol. 419, pp. 25-31.

Fujii, H., Ueji, R., Morisada, Y. and Tanigawa, H. (2014), Scripta. Mater.: High strength and ductility of friction-stir-welded steel joints due to mechanically stabilized metastable austenite, Vol. 70, pp. 39-42.

Gaafer, A. M., Mahmoud, T. S. and Mansour, E. H. (2010), Mater. Sci. Eng. A: Microstructural and mechanical characteristics of AA7020-O Al plates joined by friction stir welding, Vol. 527, pp. 7424-7429.

Gaitonde, V. N., Karnik, S. R. and Davim, J. P. (2008), J. Mater. Process Tech.: Taguchi multiple-performance characteristics optimization in drilling of medium density fibre board (MDF) to minimize delamination using utility concept, Vol. 196, pp. 73-77.

Galvao, I., Oliveira, J. C., Loureiro, A. and Rodrigues, D. M. (2012), Intermetallics: Formation and distribution of brittle structures in friction stir welding of aluminium and copper: Influence of shoulder geometry, Vol. 22, pp. 122-128.

Ghetiya, N. D. and Patel, K. M. (2014), 2nd International Conference on Innovations in Automation and Mechatronics Engineering, Procedia Technology: Prediction of tensile strength in friction stir welded aluminium alloy using artificial neural network, Vol. 14, pp. 274-281.

Ghidini, T., Vugrin, T. and Dalle Donne, C. (2005), Welding International: Residual stresses, defects and non-destructive evaluation of FSW joints, Vol. 19, pp. 783-790.

Ghosh, M., Kumar, K., Kailas, S. V. and Ray, A. K. (2010), Mater. Design.: Optimization of friction stir welding parameters for dissimilar aluminum alloys, Vol. 31, pp. 3033-3037.

Giles, T. L., Oh-ishi, K., Zhilyaev, A. P., Swaminathan, S., Mahoney, M. W. and MCnelley, T. R. (2009), Metall. Mater. Trans. A: The effect of friction stir processing on the microstructure and mechanical properties of an aluminum lithium alloy, Vol. 40 A, pp. 104-115.

Goldberg, D. E. (1989), Genetic algorithms in search, optimization and machine learning, Addison Wesley, Reading mass.

Grujicic, M., Arakere, G., Pandurangan, B., Hariharan, A., Yen, C. F. and Cheeseman, B. A. (2010), J. Mater. Eng. Perform.: Development of a robust and cost-effective friction stir welding process for use in advanced military vehicles, Vol. 19, pp. 1256-1263.

Gunaraj, V. and Murugan, N. (1999), J. Mater. Process. Tech.: Application of response surface methodology for predicting weld bead quality in submerged arc welding of pipes, Vol. 88, pp. 266-275.

Gupta, R. K., Das, H. and Pal, T. K. (2012), J. Mater. Eng. Perform.: Influence of processing parameters on induced energy, mechanical and corrosion properties of FSW butt joint of 7475 AA, Vol. 21, No. 8, pp. 1645-1654.

Gupta, V. and Murthy, P. N. (1982), An Introduction to Engineering Design Methods: Tata McGraw-IEII, New Delhi.

Haghshenas, M., Abdel-Gwad, A., Omran, A. M., Gokçe, B., Sahraeinejad, S. and Gerlich, A. P. (2014), Mater. Design.: Friction stir weld assisted diffusion bonding of 5754 aluminum alloy to coated high strength steels, Vol. 55, pp. 442-449.

Han, W., Kimura, A., Tsuda, N., Serizawa, H., Chen, D., Je, H., Fujii, H., Ha, Y., Morisada, Y. and Noto, H. (2014), Journal of Nuclear Materials: Effects of mechanical force on grain structures of friction stir welded oxide dispersion strengthened ferritic steel, Vol. 455, pp. 46-50.

Hao, H.L., Ni, D. R., Huang, H., Wang, D. Xiao, B. L., Nie, Z. R. and Ma, Z.Y. (2013), Mater. Sci. Eng. A: Effect of welding parameters on microstructure and mechanical properties of friction stir welded Al-Mg-Er alloy, Vol. 559, pp. 889-896.

Hassan, Kh. A. A., Wynne, B. P. and Prangnell, P. B. (2003), Proceedings of the Fourth International Friction Stir Welding Symposium: TWI, Cambridge, UK

Haykin, S. (2004), Neural networks - A comprehensive foundation, New Delhi: Pearson Education, 2nd Edition.

Heidari, H. and Razmi, H. (2012), Trans. Talanta.: Multi-response optimization of magnetic solid phase extraction based on carbon coated Fe_3O_4 nano-particles using desirability function approach for the determination of the organophosphorus pesticides in aquatic samples by HPLC-UV, Vol. 99, pp. 13-21.

Heidarzadeh, A., Khodaverdizadeh, H., Mahmoudi, A. and Nazar, E. (2012), Mater. Design.: Tensile behavior of friction stir welded AA 6061-T4 aluminum alloy joints, Vol. 37, pp. 166-173.

Heurtier, O. P., Jones, M. J., Desrayaud, C., Driver, J. H., Montheillet, F. and Allehaux, D. (2006), J. Mater. Process. Technol.: Mechanical and thermal modeling of friction stir welding, Vol. 171, pp. 348-357.

Holland, J. H., (1975), Adaptation in Natural and Artificial System, Ann Arbor, MI: University of Michigan Press, 406p.

Hu, Z. L., Yuan, S. J., Wang, X. S., Liu, G., Liu, H. J. (2012), Scripta. Mater.: Microstructure and mechanical properties of Al-Cu-Mg alloy tube fabricated by friction stir welding and tube spinning, Vol. 66, pp. 427-430.

Huang, Y. X., Han, B., Tian,Y., Liu, H. J, Lv, S. X., Feng, J. C., Leng, J. S. and Lio, Y. (2011), Sci. Technol. Weld. Joi.: New technique of filling friction stir welding, Vol. 16 (3), pp. 497-501.

References

Huang,Y. X., Wan, L.,Lv, S. X. and Feng, J. C. (2013), Sci. Technol. Weld. Joi.: Novel design of tool for joining hollow extrusion by friction stir welding, Vol. 18, No. 3, pp. 239-246.

Hui-jie, L. and Hui-jie, Z. (2009), Trans. Nonferrous Met. Soc. China: Repair welding process of friction stir welding groove defect, Vol. 19, pp. 563-567.

Hui-jie, L., Hui-jie, Z., Yong-xian, H. and Lei, Y. (2010), Trans. Nonferrous Met. Soc. China: Mechanical properties of underwater friction stir welded 2219 aluminum alloy, Vol. 20, pp. 1387-1391.

Hwang, Y. M., Kang, Z. W., Chiou, Y. C. and Hsu, H. H. (2008), Int. J. Mach. Tool. Manu.: Experimental study on temperature distributions within the workpiece during friction stir welding of aluminum alloys, Vol. 48, pp. 778-787.

Hyung-Seop Shin, Yoon-Chul Jung and Jin-Kyu Lee (2012), Met. Mater. Int: Influence of tool speeds on dissimilar friction stir spot welding characteristics of bulk metallic glass/Mg alloy, Vol. 18, pp. 685-689.

Imam, M., Biswas, K. and Racherla, V. (2013), Mater. Design.: Effect of weld morphology on mechanical response and failure of friction stir welds in a naturally aged aluminium alloy, Vol. 44, pp. 23-34.

Inada, K., Fujii, H., Ji, Y. S., Sun, Y. F. and Morisada, Y. (2010), Sci. Technol. Weld. Joi.: Effect of gap on FSW joint formation and development of friction powder processing, Vol. 15, pp. 131-136.

Izadi, H., Nolting, A., Munro, C., Bishop, D. P., Plucknett, K. P. and Gerlich, A. P. (2013), J. Mater. Process. Tech.: Friction stir processing of Al/SiC composites fabricated by powder metallurgy, Vol. 213, pp. 1900-1907.

Izadi, H., Sandstrom, R. and Gerlich, A. P. (2014), Metall. Mater. Trans. A: Grain growth behavior and Hall–Petch strengthening in friction stir processed Al 5059, Vol. 45, pp. 5635-5644.

Jiang, W. H. and Kovacevic R. (2004), Proc. Instn. Mech. Engrs, J. Engineering Manufacture.: Feasibility study of friction stir welding of 6061-T6 aluminium alloy with AISI 1018 steel, Vol. 218, pp. 1323-1331.

Jolu, T. L., Morgeneyer, T. F., Gourgues-Lorenzon, A. F. (2010), Sci. Technol. Weld. Joi.: Effect of joint line remnant on fatigue lifetime of friction stir welded Al-Cu-Li alloy, Vol. 15, pp. 694-698.

Kampmann, R. and Wagner, R. (1991), Materials science and technology: Vol. 5, Weinheim, VCH.

Kandasamy, J. M., Hussain, M. and Rajesham, S. (2011), Int. Journal on Mechanical & Automobile Engg.: Modifications in FSW fixture design for stronger IMC and superior mechanical properties in AA7075 alloys, Vol. 17, pp. 21-26.

Karande, P., Gauri, S. K. and Chakraborty, S. (2013), Mater. Design.: Applications of utility concept and desirability function for materials selection, Vol. 45, pp. 349-358.

Karthikeyan, L. and Senthil Kumar, V. S. (2011), Mater. Design.: Relationship between process parameters and mechanical properties of friction stir processed AA6063-T6 aluminum alloy, Vol. 32, pp. 3085-3091.

Kennedy, J., and Eberhart, R. C. (1995), Proceedings of IEEE international conference on neural networks: Particle Swarm Optimization, pp. 1942 -1948.

Khalid Rafi, H., Janaki Ram, G. D., Phanikumar, G. and Prasad Rao, K. (2010), Mater. Design.: Microstructure and tensile properties of friction welded aluminum alloy AA7075-T6, Vol. 31, pp. 2375-2380.

Khodabakhshi, F., Haghshenas, M., Sahraeinejad, S., Chen, J., Shalchi, B., Li, J. and Gerlich, A. P. (2014), Materials Characterization: Microstructure-property characterization of a friction-stir welded joint between AA5059 aluminum alloy and high density polyethylene, Vol. 98, pp. 73-82.

Khodabakhshi, F., Simchi, A., Kokabi, A. H., Gerlich, A. P. and Nosko, M. (2014), Mater. Design.: Effects of post-annealing on the microstructure and mechanical properties of friction stir processed Al-Mg-TiO_2 nanocomposites, Vol. 63, pp. 30-41.

Khodir, S. A. and Shibayanagi, T. (2008), Mater. Sci. Eng. B: Friction stir welding of dissimilar AA2024 and AA7075 aluminum alloys, Vol. 148, pp. 82-87.

Khodir, S. A., Morisada, Y., Ueji, R. and Fujii, H. (2012), Mater. Sci. Eng.A: Microstructures and mechanical properties evolution during friction stir welding of SK4 high carbon steel alloy, Vol. 558, pp. 572-578.

Khorrami, M. S., Kazeminezhad, M. and Kokabi, A. H. (2012a), Mater. Sci. Eng. A: Mechanical properties of severely plastic deformed aluminum sheets joined by friction stir welding, Vol. 543, pp. 243-248.

Khorrami, M. S., Kazeminezhad, M. and Kokabi, A. H. (2012b), Mater. Design.: Microstructure evolutions after friction stir welding of severely deformed aluminum sheets, Vol. 40, pp. 364-372.

Kim, I. S., Jeong, Y. J., Lee, C. W. and Yarlagadda, P. K. D. V. (2003), The Int. J. Adv. Manuf. Tech.: Prediction of welding parameters for pipeline welding using an intelligent system, Vol. 22, pp. 713-719.

Kim, W. K., Won, S. T. and Goo, B. C. (2010), Int. J. Precis. Eng. Manuf.: A study on mechanical characteristics of the friction stir welded A6005-T5 extrusion, Vol. 11, pp. 931-936.

Kim, Y. G., Fujii, H., Tsumur, T., Komazaki, T. and Nakata, K. (2006), Mater. Lett.: Effect of welding parameters on microstructure in the stir zone of fsw joints of aluminum die casting alloy, Vol. 60, pp. 3830-3837.

Kimapong, K. and Watanabe, T. (2004), Weld. J.: Friction stir welding of aluminum alloy to steel, pp. 277-282.

Kitamura, K., Fujii, H., Iwata, Y., Sun, Y. S. and Morisada Y. (2013), Mater. Design.: Flexible control of the microstructure and mechanical properties of friction stir welded Ti-6Al-4V joints, Vol. 46, pp. 348-354.

Koilraj, M., Sundareswaran, V., Vijayan, S. and Koteswara Rao, S. R. (2012), Mater. Design.: Friction stir welding of dissimilar aluminum alloys AA2219 to AA5083- Optimization of process parameters using Taguchi technique, Vol. 42, pp. 1-7.

Konkol, P. J. and Mruczek, M. F. (2007), Weld. J.: Comparison of friction stir weldments and submerged arc weldments in HSLA-65 steel, Vol. 7, pp. 187-195.

Kumar, A., Mahapatra, M. M., Jha, P. K., Mandal, N. R. and Venkateswarlu, D. (2014), Mater. Design.: Influence of tool geometries and process variables on friction stir butt welding of Al–4.5%Cu/TiC in situ metal matrix composites, Vol. 59, pp. 406-414.

Kumar, K. and Kailas, Satish V. (2008a), Mater. Design.: On the role of axial load and the effect of interface position on the tensile strength of a friction stir welded aluminium alloy, Vol. 29, pp. 791-797.

Kumar, K. and Kailas, Satish V. (2008b), Mater. Sci. Eng., A: The role of friction stir welding tool on material flow and weld formation, Vol. 485, pp. 367-374.

Kumar, R., Pragash, M. S. and Varghese, S. (2013), Middle-East Journal of Scientific Research: Optimizing the process parameters of fsw on az31b mg alloy by Taguchi-grey method, Vol. 15, pp. 161-167.

Kumar, R., Singh, K. and Pandey, S. (2012), Trans. Nonferrous Met. Soc. China: Process forces and heat input as function of process parameters in AA5083 friction stir welds, Vol. 22, pp. 288-298.

Kumbhar, N. T., Sahoo, S. K., Samajdar, I., Dey, G. K. and Bhanumurthy, K. (2011), Mater. Design.: Microstructure and microtextural studies of friction stir welded aluminium alloy 5052, Vol. 32, pp. 1657-1666.

Kurt, A., Uygur, I. and Cete, E. (2011), J. Mater. Process. Tech.: Surface modification of aluminium by friction stir processing, Vol. 211, pp. 313-317.

Kurt, A., Uygur, I. and Paylasan, U. (2011), Weld. J.: Effect of friction welding parameters on mechanical and microstructural properties of dissimilar AISI 1010-ASTM B22 joints, Vol. 90, pp. 102-106.

Kwon, Y. J., Shim, S. B. and Park, D. H. (2009), Trans. Nonferrous Met. Soc. China: Friction stir welding of 5052 aluminum alloy plates, Vol. 19, pp. 23-27.

Lakshminarayanan, A. K. and Balasubramanian, V. (2008), Trans. Nonferrous Met. Soc. China: Process parameters optimization for friction stir welding of RDE-40 aluminium alloy using Taguchi technique, Vol. 18, pp. 548-554.

Lakshminarayanan, A. K. and Balasubramanian, V. (2009), Trans. Nonferrous Met. Soc. China: Comparison of RSM with ANN in predicting tensile strength of friction stir welded AA7039 aluminium alloy Joints, Vol. 19, pp. 9-18.

Lakshminarayanan, K., Balasubramanian, V. and Elangovan, K. (2009), Int. J. Adv. Manuf. Tech.: Effect of welding processes on tensile properties of AA6061 aluminium alloy joints, Vol. 40, pp. 286-296.

Lamarre, A. and Moles, M. (2000), 15th World Conference on Non-destructive Testing Roma (Italy): Ultrasound phased array inspection technology for the evaluation of friction stir welds, pp. 15-21.

Lammlein, D. H., DeLapp, D. R., Fleming, P. A., Strauss, A. M. and Cook, G. E. (2009), Mater. Design.: The application of shoulderless conical tools in friction stir welding: An experimental and theoretical study, Vol. 30, pp. 4012-4022.

Leal, R. M. and Loureiro, A. (2008), Mater. Design.: Effect of overlapping friction stir welding passes in the quality of welds of aluminium alloys, Vol. 29, pp. 982-991.

Leal, R. M., Leitao, C., Loureiro, A., Rodrigues, D. M. and Vila, P. (2008), Mater. Sci. Eng. A: Material flow in heterogeneous friction stir welding of thin aluminium sheets: Effect of shoulder geometry, Vol. 498, pp. 384-391.

Leal, R. M., Sakharova, N., Vilac, P., Rodrigues, D. M. and Loureiro, A. (2011), Sci. Technol. Weld. Joi.: Effect of shoulder cavity and welding parameters on friction stir welding of thin copper sheets, Vol. 16, pp. 146-152.

Leitao, C., Louro, R. and Rodrigues, D. M. (2012), Mater. Design.: Analysis of high temperature plastic behaviour and its relation with weldability in friction stir welding for aluminium alloys AA5083-H111 and AA6082-T6, Vol. 37, pp. 402-409.

Lertora, E. and Gambaro, C. (2010), Int. J. Mater. Form.: AA8090 Al-Li alloy fsw parameters to minimize defects and increase fatigue life, Vol. 3, pp. 1003-1006.

Li D., Cui Z., Yang Q., Sun B. and Sun M. (2012), J. Shanghai Jiaotong Univ. (Sci.): Microstructure and property of friction stir welding joint of 7075Al and AZ31BMg, Vol. 17, No. 6, pp. 679-683.

Li, B. and Shen, Y. (2012), Mater. Design.: A feasibility research on friction stir welding of a new-typed lap-butt joint of dissimilar Al alloys, Vol. 34, pp. 725-731.

Li, B., Shen, Y. and Hu, W. (2011), Mater. Design.: The study on defects in aluminum 2219-T6 thick butt friction stir welds with the application of multiple non-destructive testing methods, Vol. 32, pp. 2073-2084.

Liang, X., Li, H., Li, Z., Hong, T., Ma, B., Liu, S. and Liu, Y. (2012), Mater. Design.: Study on the microstructure in a friction stir welded 2519-T87 Al alloy, Vol. 35, pp. 603-608.

Liao, T. W. and Daftardar, S. (2009), Sci. Technol. Weld. Joi.: Model based optimization of friction stir welding processes, Vol. 14, no. 5, pp. 426-435.

Lightfoot, M. P., Bruce, G. J., Mcpherson, N. A. and Woods, K. (2005), Weld. J.: The application of artificial neural networks to weld-induced deformation in ship plate, Vol. 84, No. 2, pp. 23-30.

Lim, D. C. and Gweon, D. G. (1999), J. Manuf. Process.: In-Process joint strength estimation in pulsed laser spot welding using artificial neural networks, Vol. 18, No. 2, pp. 31-42.

Lim, S. H., Lee, C. M. and Chung, W. J. (2006), Int. J. Precis. Eng. Manuf.: A study on the optimal cutting condition of a high speed feeding type laser cutting machine by using Taguchi method, Vol. 7, pp. 18-23.

Lima, D. K., Shibayanagi, T. and Gerlich, A. P. (2009), Materials Science and Engineering A: Synthesis of multi-walled CNT reinforced aluminium alloy composite via friction stir processing, Vol. 507, pp. 194-199.

Liu, F. C. and Ma, Z. Y. (2008), Metall. Mater. Trans. A: Influence of tool dimension and welding parameters on microstructure and mechanical properties of friction-stir-welded 6061-T651 aluminum alloy, Vol. 29, pp. 362-373.

Liu, H. J., Li, J. Q. and Duan, W. J. (2012), Int. J. Adv. Manuf. Techno.: Friction stir welding characteristics of 2219-T6 aluminum alloy assisted by external non-rotational shoulder, Vol. 64, pp. 1685-1694.

Liu, H. J., Zhang, H. J. and Yu, L. (2011a), J. Mater. Eng. Perform.: Homogeneity of Mechanical Properties of Underwater Friction Stir Welded 2219-T6 Aluminum Alloy, Vol. 20, No. 8, pp. 1419-1422.

Liu, H. J., Zhang, H. J. and Yu, L. (2011b), Mater. Design.: Effect of welding speed on microstructures and mechanical properties of underwater friction stir welded 2219 aluminum alloy, Vol. 32, pp. 1548-1553.

Liu, H. J., Zhou, L. and Liu, Q. W. (2009), Scripta. Mater.: Microstructural evolution mechanism of hydrogenated Ti-6Al-4V in the friction stir welding and post-weld dehydrogenation process, Vol. 61, pp. 1008-1011.

Liu, H., Pan, Q., Kong, Q., Tang, X., Su, L., Li, X., Sun, J. and Yang, G. (2007), Welding & Joining: Review of research on friction stir welding defects.

Liu, H., Zhang, H., Pan, Q. and Yu, L. (2012), Int. J. Mater. Form.: Effect of friction stir welding parameters on microstructural characteristics and mechanical properties of 2219-T6 aluminum alloy joints, Vol. 5, pp. 235-241.

Lombard, H., Hattingh, D. G., Steuwer, A. and James, M. N. (2006), Proceedings of Crack Paths, Parma Italy: Relationships among FSW process parameters, defects, crack paths and fatigue strength in 5083-H321 aluminium alloy.

Longhurst, W. R., Strauss, A. M., Cook, G. E. and Fleming, P. A. (2010), Int. J. Adv. Manuf. Techno.: Torque control of friction stir welding for manufacturing and automation, Vol. 51, pp. 905-913.

Lorrain, O., Favier, V., Zahrouni, H. and Lawrjaniec, D. (2010), Int. J. Mater. Form. Friction stir welding using unthreaded tools: analysis of the flow, Vol. 3, pp. 1043-1046.

Lorraina, O., Favier, V., Zahrouni, H. and Lawrjaniec, D. (2010), J. Mater. Process. Tech.: Understanding the material flow path of friction stir welding process using unthreaded tools, Vol. 210, pp. 603-609.

Malarvizhi, S. and Balasubramanian, V. (2011), J. Mater. Eng. Perform.: Effects of welding processes and post-weld aging treatment on fatigue behavior of AA2219 aluminium alloy joints, Vol. 20, pp. 359-367.

Mamdani, E. H. and Assilian, S. (1975), Int. J. of Man-Machine Studies: An experiment in linguistic synthesis with a fuzzy logic controller, Vol. **7**, pp. 1-13.

Manvatkar, V. D., Arora, A., De, A. and DebRoy, T. (2012), Sci. Technol. Weld. Joi.: Neural network models of peak temperature, torque, traverse force, bending stress and maximum shear stress during friction stir welding, Vol. 17, pp. 460-466.

Manvatkar, V., De, A., Svensson, L. E. and Deb Roy, T. (2015), Scripta. Mater.: Cooling rates and peak temperatures during friction stir welding of a high-carbon steel, Vol. 94, pp. 36-39.

McNelley, T. R., Swaminathan, S. and Su, J. Q. (2008), Scripta. Mater.: Recrystallization mechanisms during friction stir welding/processing of aluminum alloys, Vol. 58, pp. 349-354.

Mehta, M., Arora, A., De, A. and DebRoy, T. (2012), Metall. Mater. Trans. A: Tool Geometry for friction stir welding-Optimum shoulder diameter, Vol. 42, pp. 2716-2722.

Mehta, M., De, A. and DebRoy, T. (2014), Sci. Technol. Weld. Joi.: Material adhesion and stresses on friction stir welding tool pins, Vol. 19, pp. 534-540.

Miles, M. P., Nelson, T. W., Steel, R., Olsen, E. and Gallagher, M. (2009), Sci. Technol. Weld. Joi.: Effect of friction stir welding conditions on properties and microstructures of high strength automotive steel, Vol. 14, pp. 228-232.

Mishra, R. S. and Ma, Z. Y. (2005), Mater. Sci. Eng. R: Friction stir welding and processing, Vol. 50, pp. 1-78.

Mishra, R. S. and Mahoney M. W. (2007), Friction Stir Welding and Processing, USA, ASM International,

Miyano, Y., Fujii, H., Sun, Y., Katada, Y., Kuroda, S. and Kamiya, O. (2011), Mater. Sci. Eng. A: Mechanical properties of friction stir butt welds of high nitrogen-containing austenitic stainless steel, Vol. 528, pp. 2917-2921.

Miyazawa, K. T., Iwamoto, Y., Maruko, T. and Fujii, H. (2012), Sci. Technol. Weld. Joi.: Friction stir welding of 304 stainless steel using Ir based alloy tool, Vol. 17, pp. 207-212.

Miyazawa, T., Iwamoto, Y., Maruko, T. and Fujii, H. (2011), Sci. Technol. Weld. Joi.: Development of Ir based tool for friction stir welding of high temperature materials, Vol. 16, pp. 188-192.

Mofid, M. A., Abdollah-zadeh, A. and Ghaini, F. M. (2012), Mater. Design.: The effect of water cooling during dissimilar friction stir welding of Al alloy to Mg alloy, Vol. 36, pp. 161-167.

Montgomery D. C. (2006), Design and Analysis of Experiments [M], New York: John-Wiley & Sons, Inc, 4th Edition.

Montgomery, D. C. (1984), Design and analysis of experiments, New York: John Wiley and Sons, 2nd Edition.

Moreira, P. M. G. P., Santos, T., Tavares, S. M. O., Richter-Trummer, V., Vilaça, P. and Castro, P. M. S. T. (2009), Mater. Design.: Mechanical and metallurgical characterization of friction stir welding joints of AA6061-T6 with AA6082-T6, Vol. 30, pp. 180-187.

Movahedi, M., Kokabi, A. H., Seyed Reihani, S. M. and Najafi, H. (2012), Sci. Technol. Weld. Joi.: Effect of tool travel and rotation speeds on weld zone defects and joint strength of aluminium steel lap joints made by friction stir welding, Vol. 17, No. 2, pp. 162-167.

Murphy, T. E., Tsui, K. L. and Allen, J. K. (2005), Res. Eng. Des.: A review of robust design methods for multiple responses, Vol. 16, pp. 118-32.

Nagesh, D. S. and Datta, G. L. (2010), Appl. Soft. Comput.: Genetic algorithm for optimization of welding variables for height to width ratio and application of ANN for prediction of bead geometry for TIG welding process, Vol. 10, No. 3, pp. 897-907.

Nandan, R., Prabu, B. Z., De, A. and Deb Roy, T. (2007), Weld. J.: Improving reliability of heat transfer and materials flow calculations during friction stir welding of dissimilar aluminum alloys, Vol. 86, pp. 313-312.

Nikulin, L., Malopheyev, S., Kipelova, A. and Kaibyshev, R. (2012), Materials Letters: Effect of SPD and friction stir welding on microstructure and mechanical properties of Al-Cu-Mg-Ag sheets, Vol. 66, pp. 311-313.

Okuyucu, H., Kurt, A. and Arcaklioglu, E. (2007), Mater. Design.: Artificial neural network application to the friction stir welding of aluminum plates, Vol. 28, pp. 78-84.

Ouyang, J., Yarrapareddy, E. and Kovacevic, R. (2006), J. Mater. Process. Tech.: Microstructural evolution in the friction stir welded 6061 aluminum alloy (T6-temper condition) to copper, Vol. 172, pp. 110-122.

Padmanaban, G. and Balasubramanian, V. (2010), Int. J. Adv. Manuf. Techno.: An experimental investigation on friction stir welding of AZ31B magnesium alloy, Vol. 49, pp. 111-121.

Paglia, C. S. and Buchheit, R. G. (2008), Scripta. Mater.: A look in the corrosion of aluminum alloy friction stir welds, Vol. 58, pp. 383-387.

Pal, S., Malviya, S., Pal, S. K. and Samantaray, A. K. (2009), Int. J. Adv. Manuf. Technol.: Optimization of quality characteristics parameters in a pulsed metal inert gas welding process using grey-based Taguchi method, Vol. 44, pp. 1250-1260.

Pal, S., Pal, S. K. and Samantaray, A. K. (2007), Sci. Technol. Weld. Joi.: Radial basis function neural network model based prediction of weld plate distortion due to pulsed metal inert gas welding, Vol. 12, No. 8, pp. 725-731.

Palanivel, R. and Koshy Mathews, P. (2012), Journal of Central South University: Prediction and optimization of process parameter of friction stir welded AA5083- H111 aluminum alloy using response surface methodology, Vol. 19, pp. 1-8.

Parida, B., Pal, S., Biswas, P., Mahapatra, M. M. and Tikader, S. (2011), International Journal of Applied Research in Mechanical Engineering: Mechanical and micro-structural study of friction stir welding of Al-alloy, Vol. I, pp. 69-74.

Periyasamy, P., Mohan, B., Balasubramanian, V., Rajakumar, S. and Venugopal, S. (2013), Trans. Nonferrous Met. Soc. China: Multi-objective optimization of friction stir welding parameters using desirability approach to join Al/SiCp metal matrix composites, Vol. 23, pp. 942-955.

Pilchak, A. L., Tang, W., Sahiner, H., Reynolds, A. P. and Williams, J. C. (2011), Metall. Mater. Trans. A: Microstructure evolution during friction stir welding of mill-annealed Ti-6Al-4V, Vol. 42A, pp. 745-762.

Prado, R. A., Murr, L. E., Soto, K. F. and McClure, J. C. (2003), Mater. Sci. Eng. A: Self-optimization in tool wear for friction-stir welding of Al 6061 +20% Al_2O_3 MMC, Vol. 349, pp. 156-165.

Prasanna, P., Penchalayya, Ch. and Anandamohana Rao, D. (2013), International Journal of Engineering Research and Applications: Optimization and validation of process parameters in friction stir welding on AA 6061 aluminum alloy using gray relational analysis, Vol. 3, pp. 1471-1481.

Pratihar, D. K. (2009), Soft Computing: Narosa publishing house, New Delhi, India.

Puviyarasan, M. and Senthil Kumar, V. S. (2012), Procedia Eng.: Optimization of friction stir process parameters in fabricating AA6061/SiCp composites, Vol. 38, pp. 1094-1103.

Rafi, H. K., Janaki Ram, G. D., Phanikumar, G. and Rao, K. P. (2010), Mater. Design.: Microstructure and tensile properties of friction welded aluminum alloy AA7075-T6, Vol. 31, pp. 2375-2380.

Rahim. A., Sharma, U. K., Murugesan, K., Sharma, A. and Arora, P. (2012), J. Struct. Fire Eng.: Optimization of post fire residual compressive strength of concrete by Taguchi method, Vol. 3, pp.169-80.

Rai, R., De, A., Bhadeshia, H. K. D. H. and DebRoy, T. (2011), Sci. Technol. Weld. Joi.: Review: friction stir welding tools, Vol. 16, pp. 325-342.

Rajakumar S. and Balasubramanian V. (2012), Mater. Design.: Establishing Relationships between Mechanical Properties of Aluminium Alloys and Optimized Friction stir welding Process Parameters, Vol. 40, pp. 17-35.

Rajakumar, S. and Balasubramanian, V. (2012), J. Mater. Eng. Perform.: Multi-response optimization of friction-stir-welded AA1100 aluminum alloy joints, Vol. 21, pp. 809-822.

Rajakumar, S. and Balasubramanian, V. (2012), Mater. Design.: Correlation between weld nugget grain size, weld nugget hardness and tensile strength of friction stir welded commercial grade aluminium alloy joints, Vol. 34, pp. 242-251.

Rajakumar, S., Balasubramanian, V. and Razalrose, A. (2013a), Mater. Design.: Friction stir and pulsed current gas metal arc welding of AZ61A magnesium alloy: A comparative study, Vol. 49, pp. 267-278.

Rajakumar, S., Muralidharan, C. and Balasubramanian, V. (2010), Trans. Nonferrous Met. Soc. China: Establishing empirical relationships to predict grain size and tensile strength of friction stir welded AA 6061-T6 aluminium alloy joints, Vol. 20, pp. 1863-1872.

Rajakumar, S., Muralidharan, C. and Balasubramanian, V. (2011a), Mater. Design.: Predicting tensile strength, hardness and corrosion rate of friction stir welded AA6061-T6 aluminium alloy joints, Vol. 32, pp. 2878-2890.

Rajakumar, S., Muralidharan, C., Balasubramanian, V. (2011b), Mater. Design.: Influence of friction stir welding process and tool parameters on strength properties of AA7075-T6 aluminium alloy joints, Vol. 32, pp. 535-549.

Rajakumar, S., Razalrose, A. and Balasubramanian, V. (2013b), Int. J. Adv. Manuf. Techno.: Friction stir welding of AZ61A magnesium alloy A parametric study, Vol. 68, pp. 277-292.

Ramanjaneyulu, K., Madhusudhan Reddy, G., Venugopal Rao, A. and Markandeya, R. (2013), Journal of Materials Engineering and Performance: Structure-property correlation of aa2014 friction stir welds: Role of tool pin profile, Vol. 22, pp. 2224-2240.

Ramesh Babu, S., Senthil Kumar, V. S., Karunamoorthy, L. and Madhusudhan Reddy, G. (2014), Mater. Design.: Investigation on the effect of friction stir processing on the superplastic forming of AZ31B alloy, Vol. 53, pp. 338-348.

Razal Rose, Manisekar, K. and Balasubramanian, V. (2012), J. Mater. Eng. Perform.: Influences of welding speed on tensile properties of friction stir welded AZ61A magnesium alloy, Vol. 21, pp. 257-265.

Record, J. H., Covington, J. L., Nelson, T. W., Sorensen, C. D. and Webb, B. W. (2007), Weld. J.: A look at the statistical identification of critical process parameters in friction stir welding, Vol. 4, pp. 97-103.

Ren, S. R., Ma, Z. Y. and Chen, L. Q. (2007), Scripta. Mater.: Effect of welding parameters on tensile properties and fracture behavior of friction stir welded Al-Mg-Si alloy, Vol. 56, pp. 69-72.

Ren, S. R., Ma, Z. Y. and Chen, L. Q. (2008), Mater. Sci. Eng., A: Effect of initial butt surface on tensile properties and fracture behavior of friction stir welded Al-Zn-Mg-Cu alloy, Vol. 479, pp. 293-299.

Rhodes, C. G., Mahoney, M. W., Bingel, W. H. and Calabrese, M. (2003), Scripta. Mater.: Fine-grain evolution in friction-stir processed 7050 aluminum, Vol. 48, pp. 1451-1455.

Richter-Trummer, V., Suzano, E., Beltrao, M., Roos, A., dos Santos, J. F. and de Castro, P. M. S. T. (2012), Mater. Sci. Eng. A: Influence of the FSW clamping force on the final distortion and residual stress field, Vol. 538, pp. 81-88.

Robson, J. D., Upadhyay, P. and Reynolds, A. P. (2010), Sci. Technol. Weld. Joi.: Modelling microstructural evolution during multiple pass friction stir welding, Vol. 15, pp. 613-618.

Rodrigues, D. M., Loureiro, A., Leitao, C., Leal, R. M., Chaparro, B. M. and Vilaca, P. (2009), Journals for Mater. Design.: Influence of friction stir welding parameters on the micro-structural and mechanical properties of AA 6016-T4 thin welds, Vol. 30, pp. 1913-1921.

Rosado, L. S., Santos, T. G., Piedade, M., Ramos, P. M. and Vilaca P. (2010), Measurement: Advanced technique for non-destructive testing of friction stir welding of metals. Vol. 43, pp. 1021-1030.

Roshan, S. B., Jooibari, M. B., Teimouri, R., Asgharzadeh-Ahmadi, G., Falahati-Naghibi, M. and Sohrabpoor, H. (2013), Int. J. Adv. Manuf. Techno.: Optimization of friction stir welding process of AA7075 aluminum alloy to achieve desirable mechanical properties using ANFIS models and simulated annealing algorithm, Vol. 69, pp. 1803-1818.

Saeid, T., Abdollah-zadeh, A., Assadi, H. and Ghaini, F. M. (2008), Mater. Sci. Eng. A: Effect of friction stir welding speed on the microstructure and mechanical properties of a duplex stainless steel, Vol. 496, pp. 262-268.

Sakthivel, T. and Mukhopadhyay, J. (2007), J. Mater. Sci.: Microstructure and mechanical properties of friction stir welded copper, Vol. 42, pp. 8126-8129.

Sakthivel, T., Senegar, G. S. and Mukhopadhyay, J. (2009), Int. J. Adv. Manuf. Tech.: Effect of welding speed on micro-structure and mechanical properties of friction-stir welded aluminum, Vol. 43, pp. 468-473.

Salehi, V. M., Saadatmand, M. and Mohandesi, J. A. (2012), Trans. Nonferrous Met. Soc. China: Optimization of process parameters for producing AA6061/SiC nano-composites by friction stir processing, Vol. 22, pp. 1055-1063.

Salem, H. G. (2003), Scripta. Mater.: Friction stir weld evolution of dynamically recrystallized AA2095 weldments, Vol. 49, pp. 1103-1110.

Santos, T., Vilaça, P. and Quintino, L. (2007), Developments in NDT focusing defects in FSW of aluminium alloys. IIW Doc III -1426-07.

Santosa, T.G., Vilac¸ P. and Miranda, R. M. (2011), J. Mater. Process. Tech.: Electrical conductivity field analysis for evaluation of FSW joints in AA6013 and AA7075 alloys, Vol. 211, pp. 174-180.

Sarsilmaz, F. and Caydas, U. (2009), Int. J. Adv. Manuf. Tech.: Statistical analysis on mechanical properties of friction stir welded AA1050/AA5083 couples, Vol. 43, pp. 248-255.

Sathiya, P., Panneerselvam, K. and Soundararajan, R. (2012), Opt. Laser. Technol.: Optimal design for laser beam butt welding process parameter using artificial neural networks and genetic algorithm for super austenitic stainless steel, Vol. 44, No. 6, pp. 1905-1914.

Sato, Y. S. and Kokawa, H. (2001), Matall. Mater. Trans. A: Distribution of tensile property and micro-structure in friction stir weld of 6063 aluminum, Vol. 32, pp. 3023-3031

Scialpi, A., De Filippis, L. A. C., Cavaliere, P. (2007), Journals for Mater. Design.: Influence of shoulder geometry on microstructure and mechanical properties of friction stir welded 6082 aluminum alloy, Vol. 28, pp. 1124-1129.

Scialpi, A., Giorgi, M. D., Filippis, L. A. C. D., Nobile, R. and Panella, F. W. (2008), Mater. Design.: Mechanical analysis of ultra-thin friction stir welding joined sheets with dissimilar and similar materials, Vol. 29, pp. 928-936.

Shahri, M. M. and Sandström, R. (2012), J. Mater. Process. Tech.: Influence of fabrication stresses on fatigue life of friction stir welded aluminium profiles, Vol. 212, pp. 1488-1494.

Shanmuga Sundarama, N. and Murugan, N. (2010), Mater. Design.: Tensile behavior of dissimilar friction stir welded joints of aluminium alloys, Vol. 31, pp. 4184-4193.

Sharma, C., Dwivedi, D. K. and Kumar, P. (2012), Mater. Design.: Effect of welding parameters on microstructure and mechanical properties of friction stir welded joints of AA7039 aluminum alloy, Vol. 36, pp. 379-390.

Shojaeefard, M. H., Behnagh, R. A., Akbari, M., Givi, M. K. B. and Farhani, F. (2013), Mater. Design.: Modelling and pareto optimization of mechanical properties of friction stir welded AA7075/AA5083 butt joints using neural network and particle swarm algorithm, Vol. 44, pp. 190-198.

Shojaeefard, M. H., Khalkhali, A., Akbari, M. and Tahani, M. (2013), Mater. Design.: Application of Taguchi optimization technique in determining aluminum to brass friction stir welding parameters, Vol. 52, pp. 587-592.

Silva, A. A. M., Arruti, E., Janeiro, G., Aldanondo, E., Alvarez, P. and Echeverria, A. (2011), Mater. Design.: Material flow and mechanical behaviour of dissimilar AA2024-T3 and AA7075-T6 aluminium alloys friction stir welds, Vol. 32, pp. 2021-2027.

Simar, A., Br´echet, Y., Meester, B., Denquin, A. and Pardoen, T. (2008), Mater. Sci. Eng. A: Microstructure, local and global mechanical properties of friction stir welds in aluminium alloy 6005A-T6, Vol. 486, pp. 85-95.

Simoncini, M. and Forcellese, A. (2012), Mater. Design.: Effect of the welding parameters and tool configuration on micro- and macro-mechanical properties of similar and dissimilar FSWed joints in AA5754 and AZ31 thin sheets, Vol. 41, pp. 50-60.

Sivasakthivel, T., Murugesan, K. and Thomas, H. R. (2014), Appl Energy: Optimization of operating parameters of ground source heat pump system for space heating and cooling by Taguchi method and utility concept, Vol. 116, pp. 76-85.

Song, M. and Kovacevic R. (2003), International Journal of Machine Tools & Manufacture: Thermal modeling of friction stir welding in a moving coordinate system and its validation, Vol. 43, pp. 605-615.

Soundararajan, V., Yarrapareddy, E. and Kovacevic, R. (2007), J. Mater. Eng. Perform.: Investigation of the friction stir lap welding of aluminum alloys AA 5182 and AA 6022, Vol. 16, pp. 477-484.

Soundararajan, V., Zekovic, S. and Kovacevic R. (2005), International Journal of Machine Tools & Manufacture: Thermo-mechanical model with adaptive boundary conditions for friction stir welding of Al 6061, Vol. 45, pp. 1577-1587.

Squeo, E. A., Bruno, G., Guglielmotti, A. and Quadrini F. (2007), The Annals of "Dunărea de jos" University of Galaţi Fascicle V: Friction stir welding of polyethylene sheets, pp. 241-246.

Srinivasan, P. B., Arora, K. S., Dietzel, W., Pandey, S. and Schaper, M. K. (2010), J. Alloy. Compd.: Characterization of microstructure, mechanical properties and corrosion behaviour of an AA2219 friction stir weldment, Vol. 492, pp. 631-637.

Srinivasu R., Sambasiva Rao, A., Madhusudhan Reddy, G. and Srinivasa Rao, K. (2014), Defense Technology: Friction stir surfacing of cast A356 aluminium-silicon alloy with boron carbide and molybdenum disulphide powders, http://dx.doi.org/10.1016/j.dt.2014.09.004, pp. 1-7.

Steuwer, A., Barnes, S. J., Altenkirch, J., Johnson, R. and Withers, P. J. (2011), Matall. Mater. Trans. A: Friction stir welding of HSLA-65 Steel: Part II. The influence of weld speed and tool material on the residual stress distribution and tool wear, Vol.43, No. 7, pp. 2356-2365.

Steuwer, A., Dumont, M., Altenkirch, J., Birosca, S., Deschamps, A., Prangnell, P. B. and Withers, P. J. (2011), Acta Materialia: A combined approach to microstructure mapping of an Al–Li AA2199 friction stir weld, Vol. 59, pp. 3002-3011.

Storn, R. and Price, V. (1997), J. Global Optim.: Differential Evolution-A simple and efficient heuristic for global optimization over continuous spaces, Vol. 11, pp. 341-359.

Su, J. Q., Nelson, T. W. and Sterling, C. J. (2005), Mater. Sci. Eng. A: Microstructure evolution during FSW/FSP of high strength aluminum alloys, Vol. 405, pp. 277-286.

Su, J. Q., Nelson, T. W., Mishra, R. and Mahoney, M. (2003), Acta Mater: Microstructural investigation of friction stir welded 7050-T651 aluminium, Vol. 51, pp. 713-729.

Su, P., Gerlich, A., North, T. H. and Bendzsak, G. J. (2006), Sci. Technol. Weld. Joi.: Material flow during friction stir spot welding, Vol. 11, pp. 61-71.

Subbaiah, K., Geetha, M., Govindaraju, M. and Rao, S. R. K. (2012), T. Indian I. Metals: mechanical properties of friction stir welded cast Al-Mg-Sc alloys, Vol. 65, pp. 155-158.

Sudhakar, I., Madhu, V., Madhusudhan Reddy, G. and Srinivasa Rao, K. (2014), Defense Technology: Enhancement of wear and ballistic resistance of armour grade AA7075 aluminium alloy using friction stir processing, http://dx.doi.org/10.1016/j.dt.2014.08.003, pp. 1-8.

Suhuddin, U.F.H., Fischer, V. and dos Santos, J. F. (2013), Scripta. Mater.: The thermal cycle during the dissimilar friction spot welding of aluminum and magnesium alloy, Vol. 68, pp. 87-90.

Sullivan, A., Derrya, C., Robson, J. D., Horsfall, I. and Prangnell, P. B. (2011), Mater. Sci. Eng. A: Microstructure simulation and ballistic behaviour of weld zones in friction stir welds in high strength aluminium 7xxx plate, Vol. 528, pp. 3409-3422.

Sun, Y. F., Fujii, H., Imagawa, K., Yokoyama, Y., Kimura, H. and Akihisa Inoue (2012), Materials Transactions: Interface microstructure and mechanical properties of dissimilar friction stir welded joints between $Zr_{55}Cu_{30}Ni_5Al_{10}$ bulk metallic glass and pure Al, Vol. 53, No. 6, pp. 1106-1112.

Sun, Y. F., Konishi, Y., Kamai, M. and Fujii, H. (2013), Mater. Design.: Microstructure and mechanical properties of S45C steel prepared by laser-assisted friction stir welding, Vol. 47, pp. 842-849.

Sun, Y. F., Xu, N. and Fujii, H. (2014), Mater. Sci. Eng.A: The microstructure and mechanical properties of friction stir welded Cu-30Zn brass alloys, Vol. 589, pp. 228-234.

Taghi, M., Baghmisheh, V. and Pavesic, N. (2004), Neurocomputing: Training RBF networks with selective back propagation, Vol. 62, pp. 39-64.

Tansel, I. N., Demetgul, M., Okuyucu, H. and Yapici, A. (2010), Int. J. Adv. Manuf. Techno.l: Optimizations of friction stir welding of aluminum alloy by using genetically optimized neural network, Vol. 48, pp. 95-101.

Teimouri, R. and Baseri, H. (2013), J. Intell. Manuf.: Forward and backward predictions of the friction stir welding parameters using fuzzy-artificial bee colony-imperialist competitive algorithm systems, DOI 10.1007/s10845-013-0784-4.

Telmo G. S., Pedro Vilaça, Luís Rosado, Moisés Piedade, Pedro M. Ramos (2010), Proc. European Conf. on Non-Destructive Testing, Moscow, Russia: Developments in NDT of friction stir welding using eddy currents, Vol. 2, pp. 88-89.

Thomas, W. M., Nicholas, E. D., Needhman, J. C., Murch, M. G., Temple-Smith, P., Dawes, C. J. (1991), International patent application PCT/GB92/02203 and GB patent application 9125978.8, UK Patent office, London.

Thomas, W. M., Norris, I. M., Staines, D. J. and Lucas, W. (2005), The evaluation of root defects in FSW by 'through-hole' impact testing-preliminary studies. http://www.twi.co.uk/technical-knowledge/published-papers/the-evaluation-of-root-defects-in-fsw-by-through-hole-impact-testing-preliminary-studies-july-2005/, Dated: 13/05/2013.

Thompson, B. and Babu, S. S. (2010), Weld. J.: Tool degradation characterization in the friction stir welding of hard metals, Vol. 89, pp. 256-261.

Toktas, A. and Toktas, G. (2012), J. Mater. Eng. Perform.: Effect of welding parameters and aging process on the mechanical properties of friction stir-welded 6063-T4 Al alloy, Vol. 21, pp. 936-945.

Tozaki, Y., Uematsu, Y., Tokaji, K. (2007), Int. J. Mach. Tool Manu.: Effect of tool geometry on microstructure and static strength in friction stir spot welded aluminium alloys, Vol. 47, pp. 2230-2236.

Trimble, D., Monaghan, J. and O'Donnell, G. E. (2012), CIRP Annals Manufacturing Technology: Force generation during friction stir welding of AA2024-T3, Vol. 61, pp. 9-12.

Uematsu, Y., Tokaji, K., Tozaki, Y., Kutita, T. and Murata, S. (2008), Int. J. Fatigue: Effect of re-filling probe hole on tensile failure and fatigue behavior of friction stir spot welded joints in Al-Mg-Si alloy, Vol. 30, pp. 1956-1966.

Venkateswaran, P. and Reynolds, A. P. (2012), Mater. Sci. Eng. A: Factors affecting the properties of friction stir welds between aluminum and magnesium alloys, Vol. 545, pp. 26-37.

Venkateswarlu, G., Devaraju, D., Davidson, M. J., Kotiveerachari, B. and Tagore, G. R. N. (2013), Mater. Design.: Effect of overlapping ratio on mechanical properties and formability of friction stir processed Mg AZ31B alloy, Vol. 45, pp. 480-486.

Vidal, C., Infante, V. and Vilaca, P. (2010), Procedia Eng.: Assessment of improvement techniques effect on fatigue behavior of friction stir welded aerospace aluminium alloys, Vol. 2, pp. 1605-1616.

Vijay, S. J. and Murugan, N. (2010), Mater. Design.: Influence of tool pin profile on the metallurgical and mechanical properties of friction stir welded Al-10 wt.% TiB_2 metal matrix composite, Vol. 31, pp. 3585-3589.

Vijayan, S., Raju, R. and Rao, S. R. K. (2010), Mater. Manuf. Process: Multi-objective optimization of friction stir welding process parameters on aluminum alloy aa 5083 using taguchi-based grey relation analysis, Vol. 25, pp. 1206-1212.

Wagner, R. and Kampmann, R. (1991), Homogeneous second phase precipitation Materials Science and Technology: A Comprehensive Treatment Vol. 5, ed. Cahn, R., Haasen, W. P. and Kramer, E. J. (Weinheim: Wiley-VCH), pp. 213-303.

Walia, R. S., Shan, H. S. and Kumar, P. (2006), Mater. Manuf. Process.: Multi-response optimization of CFAAFM process through Taguchi method and utility concept, Vol. 21, pp. 907-914.

Wang, H., Colegrove, Mayer, H. M., Campbell, L. and Robson, R. D. (2010), Advanced Materiala Research: Material constitutive behaviour and microstructure study on aluminium alloys for friction stir welding, Vol. 89, pp. 615-620.

Wang, H., Colegrove, P. A. and Santos, J. F. (2013), Computational Materials Science: Numerical investigation of the tool contact condition during friction stir welding of aerospace aluminium alloy, Vol. 71, pp. 101-108.

Wei, L. Y. and Nelson, T. W. (2011), Weld. J.: Correlation of microstructures and process variables in FSW HSLA-65 steel, Vol. 5, pp. 95-101.

Wei, S., Hao, C. and Chen, J. (2007), Mater. Sci. Eng. A: Study of friction stir welding of 01420 aluminum-lithium alloy, Vol. 452-453, pp. 170-177.

William, J. A. (2003), Advanced Materials Processing Center MET: Mechanical friction stir joining: Characteristic defects.

Xie, G. M., Ma, Z. Y., Geng, L. and Chen, R. S. (2007), Mater. Sci. Eng. A: Microstructural evolution and mechanical properties of friction stir welded Mg-Zn-Y-Zr alloy, Vol. 471, pp. 63-68.

Xu, N., Ueji, R. and Fujii, H. (2014), Mater. Sci. Eng.A: Enhanced mechanical properties of 70/30 brass joint by rapid cooling friction stir welding, Vol. 610, pp. 132-138.

Xu, W. F., Liu, J. H., Chen, D. L., Luan, G. H. and Yao, J. S. (2012), Mater. Sci. Eng. A: Improvements of strength and ductility in aluminum alloy joints via rapid cooling during friction stir welding, Vol. 548, pp. 89-98.

Xu, W., Liu, J. and Zhu, H. (2011), J. Mater. Sci.: A study on the hardness and elastic modulus of friction stir welded aluminum alloy thick plate joints using micro-indentation, Vol. 46, pp. 1161-1166.

Xu,, N., Ueji, R., Morisada, Y. and Fujii, H. (2014), Mater. Design.: Modification of mechanical properties of friction stir welded Cu joint by additional liquid CO_2 cooling, Vol. 56, pp. 20-25.

Xue, P., Komizo, Y., Ueji, R. and Fujii, H. (2014), Mater. Sci. Eng.A: Enhanced mechanical properties in friction stir welded low alloy steel joints via structure refining, Vol. 606, pp. 322-329.

Xue, P., Ni, D. R., Wang, D., Xiao, B. L., Ma, Z. Y. (2011), Mater. Sci. Eng., A: Effect of friction stir welding parameters on the microstructure and mechanical properties of the dissimilar Al–Cu joints, Vol. 528, pp. 4683-4689.

Xue, P., Xiao, B. L., Zhang, Q. and Ma, Z. Y. (2011), Scripta. Mater.: Achieving friction stir welded pure copper joints with nearly equal strength to the parent metal via additional rapid cooling, Vol. 64, pp. 1051-1054.

Yadav, D. and Bauri, R. (2012), Mater. Sci. Eng., A: Effect of friction stir processing on microstructure and mechanical properties of aluminium, Vol. 539, pp. 85 - 92.

Yan, D. P., Chen, Z. W. and Littlefair, G. (2010), FSW of thick section 6061 Al alloys using scroll shoulder tool: Tool design, weld zone forming mechanism and weld quality control, LAP Lambert Academic Publishing.

Yang, Y., Kalya, P., Landers, R. G. and Krishnamurthy, K. (2008), Int. J. Mach. Tool Manu.: Automatic gap detection in friction stir butt welding operations, Vol. 48, pp. 1161-1169.

Yeni, C., Sayer, S., Ertugrul, O. and Pakdil, M. (2008), Achieves of Mater. Sci. Eng.: Effect of post weld-aging on the mechanical and micro-structural properties of friction-stir welded aluminum alloy 7075, Vol. 34, pp. 105-109.

Yigezu, B. S., Venkateswarlu, D., Mahapatra, M. M., Jha, P. K. and Mandal, N. R. (2014), Mater. Design.: On friction stir butt welding of Al + 12Si/10 wt%TiC in situ composite, Vol. 54, pp. 1019-1027.

Yu-hua, C., Quan, N. I. and Li-ming, K. E. (2012), Trans. Nonferrous Met. Soc. China: Interface characteristic of friction stir welding lap joints of Ti/Al dissimilar alloys, Vol. 22, pp. 299-304.

Zadeh, A., Saeid, T. and Sazgari, B. (2008), J. Alloy. Compd. : Microstructural and mechanical properties of friction stir welded aluminum/copper lap joints, Vol. 460, pp. 535-538.

Zadeh, L. A. (1965), Information and Control: Fuzzy sets, Vol. **8**, pp. 338-353.

Zadpoor, A. A., Sinke, J. and Benedictus, R. (2010), Metall. Mater. Trans. A: Global and local mechanical properties and microstructure of friction stir welds with dissimilar materials and/or thicknesses. Vol. 41, No. 13, pp. 3365-3378.

Zaeh, M. F. and Gebhard, P. (2010), Prod. Eng. Res. Devel.: Dynamical behaviour of machine tools during friction stir welding, Vol. 4, pp. 615-624.

Zahmatkesh, B,, Enayati, M. H. and Karimzadeh, F. (2010), Mater. Design.: Tribological and microstructural evaluation of friction stir processed Al2024 alloy, Vol. 31, pp. 4891-4896.

Zhang, H. J., Liu, H. J. and Yu, L. (2012), J. Mater. Eng. Perform.: Effect of water cooling on the performances of friction stir welding heat-affected zone, Vol. 21, No. 7, pp. 1182-1187.

Zhang, Z., Liu, Y. L. and Chen, J. T. (2009), Int. J. Adv. Manuf. Techno.: Effect of shoulder size on the temperature rise and the material deformation in friction stir welding, Vol. 45, pp. 889-895.

Zhang, Z., Xiao, B. L. and Ma, Z. Y. (2012), J. Mater. Sci.: Effect of welding parameters on microstructure and mechanical properties of friction stir welded 2219Al-T6 joints, Vol. 47, pp. 4075-4086.

Zhou, L., Liu, H. J. and Liu, Q. W. (2010), J. Mater. Sci.: Effect of process parameters on stir zone microstructure in Ti-6Al-4V friction stir welds, Vol. 45, pp. 39-45.

Appendix-I

Table 1 Fuzzy Rule Base

Rule No.	Antecedent part					Consequent (Rule output)
	UTS	YS	% Elng.	WBT	HRD	
1	S	S	S	S	S	VVL
2	S	S	S	S	M	VVL
3	S	S	S	S	L	VL
4	S	S	S	M	S	VVL
5	S	S	S	M	M	VL
6	S	S	S	M	L	L
7	S	S	S	H	S	VL
8	S	S	S	H	M	L
9	S	S	S	H	L	LM
10	S	S	M	S	S	VVL
11	S	S	M	S	M	VL
12	S	S	M	S	L	L
13	S	S	M	M	S	VL
14	S	S	M	M	M	L
15	S	S	M	M	L	LM
16	S	S	M	H	S	L
17	S	S	M	H	M	LM
18	S	S	M	H	L	M
19	S	S	H	S	S	VL
20	S	S	H	S	M	L
21	S	S	H	S	L	LM
22	S	S	H	M	S	L
23	S	S	H	M	M	LM
24	S	S	H	M	L	M
25	S	S	H	H	S	LM
26	S	S	H	H	M	M
27	S	S	H	H	L	MH
28	S	M	S	S	S	VVL
29	S	M	S	S	M	VL
30	S	M	S	S	L	L
31	S	M	S	M	S	VL
32	S	M	S	M	M	L

33	S	M	S	M	L	LM
34	S	M	S	H	S	L
35	S	M	S	H	M	LM
36	S	M	S	H	L	M
37	S	M	M	S	S	VL
38	S	M	M	S	M	L
39	S	M	M	S	L	LM
40	S	M	M	M	S	L
41	S	M	M	M	M	LM
42	S	M	M	M	L	M
43	S	M	M	H	S	LM
44	S	M	M	H	M	M
45	S	M	M	H	L	MH
46	S	M	H	S	S	L
47	S	M	H	S	M	LM
48	S	M	H	S	L	M
49	S	M	H	M	S	LM
50	S	M	H	M	M	M
51	S	M	H	M	L	MH
52	S	M	H	H	S	M
53	S	M	H	H	M	MH
54	S	M	H	H	L	H
55	S	H	S	S	S	VL
56	S	H	S	S	M	L
57	S	H	S	S	L	LM
58	S	H	S	M	S	L
59	S	H	S	M	M	LM
60	S	H	S	M	L	M
61	S	H	S	H	S	LM
62	S	H	S	H	M	M
63	S	H	S	H	L	MH
64	S	H	M	S	S	L
65	S	H	M	S	M	LM
66	S	H	M	S	L	M
67	S	H	M	M	S	LM
68	S	H	M	M	M	M
69	S	H	M	M	L	MH
70	S	H	M	H	S	M
71	S	H	M	H	M	MH
72	S	H	M	H	L	H
73	S	H	H	S	S	LM

74	S	H	H	S	M	M
75	S	H	H	S	L	MH
76	S	H	H	M	S	M
77	S	H	H	M	M	MH
78	S	H	H	M	L	H
79	S	H	H	H	S	MH
80	S	H	H	H	M	H
81	S	H	H	H	L	VH
82	M	S	S	S	S	VVL
83	M	S	S	S	M	VL
84	M	S	S	S	L	L
85	M	S	S	M	S	VL
86	M	S	S	M	M	L
87	M	S	S	M	L	LM
88	M	S	S	H	S	L
89	M	S	S	H	M	LM
90	M	S	S	H	L	M
91	M	S	M	S	S	VL
92	M	S	M	S	M	L
93	M	S	M	S	L	LM
94	M	S	M	M	S	L
95	M	S	M	M	M	LM
96	M	S	M	M	L	M
97	M	S	M	H	S	LM
98	M	S	M	H	M	M
99	M	S	M	H	L	MH
100	M	S	H	S	S	L
101	M	S	H	S	M	LM
102	M	S	H	S	L	M
103	M	S	H	M	S	LM
104	M	S	H	M	M	M
105	M	S	H	M	L	MH
106	M	S	H	H	S	M
107	M	S	H	H	M	MH
108	M	S	H	H	L	H
109	M	M	S	S	S	VL
110	M	M	S	S	M	L
111	M	M	S	S	L	LM
112	M	M	S	M	S	L
113	M	M	S	M	M	LM
114	M	M	S	M	L	M

115	M	M	S	H	S	LM
116	M	M	S	H	M	M
117	M	M	S	H	L	MH
118	M	M	M	S	S	L
119	M	M	M	S	M	LM
120	M	M	M	S	L	M
121	M	M	M	M	S	LM
122	M	M	M	M	M	M
123	M	M	M	M	L	MH
124	M	M	M	H	S	M
125	M	M	M	H	M	MH
126	M	M	M	H	L	H
127	M	M	H	S	S	LM
128	M	M	H	S	M	M
129	M	M	H	S	L	MH
130	M	M	H	M	S	M
131	M	M	H	M	M	MH
132	M	M	H	M	L	H
133	M	M	H	H	S	MH
134	M	M	H	H	M	H
135	M	M	H	H	L	VH
136	M	H	S	S	S	L
137	M	H	S	S	M	LM
138	M	H	S	S	L	M
139	M	H	S	M	S	LM
140	M	H	S	M	M	M
141	M	H	S	M	L	MH
142	M	H	S	H	S	M
143	M	H	S	H	M	MH
144	M	H	S	H	L	H
145	M	H	M	S	S	LM
146	M	H	M	S	M	M
147	M	H	M	S	L	MH
148	M	H	M	M	S	M
149	M	H	M	M	M	MH
150	M	H	M	M	L	H
151	M	H	M	H	S	MH
152	M	H	M	H	M	H
153	M	H	M	H	L	VH
154	M	H	H	S	S	M
155	M	H	H	S	M	MH

156	M	H	H	S	L	H
157	M	H	H	M	S	MH
158	M	H	H	M	M	H
159	M	H	H	M	L	VH
160	M	H	H	H	S	H
161	M	H	H	H	M	VH
162	M	H	H	H	L	VVH
163	H	S	S	S	S	VL
164	H	S	S	S	M	L
165	H	S	S	S	L	LM
166	H	S	S	M	S	L
167	H	S	S	M	M	LM
168	H	S	S	M	L	M
169	H	S	S	H	S	LM
170	H	S	S	H	M	M
171	H	S	S	H	L	MH
172	H	S	M	S	S	L
173	H	S	M	S	M	LM
174	H	S	M	S	L	M
175	H	S	M	M	S	LM
176	H	S	M	M	M	M
177	H	S	M	M	L	MH
178	H	S	M	H	S	M
179	H	S	M	H	M	MH
180	H	S	M	H	L	H
181	H	S	H	S	S	LM
182	H	S	H	S	M	M
183	H	S	H	S	L	MH
184	H	S	H	M	S	M
185	H	S	H	M	M	MH
186	H	S	H	M	L	H
187	H	S	H	H	S	MH
188	H	S	H	H	M	H
189	H	S	H	H	L	VH
190	H	M	S	S	S	L
191	H	M	S	S	M	LM
192	H	M	S	S	L	M
193	H	M	S	M	S	LM
194	H	M	S	M	M	M
195	H	M	S	M	L	MH
196	H	M	S	H	S	M

197	H	M	S	H	M	MH
198	H	M	S	H	L	H
199	H	M	M	S	S	LM
200	H	M	M	S	M	M
201	H	M	M	S	L	MH
202	H	M	M	M	S	M
203	H	M	M	M	M	MH
204	H	M	M	M	L	H
205	H	M	M	H	S	MH
206	H	M	M	H	M	H
207	H	M	M	H	L	VH
208	H	M	H	S	S	M
209	H	M	H	S	M	MH
210	H	M	H	S	L	H
211	H	M	H	M	S	MH
212	H	M	H	M	M	H
213	H	M	H	M	L	VH
214	H	M	H	H	S	H
215	H	M	H	H	M	VH
216	H	M	H	H	L	VVH
217	H	H	S	S	S	LM
218	H	H	S	S	M	M
219	H	H	S	S	L	MH
220	H	H	S	M	S	M
221	H	H	S	M	M	MH
222	H	H	S	M	L	H
223	H	H	S	H	S	MH
224	H	H	S	H	M	H
225	H	H	S	H	L	VH
226	H	H	M	S	S	M
227	H	H	M	S	M	MH
228	H	H	M	S	L	H
229	H	H	M	M	S	MH
230	H	H	M	M	M	H
231	H	H	M	M	L	VH
232	H	H	M	H	S	H
233	H	H	M	H	M	VH
234	H	H	M	H	L	VVH
235	H	H	H	S	S	MH
236	H	H	H	S	M	H
237	H	H	H	S	L	VH

238	H	H	H	M	S	H
239	H	H	H	M	M	VH
240	H	H	H	M	L	VVH
241	H	H	H	H	S	VH
242	H	H	H	H	M	VVH
243	H	H	H	H	L	VVH

VVL-Very very low; VL-Very low; L-low; LM-between low and medium; M-medium; MH-between medium and high; H-high; VH-very high; VVH-very very high

Appendix-II

The mean square error (MSE) at n^{th} iteration is defined as:

$$MSE(n) = \xi(n) = \frac{1}{2Nl_O}\sum_i^N \sum_k^{l_O} \left(T_k^i - O_{kO}^i(n)\right)^2 \quad \text{(A.1)}$$

where, N is the total number of training patterns, l_O is the total number of output neuron, T_k^i is the target output of k^{th} output neuron for i^{th} input pattern and $O_{kO}^i(n)$ is the output at n^{th} iteration from k^{th} output neuron with i^{th} input pattern which can be calculated as follows:

$$O_{kO}^i(n) = \frac{1}{(1+e^{-S_{kO}^i(n)})} \quad \text{(A.2)}$$

where

$$S_{kO}^i(n) = \sum_{j=0}^H V_{jk}(n) R_j^i(n) \quad \text{(A.3)}$$

and

$$R_j^i(n) = e^{-\left(\frac{\left\|Y_i - C_j(n)\right\|^2}{2(\sigma_j(n))^2}\right)} \quad \text{(A.4)}$$

where, $S_{kO}^i(n)$ is the is weighted sum of the k^{th} output neuron with i^{th} input pattern in the n^{th} iteration, $V_{jk}(n)$ is the connection weight between the j^{th} hidden neuron and the k^{th} output neuron at the n^{th} iteration, $R_j^i(n)$ is the output of j^{th} hidden neuron with i^{th} input pattern in the n^{th} iteration, Y_i is the i^{th} input pattern, $C_j(n)$ is the is the j^{th} centre of the Gaussian function at the n^{th} iteration and $\sigma_j(n)$ is the spread of j^{th} Gaussian function at the n^{th} iteration.

Part A- Weight updatation equation

By applying the chain rule for derivatives we get

$$\frac{\partial \xi(n)}{\partial V_{jk}(n)} = \frac{\partial \xi(n)}{\partial O_{kO}^i(n)} \frac{\partial O_{kO}^i(n)}{\partial S_{kO}^i(n)} \frac{\partial S_{kO}^i(n)}{\partial V_{jk}(n)} \quad \text{(A.5)}$$

The computation of all the three terms on the right hand side of **Eq. A.5** are as follows.

Computing 1st term:

$$\frac{\partial \xi(n)}{\partial O_{kO}^i(n)} = -\frac{1}{Nl_O}\sum_i^N \sum_k^{l_O}\left(T_k^i - O_{kO}^i\right) \quad \text{(A.6)}$$

Computing 2nd term:

$$\frac{\partial O_{kO}^i(n)}{\partial S_{kO}^i(n)} = \frac{O_{kO}^i(n)}{\left(1 - O_{kO}^i(n)\right)} \quad \text{(A.7)}$$

Computing 3rd term:

$$\frac{\partial S_{kO}^{i}(n)}{\partial V_{jk}(n)} = R_j^i(n) \tag{A.8}$$

By putting all partial derivatives together we obtain,

$$\frac{\partial \xi(n)}{\partial O_{kO}^{i}(n)} = -\frac{1}{Nl_O}\sum_i^N \sum_k^{l_O}\left(T_k^i - O_{kO}^i\right)O_{kO}^i(n)\left(1 - O_{kO}^i(n)\right)R_j^i(n) \tag{A.9}$$

Part B- Center updatation equation

By applying the chain rule for derivatives we get,

$$\frac{\partial \xi(n)}{\partial C_j(n)} = -\frac{1}{Nl_O}\sum_i^N \sum_k^{l_O}\frac{\partial \xi(n)}{\partial O_{kO}^{i}(n)}\frac{\partial O_{kO}^{i}(n)}{\partial S_{kO}^{i}(n)}\frac{\partial S_{kO}^{i}(n)}{\partial R_j^i(n)}\frac{\partial R_j^i(n)}{\partial C_j(n)} \tag{A.10}$$

Computing 1st and 2nd term: Same as **Eq. A.6** and **Eq.A.7**, respectively

Computing 3rd term:

$$\frac{\partial S_{kO}^{i}(n)}{\partial R_j^i(n)} = V_{jk}(n) \tag{A.11}$$

Computing 4th term:

$$\frac{\partial R_j^i(n)}{\partial C_j(n)} = R_j^i(n)\frac{\left(Y_i - C_j(n)\right)}{(\sigma_j(n))^2} \tag{A.12}$$

By putting all partial derivatives together we obtain,

$$\frac{\partial \xi(n)}{\partial C_j(n)} = -\frac{1}{Nl_O}\sum_i^N \sum_k^{l_O}\left(T_k^i - O_{kO}^i\right)O_{kO}^i(n)\left(1 - O_{kO}^i(n)\right)V_{jk}(n)R_j^i(n)\frac{\left(Y_i - C_j(n)\right)}{(\sigma_j(n))^2} \tag{A.13}$$

Part C- Updatation equation for width of Gaussian function

By applying the chain rule for derivatives we get,

$$\frac{\partial \xi(n)}{\partial (\sigma_j(n))^2} = -\frac{1}{Nl_O}\sum_i^N \sum_k^{l_O}\frac{\partial \xi(n)}{\partial O_{kO}^{i}(n)}\frac{\partial O_{kO}^{i}(n)}{\partial S_{kO}^{i}(n)}\frac{\partial S_{kO}^{i}(n)}{\partial R_j^i(n)}\frac{\partial R_j^i(n)}{\partial (\sigma_j(n))^2} \tag{A.14}$$

Computing 1st, 2nd and 3rd term: Same as **Eq. A.6**, **Eq. A.7** and **Eq. A.11**, respectively

Computing 4th term:

$$\frac{\partial R_j^i(n)}{\partial \sigma_j(n)} = R_j^i(n)\frac{\left(Y_i - C_j(n)\right)^2}{2(\sigma_j(n))^4} \tag{A.15}$$

By putting all partial derivatives together we obtain,

$$\frac{\partial \xi(n)}{\partial \sigma_j(n)} = -\frac{1}{Nl_O}\sum_i^N \sum_k^{l_O}\left(T_k^i - O_{kO}^i\right)O_{kO}^i(n)\left(1 - O_{kO}^i(n)\right)V_{jk}(n)R_j^i(n)\frac{\left(Y_i - C_j(n)\right)^2}{2\left(\sigma_j(n)\right)^4} \tag{A.16}$$

Publications

Journals

1. ***Biswajit Parida****, Sukhomay Pal,* "Design and Development of Fixture and Force Measuring System for Friction Stir Welding Process Using Strain Gauges", Journal of Mechanical Science and Technology, Vol. 29 (2) (2015) 739-749.
2. ***Biswajit Parida****, Sukhomay Pal,* "A fuzzy based grey Taguchi approach for the optimization of multiple weld quality properties in friction stir welding process" Science and Technology of Welding and Joining, Vol. 20 (1) (2015) 35-41.
3. ***Biswajit Parida****, Sukhomay Pal,* "Assessment of Contribution of Process Parameters on Weld Qualities in Friction Stir Welding" International Journal of Materials and Product Technology, *(Under Review).*
4. ***Biswajit Parida****, Sukhomay Pal,* "Finding Appropriate Starting Position and Elimination of the End Hole Problems in FSW", Welding Journal, American Welding Society, *(Under Review).*
5. ***Biswajit Parida****, Sukhomay Pal,* "Application of Various Methods for Optimization of Multi-response Quality Characteristics in Friction Stir Welding", International Journal of Advanced Manufacturing Technology, *(Under Review).*
6. ***Biswajit Parida****, Sukhomay Pal,* "A Hybrid Neuro Evolutionary Algorithm Technique for Optimization of FSW Process Parameters", Applied Soft Computing, *(Under Review).*
7. ***Biswajit Parida****, Sukhomay Pal,* "An Overall Review of Research Work in Friction Stir Welding Process", CIRP Journal of Manufacturing Science and Technology, *(Under Review).*
8. ***Biswajit Parida****, Sukhomay Pal,* "Prediction of Weld Quality Using Artificial Neural Network Models for Friction Stir Welded Aluminium Alloys. *(Under Preparation).*

Conferences

1. ***Biswajit Parida*** *and Sukhomay Pal,* "Effect of Process Parameters on Tensile Properties of Friction Stir Welded Joints" 5th International and 26th All India Manufacturing Technology, Design and Research Conference (AIMTDR 2014), 12-14th December, (2014), IIT, Guwahati.
2. ***Biswajit Parida*** *and Sukhomay Pal,* "Effect of Tool Geometry and RPM on Tensile Properties of Friction Stir Welded Aluminium Joints" Twenty-Third International Conference on Processing and Fabrication of Advanced Materials (PFAM-XXIII), 5-7th December, (2014), IIT, Roorkee.
3. ***Biswajit Parida*** *and Sukhomay Pal,* "Statistical Analysis on Tensile Property of Friction Stir Welded Aluminium Alloy" International Institute of Welding - International Congress (ICIIW 2014), 9-11th April, (2014), New Delhi.
4. ***Biswajit Parida*** *and Sukhomay Pal,* "Effect of Friction Stir welding Parameters and Tool Geometry on Shoulder-Workpiece Interface Temperature" International Conference on Intelligent Robotics, Automation and Manufacturing (IRAM 2013), 16-18th December, (2013), IIT, Indore.
5. ***Biswajit Parida****, Prakash Kumar Sahu, Sukhomay Pal,* "Effect of Process Parameters and Tool Geometry on Microhardness of Friction Stir Welded Joints." An International Conference on Precision, Meso, Micro and Nano Engineering (COPEN-8 2013), 13-15th December, (2013), NIT, Calicut.
6. *Shivdayal Vishwakarma,* ***Biswajit Parida*** *and Sukhomay Pal,* "Design and Development of Force and Torque Measuring System for Use in Friction Stir Welding Process" International Symposium on Processing and Fabrication of Advanced Materials (PFAM-21), 10-13th December, (2012), IIT, Guwahati.
7. ***Biswajit Parida*** *and Sukhomay Pal,* "Overview of Friction Stir Welding" International Conference on Mechatronics, Robotics and Manufacturing (ICMRM 2011), 11-12th December, (2011), IIMT, Bhubaneswar.